

UNIVERSIDAD DE GRANADA



Tesis Doctoral

**Time Domain Discontinuous Galerkin
Methods for Maxwell equations**

Memoria presentada por

Luis Manuel Diaz Angulo

para optar al grado de Doctor por la Universidad de Granada

Realizada en la

Facultad de Ciencias

Departamento de Electromagnetismo y Física de la Materia

en el programa de doctorado de

Física y Matemáticas

Bajo la dirección de los Doctores:

Mario Fernandez Pantoja

Salvador González García

Jesús Álvarez González

Editor: Editorial de la Universidad de Granada
Autor: Luis Manuel Díaz Angulo
D.L.: GR 259-2015
ISBN: 978-84-9083-284-4

Declaración de Autoría

El doctorando Luis Manuel Diaz Angulo y los directores de la tesis D. Mario Fernandez Pantoja, D. Salvador González García y D. Jesús Álvarez González, garantizamos, al firmar esta tesis doctoral, que el trabajo ha sido realizado por el doctorando bajo la dirección de los directores de la tesis y hasta donde nuestro conocimiento alcanza, en la realización del trabajo, se han respetado los derechos de otros autores a ser citados, cuando se han utilizado sus resultados o publicaciones.

Granada, 18 de Septiembre de dos mil catorce

Director/es de la Tesis

Doctorando

Fdo. Mario Fernandez Pantoja

Fdo. Luis Manuel Diaz Angulo

Fdo. Salvador González García

Fdo. Jesús Álvarez González

D. Mario Fernandez Pantoja, Doctor en Ciencias Físicas, Profesor Titular de Electromagnetismo del Departamento de Electromagnetismo y Física de la Materia de la Facultad de Ciencias de la Universidad de Granada,

D. Salvador González García, Doctor en Ciencias Físicas, Profesor Titular de Electromagnetismo del Departamento de Electromagnetismo y Física de la Materia de la Facultad de Ciencias de la Universidad de Granada, y

D. Jesús Álvarez González, Doctor en Físicas y Ciencias del Espacio por la Universidad de Granada, Ingeniero Senior de Compatibilidad Electromagnética y Antenas en la empresa Airbus Defense and Space. Miembro, como Investigador, del Grupo de Electromagnetismo de la Universidad de Granada. Profesor en el Master Integración de Sistemas de Aeronaves impartido por la Universidad Carlos III de Madrid.

CERTIFICAN

Que el trabajo de investigación que se presenta en esta Memoria, titulado TIME DOMAIN DISCONTINUOUS GALERKIN METHODS FOR MAXWELL'S EQUATIONS, ha sido realizado en este Departamento por el Licenciado en Física D. Luis Manuel Diaz Angulo bajo nuestra dirección, y constituye su Tesis Doctoral.

Con esta fecha autorizamos su presentación ante la Comisión de Doctorado de la Universidad de Granada.

Granada, 18 de Septiembre de dos mil catorce

Fdo. Mario Fernandez Pantoja

Fdo. Salvador González García

Fdo. Jesús Álvarez González

A mi madre y hermano

En memoria de mi padre y abuelos

– Suppose the abdominal illness is caused precisely in the way you have described, –said a physician with a thick Danish accent–. Do you then suggest a cure?

– I know of no cure.

There were groans.

– Then why does it matter a whitewash whether or not we understand the origin of the disease? –Others voiced agreement, forgetting how much they loathed Danes in their unified eagerness to oppose the newcomer.

– Medicine is like the slow raising of masonry, –Rob said–, We are fortunate, in a lifetime, to be able to lay a single brick. If we can explain the disease, someone yet unborn may devise a cure.

Noah Gordon, *The physician*

– Supongamos que la enfermedad abdominal se desarrolle precisamente de la forma que habéis descrito –dijo un médico con fuerte acento danés–. ¿Sugerís alguna cura?

– No conozco ninguna cura.

Se oyeron protestas.

– Entonces, ¿que importancia puede tener un gusanito si no conocemos el origen de la enfermedad? –vocearon otros, olvidando cuanto odiaban a los daneses, con tal de unirse en su oposición al recién llegado.

– La medicina es como una lenta obra de albañilería –razonó Rob–. Somos afortunados si en el plazo de una vida podemos poner un solo ladrillo. Y si podemos explicar la enfermedad, alguien que aun no ha nacido estará en condiciones de conseguir su curación.

Noah Gordon, *El médico*

Agradecimientos

Esta página es, en cierto modo, parte del prólogo de una obra y también el epílogo de una etapa. Esta página está dedicada a todos los que han estado ahí, no sólo aguantándome, si no apoyándome y sacrificándose de muchas formas distintas para que yo haya podido escribir este tostón de difícil lectura.

En primer lugar, me gustaría agradecer a mi madre y a mi hermano por haber estado ahí siempre que les he necesitado.

Nada de esto hubiera sido posible sin las personas que forman el Grupo de Electromagnetismo de Granada, cuyo trabajo ha sido imprescindible para que esto haya salido adelante: en primer lugar a Rafael por haberme dado la oportunidad de desarrollar mi labor en el GEG, a Amelia por el tiempo y cariño que ha dedicado en todos los aspectos formales, a Carlos, Javi, Miguel, Enrique... por haber compartido muchas de las frustraciones y alegrías con las que nos hemos encontrado a lo largo de estos años. En particular me gustaría agradecer a Salvador todo su trabajo. Es el mejor director que he podido tener, ha puesto una cantidad enorme de esfuerzo personal para que yo pudiera tener el tiempo de investigar lo que aquí aparece. Su guía y consejos han sido, sin duda, esenciales. A Mario por su dirección en el proyecto de investigación que ha servido para financiar este trabajo. Agradezco también particularmente al Jesús por ayudarme a entender, con infinita paciencia, las innumerables sutilezas del método que es objeto de estudio en esta tesis.

También me gustaría agradecer a Fernando L. Teixeira y a Stephane Lanteri el haberme permitido realizar estancias en sus centros de investigación, ambas han sido experiencias inolvidables.

Y por supuesto a todas las personas que han estado conmigo en esta etapa que ahora se cierra: Flora, los Zorongos, Joaquín, la peña de comedores y tantos otros.

A todos, sinceramente, gracias.

The work described in this dissertation has been partially funded through the European Community's Seventh Framework Programme FP7/2007-2013, under grant agreement no 205294 (HIRF SE project), and his work is partially funded by the National Projects TEC2010-20841-C04-04, TEC2013-48414-C3-01, CSD2008-00068, P09-TIC-5327, P12-TIC-1442, and from the GENIL excellence network.

Abstract

This dissertation presents a collection of academic works published or submitted for publication in scientific journals. It is composed of 14 chapters, each corresponding to an article, grouped in six different parts.

The first part (Chapter 1) is a review of the state of the art of the Discontinuous Galerkin Time Domain (DGTD) method which is the main topic of this work. It serves as an introduction for the rest of the text as it explains the mathematical foundations and the techniques used to model different electromagnetic phenomena.

The second part (Chapters 2, 3, and 4) is focused on the DG semi-discretization. Chapter 2 investigates the presence of spurious modes and provides ways to eliminate their presence. Chapter 3 presents an hybridization of the Continuous Galerkin (CG) and DG techniques as a way to reduce memory consumption and improve computational efficiency. Finally, in Chapter 4, an study on the accuracy of the DG method is presented.

The third part (Chapters 5 and 6) discusses two techniques that can be used for the time integration of the method. In Chapter 5, a novel Local Time-Stepping (LTS) technique is presented. Chapter 6 presents a method in which a DG formalism is used also for the discretization of time resulting in the Space-Time DG (STDG) method.

The fourth part (Chapters 7 and 8). Covers the topic of modeling. Chapter 7 is dedicated to the modeling of electromagnetic sources and Chapter 8 is dedicated to the accurate modeling of anisotropic materials.

The fifth part (Chapters 9, 10, and 11) presents a comparison of some results using DGTD or other methods in different scenarios.

The sixth part (Chapters 12, 13, and 14) presents other works that have been carried out during this period of research.

Contents

Declaración de Autoría	I
Agradecimientos	IX
Abstract	XIII
List of Figures	XXI
List of Tables	XXVII
Abbreviations	XXIX
I An Introduction to DGTD	1
1 Discontinuous Galerkin Time Domain Methods in Computational Electrodynamics: State of the Art	3
1.1 Introduction	4
1.2 Overview of time-domain numerical methods	5
1.2.1 Finite Differences in Time Domain (FDTD)	5
1.2.2 Finite Volume Methods (FVTD)	6
1.2.3 Finite Element Methods (FEMTD)	6
1.2.4 Discontinuous Galerkin Methods	7
1.3 Applications of DGTD	7
1.3.1 Multi-scale problems	8
1.3.2 Electromagnetic Compatibility (EMC)	8
1.3.3 Antennas	8
1.3.4 Waveguides	9
1.3.5 Radar Cross Section	9
1.3.6 Ground Penetrating Radar (GPR)	9
1.4 The Discontinuous Galerkin Method	9
1.4.1 The Galerkin method	10
1.4.2 Numerical flux	12
1.4.3 Semi-discretized form	14
1.4.4 Boundary conditions	15

1.4.4.1	Perfectly Electric Conducting (PEC)	15
1.4.4.2	Perfectly Magnetic Conducting (PMC)	15
1.4.4.3	Silver-Mueller Absorbing (SMA)	16
1.4.5	Convergence and spurious modes	16
1.4.5.1	Convergence	17
1.4.5.2	Spurious modes	18
1.4.6	Vector/Nodal basis functions	19
1.4.6.1	Vector basis functions	20
1.4.6.2	Nodal basis functions	20
1.4.7	Curved cells	22
1.4.8	Non-conformal meshes	23
1.4.9	Hybrid meshes	24
1.5	Time integration	24
1.5.1	Leapfrog time integration	26
1.5.1.1	Second order leapfrog (LF2)	26
1.5.1.2	Convergence and spectral properties	27
1.5.1.3	Higher order LF	27
1.5.2	Low-Storage Explicit Runge Kutta time integration	28
1.5.2.1	Convergence and spectral properties	29
1.5.3	Achieving larger global timesteps	29
1.5.3.1	Local Time Stepping (LTS)	29
1.5.3.2	Implicit-Explicit (IMEX) schemes	31
1.5.3.3	Predictor-Corrector time integration	31
1.5.3.4	Tailored LSERK schemes	31
1.5.3.5	Strong Stability Preserving RK (SSP-RK) schemes	31
1.5.3.6	Space-time Discontinuous Galerkin (STDG)	32
1.6	Electromagnetic Sources	32
1.6.1	Plane wave	32
1.6.2	Local sources and radiation patterns	33
1.6.3	Waveports	34
1.6.3.1	TEM port	34
1.6.3.2	Waveguide modes	34
1.7	Advanced material modeling	36
1.7.1	Conformal Perfectly Matched Layer	36
1.7.1.1	Anisotropic Conformal PML	38
1.7.1.2	Cartesian PML	39
1.7.1.3	Constant/Varying conductivities	41
1.7.2	Dispersive materials	42
1.7.2.1	General Formulation	42
1.7.2.2	Stability of dispersive models	43
1.7.3	Anisotropic materials	44
1.8	Subcell models	44
1.8.1	Lumped elements	45
1.8.2	Thin layers	45
1.8.3	Thin wire geometries	48
1.9	Computational implementation	48
1.9.1	Geometrical discretization	48

1.9.2	Preprocessing	49
1.9.2.1	Selection of basis functions	49
1.9.2.2	LTS Level classification	49
1.9.3	Parallelization	50
II	On Discontinuous Galerkin Method Theory	53
2	A spurious-free Discontinuous Galerkin Time Domain method for the accurate modeling of microwave filters	55
2.1	Introduction	56
2.2	DGTD fundamentals	57
2.2.1	Vector formulation	57
2.2.2	Scalar-basis (nodal) formulation	60
2.2.3	Numerical fluxes	61
2.3	Numerical dispersion and dissipation	62
2.4	Application to waveguide filters	69
2.5	Conclusions	74
3	A Nodal Hybrid Continuous-Discontinuous Galerkin Time Domain Method for Maxwell's Equations	77
3.1	Introduction	78
3.2	Nodal Galerkin TD Formulations for Maxwell Equations	80
3.2.1	Continuous Galerkin	81
3.2.2	Discontinuous Galerkin	81
3.3	CGTD vs DGTD: the CDGTD method	82
3.4	Numerical properties	84
3.4.1	Convergence	86
3.4.2	Spectral properties	87
3.5	Computational cost	87
3.6	Numerical test: 2D cavity	95
3.6.1	Resonances	95
3.6.2	Convergence with respect to h-refinement	95
3.7	Conclusions	97
4	An analysis of the Leap-Frog Discontinuous Galerkin method for Maxwell's equations	101
4.1	Introduction	102
4.2	LFDG algorithm	103
4.2.1	Semi-discrete DG formulation	103
4.2.2	Leap-Frog time integration formulation	104
4.3	Description of the eigenvalue problems	105
4.3.1	DG semi-discrete scheme	105
4.3.2	Fully discrete LFDG algorithm	107
4.4	Convergence analysis	108
4.5	Anisotropy analysis	113
4.6	Computational cost vs. accuracy	116
4.7	Conclusions	119

III	On Time Integration techniques	121
5	Causal-Path Local Time-Stepping in the Discontinuous Galerkin Method for Maxwell’s equations	123
5.1	Introduction	124
5.2	Discontinuous Galerkin Semidiscretization	125
5.3	Time integration	126
5.3.1	Second-order Leap-Frog (LF2)	127
5.3.2	Low-Storage Explicit Runge–Kutta (LSERK4)	127
5.4	The Causal–Path LTS technique	128
5.4.1	LF2-CPLTS	130
5.4.2	LSERK4-CPLTS	131
5.5	Numerical Results	132
5.5.1	Reflection caused by a non-homogeneous mesh	133
5.5.2	PEC cavity resonances	135
5.5.3	RCS Analysis of a PEC Sphere	139
5.6	Tier assortment	140
5.7	Conclusions	143
6	Space-Time Discontinuous Galerkin	149
6.1	Introduction	150
6.2	Implicit Formulation	150
6.3	An explicit scheme	153
6.4	Numerical Analysis	154
6.5	Numerical Results	155
6.6	Conclusions	156
IV	On modeling	157
7	Source and boundary implementation in vector and scalar DGTD	159
7.1	Introduction	160
7.2	DGTD fundamentals	161
7.2.1	Scalar basis formulation	161
7.2.2	Vector–basis formulation	165
7.3	Boundary conditions	166
7.4	Results	168
7.4.1	Plane–wave generation	168
7.4.2	ABCs	169
7.5	Conclusions	170
8	3-D Discontinuous Galerkin Time-Domain Method for Anisotropic Materials	173
8.1	Introduction	174
8.2	DGTD fundamentals	174
8.3	Riemann problem (isotropic case)	175
8.4	Upwind flux for anisotropic materials	178
8.5	Semi-Discrete Scheme	180

8.6	Validation	181
8.7	Conclusions	182
V	On validation	183
9	A leap-frog discontinuous Galerkin time-domain method for HIRF assessment	185
9.1	Introduction	186
9.2	Formulations	187
9.2.1	DG formulation	187
9.2.2	LFDG algorithm	190
9.2.3	Conformal UPML formulation	191
9.2.4	The LFDG algorithm in PML regions	195
9.3	Numerical Validation in HIRF	196
9.3.1	Medium size 3D Object	196
9.3.2	Aircraft Simulation Case	197
9.4	Conclusions	203
10	DGTD for a Class of Low-Observable Targets: A Comparison with MoM and (2,2) FDTD	205
10.1	Introduction	206
10.2	LFDG fundamentals	206
10.3	MoM CCIE fundamentals	208
10.4	NASA Almond Benchmark	210
10.5	Conclusions	213
11	Discontinuous Galerkin Time Domain Method for GPR simulation	215
11.1	Introduction	215
11.2	DGTD theory	216
11.2.1	Vector elements formulation	216
11.2.2	Nodal elements formulation	220
11.3	Validation	221
11.4	Application to GPR problems	224
11.4.1	Object presence discrimination	224
11.4.2	Radargram simulation	225
11.5	Conclusions	226
VI	Other works	229
12	FDTD Modeling of Graphene Devices Using Complex Conjugate Dispersion Material Model	231
12.1	Introduction	232
12.2	Formulation of the dispersion model	233
12.2.1	Graphene conductivity	233
12.2.2	Complex conjugate pole-residue pair model	233
12.2.3	FDTD algorithm	236

12.3 Numerical Validation	236
12.4 Conclusion	237
13 Efficient excitation of Waveguides Crank Nicolson FDTD	239
13.1 Introduction	240
13.2 Discrete problem	240
13.3 Implementation into CN–FDTD	244
13.4 Results	244
13.5 Conclusions	245
14 Improving the SAR distribution in Petri-dish cell cultures	247
14.1 Introduction	248
14.2 Circular Petri dish	249
14.3 Elliptical Petri dishes	252
14.4 Metallic additions	253
14.5 Conclusions	256
A Resumen	257
A.1 Contribuciones Científicas y Futuras Líneas de Trabajo	259
A.1.1 Contribuciones Científicas	259
A.1.2 Futuras Líneas de Trabajo	261
Bibliography	263

List of Figures

1.1	Notation used for the definition of the numerical fluxes.	13
1.2	Normalized spectrum of the DG operator for a cubic domain (meshed with 24 tetrahedra) with periodic boundary conditions. We cannot see how the centered flux does not provide an isolated kernel, contrary to the upwind and penalized fluxes.	19
1.3	Power spectrum of the electric field at an arbitrary point inside a 1 m PEC cavity. The effect of the non-attenuation of the centered flux spectrum can be appreciated compared with the upwind and penalized fluxes.	19
1.4	Mapping from the reference element for linear (first geometrical order) and quadratic (second geometrical order) tetrahedrons.	23
1.5	RCS at 450 MHz of a 1m radius PEC sphere meshed with the same number of linear and quadratic tetrahedrons and a spatial basis of order $p = 3$. Results obtained with GEG-UGR SEMBA software (www.ugrfdtd.es).	24
1.6	Dissipation factors (left) and normalized phase velocities (right) for the LSERK4 (up) and LF2 (down) schemes. All the semi-discrete eigenvalues calculated depicted in figure 1.2 must lie within the regions delimited by the thick red line to ensure the stability of the fully discrete scheme. LF2 supports two modes arising from two solutions for the growing factor only the positive one is represented, please notice that the final form of the dissipation and phase velocities will depend on the combination of the two modes [1].)	26
1.7	Scattered field (orange) and total field regions (blue). The elements that need to have altered fluxes are marked in darker colors.	33
1.8	Darboux frame.	37
1.9	Bistatic RCS of an isotropic/anisotropic sphere ($D = 1.2\lambda$ and $\lambda = 1.0m$). LFDG results are compared to those appearing in [2], and computed with Ansoft HFSS.	45
1.10	Two-port representation of the air-embedded panel illuminated by a TEM plane wave.	46
1.11	Magnetic field controlled circuit representation of a thin layer.	46
1.12	Assortment of tiers for the use of a LTS technique.	50
1.13	Distribution of the mesh among the different MPI processes.	51
2.1	Numerical dispersion of a one dimensional, centered flux DGTD Scheme	65
2.2	Numerical dispersion of a one dimensional, upwind flux DGTD Scheme	66
2.3	Spectrum of the DG operator for a cubic domain (meshed with 24 tetrahedra) with PBC	68

2.4	Power spectrum PEC cavity.	69
2.5	Dual-mode circular waveguide filter dimensions and problem setup	71
2.6	Dual-mode circular waveguide filter near fields computation.	72
2.7	Dual-mode circular waveguide filter response. Measured and computed data comparison.	72
2.8	Evolution of the energy inside the dual-mode circular waveguide filter.	73
2.9	Single resonator composed of a rectangular cavity loaded by a dielectric cylindrical puck.	74
2.10	Evolution of the energy inside the single resonator filter.	74
2.11	S21 response of the single resonator filter. Measured and computed data comparison.	75
3.1	Convergence rates for DGTD and CDGTD schemes with upwind fluxes. Non-aligned values correspond to other modes also supported by the solutions but that do not correspond to the free-space mode.	86
3.2	Convergence rates for DGTD and CDGTD schemes with centered fluxes.	86
3.3	Eigenvalues spectrum loci for upwind fluxes schemes with polynomial basis up to order 3.	88
3.4	Eigenvalues spectrum loci for upwind fluxes schemes with polynomial basis of order $P = 2$, for different number of elements clustered.	89
3.5	Eigenvalues spectrum loci for upwind fluxes schemes with polynomial basis of different order for DGTD (black) and CDGTD with $K_c = 2$ (blue) schemes. As it can be seen, modes that do not belong to the physical eigenspectrum (dashed red) have large imaginary parts and are therefore quickly attenuated.	90
3.6	Different clusters assemblies considered for 2D and 3D CDG.	92
3.7	Resonances in a unit square PEC cavity for different methods. The simulations run up to a final time $T = 200$. The basis order is $P = 2$ and the mesh is a cross-hatch grid with $h = 1/8$. The CDGTD results have been obtained by clustering all cross-hatch cells. With centered fluxes, the CGTD and CDGTD method have some visible spurious modes polluting the spectrum at $\omega \simeq 1.7, 2.2, 2.8 \dots$	94
3.8	$h = 1/4$ and $h = 1/16$ meshes used to compute the resonant cavity results. Each of the cross-hatch elements is assembled to form a cluster.	97
3.9	A suitable partially structured mesh in which the CDGTD formalism would preferably be used only in cross-hatch regular tetrahedron clusters.	98
3.10	Interfacing between the simple-hatch cluster and a hex cell for $P = 2$	98
3.11	A region with high stiffness (grayed) can be assembled into a CDG cluster to improve the maximum time step allowed. The rest of the mesh can be evolved using a classical DGTD scheme.	99
4.1	Geometry under analysis for the eigenvalue problem	106
4.2	Convergence and influence of the τ parameter in the error of the DG operator for different p orders	109
4.3	Convergence of the physical mode for the LFDG algorithm with $\tau = 0.1$ and $\Delta t = 0.7\Delta t_{max}$	111

4.4	Influence of Δt in the error of the LFDG algorithm.	112
4.5	Convergence of the dispersion and dissipation errors of the LFDG algorithm computed with the numerical test	113
4.6	Anisotropy of the error for $\tau = 0.1$, $p = 2$ and $h = 0.2$	114
4.7	3D representations of the anisotropy of the error for $\tau = 0.1$, $h = 0.25$	115
4.8	Cuts of the dispersion error comparing the DG operator and the LFDG algorithm for order $p = 2$ and $h = 0.2$	115
4.9	Computational cost of the LFDG algorithm.	117
5.1	n -depth neighbourhood concept	130
5.2	Schematic view of the LF2-CPLTS algorithm for the case $h_1 = h_2 = 1/2$	131
5.3	LSEK4-CPLTS sketch	133
5.4	Meshes used for the study numerical reflections by an inhomogeneous mesh.	136
5.5	Numerical reflection from a single interface with ratio of 15:1	137
5.6	Numerical reflection from a single interface with ratio of 75:1	137
5.7	Numerical reflection from a slab with ratio of 7.5:1.	137
5.8	Resonances in a 1 m PEC cavity with slab meshing	138
5.9	Energy evolution in a 1 m PEC cavity with slab meshing.	139
5.10	Evolution of the $(E_{\text{analytical}} - E_{\text{numerical}})^2$ error at the center of the 1 m PEC cavity with slab meshing for a three harmonics initial condition.	139
5.11	Boundary conditions for the RCS case.	141
5.12	Bi-static RCS for a 1 m PEC sphere at different frequencies	142
5.13	Tier assortment for LSEK4. Tier 1 is not represented.	144
5.14	Elements in LSEK4 where some operations are required by the smaller tiers	144
5.15	Tier assortment for LF2-CPLTS.	145
5.16	Tier assortment for LF2-LTS.	146
5.17	Tier assortment for LSEK4-CPLTS	147
5.18	Tier assortment for LF2-CPLTS	147
5.19	Tier assortment for LF2-LTS	147
6.1	Notation: a space-time element (in gray) with $P^t = P^x = 3$	152
6.2	Dissipative (up)/dispersive (down) convergence rates of the eigenvalues of the evolution operator \mathcal{H} for different orders & h_t	155
6.3	Response to a white noise in the E-STDG and STDG schemes with $P^t = 4$, $h_t = 0.1$, $P^x = 4$, $K_x = 8$, $h_x = 0.125$ after a time of 100. Vertical dashed lines represent the analytical modes.	156
7.1	Total Field/Scattered Field decomposition.	168
7.2	Scattered field error as a function of the minimum space resolution	169
7.3	Energy decay in the simulation region after dipole illumination	171
7.4	Bistatic RCS of a 1 m radius PEC sphere at 300 MHz (DGTD)	171
7.5	Bistatic RCS of a 1 m radius PEC sphere at 300 MHz (FDTD)	172
8.1	Surface interface $\partial\mathcal{T}_m$ between two elements containing different materials	176
8.2	1D space-time (n - t plane) structure of the solution to the Riemann problem	178

8.3	Space–time structure of the anisotropic Riemann problem.	180
8.4	Bistatic RCS of an anisotropic/isotropic sphere ($D = 1.2\lambda$)	182
9.1	Conformal UPML setup.	192
9.2	Setup of the medium size 3D object.	197
9.3	Reception aperture results of the medium size 3D object.	198
9.4	External and internal geometry of the aircraft-simulation case.	199
9.5	Simulation setup for the aircraft-simulation case.	199
9.6	Screen shots of the aircraft-simulation case.	200
9.7	Computed transfer functions for the aircraft-simulation case.	200
10.1	Geometry of the NASA almond.	211
10.2	Snapshot of the NASA almond mesh	211
10.3	Bistatic RCS at 1 GHz of coated NASA almond (MoM,LFDG)	212
10.4	Monostatic RCS of the NASA almond for MoM and LFDG	213
10.5	Bistatic RCS of the NASA almond for (MoM,FDTD,LFDG)	213
11.1	Bistatic RCS of a 1 m radius PEC sphere at 300 MHz (DGTD)	222
11.2	Bistatic RCS of a 1 m radius PEC sphere at 300 MHz (FDTD)	223
11.3	Computational lay–out of the GPR detection system. PML boundary conditions are placed at the curved/straight boundaries.	223
11.4	Geometry of the TEM horn antenna.	224
11.5	Electric field observed with and without a buried sphere	225
11.6	Snapshot of the E_z field for the land-mine detection problem	227
11.7	Synthetic radargram for the landmine case	228
12.1	Surface conductivity of graphene for different μ_c	234
12.2	Comparison of the complex permittivity found by vector fitting to that found from the Kubo model.	235
12.3	Electric field of two parallel graphene sheets system (three modes)	237
12.4	Electric field of two parallel graphene sheets (anti-symmetric mode)	238
13.1	Arrangement of the fields at an edge of the guide	242
13.2	TE mode for a ridged rectangular waveguide	245
13.3	Propagation along the Z axis of the E_z component of a TM_{11} mode	246
14.1	Petri dish geometry	250
14.2	3D view of half Petri dish including the liquid and the meniscus	250
14.3	Average SAR calculated over the S_I region for different heights of the liquid.	251
14.4	Coefficient of variation in the S_I region for different heights of the liquid.	252
14.5	SAR distribution in the S_I region with a liquid height $h = 5\text{mm}$	252
14.6	Average SAR for different values of S_x and S_y	254
14.7	Inhomogeneity factor for different values of S_x and S_y	254
14.8	Geometry of the different metallic additions	255
14.9	Inhomogeneity factors for different metallic shapes calculated from 2 to 3 GHz.	255

14.10 Average SAR compared for the different metallic shapes from 2 to 3 GHz.	256
---	-----

List of Tables

1.1	Comparative summary of numerical methods with typical formulations	5
1.2	Parameters to yield centered, upwind, and partially penalized numerical fluxes.	13
1.3	Comparison of vector and nodal basis	19
1.4	Comparison of different time integration methods	25
1.5	Coefficients for the LSERK4 method	28
2.1	Number of elements (M) for each set of basis functions for the DMCWF case	71
2.2	Local time stepping level distribution for DMCWF problem.	71
2.3	Computational requirements of the different cases	73
2.4	Number of elements used for the single resonator case	75
3.1	Convergence rates using upwind and centered fluxes. Highlighted cells indicate the dominant term.	87
3.2	Maximum real parts and spectral radius. The increase on clustered elements allow the use of larger time steps. Note that for centered fluxes the real part is always zero up to machine precision and therefore the spectral radius is equal to the maximum real value.	89
3.3	DOF and a estimation of the computational costs of the DGTD and CDGTD schemes for a 2D cross-hatch cluster.	92
3.4	DOF and a estimation of the computational costs of the DGTD and CDGTD schemes for a 3D cross-hatch cluster.	93
3.5	L^2 error norm for different resolutions of the first mode of a unit square cavity after a simulated time of $4/\sqrt{2}$ (2 cycles). For all CDGTD cases, the time steps can be larger than those for DGTD, with smaller improvements for centered than for upwind flux. The number of DOFs with the CDGTD cross-hatch configuration are 40 ~ 60% less depending on the spatial order. Convergence ratios remain similar for all cases, except for the case $P = 1$, where a clear improvement is observed.	96
4.1	Results of the computational cost analysis for an accuracy of 10^{-2} per wavelength.	118
5.1	LSERK4 Coefficients	128
5.2	Element Tier assorting for LTS in the plane wave reflection.	135
5.3	Element Tier assorting for LTS in the resonant cavity and RCS problems.	140

9.1	Parameters of the different numerical flux functions	189
9.2	Number of elements used for the Aircraft Simulation Case	201
9.3	LTS level distribution for the Aircraft Simulation	201
9.4	FDTD vs LFDG Comparison.	202
12.1	Fitted pole-residue pairs for the graphene model used	235
13.1	Closed form of the discrete TE and TM modes for a rectangular waveguide of size $a \times b$	243

Abbreviations

ABC	Absorbing Boundary Condition
ADE	Auxiliary Differential Equation
ADER	Arbitrary High Order DERivatives
BEM	Boundary Element Method
CAD	Computer-Aided Design
CCIE	Current and Charge Integral Equation
CCPR	Complex-Conjugate Pole-Residue
CEM	Computational ElectroMagnetics
CFD	Computational Fluid Dynamics
CFL	Courant Friederichs Lewy
CDG	Continuous-Discontinuous Galerkin
CG	Continuous Galerkin
CP-LTS	Causal-Path Local Time Stepping
CPML	Conformal PML
CN	Crank-Nicolson
DG	Discontinuous Galerkin
DGTD	Discontinuous Galerkin Time Domain
DMCWF	Dual-Mode Circular Waveguide Filter
DOF	Degree Of Freedom
EMC	ElectroMagnetic Compatibility
EMI	ElectroMagnetic Interference
E-STDG	Explicit STDG
FD	Frequency Domain
FDTD	Finite Differences Time Domain
FE or FEM	Finite Elements Method
FEMTD	Finite Elements Time Domain
FIT	Finite Integration Technique
FVTD	Finite Volumes Time Domain
GPR	Ground Penetrating Radar
HDG	Hybridizable Discontinuous Galerkin

HIRF	H igh I ntensity R adiated F ields
IC	I ntegrated C ircuit
IR	I nfra- R ed
IMEX	I Mplicit E Xplicit
LDG	L ocal D iscontinuous G alerkin
LF2	2 nd order L eap- F rog
LGL	L egendre G auss L obatto
LHS	L eft H and S ide
LO	L ow O bservable
LSRK4	4 th Order L ow- S torage R unge- K utta
LTS	L ocal T ime S tepping
MFC	M agnetic F ield C ontrolled
MIM	M etal I nsulator M etal
MLFMM	M ulti L evel F ast M ultipole M ethod
MoM	M ethod o f M oments
MPI	M essage P assing I nterface
ODE	O rdinary D ifferential E quation
OMP	O pen M ulti- P rocessing
PBC	P eriodic B oundary C ondition
PDE	P artial D ifferential E quation
PEC	P erfect E lectric C onductor
PMC	P erfect M agnetic C onductor
PML	P erfectly M atched L ayer
RAM	R adar A bsorber M aterial
RCS	R adar C ross S ection
RF	R adio F requency
RHS	R ight H and S ide
SAR	S pecific A bsorption R ate
SEMBA	S imulador E lectro M agnético de B anda A ncha
SFZ	S cattered- F ield Z one
SIBC	S urface I mpedance B oundary C ondition
SMA	S ilver- M uller A bsorbing
SMA	S ub M iniature version A
SPP	S urface P lasmon P olariton
SSP-RK	S trong S tability P reserving R unge- K utta
STDG	S pace T ime D iscontinuous G alerkin
TD	T ime D omain
TE	T ransversal E lectric

TEM	T ransversal E lectro M agnetic
TFZ	T otal- F ield Z one
TLM	T ransmission L ine M ethod
TM	T ransversal M agnetic
UPML	U niaxial P ML
VHF	V ery H igh F requency
VSWR	V oltage S tanding- W ave R atio

Part I

An Introduction to DGTD

Chapter 1

Discontinuous Galerkin Time Domain Methods in Computational Electrodynamics: State of the Art

L. D. Angulo, J. Alvarez, M. F. Pantoja, S. G. Garcia, and A. R. Bretones. Discontinuous galerkin time domain methods in computational electrodynamics: State of the art. *Forum for Electromagnetic Research Methods and Application Technologies (FERMAT)*, Submitted

Abstract

This text reviews the state of the art of the Discontinuous Galerkin (DG) method applied to the solution of the Maxwell's equations in Time Domain (TD). The work is divided into two parts. In the first part, the mathematical formulation of the DGTD method, together with a review and discussion on the different ways to implement it is presented. The second part presents models and techniques to address usual needs in electromagnetic simulations such as plane wave illumination, local electromagnetic sources, wave port modeling, dispersive and/or anisotropic materials and sub-cell models, including lumped elements, thin layers, surface impedances, and thin wires.

1.1 Introduction

In the last years Discontinuous Galerkin time-domain (DGTD) techniques have reached a significant level of maturity demonstrating their capability of obtaining highly accurate results at an affordable computational cost. They have successfully been used to solve many kinds of differential equations in fields including: Computational Fluid Dynamics [4], Magnetohydrodynamics [5], Quantum mechanics [6], and Elastodynamics [7, 8]. In this paper, we will review some of the existing DGTD techniques with special emphasis on applications to Computational Electromagnetics (CEM).

The DG spatial discretization permits us to take advantage of using unstructured high-order finite elements. This allows an accurate discretization of the geometry using different sizes and types of cells (h -adaptivity), and also to obtain high-order convergence of the electromagnetic (EM) solution depending on the order of basis functions within each cell (p -adaptivity). The TD nature of the method, compared to its frequency-domain (FD) counterpart, offers benefits in several kinds of EM problems such as those where we need to study a transient field effect of an arbitrary time-signal excitation (e.g. lightning strikes, EMC coupling, ultra-wideband antennas), or the non-linear behavior of materials, components or networks, where TD offers a direct and efficient approach. To solve these problems, we have developed a solver: SEMBA (Simulador Electromagnetico de Banda Ancha) [9]. SEMBA implements many of the techniques that are reviewed in this text such as vector/nodal basis, centred/penalized/upwind fluxes, special materials, Local Time Stepping (LTS) techniques, hp -adaptivity, and OpenMP/MPI parallelization. These techniques have been thoroughly tested in a wide range of problems, demonstrating to provide robust and efficient solutions [10–26].

However, the aim of this paper is not restricted to describing only those directly tested by ourselves, but also to make a full review of the state-of-the-art including contributions found in the most recent literature. This text is divided into two parts: The first part (Sections 1.4 and 1.5) describes the mathematical foundation of the method, alternative introductory texts on this topic are [27–29]. Much of what is done in this part can be generalized to other partial differential equations (PDEs). The second part of this work (Sections 1.6, 1.7 and 1.8, and 1.9) is more specifically focused on the application of the method to real engineering problems. Several techniques to simulate electromagnetic sources, special materials (such as dispersive and anisotropic), and several sub-cell models will be introduced. Other text for some of the topics discussed in this part is [30].

1.2 Overview of time-domain numerical methods

Let us start by reviewing how DGTD relates to other TD numerical methods focusing on the most common full-wave methods used in CEM. The main features of the typical configurations of the techniques described below are summarized in table 1.1.

TABLE 1.1: Comparative summary of numerical methods with typical formulations

	FDTD	FVTD	DGTD	FEMTD (others)
Order of accuracy ^{a b}	$h^{2,c}$	h	h^{2p+1}	h^{2p}
Geometry adaptivity	No ^d	Yes	Yes	Yes
Spurious modes	No	No	Yes ^e /No ^f	Yes ^g /No ^h
Energy conservative ^b	Yes	Yes	Yes ^e /No ^f	Yes
Explicit form	Yes	Yes	Yes	No ⁱ
LTS, IMEX or similar	No	Yes	Yes	No
Parallel. simplicity	High	High	High	Low
Memory usage ^j	High	Very High	Low	Very Low
Memory locality	Very High	Low	High ^k	High ^k
Uses dual mesh	Yes	No	No ^l	No
Allows non-conformal mesh	No	Yes	Yes	No
h adaptivity	Yes	Yes	Yes	Yes
p adaptivity	No	No	Yes	Yes

^aFor global L^2 norm.

^bConsidering Spatial semi-discretization only.

^cHigher order spatial semi-discretizations are also available [31].

^dCan be alleviated with conformal [32] and subgridding [33] techniques.

^eWith centered fluxes.

^fWith penalized fluxes.

^gFor nodal basis

^hFor vector basis.

ⁱBut can be approximated [34].

^jFor a structured mesh. Not considering semi-discretized operators.

^kFor high orders.

^lImprovements using a dual mesh have been reported by [35].

1.2.1 Finite Differences in Time Domain (FDTD)

FDTD is a mature technique that has been extensively developed for more than 50 years. The classical FDTD method [36] employs a second order finite centered approximations for space and time derivatives in Maxwell's curl equations. This technique places the samples of the electric field in a rectilinear Cartesian grid while the magnetic field is sampled in the dual of this grid, resulting in what is known as the Yee's cell [37]. The fields are then advanced in a marching-on-in-time fashion using a second order leap-frog (LF2) algorithm. The final scheme is second order convergent with respect to spatial and temporal refinement.

The main advantages of the FDTD method are its computational efficiency, its naturally spurious free solutions and the fact that it is energy conservative. On the other hand, the need of a rectilinear grid and the staggering of the fields sampling imply a high degeneration of the geometrical information due to stair-casing effects. However, the FDTD method can be used together with geometrically conformal [32] or subgridding [33] techniques that alleviate this limitation. Higher order FDTD techniques can be formulated, but they require a larger stencil [31, 38, 39] that reduces significantly its computational efficiency. The Finite Integration Technique (FIT) and the Transmission Line Method (TLM) are closely related to FDTD. FIT starts from the Maxwell's curl equations in integral form and TLM from equivalent transmission line equations. The resulting algorithms share most of the features that we find in the FDTD method.

1.2.2 Finite Volume Methods (FVTD)

The FVTD technique emerged as an alternative to FDTD aiming to overcome its geometrical discretization constraints, avoiding the staggered spatial discretization of the fields. The most common formulation of FVTD is carried on tetrahedral elements for the Maxwell's curl equations [40–42]. The scheme is formulated by defining a system of equations in which the time derivative of the \vec{E} fields integrated in volume equals to the sum of all surface integrals of the spatial derivative of \vec{H} terms and vice-versa. The spatial semi-discretization is then evolved, similarly to the FDTD method, using an LF2 algorithm. The main drawback of FVTD is that its order of convergence is 1 [43] which is quite low. Moreover, the timestep is limited by a condition that depends on the shape of the elements and that is more restrictive than for the FDTD method. A way to mitigate this time-stepping constraint is to use local time stepping (LTS) techniques [40]. LTS can also be used for DGTD as we will describe in Section 1.5. FVTD can be formally seen as a zero-order DGTD method.

1.2.3 Finite Element Methods (FEMTD)

A variety of time-domain FEM schemes has been proposed [44] based on Maxwell's curl-curl equation or the hyperbolic system of curl equations (Ampere's and Faraday's laws). The second-order vector-wave curl-curl equation, typically solved by FEM in FD, can also be solved by FEM in TD [45–54] requiring only the computation of a single field (electric or magnetic). Its major drawback is that a global linear system of equations needs to be solved at each timestep. To reduce the number of

timesteps, unconditionally implicit time-integration schemes, e.g. Newmark-beta, can be used, at the expense of yielding quite ill-conditioned matrices [55].

Alternatives to the single-field scheme are found by employing the two first-order coupled Maxwell's curl equations, either formulated by considering the electric field intensity \vec{E} and the magnetic flux density \vec{B} (E-B), or the electric field intensity \vec{E} and magnetic field intensity \vec{H} (E-H). These formulations offer certain advantages with respect to the single-field formulation, such as the possibility of using different expansion functions, avoiding spurious solutions. Moreover, the first-order time derivatives allow the use of a conventional LF2 time-integration method eliminating the need of saving previous states in memory. However, because of the tangential-continuity condition, they still require to solve a sparse linear system at each timestep, resulting in a computational cost comparable to that of the single-field scheme [56–61].

1.2.4 Discontinuous Galerkin Methods

A different family of FEM is found by relaxing the tangential-continuity condition, yielding the so-called discontinuous Galerkin methods (DGM). The continuity is imposed on numerical fluxes rather than on the tangential field components in order to connect the solution between adjacent elements. The main advantage of DGM over other FEM methods in TD is the fact that the linear system to be solved becomes block-diagonal by only requiring a single inversion of K square matrices of $N \times N$ elements (with K the number of elements and N the number of basis functions per element) which can be done at the pre-processing stage. One of the drawbacks is that the degrees of freedom (DOF) at the element interfaces are duplicated, a minor price considering the improvement in computational efficiency of the resulting explicit semi-discrete scheme [13, 22, 27, 62].

1.3 Applications of DGTD

The spectrum of engineering applications of CEM is extremely wide giving rise to a need of different numerical methods as there is not an ever-suitable method capable of solving all types of real-world EM problems [63]. The following is a non-exhaustive list of some areas where DGTD methods can be of particular interest:

1.3.1 Multi-scale problems

Any problem exhibiting disparate sizes, such as IC packaging or in-place antenna simulations, can greatly benefit from a DGTD approach [23, 25, 29, 64, 65] combined with LTS and *hp* adaptivity techniques.

1.3.2 Electromagnetic Compatibility (EMC)

EMC problems are an increasingly big concern for industry. Aircraft and car manufacturers perform CEM analysis to detect and solve possible EMC issues in eager stages of design. Simulations are usually performed to back measured data. However, sometimes measurements are difficult to perform, as in the case of lightning strikes or High-Intensity Radiated Fields (HIRF), and manufacturers have no other option than to rely exclusively on simulations. The degree of confidence put into this simulations is such that they have been allowed as valid tests for certification purposes [18, 66]. To perform EMC simulations a DGTD code often must include models for sub-cell thin wires and composites layers (Section 1.8) [17, 67, 68]. Moreover, these simulations are usually performed over electrically large problems and a high performance and accuracy simulation is a requirement.

1.3.3 Antennas

An essential characteristic for the accurate simulation of wideband antenna systems is the modeling of their intricate geometrical details [15, 25]. In these kinds of structures, an accurate modeling is critical in zones with small geometrical details, such as feeding ports. Frequency domain (FD) methods, such as the Method of Moments (MoM) or the Finite Element Method (FEM), are the usual choices for their capability of accurately modeling fine geometrical details. However, FD methods may become computationally inefficient for ultra-wideband analysis, since each frequency needs a complete simulation, typically involving a linear system resolution. Time-domain methods are a natural alternative for these purposes. Among them, DGTD methods are ideally suited for this purpose. LTS techniques, which are reviewed in Section 1.5 allow us to handle antenna geometries efficiently. Some techniques to model ports are described in section 1.6.3.

1.3.4 Waveguides

Like antennas, the simulation of waveguides usually needs the modeling of intricate geometries where DGTD offers an efficient solution. TD simulations allow us to estimate the resonant frequencies of these structures in a single run. Waveguides are usually very resonant structures where the absence of spurious modes is a must [13], a discussion on how to keep spurious modes under control is carried out in Section 1.4.5. Moreover, the electromagnetic waves, often imping at grazing angles of incidence at the terminations of the waveguide. This makes necessary the use of an special treatment at the terminations such as the use of Perfectly Matched Layers (PMLs) described in Section 1.7.1 or the multi-modal pseudo-analytical termination presented in [69].

1.3.5 Radar Cross Section

The analysis of the Radar Cross Section (RCS) of aircrafts can also be carried out with DGTD methods in an efficient manner [21, 23]. In this case, the TD nature allows us to efficiently perform mono-static RCS in a single run. The LTS technique, PMLs, Huygens sources (Section 1.6.1), and the ability to model complex geometries enables the method for this task. A comparison with other numerical techniques is presented in [21] where, for a broadband solution, the DGTD method is demonstrated to be competitive with other methods classically used for this task such as the MoM.

1.3.6 Ground Penetrating Radar (GPR)

GPR techniques can benefit from simulations when new antennas are being designed or complex geometries are under study. Simulations can help to understand in-the-field obtained data. Moreover, ground materials are usually dispersive and non-homogeneous, FEM and DGTD can model materials with gradually changing electrical properties in cells. Dispersive and lossy ground media can also be included [12, 70].

1.4 The Discontinuous Galerkin Method

Maxwell's curl equations for lossless isotropic linear media without sources are

$$\mu \frac{\partial \vec{H}}{\partial t} = -\nabla \times \vec{E} \quad (1.1)$$

$$\varepsilon \frac{\partial \vec{E}}{\partial t} = \nabla \times \vec{H} \quad (1.2)$$

with ε and μ being respectively the electric permittivity and the magnetic permeability that, for simplicity, we will assume to be homogeneous and isotropic. Dispersive media are treated in Section 1.7.2.

1.4.1 The Galerkin method

Let us call Ω the region where we want to solve equations (1.1) and (1.2) applying a DG formalism. This region Ω is tessellated with K non-overlapping elements V_k fully covering the computational domain Ω_K

$$\Omega \simeq \Omega_K = \bigcup_k^K V_k \quad (1.3)$$

For simplicity, we will suppress the subscripts k everywhere except in V_k , uniquely identifying the element where we are working. We assume that they can be inferred from the element where the Galerkin integrals are carried on. Within each element, the fields $\vec{E}(t, \vec{r})$ and $\vec{H}(t, \vec{r})$ are approximated by a projection over a set of N vector-basis functions

$$\mathcal{B} = \left\{ \vec{\psi}_1(\vec{r}), \vec{\psi}_2(\vec{r}), \dots, \vec{\psi}_N(\vec{r}) \right\} \quad (1.4)$$

The Galerkin problem consists on minimizing the inner product of the fields, projected over \mathcal{B} with respect to each of the functions basis (1.4) within each element V_k , leading to formulate eqs. (1.1) and (1.2) in weak form as

$$\int_{V_k} \vec{\psi}_i \cdot \left[\mu \frac{\partial \vec{H}}{\partial t} + \nabla \times \vec{E} \right] dV = 0 \quad (1.5)$$

$$\int_{V_k} \vec{\psi}_i \cdot \left[\varepsilon \frac{\partial \vec{E}}{\partial t} - \nabla \times \vec{H} \right] dV = 0 \quad (1.6)$$

with: $i = 1, \dots, N$

Let us now to explicitly write the approximation \vec{E} and \vec{H} as the projection over the same basis, \mathcal{B} . Thus

$$\vec{E} \simeq \vec{E}^h = \sum_j^N E_j^h(t) \vec{\psi}_j(\vec{r}) \doteq \vec{\psi}^T \mathbf{E} \quad (1.7)$$

$$\vec{H} \simeq \vec{H}^h = \sum_j^N H_j^h(t) \vec{\psi}_j(\vec{r}) \doteq \vec{\psi}^T \mathbf{H} \quad (1.8)$$

with

$$\vec{\psi} = [\vec{\psi}_1, \dots, \vec{\psi}_N]^T \quad (1.9)$$

$$\mathbf{E} = [E_1^h, \dots, E_N^h]^T \quad (1.10)$$

$$\mathbf{H} = [H_1^h, \dots, H_N^h]^T \quad (1.11)$$

Inserting (1.7) and (1.8) into (1.5) and (1.6) we obtain the Galerkin semi-discretization

$$\int_{V_k} \vec{\psi}_i \cdot \left[\mu \vec{\psi}^T \frac{\partial \mathbf{H}}{\partial t} + (\nabla \times \vec{\psi}^T) \mathbf{E} \right] dV = 0 \quad (1.12)$$

$$\int_{V_k} \vec{\psi}_i \cdot \left[\varepsilon \vec{\psi}^T \frac{\partial \mathbf{E}}{\partial t} - (\nabla \times \vec{\psi}^T) \mathbf{H} \right] dV = 0 \quad (1.13)$$

with: $i = 1, \dots, N$

The first terms of eq. (1.12) and (1.13) serve us to introduce the mass matrix, \mathcal{M} ,

$$[\mathcal{M}]_{ij} = \int_{V_k} \vec{\psi}_i(\vec{r}) \cdot \vec{\psi}_j(\vec{r}) dV \quad (1.14)$$

The curl terms of eq. (1.12) and (1.13) result in the stiffness matrix, \mathcal{S} ,

$$[\mathcal{S}]_{ij} = \int_{V_k} \vec{\psi}_i(\vec{r}) \cdot \nabla \times \vec{\psi}_j(\vec{r}) dV \quad (1.15)$$

In the form stated in (1.12) and (1.13) we are not specifying how the tangential components of the fields within each element relate to each other. If we enforce the fields, \vec{E}^h and \vec{H}^h to be globally continuous, this technique is called the Continuous Galerkin Time Domain (CGTD) or FEMTD method. The approximated fields,

then, fulfill in a strong way

$$\begin{aligned}\hat{n}_f \times \vec{E}_f^h &= \hat{n}_f \times \vec{E}_f^{h+} \\ \hat{n}_f \times \vec{H}_f^h &= \hat{n}_f \times \vec{H}_f^{h+}\end{aligned}\quad (1.16)$$

where the superscript + indicates the field neighboring the element across face f . The main drawback of the resulting algorithm is that it requires the solution of a large system of linear equations.

1.4.2 Numerical flux

The DG method [71] relies on enforcing continuity of the numerical flux across face f rather than field components as in (1.16). Using basic vector identities, the curl terms in (1.12) and (1.13) can also be expressed as

$$\begin{aligned}& \int_{V_k} \vec{\psi}_i(\vec{r}) \cdot (\nabla \times \vec{E}_f^h) dV = \\ &= \int_{V_k} \nabla \cdot (\vec{E}_f^h \times \vec{\psi}_i) dV + \int_{V_k} (\nabla \times \vec{\psi}_i) \cdot \vec{E}_f^h dV \\ &= \oint_{\partial V_k} \vec{\psi}_i \cdot (\hat{n} \times \vec{E}_f^h) d(\partial V) + \int_{V_k} (\nabla \times \vec{\psi}_i) \cdot \vec{E}_f^h dV\end{aligned}\quad (1.17)$$

where \hat{n} is a unit vector pointing outwards the element. The first term of the RHS of Eq.1.17 ($\hat{n} \times \vec{E}_f^h$) is substituted by the flux function across face f ($\hat{n} \times \vec{E}_f^{h,*}$).

Therefore, instead of plugging (1.16) into (1.17) and then into (1.12) and (1.13), we define numerical values of the tangential fields on $\partial V_{(f,k)}$, henceforth called numerical fluxes, $\vec{E}_f^{h,*}$ and $\vec{H}_f^{h,*}$, which do not need to match any of the values of the tangential fields on any side of ∂V_k but will depend on them.

$$\begin{aligned}\hat{n}_f \times \vec{E}_f^{h,*} &= \hat{n}_f \times \vec{E}_f^{h,*} \left(\vec{E}_f^h, \vec{E}_f^{h,+}, \vec{H}_f^h, \vec{H}_f^{h,+} \right) \\ \hat{n}_f \times \vec{H}_f^{h,*} &= \hat{n}_f \times \vec{H}_f^{h,*} \left(\vec{H}_f^h, \vec{H}_f^{h,+}, \vec{E}_f^h, \vec{E}_f^{h,+} \right)\end{aligned}\quad (1.18)$$

An interesting feature of DG methods is that we have several possibilities for choosing the numerical flux as long as they satisfy the following conditions [72]:

- Consistency: $\vec{E}_f^{h,*}(\vec{E}_f^h, \vec{E}_f^h, \vec{H}_f^h, \vec{H}_f^h) = \vec{E}_f^h$
- Continuity: $\vec{E}_f^{h,*}$ is at least Lipschitz continuous.

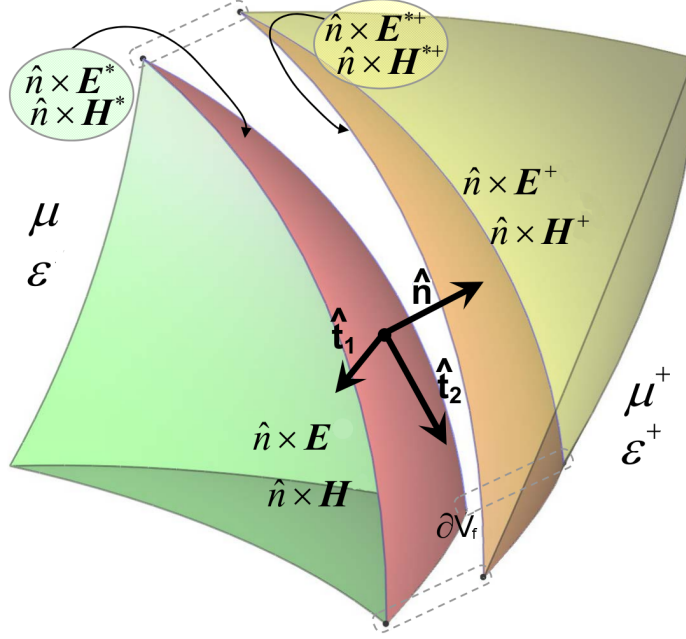


FIGURE 1.1: Notation used for the definition of the numerical fluxes.

TABLE 1.2: Parameters in Equation (1.19) to yield centered, upwind, and partially penalized numerical fluxes.

Numerical flux	Centered	Upwind	Penalized
κ_E	1/2	$\frac{Y^+}{Y+Y^+}$	$\frac{Y^+}{Y+Y^+}$
κ_H	1/2	$\frac{Z^+}{Z+Z^+}$	$\frac{Z^+}{Z+Z^+}$
ν_H	0	$\frac{1}{Y+Y^+}$	$\frac{\tau}{Y+Y^+}$
ν_E	0	$\frac{1}{Z+Z^+}$	$\frac{\tau}{Z+Z^+}$
Dispersion conv. (1-D)	h^{2p+1} (p odd)	h^{2p+3}	h^{2p+3}
Dissipation conv. (1-D)	-	h^{2p+2}	h^{2p+3}
Dispersion conv. (3-D)	h^{2p+2}	h^{2p+2}	h^{2p+2}
Dissipation conv. (3-D)	-	h^{2p+1}	h^{2p+1}
Spurious modes	Present	Attenuated	Attenuated

- Monotonicity: $E_f^{h,*}$ is a non-decreasing function of E_f^h and H_f^h and a non-increasing function of $E_f^{h,+}$ and $H_f^{h,+}$.

The properties of the scheme will greatly depend on the choice of the flux [62]. We will focus on the three most common choices: the centered flux, the upwind flux and the partially penalized flux. A general form for all of them is

$$\begin{aligned}
\hat{n}_f \times \vec{E}_f^{h,*} &= \\
&= \hat{n}_f \times \left(\vec{E}_f^h + \kappa_E [[\vec{E}^h]]_f + \nu_H \hat{n}_f \times [[\vec{H}^h]]_f \right) \\
\hat{n}_f \times \vec{H}_f^{h,*} &= \\
&= \hat{n}_f \times \left(\vec{H}_f^h + \kappa_H [[\vec{H}^h]]_f - \nu_E \hat{n}_f \times [[\vec{E}^h]]_f \right)
\end{aligned} \tag{1.19}$$

with

$$[[\vec{E}^h]]_f = \vec{E}_f^{h,+} - \vec{E}_f^h \quad (1.20)$$

$$[[\vec{H}^h]]_f = \vec{H}_f^{h,+} - \vec{H}_f^h \quad (1.21)$$

Table 1.2 shows the expressions for the κ and ν factors for centered, upwind, and partially penalized numerical fluxes. The terms which are multiplied by ν factors are known as penalization or upwind terms and come from the solution of the Riemman problem [73]. In the case of partially penalized fluxes, those are multiplied by the τ parameter. These terms introduce some dissipation to the scheme [74–76] but are essential to avoid the propagation of non-physical or spurious modes in the computational domain [13, 62] as will be shown in Section 1.4.5 where dissipation rates are numerically evaluated in the eigenvalue problem. When $\nu = 0$ (centered flux), there is no dissipation for either physical or spurious modes, at the cost of introducing spectral pollution to the method. In between the upwind and centered fluxes, a family of partially penalized fluxes can be defined [77], through the addition to the centered flux of dissipation terms that can be tuned to attenuate the spurious modes, and improve the accuracy. Other fluxes are described in detail in [62], such as the Stabilized Upwind flux. Although these fluxes have interesting properties, they require the introduction of new DOF that would need to be evolved in time and therefore increase the computational cost; mainly for this reason it is not common to find them in the DGTD application-oriented literature.

1.4.3 Semi-discretized form

The introduction of (1.19) in eq. (1.17), together with (1.14) and (1.15) let us write (1.12) and (1.13) in the final DG semi-discretized form

$$\begin{aligned}
\mu\mathcal{M}\frac{\partial\mathbf{H}}{\partial t} &= -\mathbf{S}\mathbf{E} \\
&- \sum_{f=1}^{N_f} \kappa_E \int_{\partial V_{(f,k)}} \vec{\psi} \cdot (\hat{n}_f \times [[\vec{E}^h]]_f) d(\partial V) \\
&- \sum_{f=1}^{N_f} \nu_H \int_{\partial V_{(f,k)}} \vec{\psi} \cdot (\hat{n}_f \times \hat{n}_f \times [[\vec{H}^h]]_f) d(\partial V) \\
\varepsilon\mathcal{M}\frac{\partial\mathbf{E}}{\partial t} &= \mathbf{S}\mathbf{H} \\
&+ \sum_{f=1}^{N_f} \kappa_H \int_{\partial V_{(f,k)}} \vec{\psi} \cdot (\hat{n}_f \times [[\vec{H}^h]]_f) d(\partial V) \\
&- \sum_{f=1}^{N_f} \nu_E \int_{\partial V_{(f,k)}} \vec{\psi} \cdot (\hat{n}_f \times \hat{n}_f \times [[\vec{E}^h]]_f) d(\partial V) \tag{1.22}
\end{aligned}$$

On section 1.4.6.2 we will present some particular cases of these expressions depending on the choice of the basis.

1.4.4 Boundary conditions

The flux conditions which serve to connect adjacent elements, also serve to directly implement basic boundary conditions in a weak form, by simply modifying the jumps in (1.20).

1.4.4.1 Perfectly Electric Conducting (PEC)

The PEC condition requires the tangential component of the electric field to be null and the tangential magnetic field component to be continuous, thus

$$\begin{aligned}
\hat{n}_f \times [[\vec{E}^h]]_{\text{PEC}} &= -2 \hat{n}_f \times \vec{E}^h \\
\hat{n}_f \times [[\vec{H}^h]]_{\text{PEC}} &= 0 \tag{1.23}
\end{aligned}$$

1.4.4.2 Perfectly Magnetic Conducting (PMC)

The PMC condition is the reciprocal of the PEC one,

$$\begin{aligned}
\hat{n}_f \times [[\vec{E}^h]]_{\text{PMC}} &= 0 \\
\hat{n}_f \times [[\vec{H}^h]]_{\text{PMC}} &= -2 \hat{n}_f \times \vec{H}^h \tag{1.24}
\end{aligned}$$

1.4.4.3 Silver-Mueller Absorbing (SMA)

The first-order SMA boundary condition [41, 78] is straightly based on considering that the fields outside the computational domain propagate as plane waves normal to the interface, $\hat{n} \times \vec{E} = Z\vec{H}$ or $\hat{n} \times \vec{H} = -Y\vec{E}$. To apply this condition to (1.19) is equivalent to modify the jump terms to

$$\begin{aligned}\hat{n}_f \times [[\vec{E}^h]]_{\text{SMA}} &= -\hat{n}_f \times \vec{E}^h \\ \hat{n}_f \times [[\vec{H}^h]]_{\text{SMA}} &= -\hat{n}_f \times \vec{H}^h\end{aligned}\quad (1.25)$$

and use the following constants in (1.19)

$$\begin{aligned}\kappa_{E,\text{SMA}} &= \frac{1}{2} \\ \kappa_{H,\text{SMA}} &= \frac{1}{2} \\ \nu_{H,\text{SMA}} &= \frac{1}{2Y} \\ \nu_{E,\text{SMA}} &= \frac{1}{2Z}\end{aligned}\quad (1.26)$$

The SMA boundary condition provides an ideally null reflection coefficient for normal incidence. In practice, its performance is reduced by the numerical accuracy of the method with its absorbing characteristics rapidly degrading with the angle of incidence with respect to surface normal [79]. For this reason it is usually preferred to use Perfectly Matched Layers (PML) to truncate the computational domain, these will be described in section 1.7.1.

1.4.5 Convergence and spurious modes

Defining a state vector $\mathbf{q} = [\mathbf{E} \ \mathbf{H}]^T$ containing all DOF within element k we can rewrite eqs. (1.22) as a single equation that governs the time evolution of the system

$$\begin{aligned}\partial_t \mathbf{q}(t) &= \\ &= -(\mathcal{M}^q)^{-1} \left(\mathcal{S}^q \mathbf{q}(t) - \sum_f^{N_f} \mathcal{F}_f^q \left(\bar{\mathcal{E}}_f \mathbf{q}(t) - \bar{\mathcal{E}}_f^+ \mathbf{q}_f^+(t) \right) \right)\end{aligned}\quad (1.27)$$

Where \mathcal{S}^q group the stiffness operators and \mathcal{F}_f^q group the flux operators acting over face f . To further simplify this analysis we will change the basis of the vector space in equation (1.27) using an invertible operator \mathcal{P} on equation (1.27) that diagonalizes the locally applied operators

$$\mathcal{W} = -\mathcal{P}^{-1}(\mathcal{M}^q)^{-1} \left(\mathcal{S}^q - \sum_f \mathcal{F}_f^q \right) \mathcal{P}_k \quad (1.28)$$

We can also define the eigenmodes as

$$\mathbf{p} = \mathcal{P}^{-1} \mathbf{q} \quad (1.29)$$

and the external operators as

$$\mathcal{V}_f = -\mathcal{P}^{-1}(\mathcal{M}^q)^{-1} \mathcal{F}_f^q \bar{\mathcal{E}}_f^+ \mathcal{P} \quad (1.30)$$

This change of basis let us write equation (1.27) in the following compact form

$$\partial_t \mathbf{p}(t) = \mathcal{W} \mathbf{p}(t) + \sum_f \mathcal{V}_f \mathbf{p}_f^+(t) \quad (1.31)$$

Eq. (1.31) shows that the system can be stated as a system of $2N$ independent first order ODEs with eigenfrequencies given by the eigenvalues of \mathcal{W} . This system contains contributions coming from the fluxes through the $\mathcal{V}_f \mathbf{p}_f^+$ terms. This result is particularly useful to study the convergence, stability and other spectral properties of the scheme. Moreover, as will be discussed in section 1.5 the spectral properties of the scheme will have an important role on the maximum time-step required for stability.

1.4.5.1 Convergence

The dispersion and dissipation of the method can be studied by comparing the computed and analytical plane-wave solutions within a computational domain with periodic boundary conditions [15, 22, 27, 75, 80]. Therefore, for an initial solution \mathbf{q} with wavenumber k we obtain eigenmodes, \mathbf{p}_j as the projection of the initial solution on the diagonalized space. Each of these modes will have a numerical frequency $\omega_j(k) \in \mathbb{C}$ corresponding to the eigenvalues of \mathcal{W} . The imaginary part $\Im[\omega_j]$ corresponds to the oscillating frequency and the real part $\Re[\omega_j]$ corresponds to the numerical dissipation or amplification of eigenmode \mathbf{p}_j , if any. A necessary condition for convergency is $\Re[\omega_j] \leq 0$, which is always fulfilled by Galerkin methods. The numerical phase-velocities supported by the scheme are $c_j(k) = \omega_j/k$. Therefore, we have,

$$\lim_{k \rightarrow 0} c_{(\text{fs})}(k) = \frac{1}{\sqrt{\varepsilon \mu}} \quad (1.32)$$

or equivalently, that the numerical solution tends to the analytical one for higher resolutions. As mentioned earlier, the numerical flux will impact the dispersion and dissipation of the numerical scheme. Table 1.2 summarizes the expected dispersive and dissipative convergences for the different numerical fluxes [17, 75].

1.4.5.2 Spurious modes

The solution provided by a discrete approximation must also be spectrally correct. That is, we may obtain a low-error when the exactness of the solution is measured with global parameters in TD but observe a polluted spectrum exhibiting non-physical resonances or spurious modes in FD. Therefore, we will require certain features from the numerical spectrum [27, 81] such as:

- Non-pollution and completeness of the spectrum of eigenvalues and eigenvectors for a suitable resolution.
- Isolation of the discrete kernel modes.

A well-known drawback of nodal FEM is the presence of spurious modes [82]. E.g. in [27] it is shown that a grid sufficiently far from being quasi-structured together with a centered flux will make spurious modes arise at relatively low frequencies. These are commonly attributed to a variety of reasons, including an inexact representation of the underlying de Rham complex¹.

However, an added advantage of DGTD over FEMTD resides in its discontinuous nature that permits them to be removed if we use upwind or penalized fluxes [74, 75, 89, 90]. These fluxes are characterized by the addition of dissipative terms to Maxwell's equations, and are proven to attenuate spurious modes more strongly than physical modes. The effect in the spectrum of the eigenvalues of the use of different fluxes can be appreciated in Fig. 1.2. The use of centered fluxes makes all the eigenvalues to lie on the imaginary axis despite if they are physical or not. Fig. 1.3 shows how this issue translates into the spectrum of resonances of a PEC cavity, difficulting the identification of physical resonances.

¹One way of removing this source of spurious modes, is to resort to vector-based formulations [83–85]. Comparing vector and nodal FEM is out of the scope of this work; advantages and disadvantages of both of them have been reported in literature [86, 87] and would deserve a full work to be further analyzed. Another approach to mitigate spurious modes is by introducing penalty terms associated with the divergence of \mathbf{E} [62, 88], at the cost of adding extra terms, and DOFs, that are to be evolved at each timestep [62].

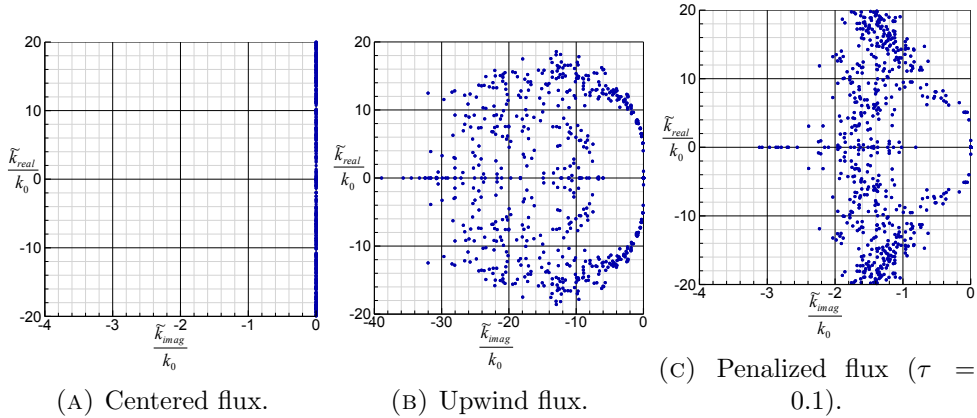


FIGURE 1.2: Normalized spectrum of the DG operator for a cubic domain (meshed with 24 tetrahedra) with periodic boundary conditions. We cannot see how the centered flux does not provide an isolated kernel, contrary to the upwind and penalized fluxes.

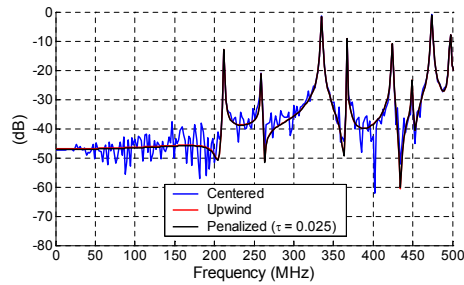


FIGURE 1.3: Power spectrum of the electric field at an arbitrary point inside a 1 m PEC cavity. The effect of the non-attenuation of the centered flux spectrum can be appreciated compared with the upwind and penalized fluxes.

1.4.6 Vector/Nodal basis functions

Let us discuss here two families of basis functions, the vector and the nodal basis.

TABLE 1.3: Comparison of vector and nodal basis

	Vector		Scalar ^a	
	Linear	Curved	Linear	Curved
\mathcal{M} size	$N \times N$		$N_p \times N_p$	
\mathcal{S} size	$N \times N$		$3(N_p \times N_p)$	
\mathcal{F} size	4 sparse matrices		$N_p \times (N_f N_{fp})$	$N_p \times (N_f N_{fp})^b$
Shared operators ^c	$\mathcal{S}, \mathcal{F}_\kappa, \mathcal{F}_\kappa^+$		\mathcal{M}, \mathcal{F}	None

^aThe number of nodes for scalar basis is $N_p = N/3$. The number of face nodes N_{fp} is $(p+1)(p+2)/2!$ for tetrahedrons and $(p+1)^2$ for hexahedrons.

^bFor curved cells, the storage and number of operations needed are significantly higher, varying depending on the implementation.

^cWithout considering identical cells in which all operators can be shared. Neglecting scaling factors.

1.4.6.1 Vector basis functions

Many authors use vector basis for the implementation of DG schemes [15, 67, 91–93]. Vector-curl conforming basis [94–97] were first proposed to solve spurious modes problems appearing in solutions using scalar basis in FEM [84]. However, these conclusions cannot be straightforwardly extrapolated to the DG case and, as has been discussed in section 1.4.3, the spurious-modes issue is solved using penalized fluxes.

We can define flux matrices based on vector basis functions that let us write (1.22) as

$$\begin{aligned}\mu\mathcal{M}\frac{\partial\mathbf{H}}{\partial t} &= -\mathcal{S}\mathbf{E} - \kappa_E(\mathcal{F}_\kappa^+\mathbf{E}^+ - \mathcal{F}_\kappa\mathbf{E}) - \nu_H(\mathcal{F}_\nu^+\mathbf{H}^+ - \mathcal{F}_\nu\mathbf{H}) \\ \varepsilon\mathcal{M}\frac{\partial\mathbf{E}}{\partial t} &= \mathcal{S}\mathbf{H} + \kappa_H(\mathcal{F}_\kappa^+\mathbf{H}^+ - \mathcal{F}_\kappa\mathbf{H}) - \nu_E(\mathcal{F}_\nu^+\mathbf{E}^+ - \mathcal{F}_\nu\mathbf{E})\end{aligned}\quad (1.33)$$

where

$$[\mathcal{F}_\kappa]_{ij} = \int_{\partial V_{(f,k)}} \vec{\psi}_i(\vec{r}) \cdot (\hat{n}_f \times \vec{\psi}_j(\vec{r})) d(\partial V) \quad (1.34)$$

$$[\mathcal{F}_\kappa^+]_{ij} = \int_{\partial V_{(f,k)}} \vec{\psi}_i(\vec{r}) \cdot (\hat{n}_f \times \vec{\psi}_j^+(\vec{r})) d(\partial V) \quad (1.35)$$

$$[\mathcal{F}_\nu]_{ij} = \int_{\partial V_{(f,k)}} \vec{\psi}_i(\vec{r}) \cdot (\hat{n}_f \times \hat{n}_f \times \vec{\psi}_j(\vec{r})) d(\partial V) \quad (1.36)$$

$$[\mathcal{F}_\nu^+]_{ij} = \int_{\partial V_{(f,k)}} \vec{\psi}_i(\vec{r}) \cdot (\hat{n}_f \times \hat{n}_f \times \vec{\psi}_j^+(\vec{r})) d(\partial V) \quad (1.37)$$

From an implementation point of view, the main advantage of the curl-conforming vector basis functions is that \mathcal{S} , \mathcal{F}_κ and \mathcal{F}_κ^+ can be shared by all the elements in a problem, since they do not depend on the geometry of the cells (size, aspect ratio and curvature) [15]. However the mass matrices are full, with a size of $N \times N$.

1.4.6.2 Nodal basis functions

With nodal basis functions some simplifications are possible. The set of nodal basis functions, \mathcal{B}_n , can be seen as a particular case of (1.4) in which

$$\mathcal{B}_n = \{l_1\hat{x}, \dots, l_{N_p}\hat{x}, l_1\hat{y}, \dots, l_{N_p}\hat{y}, l_1\hat{z}, \dots, l_{N_p}\hat{z}\} \quad (1.38)$$

with $N = 3N_p$, and N_p the number of different scalar functions, l_i . These scalar functions can be expressed, in terms of Lagrange polynomials, as

$$l_i(\vec{r}) = \prod_{j=1, j \neq i}^{N_p} \frac{\vec{r} - \vec{r}_{n,j}}{\vec{r}_{n,i} - \vec{r}_{n,j}} \quad (1.39)$$

where \vec{r}_n are the positions of the nodes within the element. We may be tempted to put the nodes \vec{r}_n equidistantly for the sake of simplicity. However, as discussed in [27] and [98], the Lagrange basis with nodes located at the Legendre-Gauss-Lobatto (LGL) quadrature points is a better choice, obtaining low condition numbers for the local matrices even at high p orders.

Using the nodal basis (1.38) we have that

$$\begin{aligned} \vec{E}^h &= \sum_{j=1}^N E_j^h \vec{\psi}_j \\ &= \sum_{j=1}^{N_p} E_j^h l_j \hat{x} + \sum_{j=N_p+1}^{2N_p} E_j^h l_j \hat{y} + \sum_{j=2N_p+1}^{3N_p} E_j^h l_j \hat{z} \\ &= \sum_{j=1}^{N_p} \vec{E}_j^h l_j \doteq \vec{\mathbf{E}}^T \mathbf{l} \end{aligned} \quad (1.40)$$

and similarly for $\vec{H}^h \doteq \vec{\mathbf{H}}^T \mathbf{l}$. When expressed using the nodal basis (1.38), the operators \mathcal{M} and \mathcal{S} are composed of blocks that decouple some Cartesian components of the vectors [86],

$$\mathcal{M} = \begin{pmatrix} \mathcal{M}_n & & \\ & \mathcal{M}_n & \\ & & \mathcal{M}_n \end{pmatrix} \quad (1.41)$$

$$\mathcal{S} = \begin{pmatrix} & -\mathcal{S}_n^z & \mathcal{S}_n^y \\ \mathcal{S}_n^z & & -\mathcal{S}_n^z \\ -\mathcal{S}_n^y & \mathcal{S}_n^x & \end{pmatrix} \quad (1.42)$$

Where \mathcal{M}_n and $\mathcal{S}_n^{x,y,z}$ have size $N_p \times N_p$. The flux terms are also simplified as they will now only need to account for fields in nodes at face f . When a nodal basis is used, the equation (1.22) can be expressed, for non-curved elements, as

$$\begin{aligned}
\mu\mathcal{M}\frac{\partial\vec{\mathbf{H}}}{\partial t} &= \\
&= -\mathcal{S}\vec{\mathbf{E}} - \sum_{f=1}^{N_f} \mathcal{F}_f \left[\hat{n}_f \times (\kappa_E [[\vec{\mathbf{E}}]]_f + \nu_H \hat{n}_f \times [[\vec{\mathbf{H}}]]_f) \right] \\
\varepsilon\mathcal{M}\frac{\partial\vec{\mathbf{E}}}{\partial t} &= \\
&= \mathcal{S}\vec{\mathbf{H}} + \sum_{f=1}^{N_f} \mathcal{F}_f \left[\hat{n}_f \times (\kappa_H [[\vec{\mathbf{H}}]]_f - \nu_E \hat{n}_f \times [[\vec{\mathbf{E}}]]_f) \right]
\end{aligned} \tag{1.43}$$

with

$$\mathcal{F}^f = \begin{bmatrix} \mathcal{F}_n^f & & \\ & \mathcal{F}_n^f & \\ & & \mathcal{F}_n^f \end{bmatrix} \tag{1.44}$$

where

$$[\mathcal{F}_n^f]_{ij} = \begin{cases} \int_{\partial V_{(f,k)}} l_i(\vec{r}) l_j(\vec{r}) d(\partial V) & \text{if } \vec{r}_{n,i} \in \partial V_{(f,k)} \\ 0 & \text{if } \vec{r}_{n,i} \notin \partial V_{(f,k)} \end{cases} \tag{1.45}$$

has a size of $N_p \times N_{fp}$ with N_{fp} being the number of nodes at face f . This implies that nodal basis scale computationally better than vector basis when we increase the order of basis functions p being this the main reason why nodal basis are usually preferred for high order schemes [27]. \mathcal{F}_n and \mathcal{M}_n will be the same for all elements except for an scaling factor, therefore we will not need to store them more than once for the entire simulation. Note however that, to obtain the equations (1.43) we assumed that \hat{n}_f was constant along for the flux integral terms in (1.22); therefore this simplification in the flux integral is not be valid if we work with curved elements (see Section 1.4.7).

1.4.7 Curved cells

One of the most appealing features of DG methods is that they can be formulated for higher order geometric elements which offer a better geometrical adaptivity [27, 99–102]. Most available open-source [103] and commercial meshers [104] offer the possibility of meshing with quadratic elements and techniques exist allowing higher orders [105]. Using quadratic elements allows us to use less of them to accurately discretize a curved surface, thus implying that their size can be larger.

The implementation of this technique requires the usage of quadrature integrals [106] because the complexity of the involved Jacobians needed to transform the reference

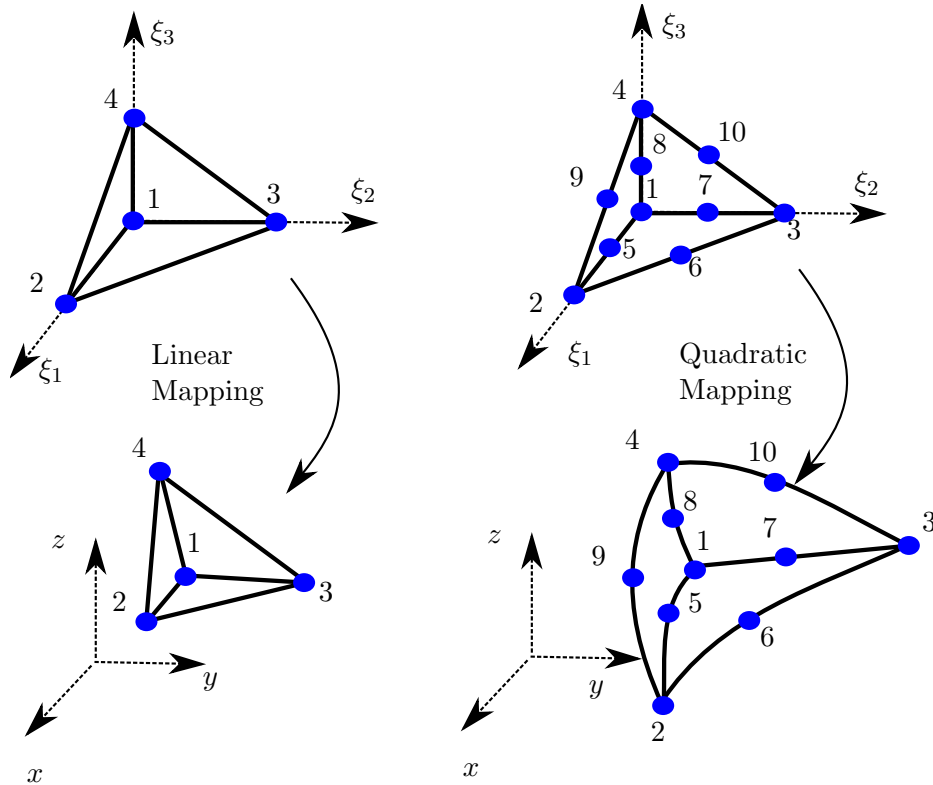


FIGURE 1.4: Mapping from the reference element for linear (first geometrical order) and quadratic (second geometrical order) tetrahedrons.

element into the actual mesh element results in integrals that cannot be solved analytically. For nodal basis, this technique needs to store information of the operators needed by the curved element thus requiring to store one flux matrix (1.45) per cubature point [27] or alternatively one operator per each term in (1.19) containing a normal unit vector. These requirements introduce a significant computational overhead both in memory a number of operations that can be a factor depending on the application.

To illustrate the possibilities of this approach, Fig. 1.5 shows a comparison of the results obtained with meshes using the same number of quadratic and linear elements. It can be appreciated that the improved geometry adaptivity provides a better result for the same number of elements.

1.4.8 Non-conformal meshes

Another advantage of using numerical fluxes to exchange information between elements is the possibility of using non-conformal interfaces between elements [107–110]. This is, to connect elements that do not share a whole face but a portion of it. This feature is interesting because there are applications with very intricate

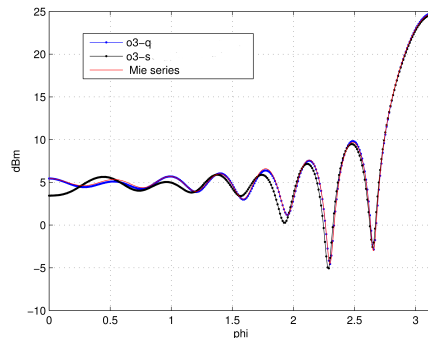


FIGURE 1.5: RCS at 450 MHz of a 1m radius PEC sphere meshed with the same number of linear and quadratic tetrahedrons and a spatial basis of order $p = 3$. Results obtained with GEG-UGR SEMBA software (www.ugrfdtd.es).

geometries where a conformal mesh may be very difficult to obtain, or domains requiring different element sizes. In DG, thanks to the flux functions, the interface between non-conformal meshes can be posed in a natural way. In [107, 109, 110] the authors find that the convergence of the method remains the same as with conformal meshes.

1.4.9 Hybrid meshes

The use of non-conformal meshes allows us to interface tetrahedrons with hexahedrons in the transition regions, as demonstrated in [109, 110], and therefore use hybrid meshes that combine several kinds of elements. Other possibility for the transition region is to use pyramidal elements, this approach has been studied in [111, 112]. As the case of non-conformal meshes, this can be done in a natural way by making use of the flux terms. The advantage of using hybrid meshes is that we can have the best of two worlds[7, 67, 91], e.g. tetrahedra can adapt better to surfaces in complicated geometries, or hexahedra for the discretization for zones where structured mesh could be used, enabling larger timesteps and a reduced number of degrees of freedom.

1.5 Time integration

In this section, we will present two time integration methods that are also the most popular choices in conjunction with the DG semidiscretizations presented in the previous section. Table 1.4 presents a summary of features of different time integration methods.

TABLE 1.4: Comparison of different time integration methods

	LF2	LSERK4	Tailored LSERK(m, n) ^a	SSP-RK(m) ^b	STDG
Order of convergence	h_t^2	h_t^4	h_t^n	h_t^m	$h_t^{2p_t+1}$
Explicit form	Yes	Yes	Yes	Yes	Pseudo
Dissipative	No	Yes	Yes	Yes	Yes/No ^c
Stages stored	1^d or 1.5^e	2	2	m	2 or $p_t + 1$
Stability region	Semi-infinite	Closed	Closed ^f	Closed ^g	Semi-infinite
LTS	Yes [23, 77]	Yes [23, 118]	Not demonstrated	Not demonstrated	Pseudo [119]
IMEX	Usually CN2 [65, 120]	Implicit RK [121]	Not demonstrated	Not demonstrated	Pseudo

^aLSERK with m stages and order n ; as described in [113, 114].^bWith m stages; as described in [74, 115].^cNon dissipative implementations [116, 117].^dWith centered fluxes.^eWith upwind fluxes.^fAnd customized to fit the eigenvalues of the DG operators [113, 114], therefore allowing larger h_t than LSERK4.^gLarger than with LSERK4, allowing larger h_t .

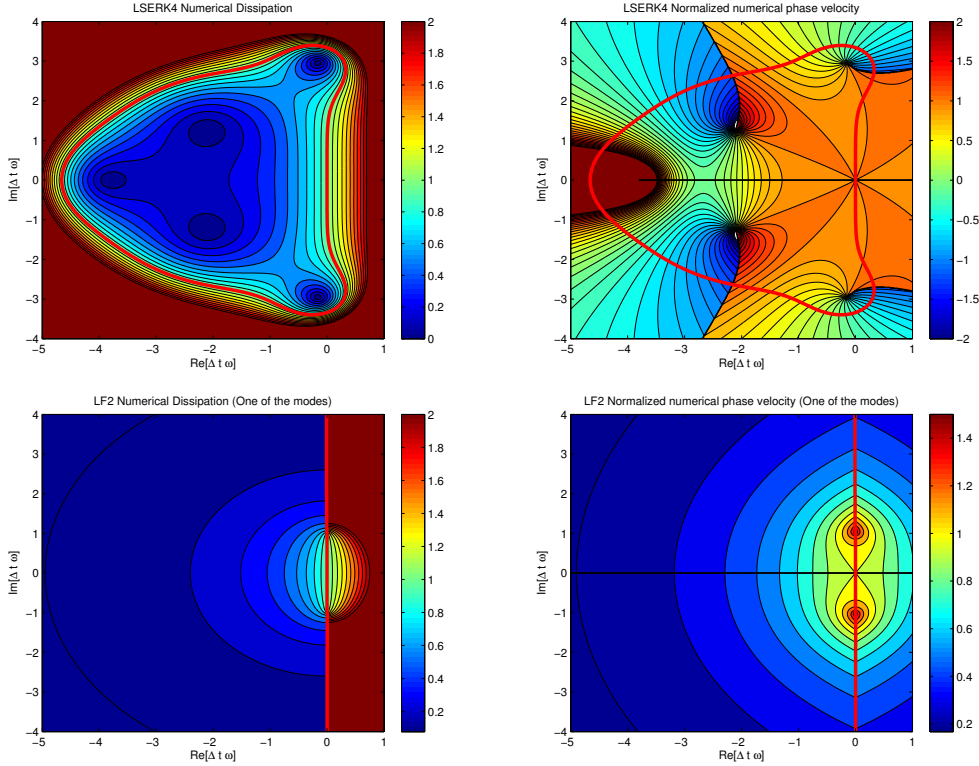


FIGURE 1.6: Dissipation factors (left) and normalized phase velocities (right) for the LSERK4 (up) and LF2 (down) schemes. All the semi-discrete eigenvalues calculated depicted in figure 1.2 must lie within the regions delimited by the thick red line to ensure the stability of the fully discrete scheme. LF2 supports two modes arising from two solutions for the growing factor only the positive one is represented, please notice that the final form of the dissipation and phase velocities will depend on the combination of the two modes [1].)

1.5.1 Leapfrog time integration

1.5.1.1 Second order leapfrog (LF2)

The second-order leap-frog method [122] is applied by alternately evolving the \mathbf{E}^n and $\mathbf{H}^{n+1/2}$ fields, arbitrarily defined at times t_n and $t_n + \Delta t/2$ respectively. This implies that we do not have a fully defined state vector in the sense of eq. (1.27) for a given time t . To obtain the future values from a present state the following algorithm is applied

$$\begin{aligned} \mathbf{E}^{n+1} &= \mathbf{E}^n + \Delta t \mathcal{L}_E^h(\mathbf{H}^{n+1/2}, \mathbf{E}^n) \\ \mathbf{H}^{n+3/2} &= \mathbf{H}^{n+1/2} + \Delta t \mathcal{L}_H^h(\mathbf{E}^{n+1}, \mathbf{H}^{n+1/2}) \end{aligned} \quad (1.46)$$

With \mathcal{L}_E^h and \mathcal{L}_H^h being the equations (1.22) respectively. When centered fluxes are used, the \mathcal{L}_E^h and \mathcal{L}_H^h operators use only $\mathbf{H}^{n+1/2}$ and \mathbf{E}^{n+1} as arguments, respectively. This implies that the scheme is reversible in time and will preserve energy as long

as the timestep used is below a maximum value h_t set by a CFL-like condition [93, 120, 122]. The use of upwind or penalized fluxes would imply the need of averaging between the next and previous semi-timesteps in the dissipation terms, thus resulting on a globally implicit scheme. To avoid this we need to use a backwards approximation [15, 64] and use the last previous known value instead of averaging.

1.5.1.2 Convergence and spectral properties

The study of the full spectrum of \mathcal{W} obtained in (1.28) is also useful as its properties impose limitations in regards to the time-integration. The LF2 method has the following stability requirement on its timestep h_t [15, 77, 123]

$$h_t \leq 1/\Im[\omega_{k,j}] \quad (1.47)$$

and therefore will be constrained by the largest imaginary part among all eigenvalues of (1.28). Equation (1.47) needs to solve a complex eigenvalue problem for each specific problem. To avoid this, we can use heuristic or analytical closed conditions [77, 90, 124]. For instance, for $p = 1$ with centered flux we have that

$$h_t \lesssim \frac{12}{8 + \sqrt{40}} \frac{V_k}{c_k \partial V_k} \quad (1.48)$$

LF algorithms have therefore a semi-infinite stability region which may be not bounded with respect to a value of the real axis depending on how the method is initialized [1]. This relieves this method from some bounds in material properties and additional algebraic constraints that are present for methods with closed stability regions [125].

1.5.1.3 Higher order LF

A N -th order leapfrog (LFN) time integrator applied to DG is discussed in [107]. These techniques can obtain high-order convergence in time avoiding the use of larger stencils. Thus, these methods allow us to retain the high-order convergence in the fully discretized numerical scheme. They also allow larger timesteps than for LF2 while retaining its symplectic non-dissipative nature. However, they will require $N/2$ times more memory storage and $N - 1$ times more arithmetic operations per timestep than LF2. This is the main reason why their usage is not widespread when higher-order convergences are demanded, where the LSERK is the most typical approach.

1.5.2 Low-Storage Explicit Runge Kutta time integration

The low-storage five-stage fourth-order Explicit Runge-Kutta method (LSERK4) [27, 113, 126] allows us to achieve a fourth-order convergence in the time integration, storing only one additional unknown per degree of freedom. For a given vector representing the state of an element k , i.e. $\mathbf{p}_k(t) = \mathbf{p}_k^n$ we can find an approximate solution state $\mathbf{p}_k(t+\Delta t) = \mathbf{p}_k^{n+1}$ applying the following algorithm, using the notation introduced in (1.31)

$$\begin{aligned} \mathbf{p}^{(0)} &= \mathbf{p}^n, \\ \mathbf{r}^{(i)} &= a_i \mathbf{r}^{(i-1)} + \Delta t \left(\mathcal{W} \mathbf{p}^{(i-1)} + \sum_f \mathcal{V}_f \mathbf{p}_f^{(i-1),+} \right), \\ \mathbf{p}^{(i)} &= \mathbf{p}^{(i-1)} + b_i \mathbf{r}^{(i)}, \\ \mathbf{p}^{(n+1)} &= \mathbf{p}^{(5)} \end{aligned} \tag{1.49}$$

with $i \in [1, \dots, 5]$ and the coefficients a_i , b_i and c_i taking the values indicated in Table 1.5 and \mathbf{r} being the residue. The LSERK4 scheme is one of the most used methods in high-order Discontinuous Galerkin semi-discretizations because its low dispersion and dissipation errors. Contrary to other RK implementations, the low-storage version requires the storage of only twice the number of degrees of freedom in the scheme at the expense of one additional stage. Despite its many advantages, LSERK4 has a higher computational cost than LF2 and the numerical dissipation it introduces can be a factor depending on the application. For this reason, a number of authors have proposed alternatives for the classical LSERK4 scheme [74, 113, 114].

TABLE 1.5: Coefficients for the low-storage five-stage fourth-order Explicit Runge-Kutta method (LSERK4)

s	a_s	b_s	c_s
1	0	$\frac{1432997174477}{9575080441755}$	0
2	$-\frac{567301805773}{1357537059087}$	$\frac{5161836677717}{13612068292357}$	$\frac{13612068292357}{9575080441755}$
3	$-\frac{2404267990393}{2016746695238}$	$\frac{1720146321549}{2090206949498}$	$\frac{22526269341429}{6820363962896}$
4	$-\frac{3550918686646}{2091501179385}$	$\frac{3134564353537}{4481467310338}$	$\frac{2006345519317}{3224310063776}$
5	$-\frac{1275806237668}{842570457699}$	$\frac{2277821191437}{14882151754819}$	$\frac{28032321613138}{2924317926251}$

1.5.2.1 Convergence and spectral properties

RK methods are constrained by the spectra of the operator \mathcal{W}_k , i.e. all the eigenvalues of \mathcal{W}_k must lie inside of the stability region of the RK scheme (Fig. 1.6). The LSERK4 method allows for slightly larger time-steps than LF2 but imposes constraints when dealing with dispersive materials [125]. LSERK methods comprise irregular closed loci in the complex plane [113, 127] in which the eigenvalues of (1.28) must lie to ensure stability. Consequently, the timestep must be chosen sufficiently small, e.g. for a nodal basis the following inequality must hold [27]

$$\Delta h_{t,k} \leq \frac{C}{c_k} \min_i \frac{\Delta h_{ki}}{2} \quad (1.50)$$

where $\min_i \Delta h_{ki}$ indicates the minimum distance between nodes in element k , c_k is the maximum speed of light in the element k , and C is a constant.

1.5.3 Achieving larger global timesteps

The presence of small-sized elements imposes constraints to the maximum size of the timestep severely affecting the computational efficiency. As we can appreciate from (1.47) and (1.50) the maximum time-step allowed to ensure stability is proportional to an inverse power of the size of the elements. This has been a topic of intense research aiming to overcome the global limitations imposed by a local condition. Some existing solutions are discussed below.

1.5.3.1 Local Time Stepping (LTS)

The most straightforward approach to deal with the global timestep restrictions imposed by the presence of local small-sized elements is to devise a LTS technique by which these elements are evolved using a smaller timestep. To do so, the elements are clustered in different groups, or tiers, according to the maximum timestep allowed by the smallest element in the tier. The interfaces between elements within the same tier are treated in the usual way; however, the interfaces between tiers will require a special treatment because the smaller tiers require field values that the larger steps do not compute.

For the LF2 method, we can find at least three alternatives:

- In [77], [122] and [93], the authors use a method, firstly devised by Montseny, in which the last available field coefficient is used when the smaller tiers require

intermediate timestep values from larger tiers. The main advantage of this technique is that it preserves the reversibility of the scheme and in consequence the scheme remains non-dissipative. On the other hand, it introduces some additional numerical dispersion, and a penalization of the stability condition.

- In [15] the LTS is accomplished interpolating the field unknowns in an interface region between the different tiers, this interpolation improves the accuracy and stability of the technique compared with Montseny's method.
- In [23] a technique called causal-path LTS (CPLTS) is applied. This technique consists on computing auxiliary fields in a shrinking buffer zone whenever they are needed by the smaller time-step tier. Once they have been used by the smaller tier, they are casted away and the higher tier is evolved using the original values. As shown in [23], the scheme has better dispersive properties than Montseny's and allows for a better assortment of tiers. However, it introduces some dissipation, it cannot be used with centered fluxes and requires more arithmetic operations.

For RK methods we can also find several alternatives:

- The CP-LTS technique previously discussed for LF2 can also be applied to RK schemes, as discussed in [23]. Although the dispersive properties do not seem to be significantly affected when low spatial orders are used, this technique introduces a significant amount of numerical dissipation.
- A similar concept is shown in [128]. First the whole domain is evolved using the higher tier timestep. Then, the values of the solution that have been polluted by the usage of a timestep larger than allowed are casted away. To compute the values in the lower tier region an interpolation in the boundary is performed.
- In [27, 129] a scheme allowing each element to be advanced with its own individual and optimal timestep is shown. This technique, called Arbitrary High-Order Derivatives (ADER) consists on expanding the solution in Taylor series in time. This time derivatives are then replaced by space derivatives using a Cauchy-Kovalevskaya procedure. The resulting scheme is high-order accurate in space and time.

1.5.3.2 Implicit-Explicit (IMEX) schemes

Another technique to improve the global efficiency of the scheme is to use an implicit time integrator in the regions presenting a higher stiffness while using a usual explicit time integrator in the remaining domain. This approach aims to benefit from the unconditional stability that is usually a characteristic of implicit schemes. However, as opposite to LTS, these techniques cannot be used recursively and a large number of unknowns of the implicit part can reduce the computational benefits for meshes with highly disparate sizes. In [121], implicit and explicit RK schemes are applied to several types of PDEs. In [65, 120], the authors show an IMEX technique applied to the Maxwell's equations using a second order Crank-Nicolson (CN2) scheme for the implicit part and a LF2 scheme for the explicit one.

1.5.3.3 Predictor-Corrector time integration

A predictor-corrector scheme is an algorithm that proceeds in two steps. First, the prediction step calculates a rough approximation. Second, the corrector step refines the initial approximation using another means. In [130] an application of a predictor-corrector scheme proposed and in [131] it is applied to a DGTD method to solve Maxwell's equations. This let the authors to significantly increase the timesteps compared with other methods at the expense of a moderate increase in memory.

1.5.3.4 Tailored LSERK schemes

In [113, 114] the authors explore the usage of higher number of stages and different orders for new LSERK schemes. The approach they take is to make assumptions over the form of the spectrum based on several typical cases and then find coefficients for the RK schemes by fitting its stability region to that spectrum. They conclude that the increase in the size of timesteps offsets the inclusion of new stages and therefore they are able to obtain improvements of up to a 40 – 50%.

1.5.3.5 Strong Stability Preserving RK (SSP-RK) schemes

In [74, 115] a Strong Stability Preserving Runge-Kutta (SSP-RK) technique is used. This scheme has a larger stability region, thus allowing us to use a larger h_t . Each timestep the method needs to evaluate m stages achieving an m order of convergence. In [74], the authors demonstrate an improvement in the number of operations needed

by the scheme. The main drawback of this methods is that it needs to store m stages, thus significantly increasing the memory consumption.

1.5.3.6 Space-time Discontinuous Galerkin (STDG)

As we have seen in previous sections, the typical approaches consist on obtaining a DG spatial semi-discretization that is then evolved with an explicit time integrator algorithm. On the contrary, the STDG approach consists on applying the DG also in the time dimension [24, 116, 117, 119, 132, 133]. The resulting scheme therefore extends to the time dimension most of the properties of spatial DG, such as the high order convergence. There are many ways of implementing this concept: some approaches arise to non-dissipative [116, 117] schemes, others result in pseudo-explicit methods [24, 119, 132], or allow a significant freedom in the election of the time-step [24].

1.6 Electromagnetic Sources

Electromagnetic sources in DGTD are almost a direct extension of the techniques already developed for FDTD [134]. For instance, those based on Huygens's principle [10, 135] employ a division of the computational domain into two zones, the Total Field Zone (TFZ) and the Scattered Field Zone (SFZ), to define the illuminated and the non-illuminated zones, respectively, being the main differences between the FDTD and DGTD implementations due to the staggered nature of FDTD.

1.6.1 Plane wave

Incident-wave conditions can be generated in a straightforward way as detailed in [10, 30]. Let us assume that, inside a TFZ, a known wave is propagating while outside it, in the SFZ, the field of this wave is null. If $\vec{E}^{\text{inc}}(t)$ and $\vec{H}^{\text{inc}}(t)$ denote the wave fields at each point of the TFZ/SFZ regions interface (Fig. 1.7), the jumps in (1.20) used to calculate the flux across the face of an element k in the TF region need to be modified according to

$$\begin{aligned}\hat{n}_f \times \vec{E}_{\text{TF}}^{h,+}(t) &= \hat{n}_f \times \left(\vec{E}^{h,+}(t) + \vec{E}^{h,\text{inc}}(t) \right) \\ \hat{n}_f \times \vec{H}_{\text{TF}}^{h,+}(t) &= \hat{n}_f \times \left(\vec{H}^{h,+}(t) + \vec{H}^{h,\text{inc}}(t) \right)\end{aligned}\tag{1.51}$$

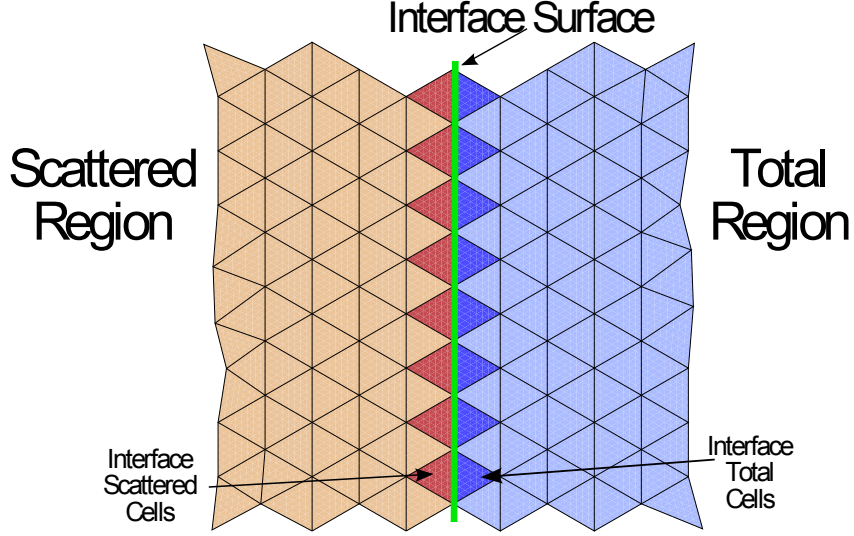


FIGURE 1.7: Scattered field (orange) and total field regions (blue). The elements that need to have altered fluxes are marked in darker colors.

If k is in the SF region the fields calculated at the face interfacing with the TFZ are modified to

$$\begin{aligned}\hat{n}_f \times \vec{E}_{\text{SF}}^{h,+}(t) &= \hat{n}_f \times \left(\vec{E}^{h,+}(t) - \vec{E}^{h,\text{inc}}(t) \right) \\ \hat{n}_f \times \vec{H}_{\text{SF}}^{h,+}(t) &= \hat{n}_f \times \left(\vec{H}^{h,+}(t) - \vec{H}^{h,\text{inc}}(t) \right)\end{aligned}\quad (1.52)$$

Note that the fields \vec{E}^{inc} and \vec{H}^{inc} , can describe any kind of waves such as plane waves, linearly or elliptically polarized, or even spherical waves with minor modifications. In FDTD, the TFZ and SFZ are separated by one cell introducing some numerical errors. On contrary, for DGTD, the discontinuous nature of the method allows us to use the same geometrical surface as the TFZ/SFZ interface. Moreover, the SFZ can be pushed directly onto the computational domain and be backed with an SMA-BC. On this surface we can also apply a near-to-far-field technique [136] can also be applied to compute RCS or radiation patterns of antennas.

1.6.2 Local sources and radiation patterns

The most obvious way to model a point current source $\vec{J}_s(t, \vec{r}_0)$ is by directly modifying the magnetic field corresponding to the node in the position \vec{r}_0 shared by it [30, 137]. Therefore using.

$$\vec{H}^{\text{inc}}(t) = \hat{n} \times \vec{J}_s(t, \vec{r}_0) \quad (1.53)$$

in (1.51) and (1.52). However, as pointed in [30, 137] the Lagrange polynomials are not able to resolve well the field values in the vicinity of \vec{r}_0 , where the fields are theoretically infinite, forcing to refine the mesh around that point and thus increasing drastically the computational cost. This justifies the introduction of an alternative solution, through the use of localized sources, described below. If we use a formalism similar to the defined for the TFZ/SFZ illumination we can avoid defining the fields in the region closest to the point source [10, 137]. Therefore, for a dipole we could use the analytical expressions describing the fields $\vec{E}^{\text{inc}}(t)$ and $\vec{H}^{\text{inc}}(t)$ at the position of the interface- These expressions are evaluated using theoretical equations such as the ones that can be found in [138] for an electric dipole. The advantage of this technique is that the field at the interface can be defined freely so it is possible to use it to define antenna radiation patterns including near fields.

1.6.3 Waveports

1.6.3.1 TEM port

A TEM mode (e.g. for a coaxial port) can be directly injected into the port in a weak manner through the flux terms by adding $\vec{E}^{h,\text{inc}}$ and $\vec{H}^{h,\text{inc}}$ to the jump terms in (1.20). For the first coaxial TEM mode these terms are

$$\begin{aligned}\vec{E}^{h,\text{inc}} &= V^{\text{inc}}(t) \frac{1}{\log(b/a)} \frac{1}{\rho} \hat{\rho} \\ \vec{H}^{h,\text{inc}} &= V^{\text{inc}}(t) \frac{1}{Z \log(b/a)} \frac{1}{\rho} \hat{\phi}\end{aligned}\tag{1.54}$$

in (1.51) and (1.52), with a and b being the inner and outer radii of the conductors forming the coaxial and V^{inc} the time variation of the excitation signal. The TEM ports are accurately truncated with a SMA boundary condition (described in section 1.4.4.3) that can be located in the same surface of the port.

1.6.3.2 Waveguide modes

Arbitrary shape wave guides In [53, 69], Lou *et al.* describe a method to excite arbitrarily shaped waveguides in a FEMTD scheme that can be simply extrapolated to DGTD. To do this, Lou starts by solving the 2D Helmholtz problem at the plane forming the waveport to get the eigenvectors and eigenfrequencies of it. Then these FD solutions are solved in TD by applying the inverse Laplace transform. This approach is also useful to truncate the waveguide in a very efficient and accurate manner. The absorption in waveguides is particularly problematic when absorbing

boundary conditions (ABC) are used, because the waves always imping over the absorbing conditions with a high angle when their frequency is close to the cut frequencies of the supported modes.

Rectangular waveguide A simplified version of [53, 69] can be implemented directly using the analytical TE and TM modes. For a rectangular waveguide we have the following analytical expressions for the supported modes [138],

$$\vec{H}_{\text{TE}_{mn}}(\omega) = \begin{pmatrix} \frac{\gamma_{mn}}{k_{mn}^2} \frac{\pi m}{a} \sin \frac{\pi m x}{a} \cos \frac{\pi n y}{b} \\ \frac{\gamma_{mn}}{k_{mn}^2} \frac{\pi n}{b} \cos \frac{\pi m x}{a} \sin \frac{\pi n y}{b} \\ \cos \frac{\pi m x}{a} \cos \frac{\pi n y}{b} \end{pmatrix} B_{mn}(\omega) \quad (1.55)$$

$$\vec{E}_{\text{TE}_{mn}}(\omega) = \begin{pmatrix} \frac{\pi n}{b} \cos \frac{\pi m x}{a} \sin \frac{\pi n y}{b} \\ -\frac{\pi m}{a} \sin \frac{\pi m x}{a} \cos \frac{\pi n y}{b} \\ 0 \end{pmatrix} B_{mn}(\omega) \frac{\eta \gamma_0}{k_{mn}^2} \quad (1.56)$$

$$\vec{H}_{\text{TM}_{mn}}(\omega) = \begin{pmatrix} \frac{\pi n}{b} \sin \frac{\pi m x}{a} \cos \frac{\pi n y}{b} \\ -\frac{\pi m}{a} \cos \frac{\pi m x}{a} \sin \frac{\pi n y}{b} \\ 0 \end{pmatrix} A_{mn}(\omega) \frac{\eta^{-1} \gamma_0}{k_{mn}^2} \quad (1.57)$$

$$\vec{E}_{\text{TM}_{mn}}(\omega) = \begin{pmatrix} \frac{\gamma_{mn}}{k_{mn}^2} \frac{\pi m}{a} \cos \frac{\pi m x}{a} \sin \frac{\pi n y}{b} \\ \frac{\gamma_{mn}}{k_{mn}^2} \frac{\pi n}{b} \sin \frac{\pi m x}{a} \cos \frac{\pi n y}{b} \\ \sin \frac{\pi m x}{a} \sin \frac{\pi n y}{b} \end{pmatrix} A_{mn}(\omega) \quad (1.58)$$

where $\gamma_{mn}(\omega) = \sqrt{\frac{(j\omega)^2}{c^2} + k_{mn}^2}$, $k_{mn}^2 = \left(\frac{m\pi}{a}\right)^2 + \left(\frac{n\pi}{b}\right)^2$, and $\eta = \sqrt{\mu/\varepsilon}$. $B_{mn}(\omega)$ and $A_{mn}(\omega)$ are the spectral components of the mode mn . In the Laplace domain, $\gamma_0 = s/c$ and $\gamma_{mn} = \sqrt{s^2/c^2 + k_{mn}^2}$, which in the time domain can be represented with the following operators [69]:

$$\gamma_0 = \mathcal{L} = \frac{1}{c} \frac{\partial}{\partial t} \quad (1.59)$$

$$\gamma_{mn} = \mathcal{H}_{mn} = \frac{1}{c} \frac{\partial}{\partial t} + h_{mn}(t)* \quad (1.60)$$

where $*$ stands for convolution in time and the impulse response of the system $h_{mn}(t)$ is given by [139]

$$h_{mn}(t) = \frac{k_{mn}}{t} J_1(k_{mn}ct) \bar{u}(t) \quad (1.61)$$

$\bar{u}(t)$ denoting the unit step function and $J_n(\cdot)$ the Bessel function of the first kind. If we are using a gaussian excitation for the mode $A_{mn} = f(t)$ of the form

$$f(t) = \bar{u}(t) \exp \left[- \left(\frac{t - \mu}{\sigma \sqrt{2}} \right)^2 \right] \quad (1.62)$$

we can write eq. (1.59) and (1.60), using a numerical convolution technique, as

$$\gamma_0 f(t^n) = \frac{1}{c} \left[\frac{\partial f(t)}{\partial t} \right]_{t=t^n} \quad (1.63)$$

$$\gamma_{mn} f(t^n) \simeq \frac{f(t^n)}{c} \frac{-2}{\sigma\sqrt{2}} \left(\frac{t^n - \mu}{\sigma\sqrt{2}} \right) + \Delta t \sum_j^n h_m(t^j) f(t^{n-j}) \quad (1.64)$$

that enables the computation of (1.55), (1.56), (1.57) and (1.58), in the time domain.

1.7 Advanced material modeling

1.7.1 Conformal Perfectly Matched Layer

Perfectly Matched Layers (PMLs) were introduced for first time in [140] as a way to truncate the computational domain in open-region scattering problems. They can actually be seen as a special kind of non-Maxwellian dispersive anisotropic material [36]. The main advantage of PMLs over other ABC is that they are largely independent of frequency, wave polarization, and angle of incidence. They also have extremely small reflection errors. PMLs are material-independent and can truncate domains with inhomogeneous, dispersive, and non-linear materials. There are several variants of PMLs [141–146], mainly developed in the FDTD context, with features particularly well suited for different applications: e.g. In [141] the author present an Auxiliary Differential Equation (ADE) form of a multipole Complex-Frequency Shifted PML that presents advantages when is extended to high order methods. Equivalent convolutional formulation can also be used [147].

The Conformal PML (CPMLs) allow us in DGTD to add PMLs extruding the outer surface of the computational domain [15, 146]. The only geometrical restriction to this formulation is that the PMLs must form a convex closed region, when viewed from the outside, or they will be dynamically unstable [148].

Let us consider the setup of Fig. 1.8 representing a right-handed reference frame called Darboux frame at a point P of an internal surface S . This frame is defined by an orthonormal local vector-basis \mathbf{u}_1 , \mathbf{u}_2 and \mathbf{u}_3 . \mathbf{u}_1 and \mathbf{u}_2 are tangent to S at a point P along the principal lines of curvature. The third component is obtained from the other two as $\mathbf{u}_3 = \mathbf{u}_1 \times \mathbf{u}_2$. We can write \mathbf{u}_i in terms of local coordinates ξ_i as $\mathbf{u}_i = (\partial\vec{r}/\partial\xi_i)/|\partial\vec{r}/\partial\xi_i|$, $i = 1, 2, 3$ where \vec{r} is the position vector. With these definitions $\xi_3 = 0$ represents the surface S . The unit vectors are functions of ξ_1 and ξ_2 only. With the defined local reference frame, the radii of curvature $r_{01}(\xi_1, \xi_2)$ and

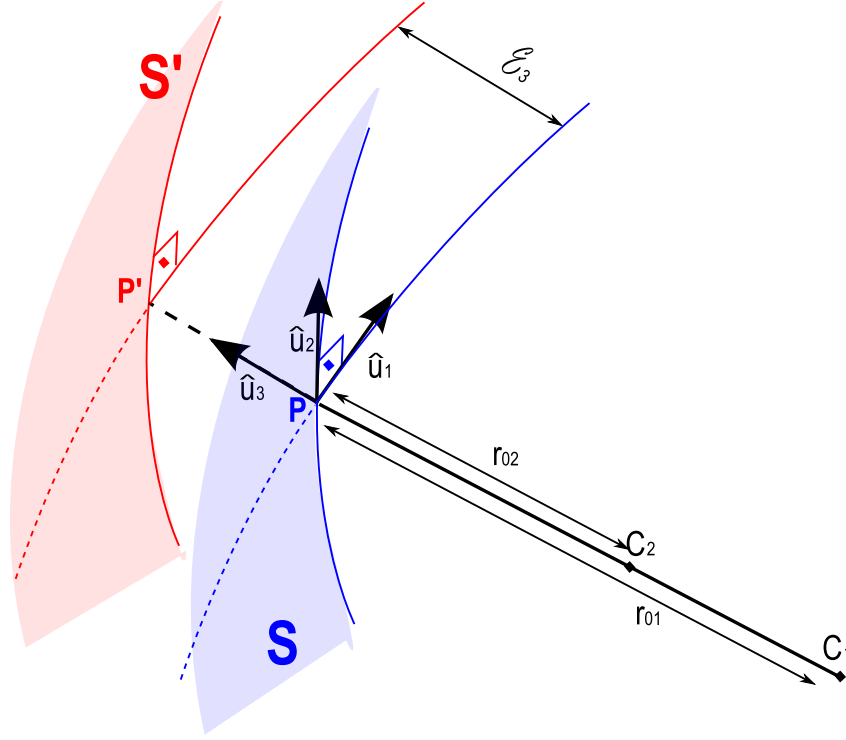


FIGURE 1.8: Darboux frame.

$r_{02}(\xi_1, \xi_2)$ are positive (for convex S') and we also have that at a point P' the radius r_j can be expressed as $r_j(\xi) = r_{0j}(\xi_1, \xi_2) + \xi_3$.

We will also use the the Lamé coefficients, h_i which in the Darboux frame are

$$h_1 = r_1/r_{01} \quad (1.65)$$

$$h_2 = r_2/r_{02} \quad (1.66)$$

$$h_3 = 1 \quad (1.67)$$

The conformal PML² can be obtained through a complex stretching on the normal coordinate ξ_3 :

$$\begin{aligned} \xi_3 \rightarrow \tilde{\xi}_3 &= \int_0^{\xi_3} s(\xi) d\xi \\ &= \int_0^{\xi_3} \left(a(\xi) + \frac{\sigma(\xi)}{j\omega} \right) d\xi \\ &= b(\xi_3) + \frac{\Delta(\xi_3)}{j\omega} \end{aligned} \quad (1.68)$$

where $a \geq 1$ and $\sigma \geq 0$. The effect of this stretching on a propagating wave can be seen by locally expanding the wave in terms of a generalized Wilcox expansion

²A Complex Frequency Shifted (CFS) formulation can be straightforwardly found [141, 149]. This presents some benefits for attenuation of low frequency waves.

[148, 150, 151] showing that there is an induced exponential decay along the normal coordinate for $\sigma \geq 0$. Also, if $a \geq 1$, additional attenuation can be achieved for evanescent waves if any.

The derivation of the CPML consists on substituting (1.68) in the system of Maxwell's equations expressed in curvilinear coordinates [152]. This leads to a system that is substantially different to the classic Maxwell's equations. For this reason, rather than solve the system of Maxwell's equations in curvilinear coordinates, we recover the original system introducing an anisotropic medium. This leads to the formulation of the anisotropic and conformal PMLs.

1.7.1.1 Anisotropic Conformal PML

Let us start by introducing a new set of fields \tilde{E}_i and \tilde{H}_i defined as

$$\tilde{E}_1 = \frac{\tilde{h}_1}{h_1} E_1, \quad \tilde{E}_2 = \frac{\tilde{h}_2}{h_2} E_2, \quad \tilde{E}_3 = s E_3 \quad (1.69)$$

$$\tilde{H}_1 = \frac{\tilde{h}_1}{h_1} H_1, \quad \tilde{H}_2 = \frac{\tilde{h}_2}{h_2} H_2, \quad \tilde{H}_3 = s H_3 \quad (1.70)$$

with

$$\tilde{h}_1 = \frac{\tilde{r}_1}{r_{01}} \quad (1.71)$$

$$\tilde{h}_2 = \frac{\tilde{r}_2}{r_{02}} \quad (1.72)$$

$$\tilde{h}_3 = 1 \quad (1.73)$$

and $\tilde{r}_i = r_{0i} + \tilde{\xi}_3$.

By introducing these new fields into the system of equations described previously we recover a Maxwellian system of equations in curvilinear coordinates, but now for an anisotropic medium whose constitutive parameters are given by $\bar{\mu} = \mu \bar{\Lambda}$ and $\bar{\varepsilon} = \varepsilon \bar{\Lambda}$, with

$$\bar{\Lambda} = \mathbf{u}_1 \mathbf{u}_1 \left(\frac{s h_1 \tilde{h}_2}{\tilde{h}_1 h_2} \right) + \mathbf{u}_2 \mathbf{u}_2 \left(\frac{s \tilde{h}_1 h_2}{h_1 \tilde{h}_2} \right) + \mathbf{u}_3 \mathbf{u}_3 \left(\frac{\tilde{h}_1 \tilde{h}_2}{s h_1 h_2} \right) \quad (1.74)$$

So we can write the Maxwell's equations in PML media as,

$$\nabla \times \vec{E} = -\bar{\mu} j \omega \vec{H} \quad (1.75)$$

$$\nabla \times \vec{H} = \bar{\varepsilon} j \omega \vec{E} \quad (1.76)$$

This means that we can achieve a reflection-less absorption of electromagnetic waves incident on a smooth, concave surface with an anisotropic constitutive tensor over the volume spanning S between S' .

1.7.1.2 Cartesian PML

The Cartesian PML is a particular case of the system described in 1.7.1.1. In this case we have that $r_{01} = r_{02} = \infty$, so that $\tilde{h}_1 = \tilde{h}_2 = 1$. Let us assume that the normal to our surface S is oriented towards the $+z$ axis and therefore $\mathbf{u}_1 = \mathbf{u}_x$, $\mathbf{u}_2 = \mathbf{u}_y$ and $\mathbf{u}_3 = \mathbf{u}_z$. Let us consider that $s = s_z(z) = 1 + \sigma_z(z)/(j\omega)$ for attenuation in the z direction. The $\sigma_z(z)$ profile is taken to minimize the reflections [15, 140] that for the parabolic case takes the form

$$\sigma_z(z) = \sigma_{\max} \left(\frac{z}{\Delta z} \right)^2 \quad (1.77)$$

being Δz the thickness of the PML. Uniaxial and biaxial PMLs can be considered an special case of the triaxial PML. By writing them explicitly we see that we only need certain DOFs depending on the direction, a fact that can be used with nodal basis to reduce the storage needs as mentioned in Section 1.4.6.2.

Uniaxial Cartesian PML For uniaxial PMLs, (1.74) reduces to

$$\bar{\bar{\Lambda}}_z = \mathbf{u}_x \mathbf{u}_x s_z + \mathbf{u}_y \mathbf{u}_y s_z + \mathbf{u}_z \mathbf{u}_z \frac{1}{s_z} \quad (1.78)$$

The x component of Faraday's law in PML media (1.75) is

$$-[\nabla \times \vec{E}]_x = \mu s_z j\omega \vec{H}_x = j\omega \mu \vec{H}_x + \sigma_z \mu \vec{H}_x \quad (1.79)$$

or, in the time domain

$$\mu \partial_t \vec{H}_x = -[\nabla \times \vec{E}]_x - \sigma_z \mu \vec{H}_x \quad (1.80)$$

and similarly for the y component. The z component is,

$$\begin{aligned}
-[\nabla \times \vec{E}]_z &= \mu \frac{j\omega \vec{H}_z}{s_z} \\
&= \mu \frac{j\omega \vec{H}_z + \sigma_z \vec{H}_z - \sigma_z \vec{H}_z}{1 + \frac{\sigma_z}{j\omega}} \\
&= \mu j\omega \vec{H}_z - \mu \frac{\sigma_z j\omega \vec{H}_z}{j\omega + \sigma_z} \\
&= \mu j\omega \vec{H}_z + \mu \vec{M}_z - \mu \sigma_z \vec{H}_z
\end{aligned} \tag{1.81}$$

with

$$j\omega \vec{M}_z = -\sigma_z \vec{M}_z + \sigma_z^2 \vec{H}_z \tag{1.82}$$

which, in the time domain

$$\begin{aligned}
\mu \partial_t \vec{H}_z &= -[\nabla \times \vec{E}]_z - \mu \vec{M}_z + \mu \sigma_z \vec{H}_z \\
\partial_t \vec{M}_z &= -\sigma_z \vec{M}_z + \sigma_z^2 \vec{H}_z
\end{aligned} \tag{1.83}$$

Similar equations can be obtained for Ampere's law (1.76) for PML media. Eq. (1.83) shows the need of introducing a new equation, called Auxiliary Differential Equation (ADE) that governs the behaviour of a polarization current, \vec{M} . This is a common feature between PMLs and Dispersive materials, described in Section 1.7.2.

Biaxial Cartesian PML When stretching in x and y directions, the tensor in (1.74) can be expressed as,

$$\begin{aligned}
\bar{\bar{\Lambda}}_{x,y} &= \bar{\bar{\Lambda}}_x(x) \bar{\bar{\Lambda}}_y(y) \\
&= \frac{s_y}{s_x} \mathbf{u}_x \mathbf{u}_x + \frac{s_x}{s_y} \mathbf{u}_y \mathbf{u}_y + s_x s_y \mathbf{u}_z \mathbf{u}_z
\end{aligned} \tag{1.84}$$

The x component of the Faraday's law, after following a similar procedure as in previous section, is

$$\mu \partial_t \vec{H}_x = -[\nabla \times \vec{E}]_x - \mu(\sigma_y - \sigma_x) \vec{H}_x - \mu \vec{M}_x \tag{1.85}$$

$$\partial_t \vec{M}_x = -\sigma_x(\sigma_y - \sigma_x) \vec{H}_x - \sigma_x \vec{M}_x \tag{1.86}$$

the y component can be obtained by switching x and y components in the previous expression. The z component is

$$\begin{aligned}
\partial_t \vec{H}_z &= -[\nabla \times \vec{E}]_z - \mu(\sigma_x + \sigma_y) \vec{H}_z - \mu \vec{M}_z \\
\partial_t \vec{M}_z &= \sigma_x \sigma_y \vec{M}_z
\end{aligned} \tag{1.87}$$

And similarly expressions can be obtained for Ampere's law (1.76).

Triaxial Cartesian PML The tensor (1.74) stretched on all directions arise the most general form

$$\bar{\bar{\Lambda}}_{x,y,z} = \bar{\Lambda}_x(x)\bar{\Lambda}_y(y)\bar{\Lambda}_z(z) \quad (1.88)$$

The x component of the Faraday's law can be expressed as,

$$\begin{aligned} -[\nabla \times \vec{E}]_x &= j\omega\mu \frac{s_z s_y}{s_x} \vec{H}_x \\ &= j\omega\mu \vec{H}_x + \mu(\sigma_z + \sigma_y - \sigma_x) \vec{H}_x \\ &\quad + \mu \frac{(\sigma_z - \sigma_x)(\sigma_y - \sigma_x)}{j\omega + \sigma_x} \vec{H}_x \\ &= j\omega\mu \vec{H}_x + \mu(\sigma_z + \sigma_y - \sigma_x) \vec{H}_x + \mu \vec{M}_x \end{aligned} \quad (1.89)$$

with

$$j\omega \vec{M}_x = -\sigma_x \vec{M}_x + (\sigma_z - \sigma_x)(\sigma_y - \sigma_x) \vec{H}_x \quad (1.90)$$

which in the time domain

$$\begin{aligned} \mu \partial_t \vec{H}_x &= -[\nabla \times \vec{E}]_x - \mu(\sigma_z + \sigma_y - \sigma_x) \vec{H}_x - \mu \vec{M}_x \\ \partial_t \vec{M}_x &= -\sigma_x \vec{M}_x + (\sigma_z - \sigma_x)(\sigma_y - \sigma_x) \vec{H}_x \end{aligned} \quad (1.91)$$

And similarly for the y and z components and the Ampere's law (1.76).

1.7.1.3 Constant/Varying conductivities

The equations (1.83), (1.87), and (1.91) together with the conductivity profile (1.77) require us to define and store additional mass matrices that are modified by the conductivities involved. This is a substantial amount of additional memory that will also impact the performance of the simulation. For certain cases the benefits of using the conductivity profile (1.77) are clear as was found in [15, 140]. If, rather than use a varying conductivity we choose a constant profile, there is no need to compute additional mass matrices and equations (1.83), (1.87), and (1.91) are significantly simplified. This however, will cause an increase in the energy reflected that may be a factor depending on the application.

Note also that the PMLs may have some stability problems if we are not careful when choosing large values for conductivity [125], particularly with time integration schemes with closed stability regions (shown in Table 1.4). A discussion on this issue will be carried on in section 1.7.2.2.

1.7.2 Dispersive materials

The simulation of dispersive media requires the introduction of new DOFs. This makes DGTD particularly well suited for the simulation of these media because, as discussed in Section 1.4, its higher convergence properties let us attain a better accuracy per DOF than other techniques. There are many models available to model dispersive media being the three most common the Debye's [70, 153, 154], Drude's [110, 155–157] and Lorentz's [158–160] models. These can present multiple poles that arise from theoretical arguments on material electromagnetic properties. In this Section we show how to adapt the complex-conjugate pole-residue pairs model (CCPR) proposed and demonstrated in [161, 162] for the FDTD technique. An interesting feature of the CCPR model is that it encompasses the other three models as they can be expressed as particular cases of it. Another important feature of the CCPR model is that we can use already known and freely available tools to obtain optimal poles and residue pairs for a given set of permittivities or permeabilities [163–165].

1.7.2.1 General Formulation

Let us consider the source-free Maxwell's equations (1.1) and (1.2) under the assumption that only homogeneous and isotropic media are present and therefore electromagnetic parameters can be assumed to be local and spatially constant. When equations (1.1) and (1.2) are stated for dispersive media in the FD, the permittivity is a frequency dependent magnitude. Following the approach of [161] we can model $\varepsilon(\omega)$ as

$$\varepsilon(\omega) = \varepsilon_0 \varepsilon_\infty + \varepsilon_0 \sum_{r=1}^R [\chi_r(\omega) + \chi_r'(\omega)] \quad (1.92)$$

with

$$\chi_r(\omega) = \frac{c_r}{j\omega - a_r} \quad \text{and} \quad \chi_r'(\omega) = \frac{c_r^*}{j\omega - a_r^*} \quad (1.93)$$

where $\varepsilon_\infty \in \mathbb{R}$ is the permittivity at an infinite frequency and $c_r, a_r \in \mathbb{C}$ are parameters chosen such that (1.92) fits the actual permittivity data of the material to be modelled. This fit can be done using the vector-fitting routines proposed in [163–165]. The number of residues and poles pairs, R , necessary to obtain a good approximation will depend on the complexity of the actual $\varepsilon(\omega)$. A necessary condition to ensure that ε is stable and causal is that the real part of a_r is negative.

Introducing model (1.92) into equation (1.2),

$$\varepsilon_0 \varepsilon_\infty \partial_t \vec{E} = \vec{\nabla} \times \vec{H} - \sigma \vec{E} - \sum_{r=1}^R \left(\partial_t \vec{P}_r + \partial_t \vec{P}'_r \right) \quad (1.94)$$

with

$$\vec{P}_r = \varepsilon_0 \chi_r \vec{E} \quad \text{and} \quad \vec{P}'_r = \varepsilon_0 \chi'_r \vec{E} \quad (1.95)$$

Considering also that if $\vec{E} \in \mathbb{R}$ then $\vec{P}'_r = \vec{P}_r^*$ we can finally rewrite (1.1) and (1.94) as a system of $R + 2$ coupled PDEs.

$$\begin{aligned} \partial_t \vec{E} &= \frac{1}{\varepsilon_0 \varepsilon_\infty} \left[\vec{\nabla} \times \vec{H} - \sigma \vec{E} - 2 \sum_{r=1}^R \Re[a_r \vec{P}_r + \varepsilon_0 c_r \vec{E}] \right] \\ \partial_t \vec{H} &= -\frac{1}{\mu} \vec{\nabla} \times \vec{E} \\ \partial_t \vec{P}_r &= a_r \vec{P}_r + \varepsilon_0 c_r \vec{E} \quad \forall r = 1, \dots, R \end{aligned} \quad (1.96)$$

With this formulation, the most commonly used dispersive media models can be obtained as particular cases:

1. A purely conductive media can be modeled using a single residue-pole pair with $a = 0$ and $c = \sigma/(2\varepsilon_0)$. This is equivalent to adding a conductivity term $\sigma \vec{E}$ into equation (1.2).
2. Poles of a Debye's model can be obtained with $c_r = \Delta \varepsilon_r / (2\tau_r)$ and $a_r = -1/\tau_r$.
3. Similarly for Lorentz's media we have that $c_r = j \Delta \varepsilon_r \omega_r^2 / (2\sqrt{\omega_r^2 - \delta_r^2})$ and $a_r = -\delta_r - j\sqrt{\omega_r^2 - \delta_r^2}$.
4. Drude's media

$$\varepsilon(\omega) = \varepsilon_\infty - \frac{\omega_r^2}{\omega + j\omega\gamma_r} \quad (1.97)$$

drive us to a two poles decomposition $a_1 = \gamma_0$, $c_1 = \omega_0^2 / (2\gamma_0)$ and $a_2 = 0$, $c_2 = -c_1$. Leading to an unstable scheme ($a_1 > 0$). Drude's media can be modeled fitting the time derivative of the susceptibilities $j\omega\chi$ and $j\omega\chi'$ driving to,

$$\chi(\omega)_s = \frac{b_s}{j\omega(j\omega - d_s)} \quad (1.98)$$

1.7.2.2 Stability of dispersive models

The stability conditions for dispersive media have been studied by several authors [125, 159, 166] finding that the DG semi-discretized scheme is stable for any physically stable model. When we introduce dispersion models, we find that the original

eigenvalues that we obtained (1.28) are affected by the new equations in (1.96). The new eigenvalues or the modification of the existing ones may make them to move out of the stability regions (Fig. 1.6) forcing us to reduce h_t to ensure the stability of the scheme. For dispersive media [154], [167] and [159] show that the DGTD and CGTD schemes with LF2 time integration schemes are stable and their solutions converge. This happens because the leap-frog schemes are only unstable depending on the imaginary part of the eigenvalues present in Maxwell's equations (1.96) as discussed in Section 1.5.1. However, when we apply the LSERK4 scheme introduced in section 1.5.2 the new eigenvalues may lead to unstable schemes if the modified eigenfrequencies fall out of the closed stability region.

1.7.3 Anisotropic materials

The DGTD method can be straightforwardly extended to anisotropic materials [14, 15, 99, 168]. Substituting ε and μ in (1.1) and (1.2) with electric permittivity and magnetic permeability symmetric positive-definite tensors $\bar{\bar{\varepsilon}}$ and $\bar{\bar{\mu}}$.

We can express $\bar{\bar{\varepsilon}}$ and $\bar{\bar{\mu}}$, and their inverses, in a local base of vectors. Following an operation splitting method similar as was done in section 1.4.2 we can derive again a one dimensional Riemann problem to deduce new conditions for the numerical fluxes (1.19). However, the fact that we are using tensors leads us to expressions for two matrices, *impedance* ($\bar{\bar{Z}}_2$) and *admittance* ($\bar{\bar{Y}}_2$), which play a role equivalent to the scalar impedance (Z) and admittance (Y) magnitudes defined for the isotropic case. Finally $\bar{\bar{Z}}_2$ and $\bar{\bar{Y}}_2$ are introduced in (1.19) to account for the anisotropic nature of the media. The rest of the scheme is also affected by the tensorial nature of $\bar{\bar{\varepsilon}}$ and $\bar{\bar{\mu}}$ but their effect is simply to scale the mass matrices (1.14) depending on the tensor values.

An example problem is shown in Fig. 1.9 (from [14]). In this problem a sphere is illuminated with a linearly polarized plane wave. The bistatic RCS is computed at a frequency for which the diameter is $D = 1.2\lambda$, with λ being the wavelength. The results are compared with a reference case [2] and with the solution provided by the Ansoft HFSS commercial software. The maximum difference found is 0.35 dB, therefore resulting in a good agreement.

1.8 Subcell models

Through a modification of the numerical flux conditions we can model a wide variety of phenomenons such as lumped elements, multi-port networks, or thin layers.

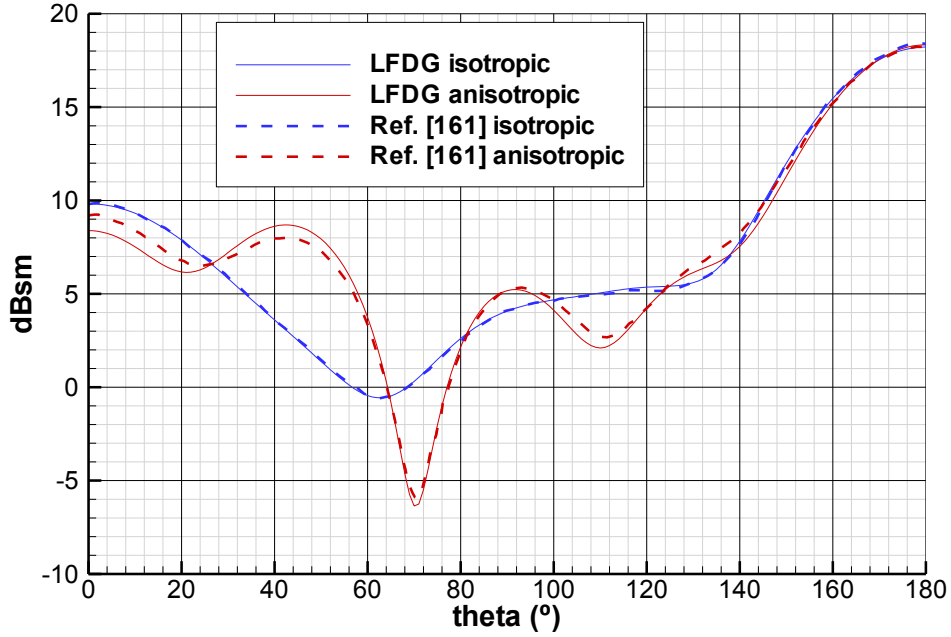


FIGURE 1.9: Bistatic RCS of an isotropic/anisotropic sphere ($D = 1.2\lambda$ and $\lambda = 1.0m$). LFDG results are compared to those appearing in [2], and computed with Ansoft HFSS.

1.8.1 Lumped elements

The modeling of passive lumped elements such as resistors, capacitors, and inductors and general combinations of them has been studied in [169–171], a generalization of the previous works for multi-port networks is carried on in [68, 172]. Lumped elements can also be seen as special cases of thin layers which are introduced in the next section.

1.8.2 Thin layers

Thin layers of any material, including anisotropic and dispersive media, is described in [173–175] for the FDTD method. Specifically for DGTD, a simple resistive layer was introduced in [67] and a rigorous formulation and validation, suitable also for curved geometries, is shown in [99] and [176]. To model thin layers, we will use a Surface Impedance Boundary Condition (SIBC) that reproduces its behavior. Note also that an SIBC defined over a free surface can also be regarded as a two-port network model (see Fig. 1.10).

Let us suppose an indefinite panel embedded in air is illuminated by a normally incident TEM plane wave. An equivalent circuit of this setup is shown in Fig. 1.11 in which \vec{E}_0 , \vec{E}_d , \vec{H}_0 and \vec{H}_d are the components of the electric and magnetic fields which are tangential to the external faces (0 and d) of the slab, respectively. Using

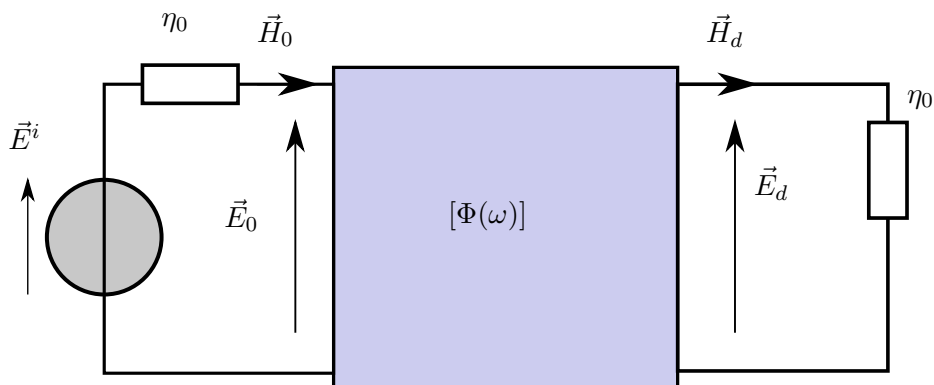


FIGURE 1.10: Two-port representation of the air-embedded panel illuminated by a TEM plane wave.

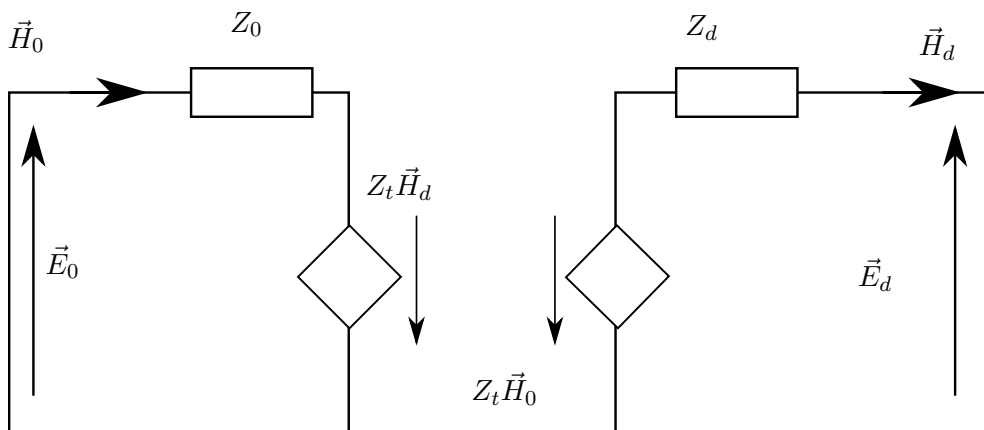


FIGURE 1.11: Magnetic field controlled circuit representation of a thin layer.

a two-port transmission line formalism we can deduce the following relationship between the field components

$$\begin{pmatrix} \vec{E}_0(\omega) \\ \vec{H}_0(\omega) \end{pmatrix} = [\Phi(\omega)] \begin{pmatrix} \vec{E}_d(\omega) \\ \vec{H}_d(\omega) \end{pmatrix} \quad (1.99)$$

with

$$\Phi_{11}(\omega) = \Phi_{22}(\omega) = \cosh(\gamma d) \quad (1.100)$$

$$\Phi_{12}(\omega) = \eta \sinh(\gamma d) \quad (1.101)$$

$$\Phi_{21}(\omega) = \eta^{-1} \sinh(\gamma d) \quad (1.102)$$

with η and γ being the intrinsic impedance and the propagation constant respectively. Note that this expressions are derived from ε and μ which can depend on ω , as the ones presented in Section 1.7.2.

Matrix equation (1.99) can be transformed, using widely known two-port network relationships [177], into the following equivalent magnetic-field-controlled (MFC) formulation:

$$\underbrace{\begin{bmatrix} \vec{E}_0 \\ \vec{E}_d \end{bmatrix}}_{\tilde{\vec{E}}} = \underbrace{\begin{bmatrix} Z_0 & -Z_t \\ -Z_d & Z_t \end{bmatrix}}_{\tilde{\mathcal{Z}}(\omega)} \underbrace{\begin{bmatrix} \vec{H}_0 \\ \vec{H}_d \end{bmatrix}}_{\tilde{\vec{H}}} \quad (1.103)$$

Fig. 1.11 shows the sketch of the circuit model of (1.103) in which the dependence of the electric field at the one side of the slab from the magnetic field at the other one is represented by MFC electric-field sources. Notice that for non-symmetrical multi-layered slabs the coefficients Φ_{11} and Φ_{22} are not coincident, even if matrix $[\Phi(\omega)]$ always satisfies the reciprocity condition; therefore, the impedances Z_0 and Z_d can assume different values, in general. The $\tilde{\mathcal{Z}}$ can be decomposed using a VF technique as the one we used in Section 1.7.2, using for instance the routines provided by [163–165]

$$\tilde{\mathcal{Z}}(\omega) = \tilde{\mathcal{Z}}_\infty + \sum_{p=1}^P \frac{\tilde{\mathcal{Z}}_p}{j\omega - a_p} \quad (1.104)$$

being $\tilde{\mathcal{Z}}_\infty$ and $\tilde{\mathcal{Z}}_p$ an approximation of the impedance matrix of the medium. With this decomposition $\tilde{\vec{E}}$ can be expressed as

$$\tilde{\vec{E}}(\omega) = \tilde{\mathcal{Q}}_\infty(\omega) + \sum_{p=1}^P \tilde{\mathcal{Q}}_p(\omega) \quad (1.105)$$

with

$$\tilde{\mathcal{Q}}_\infty = \begin{bmatrix} \vec{Q}_{0,\infty} \\ \vec{Q}_{d,\infty} \end{bmatrix} = \tilde{\mathcal{Z}}_\infty \tilde{\vec{H}} \quad (1.106)$$

and

$$\tilde{\mathcal{Q}}_p = \begin{bmatrix} \vec{Q}_{0,p} \\ \vec{Q}_{d,p} \end{bmatrix} = \tilde{\mathcal{Z}}_p \tilde{\vec{H}} \quad (1.107)$$

Making use of the ADE formalism, the infinity frequency term is

$$\tilde{\mathcal{Q}}_\infty(t) = \tilde{\mathcal{Z}}_\infty \tilde{\vec{H}}(t) \quad (1.108)$$

The frequency dependent terms arise to P new differential equations

$$\partial_t \tilde{\mathcal{Q}}_p = a_p \tilde{\mathcal{Q}}_p + \tilde{\mathcal{Z}}_p \tilde{\vec{H}}(t) \quad (1.109)$$

That are solved similarly as we did in Section 1.7.2 for dispersive materials. The calculated electric fields are used, similarly as was done in (1.23), (1.24), and (1.25), to modify the jump terms (1.20) in the following way,

$$\begin{aligned} [[\mathbf{E}]]_{\text{SIBC},0} &= 2(\mathbf{E} - \mathbf{E}_0) \\ [[\mathbf{H}]]_{\text{SIBC},0} &= 0 \end{aligned} \tag{1.110}$$

and similarly for the d side of the SIBC.

1.8.3 Thin wire geometries

Particularly in EMC, it is often needed to evaluate currents on cables. To do this, the typical approach is to model cables as thin wires that are split into segments located along the edges of the cells in the mesh [67]. On each segment, the currents and charges are evaluated following an implementation of the Holland formalism [178, 179]. These equations are discretized on each of the segments following a similar formalism as we have used in section 1.4 but this time for a one dimensional problem weakly coupled with our original semi-discretization.

A different approach is followed by [180] in which the region containing the thin wires is solved using the Time Domain Integral Equation that is then coupled to the DGTD algorithm by a modification of the numerical fluxes, similarly as was done in section 1.6.1 for plane waves.

1.9 Computational implementation

In this section we present some final remarks regarding the computational implementation of a few of the techniques previously described.

1.9.1 Geometrical discretization

An important aspect for an efficient simulation is the capability of generating complex meshes. This requirement is fulfilled by most of the commercial CAD tools.

The tool SEMBA, that we have developed, uses GiD for pre- and post-processing. GiD [104] is a commercial tool that allows pre-processing of geometries with CAD importing capabilities. These geometries can be meshed in a variety of ways, including structured and semistructured meshes, linear or quadratic elements, and

several types of elements (tetrahedrons, hexahedrons, prisms, ...). The program permits a high degree of customization that allows users to develop their own problem types. Additionally, the results obtained can be easily visualized and several post-processing tools are also offered.

There are many other applications that can offer solutions for obtaining meshes. Among the open-source tools, we highlight Gmsh [103] and OpenFoam [181].

1.9.2 Preprocessing

To increase the efficiency of the computations and implement certain capabilities it is necessary to perform some pre-processing tasks. These tasks are usually optional as they depend on the capabilities implemented in the solver.

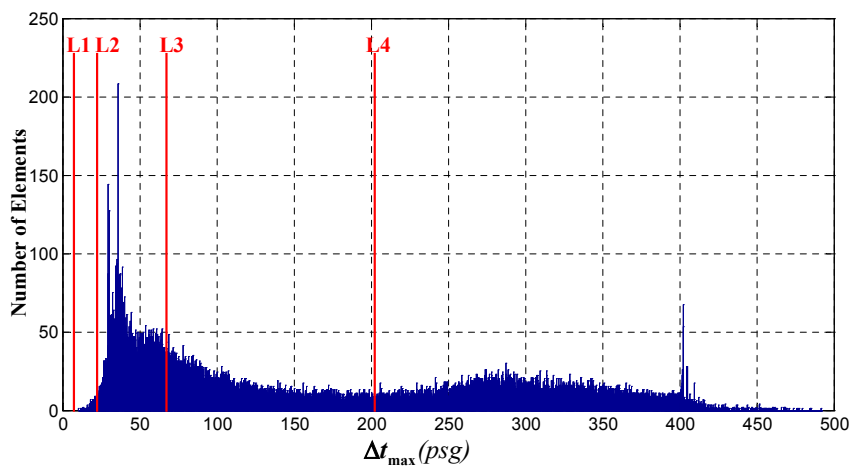
1.9.2.1 Selection of basis functions

An *a priori* hp -refinement heuristic strategy consists on choosing the size of the mesh, and the order of the basis function in each tetrahedron [15]. The target is to ensure a given accuracy level, minimizing the computational cost. The selection of the mesh size has to be made in the mesh-generation process, since there is an optimum element size that minimizes the computational cost for a required accuracy. In real meshes, the element sizes vary throughout the computational domain, and the accuracy is finally adjusted with the selection of the order p . This allow us to employ higher-order basis for larger tetrahedrons, and lower orders for smaller ones. This approach can also combine gradient spaces of reduced order $p - 1$, with rotational spaces of complete order p [85].

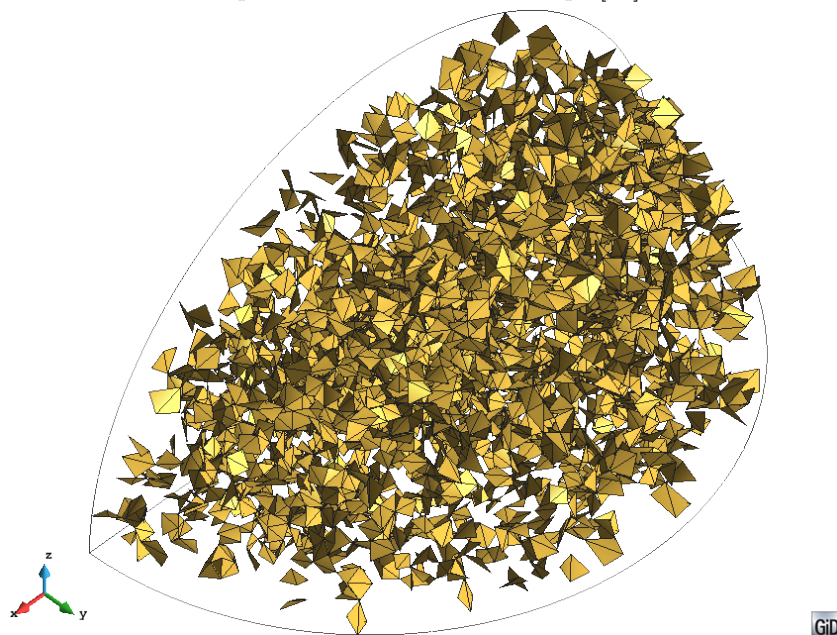
It bears noting that smaller elements need shorter timesteps, but if lower orders are used in these elements, the stability condition is also relaxed. The combination and mixing different orders of the basis functions depending on element size, makes the timestep among all the elements more homogeneous, reducing the number of levels required for the LTS algorithm.

1.9.2.2 LTS Level classification

The local time-stepping strategy described in Section 1.5.3.1 requires a classification of all the elements according to their maximum timestep. Fig. 1.12 illustrate the distribution of the timesteps for the elements in a real problem. As there are usually



(A) Example of distribution of timesteps in a real problem (described in [13]). The choice of timestep and the timesteps of different levels have been included in the plot. The estimated average timestep was 88.5 ps, compared to the minimum 10.5 ps [15].



(B) Elements evolved with the double of the minimum timestep (Tier 1) using an LTS technique for LF2 [23].

FIGURE 1.12: Assortment of tiers for the use of a LTS technique.

some costs associated with the buffering zones between time tiers [15, 23, 25, 128], the minimum timestep can be actually tuned to provide a maximum average timestep.

1.9.3 Parallelization

One key advantage of discontinuous Galerkin methods is their simplicity for the parallelization in memory-distributed hardware architecture. A feature that arises from its explicitness. This allows us to make use of the Message Passing Interface

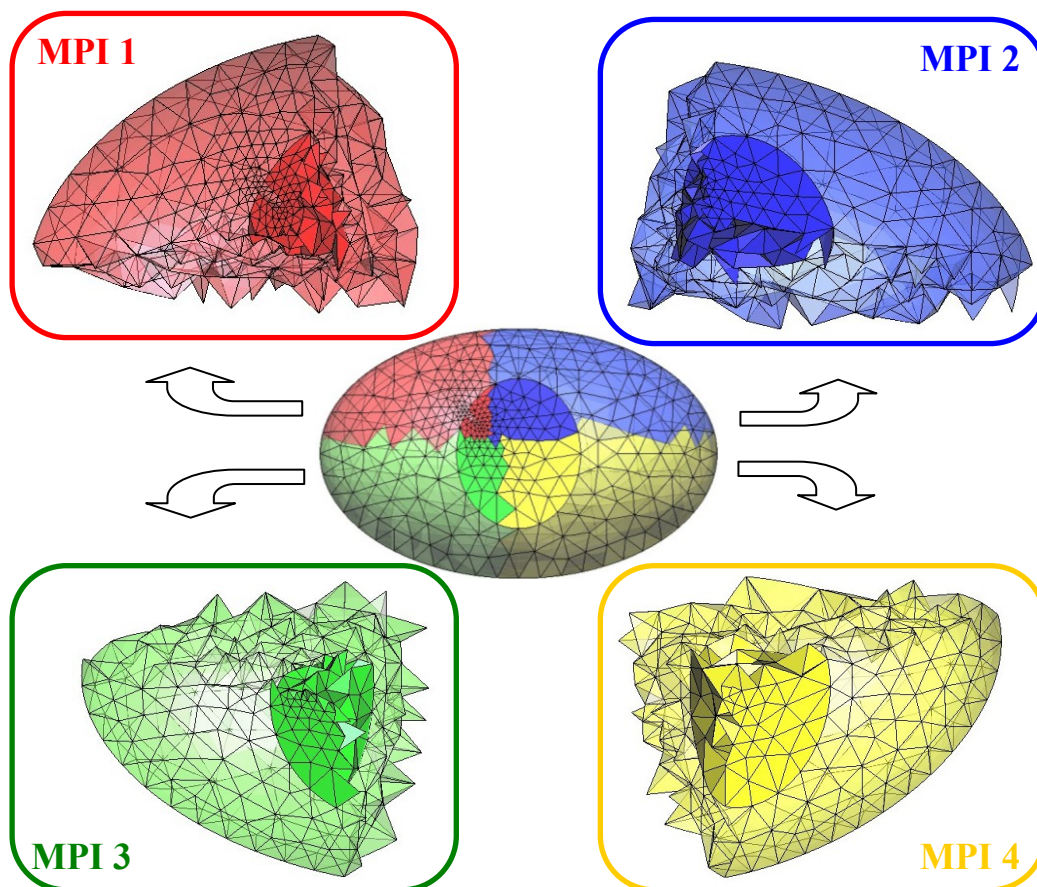


FIGURE 1.13: Distribution of the mesh among the different MPI processes.

(MPI) standard [108, 110, 182] or the GPU (CUDA/OpenCL) [122, 183, 184]. The DGTD method exhibits great boosts in performance thanks to its memory locality, the regularity of access patterns and the high arithmetic intensity [184]. There are several ways to perform the partitioning of the mesh carried out during the pre-processing stage. The simplest way is to manually define regions that are handled to the different processes (Fig. 1.13). However, as pointed out in [122], this may result in a load unbalance that reduces drastically the efficiency. To solve this issue the ParMetis library [185] can be used to partition the mesh assigning different weights to the cells depending on the number of arithmetic operations that they need. ParMetis can also be configured to provide the partition with the minimum interface, to optimize the interprocess communication. Other techniques developed for FDTD can also be used to reduce the number of interprocess communications [186].

Acknowledgments

The authors gratefully thank to the Prof. Fernando L. Teixeira and Prof. Stephane Lanteri who provided helpful insights in numerous discussions. The work described in this dissertation has been partially funded through the European Community's Seventh Framework Programme FP7/2007-2013, under grant agreement no 205294 (HIRF SE project), and his work is partially funded by the National Projects TEC2010-20841-C04-04, TEC2013-48414-C3-01, CSD2008-00068, P09-TIC-5327, P12-TIC-1442, and from the GENIL excellence network.

Part II

On Discontinuous Galerkin Method Theory

Chapter 2

A spurious-free Discontinuous Galerkin Time Domain method for the accurate modeling of microwave filters

J. Alvarez, L. D. Angulo, A. Rubio Bretones, and S.G. Garcia. A spurious-free discontinuous galerkin time-domain method for the accurate modeling of microwave filters. *Microwave Theory and Techniques, IEEE Transactions on*, 60(8):2359–2369, 2012

Abstract

The simulation of highly resonant structures requires techniques that are accurate and free of spurious-mode contamination. Spurious modes can severely corrupt the solution of a physical problem, and their suppression is a must for any numerical scheme in frequency or in time domain. In this paper, we present the application of a highly accurate spurious-free vector Discontinuous Galerkin Time Domain method to waveguide applications. We show that spurious solutions (which increase with the number of degrees of freedom of the problem) can be efficiently attenuated by using penalized fluxes. For validation, we apply our approach to the simulation of microwave filters, since their highly resonant behavior is challenging for time-domain techniques.

2.1 Introduction

The Discontinuous Galerkin Time Domain method (DGTD) is a numerical technique that is attracting attention in time-domain (TD) computational electromagnetics [27]. DGTD starts from a variational formulation to integrate the spatial part of Maxwell's time-domain (TD) curl equations, with an appropriate differential integration scheme for the time part. As in Finite Elements Methods (FEM), the space is divided into M non-overlapping elements, in each of which the solution is expanded in a set of local basis functions of arbitrary order. A weak form of Maxwell's curl equations is found element by element by employing a Galerkin test procedure. Unlike in FEM, the solution is allowed to be fully discontinuous across the boundaries between adjacent elements. Thus, local mass and stiffness matrices do not require the assembly of adjacent element terms, with the subsequent computational advantage over classical FEM. DGTD needs only the inversion square matrices of $Q \times Q$ elements (with Q the number of degrees of freedom (dofs) per element), while the system of equations of ($\simeq MQ \times MQ$) needs to be solved at each time step for FEM in TD[60, 187].

For the solution between elements sharing a common surface to be connected, continuous numerical fluxes of the tangential field components are defined at the interface in the manner used in Finite-Volume Time-Domain (FVTD) methods [188]. The simplest flux condition found in the literature is the centered one, which employs a simple average of the tangential field on each side to build the flux [189]. Another one is the upwind flux [188] used in the classical FVTD, which is found from the solution of the Riemann discontinuous initial value problem, and depends both on the electric and on the magnetic fields on each side. In between the centered and the upwind fluxes, there is a family of them, called partially penalized, which can be defined by using a parameter which penalizes the discontinuities in the tangential components in a lossy manner [27].

Classical continuous FEM methods, both in curl-curl and in the mixed formulation, are well known for supporting spurious modes, which are nonphysical solutions arising in the numerical approximation not present in the analytical problem. Especially harmful are nondivergent spurious modes (for divergence-free analytical problems) excited at non-null frequencies, since they severely corrupt near-field solutions. Many strategies to reduce them are found in the literature. For nodal (scalar basis) FEM, regularization techniques including conditions on the divergence of the solution, have been successfully employed [87]. For vector FEM, it is possible to use curl-conforming elements for which the basis vectors abide by the natural

(dis)continuity of the electromagnetic fields¹, supporting spurious modes only at null frequency [60]. Higher-order hierarchal basis functions were introduced in [85] with this purpose.

DGTD also exhibits the appearance of spurious modes [62, 74–76, 89, 90, 190]. However, an added advantage of DGTD over FEMTD resides in its discontinuous nature, which allows them to be removed due to the use of upwind/penalized fluxes [74–76, 89, 90]. As stated above, these fluxes are characterized by the addition to Maxwell’s equations of dissipative terms, and are proven to attenuate spurious modes in space more strongly than physical modes. The suppression of spurious modes becomes a critical issue for DGTD formulations of the Perfectly Matched Layer (PML) truncation condition, since instabilities appear otherwise [113]. Both DGTD for vector and scalar basis are spurious-free for penalized fluxes, and have been successfully developed by several authors [10, 27, 67, 124, 189, 191–195], finding comparable levels of accuracy. Of course, there are advantages and disadvantages of vector and nodal formulations, basically in terms of computational implementations, also depending on the time integration scheme, but these issues lie beyond the scope of the present study, and will be addressed elsewhere.

In this paper, we present an analysis of the accuracy of DGTD methods for the simulation of highly resonant structures, and we demonstrate that the impact of using different fluxes depend on the observable used for comparison. The paper is organized as follows: we first summarize the vector and nodal formulations of DTGD. We next revisit and provide a deep discussion on the topic of spurious modes for simple 1D and 3D problems, both for centered and partially penalized fluxes. Finally, we assess the accuracy of the DGTD method depending on the flux choice using microwave filters as a workbench.

2.2 DGTD fundamentals

2.2.1 Vector formulation

Let us assume Maxwell’s symmetric curl equations for linear isotropic homogeneous media in Cartesian coordinates. Now, let us divide the space in M non-overlapping elements V^m , each bounded by ∂V^m and define, element by element, locally continuous basis/test functions, and two inner products (volume and surface):

$$\mathcal{B}^m = \{\vec{\Phi}_1^m, \vec{\Phi}_2^m, \dots, \vec{\Phi}_Q^m\} \quad (2.1)$$

¹Continuity on the tangential components, and discontinuity in the normal ones.

$$\langle \vec{u}, \vec{w} \rangle_{V^m} = \int_{V^m} (\vec{u} \cdot \vec{w}) dV, \quad \langle \vec{u}, \vec{w} \rangle_{\partial V^m} = \oint_{\partial V^m} (\vec{u} \cdot \vec{w}) dS \quad (2.2)$$

Requiring the residue of Maxwell's curl TD equations to be orthogonal to each basis function element by element, we find that

$$\left\langle \vec{\Phi}_{q'}^m, \varepsilon \partial_t \vec{E}^m + \sigma_e \vec{E}^m - \nabla \times \vec{H}^m \right\rangle_{V^m} = 0 \quad (2.3)$$

$$\left\langle \vec{\Phi}_{q'}^m, \mu \partial_t \vec{H}^m + \sigma_m \vec{H}^m + \nabla \times \vec{E}^m \right\rangle_{V^m} = 0 \quad (2.4)$$

$$\forall q = (1, \dots, Q), \quad m = (1, \dots, M) \quad (2.5)$$

With $\vec{E}, \vec{H}, \sigma_e, \sigma_m, \varepsilon, \mu$ being, respectively: electric field, magnetic field, electric conductivity, magnetic conductivity, permittivity, and permeability. After some algebra, we can write Eqs. (2.3) and (2.4) respectively as

$$\begin{aligned} & \int_{V^m} (\vec{\Phi}_{q'}^m \cdot (\varepsilon \partial_t \vec{E}^m + \sigma_e \vec{E}^m) + \nabla \times \vec{\Phi}_{q'}^m \cdot \vec{H}^m) dV = \\ & \oint_{\partial V^m} \vec{\Phi}_{q'}^m \cdot (\hat{\mathbf{n}}^m \times \vec{H}^m) dS \end{aligned} \quad (2.6)$$

$$\begin{aligned} & \int_{V^m} (\vec{\Phi}_{q'}^m \cdot (\mu \partial_t \vec{H}^m + \sigma_m \vec{H}^m) - \nabla \times \vec{\Phi}_{q'}^m \cdot \vec{E}^m) dV = \\ & - \oint_{\partial V^m} \vec{\Phi}_{q'}^m \cdot (\hat{\mathbf{n}}^m \times \vec{E}^m) dS \end{aligned} \quad (2.7)$$

These relate the volume integral of the LHS to a flux integral in the RHS. Classical mixed FEMTD computes the RHS of (2.6)(2.7) by forcing the tangential component to be continuous at the interface across adjacent elements $\hat{\mathbf{n}}^m \times \vec{u}^m = \hat{\mathbf{n}}^m \times \vec{u}^{m+}$ (the superscript + denotes magnitudes from adjacent elements, and $\vec{u} = \{\vec{E}, \vec{H}\}$). However, DGTD defines continuous numerical fluxes of the tangential-field components $\hat{\mathbf{n}}^m \times \vec{u}^{m*}$ to be used instead of $\hat{\mathbf{n}}^m \times \vec{u}^m$ at the RHS of (2.6)(2.7), on each side of ∂V^m . These tangential fields do not coincide with any of the values on any side of ∂V^m , but depend linearly on them, with a general form

$$\begin{aligned} \hat{\mathbf{n}}^m \times \vec{E}^{m*} &= \hat{\mathbf{n}}^m \times \vec{E}^m + \kappa_e^m \left[\hat{\mathbf{n}}^m \times (\vec{E}^{m+} - \vec{E}^m) + \vec{M}_s \right] + \\ & \quad \nu_h^m \left[\hat{\mathbf{n}}^m \times (\hat{\mathbf{n}}^m \times (\vec{H}^{m+} - \vec{H}^m) - \vec{J}_s) \right] \\ \hat{\mathbf{n}}^m \times \vec{H}^{m*} &= \hat{\mathbf{n}}^m \times \vec{H}^m + \kappa_h^m \left[\hat{\mathbf{n}}^m \times (\vec{H}^{m+} - \vec{H}^m) - \vec{J}_s \right] - \\ & \quad \nu_e^m \left[\hat{\mathbf{n}}^m \times (\hat{\mathbf{n}}^m \times (\vec{E}^{m+} - \vec{E}^m) + \vec{M}_s) \right] \end{aligned} \quad (2.8)$$

with κ, ν appropriate coefficients (see subsection 2.2.3). In Eq. (2.8), we have included possible surface currents, required, for instance, in the implementation of Huygen's sources [10].

Assuming that the space and time dependencies of the fields can be separated, and that the spatial part is expanded within each element in a set of basis functions equal to the set of test functions (Faedo-Galerkin method), we get

$$\vec{E}^m = \sum_{q=1}^Q e_q^m(t) \vec{\Phi}_q^m(\vec{r}), \quad \vec{H}^m = \sum_{q=1}^Q h_q^m(t) \vec{\Phi}_q^m(\vec{r}) \quad (2.9)$$

a final semi-discrete algorithm is found

$$\begin{aligned} & \mu \mathbb{M} d_t H^m + (\sigma_m \mathbb{M} - \mathbb{F}_{\nu h}) H^m + \mathbb{F}_{\nu h}^+ H^{m+} = \\ & - (\mathbb{S} - \mathbb{F}_{\kappa e}) E^m - \mathbb{F}_{\kappa e}^+ E^{m+} - M_{s\kappa} + J_{s\nu} \end{aligned} \quad (2.10a)$$

$$\begin{aligned} & \varepsilon \mathbb{M} d_t E^m + (\sigma_e \mathbb{M} - \mathbb{F}_{\nu e}) E^m + \mathbb{F}_{\nu e}^+ E^{m+} = \\ & (\mathbb{S} - \mathbb{F}_{\kappa h}) H^m + \mathbb{F}_{\kappa h}^+ H^{m+} - J_{s\kappa} - M_{s\nu} \end{aligned} \quad (2.10b)$$

For this, we have defined the following.

- H^m and E^m are column vector varying in time with the field coefficients (dofs) in the element m , and H^{m+} and E^{m+} with the field coefficients (dofs) of the adjacent elements,

$$H^m = (h_1^m(t), \dots, h_Q^m(t))^T \quad (2.11a)$$

$$E^m = (e_1^m(t), \dots, e_Q^m(t))^T \quad (2.11b)$$

- $M_{s\kappa}$, $M_{s\nu}$, $J_{s\kappa}$ and $J_{s\nu}$ are column vector varying in time with the weak form of the surface source terms in the element m ,

$$M_{s\kappa} = \left(\left\langle \vec{\Phi}_1^m, \kappa_e^m \vec{M}_s(r, t) \right\rangle_{\partial V^m}, \dots \right)^T \quad (2.12a)$$

$$M_{s\nu} = \left(\left\langle \vec{\Phi}_1^m, \nu_e^m \hat{\mathbf{n}}^m \times \vec{M}_s(r, t) \right\rangle_{\partial V^m}, \dots \right)^T \quad (2.12b)$$

$$J_{s\kappa} = \left(\left\langle \vec{\Phi}_1^m, \kappa_h^m \vec{J}_s(r, t) \right\rangle_{\partial V^m}, \dots \right)^T \quad (2.12c)$$

$$J_{s\nu} = \left(\left\langle \vec{\Phi}_1^m, \nu_h^m \hat{\mathbf{n}}^m \times \vec{J}_s(r, t) \right\rangle_{\partial V^m}, \dots \right)^T \quad (2.12d)$$

- \mathbb{M} is the mass matrix,

$$[\mathbb{M}]_{q'q} = \left\langle \vec{\Phi}_{q'}^m, \vec{\Phi}_q^m \right\rangle_{V^m} \quad (2.13)$$

- \mathbb{S} is the stiffness matrix

$$[\mathbb{S}]_{q'q} = \left\langle \vec{\Phi}_{q'}^m, \nabla \times \vec{\Phi}_q^m \right\rangle_{V^m} \quad (2.14)$$

- \mathbb{F} are the flux matrices

$$[\mathbb{F}_{\kappa h}]_{q'q} = \left\langle \vec{\Phi}_{q'}^m, \kappa_h^m \hat{\mathbf{n}}^m \times \vec{\Phi}_q^m \right\rangle_{\partial V^m}$$

$$[\mathbb{F}_{\kappa e}]_{q'q} = \left\langle \vec{\Phi}_{q'}^m, \kappa_e^m \hat{\mathbf{n}}^m \times \vec{\Phi}_q^m \right\rangle_{\partial V^m} \quad (2.15a)$$

$$[\mathbb{F}_{\nu h}]_{q'q} = \left\langle \vec{\Phi}_{q'}^m, \nu_h^m \hat{\mathbf{n}}^m \times \hat{\mathbf{n}}^m \times \vec{\Phi}_q^m \right\rangle_{\partial V^m}$$

$$[\mathbb{F}_{\nu e}]_{q'q} = \left\langle \vec{\Phi}_{q'}^m, \nu_e^m \hat{\mathbf{n}}^m \times \hat{\mathbf{n}}^m \times \vec{\Phi}_q^m \right\rangle_{\partial V^m} \quad (2.15b)$$

$$[\mathbb{F}_{\kappa h}^+]_{q'q} = \left\langle \vec{\Phi}_{q'}^m, \kappa_h^m \hat{\mathbf{n}}^m \times \vec{\Phi}_q^{m+} \right\rangle_{\partial V^m}$$

$$[\mathbb{F}_{\kappa e}^+]_{q'q} = \left\langle \vec{\Phi}_{q'}^m, \kappa_e^m \hat{\mathbf{n}}^m \times \vec{\Phi}_q^{m+} \right\rangle_{\partial V^m} \quad (2.15c)$$

$$[\mathbb{F}_{\nu h}^+]_{q'q} = \left\langle \vec{\Phi}_{q'}^m, \nu_h^m \hat{\mathbf{n}}^m \times \hat{\mathbf{n}}^m \times \vec{\Phi}_q^{m+} \right\rangle_{\partial V^m}$$

$$[\mathbb{F}_{\nu e}^+]_{q'q} = \left\langle \vec{\Phi}_{q'}^m, \nu_e^m \hat{\mathbf{n}}^m \times \hat{\mathbf{n}}^m \times \vec{\Phi}_q^{m+} \right\rangle_{\partial V^m} \quad (2.15d)$$

For the time-domain integration, several approaches can be chosen. The most widely employed ones are the 2^{nd} -order leapfrog (LF) scheme based on centered differentiation², and 4th-order Runge-Kutta (RK4) [27].

2.2.2 Scalar-basis (nodal) formulation

The fundamentals of the scalar formulation are similar to those of the vector one. Now the basis and test functions are chosen to be scalar: $\mathcal{B}^m = \{\Phi_1^m, \Phi_2^m, \dots, \Phi_Q^m\}$. The weak form of Maxwell's equations is found by nullifying the next inner product of each scalar basis function with Maxwell's curl equations

$$\langle \lambda, \vec{w} \rangle_{V^m} = \int_{V^m} (\lambda \vec{w}) dV, \quad \langle \lambda, \vec{w} \rangle_{\partial V^m} = \oint_{\partial V^m} (\lambda \vec{w}) dS \quad (2.16)$$

A set of equations formally similar to (2.10) is found, now with E^m (and H^m) column matrix with the vector coefficients varying in time

$$E^m = (\vec{e}_1^m(t), \dots, \vec{e}_Q^m(t))^T \quad (2.17a)$$

²Dissipative terms related to $\tilde{F}_{\nu h}^+$ and $\tilde{F}_{\nu e}^+$ require a backward approximation when solved by LF ($H_n^m \simeq H_{n-1/2}^m$ and $E_{n+1/2}^m \simeq E_n^m$), to formulate an explicit scheme, since adjacent terms involve synchronous magnitudes.

with the sole difference in the stiffness matrix, which is instead

$$[\mathbb{S}]_{q'q} = \langle \Phi_{q'}^m, \nabla \Phi_{q^m} \rangle_{V^m} \quad (2.18)$$

Common choices for the scalar basis functions [189], are set 3D Lagrange interpolating n^{th} -order polynomials [82] and Legendre polynomials.

2.2.3 Numerical fluxes

Numerical fluxes reported in the literature can be seen as particular cases of the partial penalized flux [27, 62, 77, 113] with the form of Eq. (2.8), here rewritten for convenience as a function of a penalization parameter τ (the parameters κ, ν in (2.8), can be expressed in terms of the τ parameter by simple identification)

$$\hat{\mathbf{n}}^m \times \mathbf{E}^* = \frac{\hat{\mathbf{n}}^m \times (Y^m \mathbf{E}^m + Y^{m+} \mathbf{E}^{m+}) + Y^{m+} \mathbf{M}_s}{Y^m + Y^{m+}} - \tau \frac{\hat{\mathbf{n}}^m \times [\hat{\mathbf{n}}^m \times (\mathbf{H}^m - \mathbf{H}^{m+}) + \mathbf{J}_s]}{Y^m + Y^{m+}} \quad (2.19a)$$

$$\hat{\mathbf{n}}^m \times \mathbf{H}^* = \frac{\hat{\mathbf{n}}^m \times (Z^m \mathbf{H}^m + Z^{m+} \mathbf{H}^{m+}) - Z^{m+} \mathbf{J}_s}{Z^m + Z^{m+}} + \tau \frac{\hat{\mathbf{n}}^m \times [\hat{\mathbf{n}}^m \times (\mathbf{E}^m - \mathbf{E}^{m+}) - \mathbf{M}_s]}{Z^m + Z^{m+}} \quad (2.19b)$$

with $Z^m = 1/Y^m = (\mu^m/\varepsilon^m)^{1/2}$, and $Z^{m+} = 1/Y^{m+} = (\mu^{m+}/\varepsilon^{m+})^{1/2}$ the intrinsic impedances of the media at the element m and its adjacent $m+$, respectively.

The most common choices are: centered ($\tau = 0$), upwind ($\tau = 1$) and partial penalized numerical fluxes ($0 < \tau < 1$). The centered flux [194] is equivalent to averaging the solutions at both sides of the interface, while the upwind flux is the usual one employed in FVTD [188] arising from the solution of the Maxwell's equations with discontinuous initial values (Riemann problem) [189].

The terms for $\tau \neq 0$ produce non-null ν factors that introduce artificial dissipation in Eqs. (2.10), and this effect can be shown to be stronger for spurious modes than for physical ones [62, 74, 77]. The attenuation of the nonphysical modes is maximum for the upwind flux, and null for centered flux, which dissipates neither physical nor spurious modes. The τ parameter actually penalizes the discontinuities on the physically continuous tangential components ($\hat{\mathbf{n}} \times \hat{\mathbf{n}} \times (\vec{\mathbf{E}}^m - \vec{\mathbf{E}}^{m+})$ and $\hat{\mathbf{n}} \times \hat{\mathbf{n}} \times (\vec{\mathbf{H}}^m - \vec{\mathbf{H}}^{m+})$) by introducing a stabilization-like effect, introducing losses, if the average jump over the face is positive, and amplification in the case of negative

discontinuity. In the adjacent element the stabilization effect will take the opposite sign.

The value of the penalization parameter also has an impact on the stability constraints in the time increment, which becomes the most restrictive for the upwind flux and less restrictive for the centered flux. A tradeoff solution can be found by tuning τ to retain spurious-mode dissipation while relaxing the stability constraints. This fact is analyzed in case of Leap-Frog integration scheme in [77], and, in [113], for Runge-Kutta schemes.

2.3 Numerical dispersion and dissipation

The dispersion and dissipation of the numerical method will be studied by searching for plane-wave solutions of frequency ω and wavevector \vec{k} , in general complex. These functions, replaced in the original equations, lead to an eigenproblem, with eigenvalues providing the numerical dispersion and dissipation relationships $\omega = f(\vec{k}) = 0$, and with eigenvectors providing the numerical-structure relationships between the dofs (field components). For instance, the analytical Maxwell's equations support planewaves in free-space with the well-known dispersion relationship $\omega^2 = k^2/c^2$, and eigenvectors related by $\eta_0 \vec{H} = \hat{\mathbf{k}} \times \vec{E}$, with c and η_0 being the free-space speed of light and impedance, respectively.

A practical way to study the dispersion of a numerical scheme approaching Maxwell's equations consists of restricting the space of solution to a bounded region with periodic boundary conditions (PBC), since they can be numerically enforced in an easy way. Let us assume for simplicity a 1D-domain $x \in [0, \Delta]$ and let us search for modes fulfilling PBCs in space

$$\vec{\Psi}(x = \Delta, t) = e^{-j\alpha} \vec{\Psi}(x = 0, t), \forall t, \quad \vec{\Psi} = \{\vec{E}, \vec{H}\} \quad (2.20)$$

for arbitrary $\alpha \in [0, 2\pi)$. Plane-wave solutions of the form $e^{j(\omega t - kx)}$ (leftwards $k > 0$ and rightwards $k < 0$) comply with the PBC condition (2.20) for a infinite numerable spectrum of real wavenumbers k_n (each oscillating at a complex frequency ω_n)

$$\begin{aligned} k_n &= \pm \left(\frac{\alpha}{\Delta} + \frac{\pi}{\Delta} 2n \right), \quad n = 0, -1, +1, -2, +2, \dots \\ \omega_n &= f(k_n) \end{aligned} \quad (2.21)$$

where we will refer to $k_0 = \frac{\alpha}{\Delta}$ as a fundamental mode, and to all other k_n as harmonic modes.

Let us apply this technique to the DGTD method in a semi-discrete form in space [27]. For this, we define a column vector \vec{U} with all the dofs of a given problem and express the homogeneous semi-discrete DG equations (2.10)

$$j\omega\vec{U} = \mathcal{A}_{DG}\vec{U} \quad (2.22)$$

with \mathcal{A}_{DG} the semi-discrete DG operator. PBCs are easily enforced in DG through the flux conditions by setting

$$\begin{aligned} \hat{\mathbf{n}}^m \times \vec{E}^{m+}|_{x=\Delta} &= e^{-j\alpha}(\hat{\mathbf{n}}^m \times \vec{E}^m|_{x=0}) \\ \hat{\mathbf{n}}^m \times \vec{E}^{m+}|_{x=0} &= e^{j\alpha}(\hat{\mathbf{n}}^m \times \vec{E}^m|_{x=\Delta}) \end{aligned} \quad (2.23)$$

Plugging (2.23) into (2.22), we find a homogeneous algebraic system of equations, with a number of unknowns equal to the number of dofs. Nontrivial solutions correspond to the eigenvectors of the semi-discrete space operator. Under the assumption that the space operator is diagonalizable, there will exist a basis of eigenvectors \vec{U}_m , $m = (0, 1, \dots, \text{dofs} - 1)$, each propagating with a complex frequency $\omega = f(\tilde{k}_m)$, with \tilde{k}_m its corresponding eigenvalue.

It should be noted that the Shannon sampling theorem [196] establishes an upper limit to the maximum wavenumber which can be sampled in a spatial domain discretized with dofs samples. For instance, let us assume a one-element domain in 1D-DGTD, solved with p^{th} -order polynomials (($p+1$) electric dofs plus ($p+1$) magnetic dofs). The analytical bandwidth (2.21) which can be represented numerically is restricted to

$$|k_n| = \left| k_0 + \frac{\pi}{\Delta} 2n \right| \leq \frac{\pi}{\Delta} (p+1), \quad n = (0, -1, +1, \dots) \quad (2.24)$$

That is, for each $k_0 \neq \pi/\Delta$ there³ exist ($p+1$) leftward analytical modes $+|k_n|$ plus ($p+1$) rightward ones $-|k_n|$, which can be numerically approximated. Of course, numerical eigenvalues \tilde{k} fulfilling the Shannon sampling theorem are not necessarily proper approximation of the analytical ones k . In a broad sense, we will refer to these numerical modes which do not *properly* approximate any analytical one, as *spurious* or *nonphysical* modes.

Let us illustrate this for our simple 1D 1-element case solved by nodal-DGTD and Lagrange polynomial p^{th} -order basis. Figs.2.1,2.2 show the dispersion and dissipation relation for 1st- and 2nd-order basis (with centered and upwind fluxes). We note

³See Figs.2.1,2.2 to see the case $k_0 = \pi/\Delta$

that, for $p = 1$, there appear one rightward and one leftward solution which approximate the fundamental mode for well-resolved problems ($L \equiv k_0\Delta/(p + 1) \rightarrow 0$). Another two modes (one leftward plus rightward) solutions are found, which should correspond to the first harmonics ($|k_{-1}| = \frac{2\pi}{\Delta} - k_0$). Due to the coarse discretization of these modes, close to their own Shannon limit for $L \rightarrow 0$, the numerical phase speed is far from the analytical one. These poorly sampled modes (for a well-resolved fundamental one) with an undesired behavior are the spurious or nonphysical modes. It bears noticing that, in case of ($L \rightarrow \pi$), when $|k_{-1}| \approx 0$ and $|k_0| \approx \frac{2\pi}{\Delta}$, the situation is the opposite: the fundamental modes numerically propagate in a wrong way, providing a good approximation of what has been defined as harmonics.

For $p = 2$, a similar analysis can be made. Apart from the two fundamental modes, another four modes (two leftward plus two rightward) appear. In case of $L \rightarrow 0$, the first harmonics ($\pm k_{-1}$) can be distinguished in the numerical dispersion functions, but the second harmonics $\pm k_{+1}$ present wrong behavior on the phase speed. For different intervals of L , the different solutions, fundamental or harmonics modes, ($\pm \tilde{k}_0, \pm \tilde{k}_{-1}, \pm \tilde{k}_{+1}$) offer a better or worse approximation to the analytical solutions ($\pm k_0, \pm k_{-1}, \pm k_{+1}$). In case of upwind flux, much better approximation over more bandwidth is achieved than for centered flux.

A noteworthy point here is to analyze the dissipation relationship of the upwind flux. All modes propagate with an attenuation that is larger for poorly resolved modes than for well-resolved ones. Clearly, for the fundamental mode, dissipation is minimum for $L \rightarrow 0$. In case of the harmonics, this situation takes place for different intervals of L , where they are properly resolved. Furthermore, in all cases, good phase dispersion corresponds to low dissipation, and poor phase dispersion corresponds to a high dissipation relationship. However, for the centered flux, the numerical modes do not attenuate in any case, and poorly sampled analytical modes with wrong behavior (spurious) may appear together with the well-resolved ones in a simulation.

The definition we use here of spurious solutions is broad in the sense that it provides information for the whole spectrum of the semi-discrete space operator (which constitute a basis for all possible solutions or diagonalizable operators): it provides criteria to distinguish physical from nonphysical behavior, just in terms of the correct approximation between the analytical and numerical solutions. However, the qualification of spurious mode actually depends on the analytical problem under study. For instance, if we excite the PBC-analytical problem with the fundamental mode as initial values, we might not expect the appearance of any of the higher harmonics in its numerical counterpart. In this narrow sense, any solution apart from

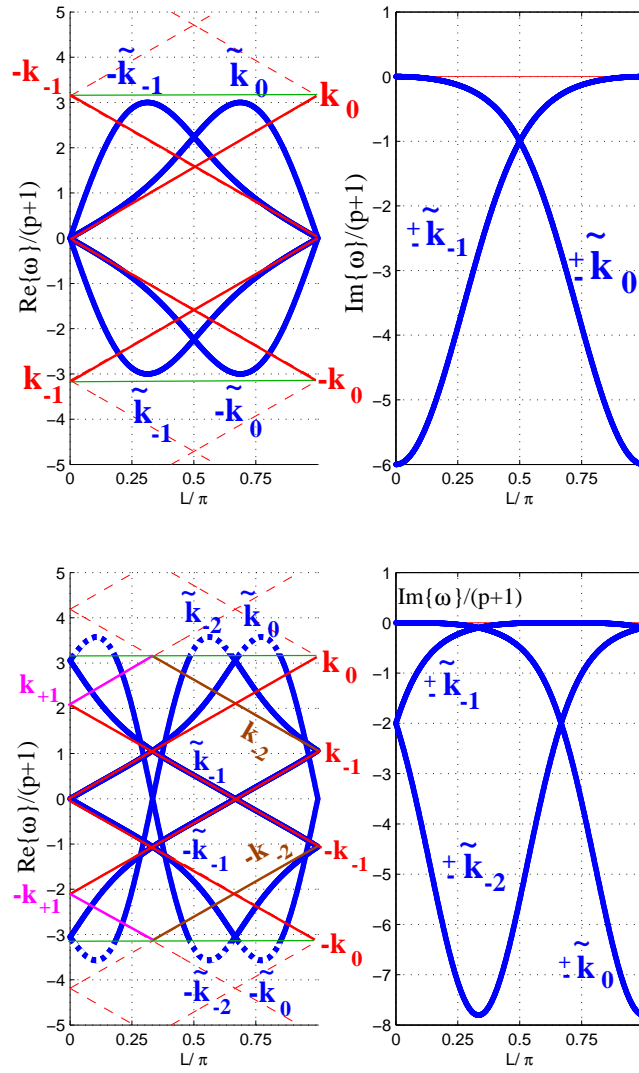


FIGURE 2.2: Numerical dispersion and dissipation $\omega = f(\tilde{k}_n)$ as a function of $L = k_0\Delta/(p+1)$, for scalar 1D-DGTD. Analytical dispersion in red $\omega = k_n = ((p+1)L + 2n\pi)/\Delta$. Sub-index in \tilde{k}_m has been added *a posteriori* according to the analytical mode matched for some L region (no identification for \tilde{k}_m has been guessed for $p=2$ in the centered case). Up: Upwind $p=1$, Bottom: Upwind $p=2$. The bandwidth allowed by Shannon theorem is delimited with green lines, while dashed lines indicate modes outside this band. Blue is used for numerical modes and red (magenta & brown) for the analytical ones. ($\Delta = 1, \mu_0 = 1, \varepsilon_0 = 1$)

that corresponding to the fundamental mode might also be considered spurious (see [62]), even if it is well resolved in space. To illustrate this, we have projected the fundamental (rightward) analytical mode k_0 , expanded in a $p = 10$ polynomial basis, into the basis of numerical eigenvectors. Since these are not orthogonal, we cannot assume a modal separation of the energy, but we still find that for a good resolution $L = 0.005$, the numerical mode propagates with $\tilde{k}_0 \approx k_0$ with an amplitude ~ 572 times higher than that of the next mode, whereas this ratio lowers to ~ 28 for a resolution of $L = 0.11$.

Let us move to a 3D case solved with hierarchical vector basis that is complete up to order $p = 2$, both for the gradient and the rotational spaces. We have meshed a cubic domain in a symmetrical way composed of 24 tetrahedrons, and enforced PBC in the x -direction (2.23) with $\alpha = k_0\Delta$, $k_0 = 2\pi$, $\Delta = 0.2$, and PBC conditions at the YZ and ZX -planes with $\alpha = 0$ (no delay).

The numerical eigenvalue \tilde{k} is plotted in Fig. 2.3. There are $2MQ = 1440$ modes corresponding to the number of dofs of the problem ($M = 24$ tetrahedrons and $Q = 30$ dofs per element). Again, we find that the spectrum of the DG operator depends heavily on the flux-evaluation scheme. It can be seen that, for the centered scheme, none of the modes supported by the numerical method has dissipation $\tilde{k}_{imag} = 0$. Therefore, all numerical modes, both well-resolved physical and poorly resolved spurious solutions, could be present in a numerical simulation and propagate on the computational domain. On the contrary, for the upwind case, we can clearly distinguish between well-resolved physical modes ⁴ and poorly resolved spurious modes by looking at their attenuation $\tilde{k}_{imag} \approx 0$. Hence, poorly resolved spurious modes decrease exponentially with spatial position and do not propagate along the computational domain. It is important to note that some undesirable dissipation also affects the well-resolved physical modes, depending on their spatial resolution.

For the penalized flux with $\tau = 0.1$, similar conclusions are drawn. As mentioned earlier, the choice of the τ parameter also has an impact on the stability conditions of the final numerical scheme. For instance, when using a LF time-integration scheme, the upper limit for stability in Δt becomes more restrictive as τ increases. The use of partial penalized flux with small values of the τ parameter has negligible effects on the stability of the scheme while keeping enough practical attenuation in the poorly resolved spurious modes. A deeper analysis of the stability is beyond of the scope of this paper and is left for treatment elsewhere.

⁴Four fundamental rightward/leftward planewaves (two polarizations) and their corresponding harmonics.

Though the above results are only for the semi-discrete problem, the time-integration scheme has an impact on the eigenvalue problem. For the simplest case of the LF time scheme for lossless media and centered flux, the dispersion relationship would become $\frac{2}{\Delta t} \sin(\omega \frac{\Delta t}{2}) = \tilde{k}$, which introduces an upper stability limit for the maximum allowable Δt , over which some mode becomes unstable, and thus so does the whole numerical scheme. For stable well-resolved schemes, the distribution of the spurious/physical modes is slightly distorted, but the conclusions are similar to those drawn for the semi-discrete scheme. Finally, let us consider a more realistic

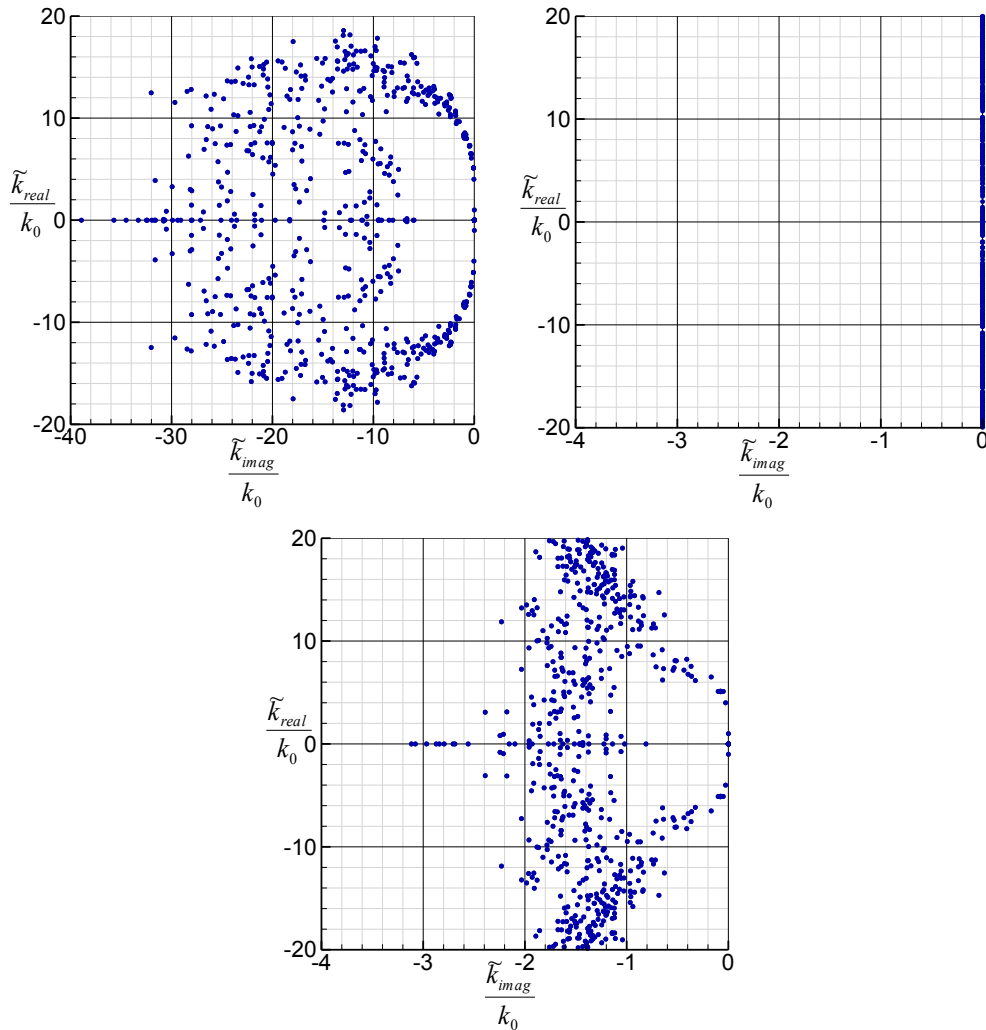


FIGURE 2.3: Spectrum of the DG operator for a cubic domain (meshed with 24 tetrahedra) with PBC ($k_0 = 2\pi$ and $p = 2$). Upwind flux (upper left), Centered flux (upper right), Partially penalized flux $\tau = 0.1$ (lower).

case: a 1m-side cubic 3D PEC cavity meshed with 5025 tetrahedrons. The fields in the cavity are then excited via an electric-current source with a Gaussian pulse time signal, with 10dB bandwidth of approximately 400 MHz. The problem has

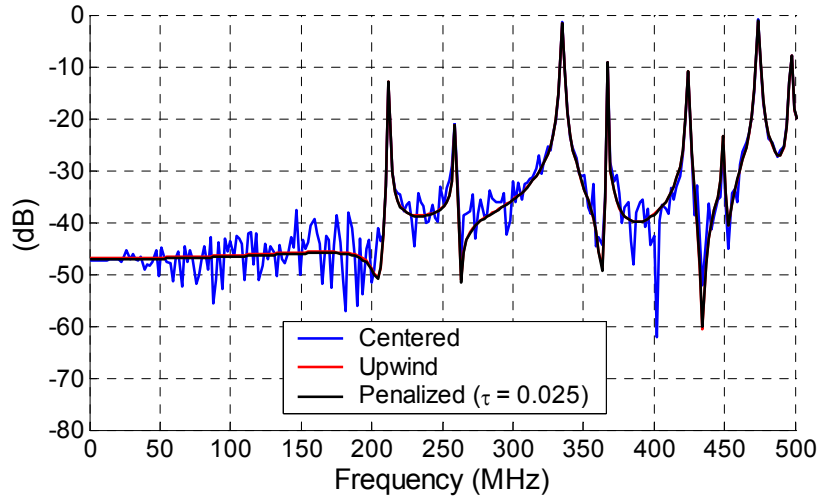


FIGURE 2.4: Power spectrum of the vertical component of electric field sampled at a point inside the cavity, computed using centered, upwind, and partial penalized ($\tau = 0.025$) fluxes, 4^{th} -order 2N-storage Runge-Kutta and $p = 2$.

been simulated up to a physical simulated time of $0.5 \mu\text{s}$ by means of a RK4 time-integration scheme. This problem was computed with centered, upwind, and partial penalized flux, with very low $\tau = 0.025$ with hierarchical vector-basis functions of complete order $p = 2$. The electric field is sampled at one point and the Fourier transform performed for the vertical component (Fig. 2.4). The power spectrum computed with centered flux is noisy and shows spectral pollution due to the presence of nonphysical spurious modes. In the case of upwind or partial penalized flux (even for such a low value of τ), we can clearly distinguish the different resonant frequencies.

2.4 Application to waveguide filters

Waveguide filters, an especially challenging type of problem for time-domain techniques, are traditionally solved by methods in FD, such as FEM, integral-equation methods, or analytical methods such as the mode matching. Due to the strong resonances that these structures present, two main features are required to deal with them in TD. One is the stability of the method, since very long simulations are necessary. The other is its accuracy, to maintain the coherence of the electromagnetic field throughout the structure. In this work, we use waveguide filters to provide proof of the robustness and accuracy of the DGTD method.

A set of enhancements have been included in our algorithm in order to optimize its computational behavior:

- Second-order curvilinear tetrahedra have been used for the accurate modeling of geometries involving curvatures.
- A *hp*-refinement heuristic strategy to choose the order of the basis function in each tetrahedron, depending on its size. To maintain uniform accuracy throughout the spatial domain, with reasonable computational effort, we used a higher-order basis for larger tetrahedra, and lower orders for smaller ones, combining gradient spaces of reduced-order $p - 1$, with rotational spaces of complete order p . It is important to note that smaller elements need shorter time steps, but if a lower order is used in these elements, the condition is relaxed. In the same way, longer time-steps can be used for larger elements combined with higher orders. The combination and mixing of different orders of the basis functions depending on element size, makes the time step between all the elements more homogeneous.
- Despite the adaptive *hp*-refinement described above, large differences in the maximum time steps for stability are found across the geometry. Thus, we have classified the elements according to this limit for the LF-scheme at several levels, and we employed different time-steps for each level. This technique, which is known as local time stepping (LTS) [77, 93], can provide dramatic savings in the CPU time.

Two types of filters have been considered: a dual-mode circular waveguide filter (DMCWF) and a single resonator based on a rectangular cavity loaded by a dielectric cylindrical puck.

The DMCWF structure has been analyzed in detail in [197] and measurements are available. The filter is composed of a circular cavity resonator that includes the input and output slots of a DMCWF. Due to the symmetries of the structure, vertical perfect magnetic conductor-wall and horizontal perfect electric conductor wall symmetry were considered in the numerical simulations, as is depicted in the simulation setup of the Figure 2.5.

It is important to note that a dense discretization of the slots is critical for accurate results. Table 2.1 gives the number of elements for each set of basis functions, while Table 2.2 gives the number of elements and time step for each level of the LTS algorithm.

Two observables have been considered:

1. A field probe inside the rectangular waveguide to record field evolution in TD. Fig. 2.6 shows different results for partially penalized ($\tau = 0.025$) and centered

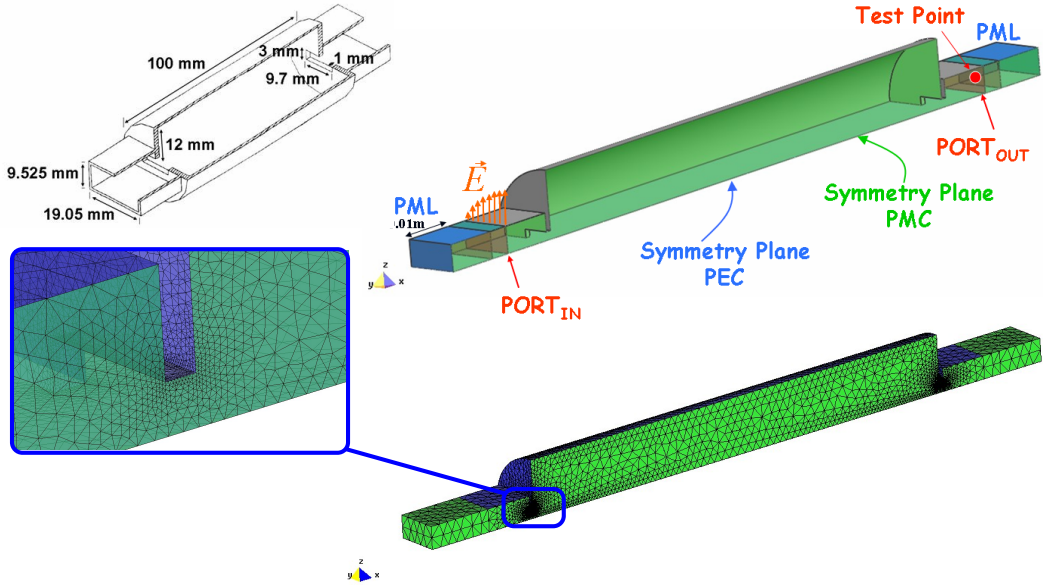


FIGURE 2.5: Dual-mode circular waveguide filter dimensions and problem setup (E_z results overimpose for both fluxes).

TABLE 2.1: Number of elements (M) for each set of basis functions for the DMCWF. GXRX stand for x order for the gradient space, y order for the rotational space

	G1R1	G1R2	G2R2	G2R3	G3R3	Total
M	38988	2258	804	2734	15102	59886
dofs	935712	90320	48240	246600	1927320	3248192

TABLE 2.2: Local time stepping level distribution for DMCWF problem.

	L1	L2	L3	L4
M	7	13101	22556	24222
Δt (ps)	$6.96 \cdot 10^{-3}$	$20.88 \cdot 10^{-3}$	$62.64 \cdot 10^{-3}$	$187.92 \cdot 10^{-3}$

flux cases. In the case of centered flux, and due to the spurious modes, E_y (and similarly for E_x , though not shown) is not null and more energy is found across the simulation (see Fig. 2.8). No noticeable difference between centered and penalized is appreciated for E_z . Note also that the energy needs considerable time to leave the filter, since the structure is very resonant. This leads to long physical simulation times to achieve accurate results.

2. The filter response in terms of the S_{21} parameter. No remarkable differences were found between centered/upwind or LF/RK4 schemes. For instance, Fig. 2.7 shows the comparison between measurement, centered, and partial penalized ($\tau = 0.025$) computed with LF and local time stepping, with excellent agreement. No influence on the S_{21} parameter appears to exist due to spurious modes, reaching excellent agreement in all cases.

Table 2.3 summarizes the computational requirements of the different simulations

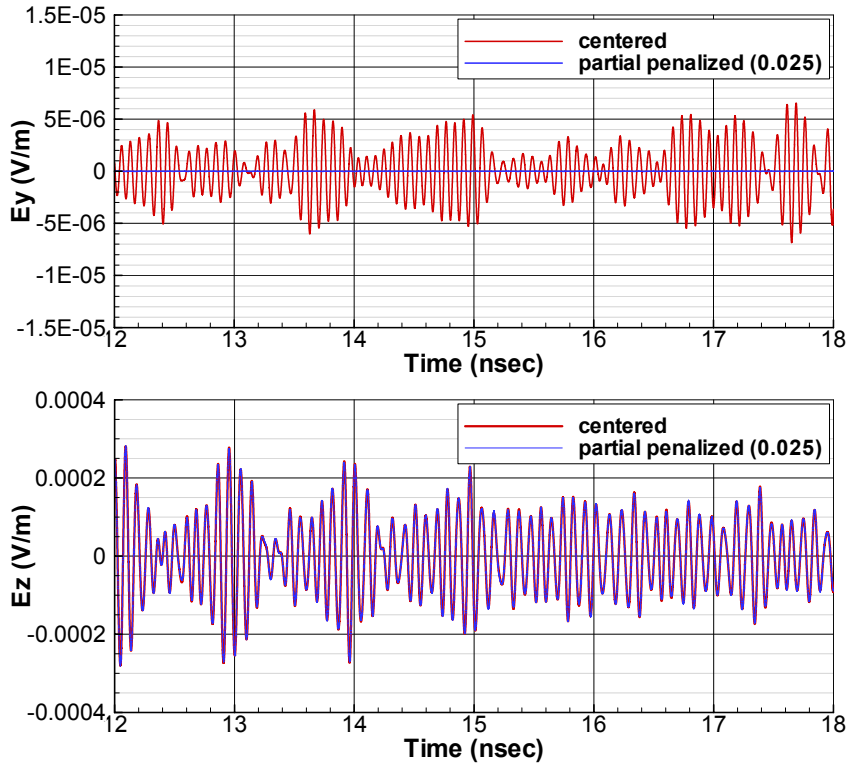


FIGURE 2.6: Dual-mode circular waveguide filter near fields computation.

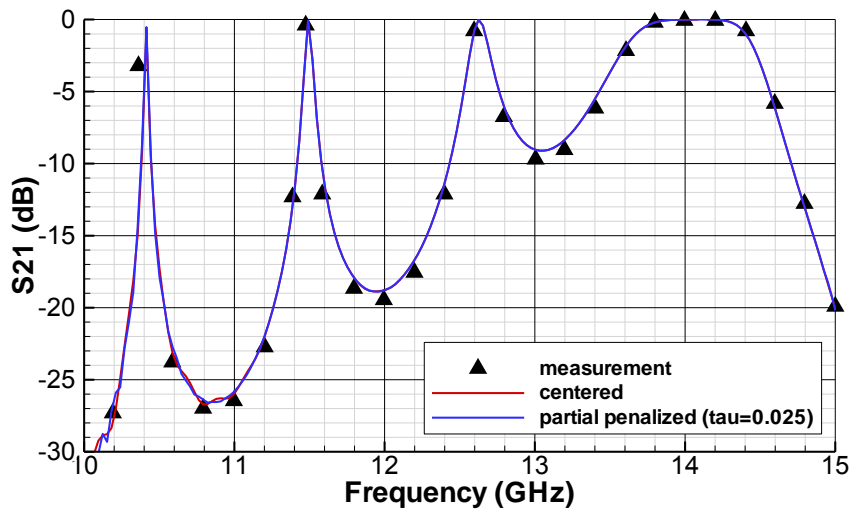


FIGURE 2.7: Dual-mode circular waveguide filter response. Measured and computed data comparison.

performed. It should be noted that the 2nd-order LF scheme, combined with a 5-level LTS provide the algorithm about 8 times faster than do non-LTS schemes for this numerical case.

The second example we will show is a microwave filter with a dielectric material, a single resonator based on a rectangular cavity loaded by a dielectric cylindrical

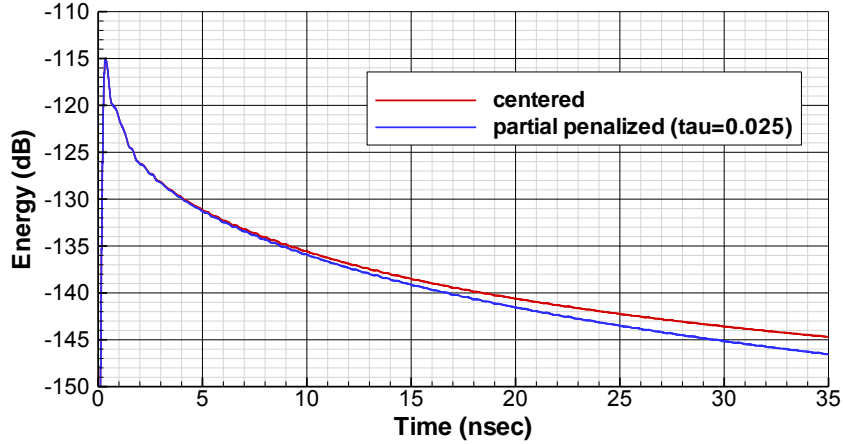


FIGURE 2.8: Evolution of the energy inside the dual-mode circular waveguide filter.

TABLE 2.3: Computational requirements of the different cases (for a 8 processors AMD OPTERON dual core 1.8GHz.). The computed physical time has been 35 ns. Fluxes: C=centered, U=upwind, P=penalized with $\tau = 0.025$.

Flux	Scheme	Δt ⁽³⁾	steps ⁽¹⁾	memory	CPU ⁽²⁾
C	RK4	24.5 - 24.5	1428572	2.0 GB	121.2 h
U	RK4	24.1 - 24.1	1452282	4.1 GB	213.3 h
C	LF	19.6 - 19.6	1785715	2.0 GB	63.5 h
P	LF	19.2 - 19.2	1822917	4.1 GB	118.5 h
C	LF,5L-LTS	6.96 - 187.9	186250	2.1 GB	8.9 h
P	LF,5L-LTS	6.81 - 183.9	190320	4.3 GB	15.5 h

⁽¹⁾ Number of steps for the maximum Δt in the problem.

⁽³⁾ Minimum-Maximum values in units of 10^{-15} s.

puck. This filter has been reported in [198] and measurements are available. Again, the rectangular cavity is excited by two rectangular slots centered on opposite lateral faces. The resonator is chosen with a high permittivity ($\epsilon_r = 29$) (see setup in Fig. 2.9). The TE_{10} mode is excited in the input port, by impressing surface magnetic currents with its profile. The backwards propagated mode is absorbed by the PML, and the forward-propagated one is the incident wave used to excite the structure. The reflected wave required to evaluate the S_{21} parameter is computed by projecting the computed electric fields with the TE_{10} profile at the output port. The energy (Fig. 2.10) takes a long time to leave the cavity due to the presence of the dielectric puck, which makes the structure very resonant. Excellent agreement in the S_{21} parameter between simulation and the measurements is found in Fig. 2.11. Only the results for a partially penalized ($\tau = 0.025$) flux are shown (similar results can be found with the centered flux, since, as with the previous filter, spurious modes has no noticeable effect on the transmission coefficient).

The computed physical time, as appears in Table 2.4, was 180 ns, which corresponds to 1980 cycles of the lowest frequency and 2880 of the highest frequency under analysis. 2nd-order leapfrog with local timestepping has been used with no instability

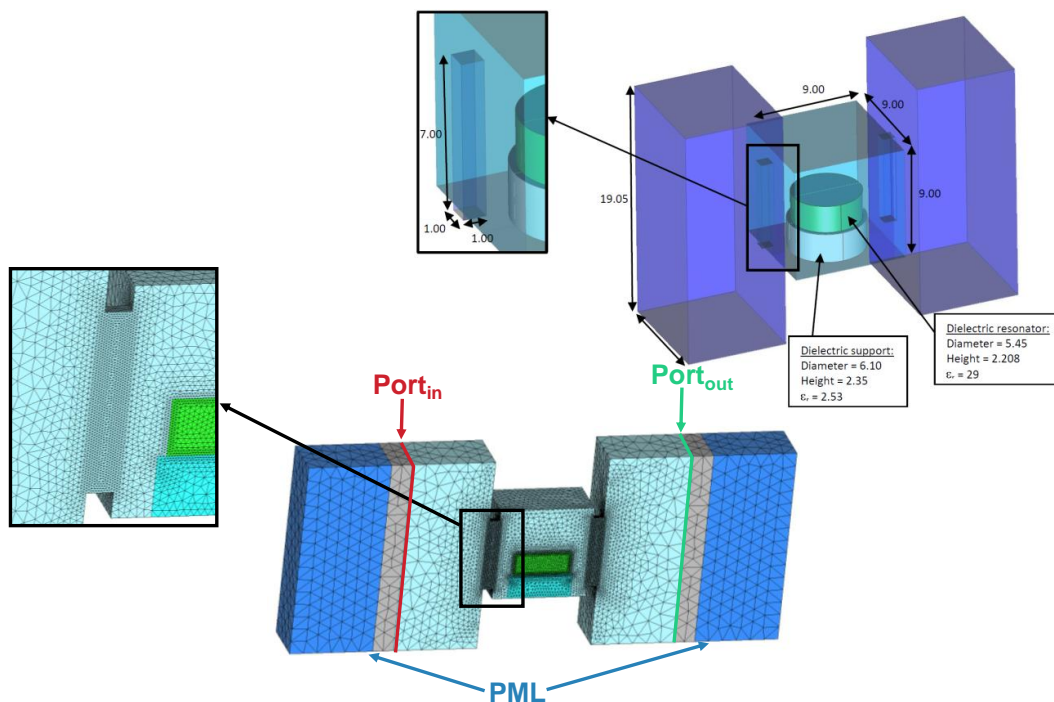


FIGURE 2.9: Single resonator composed of a rectangular cavity loaded by a dielectric cylindrical puck.

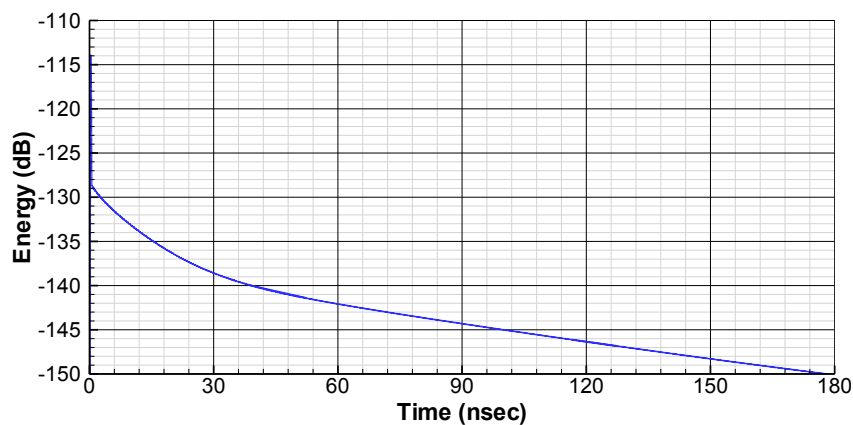


FIGURE 2.10: Evolution of the energy inside the single resonator filter.

problems. Due to the marked differences in the size of the elements, up to 6 levels in the LTS have been used, and the ratio between the shortest and largest timestep was 729. Again, depending on the size of the elements, a different order p of the basis functions has been chosen.

2.5 Conclusions

In this paper, we have presented a highly accurate vector-based DGTD. We have revisited the topic of spurious mode reduction and have shown how this can be

TABLE 2.4: Single resonator: partial penalized flux $\tau = 0.025$, 2^{nd} -order Leap Frog (6-LTS), $M = 362706$ elements, dofs=18505352, computed physical time 180.0 ns.

$LTS1$	$LTS2$	$LTS3$	$LTS4$	$LTS5$	$LTS6$
2	26	390	177768	94036	90484
0.0006	0.0018	0.0054	0.016	0.048	0.15
298	99.3	33.1	11.0	3.68	1.23
$(\mathcal{G}_0, \mathcal{R}_1)$	$(\mathcal{G}_1, \mathcal{R}_1)$	$(\mathcal{G}_1, \mathcal{R}_2)$	$(\mathcal{G}_2, \mathcal{R}_2)$	$(\mathcal{G}_2, \mathcal{R}_3)$	$(\mathcal{G}_3, \mathcal{R}_3)$
0	298113	9302	3535	27577	24177

1st row = Local time stepping level

2nd row = Number of elements for each LTS level

3rd row = Δt (in ps)

4th row = Time steps (in millions)

5th row = Basis functions (gradient,rotational) orders

6th row = Number of elements for each basis functions)

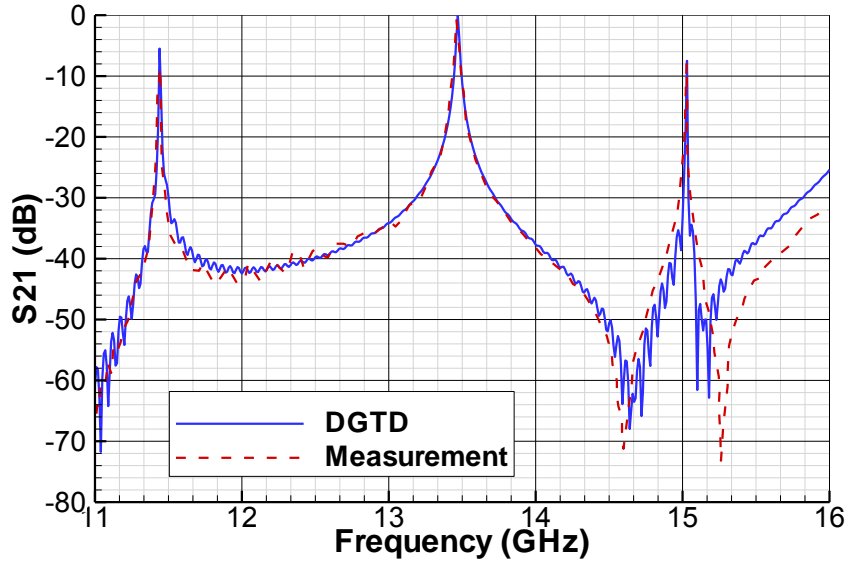


FIGURE 2.11: S21 response of the single resonator filter. Measured and computed data comparison.

minimized by means of penalized fluxes. The attenuation on the spurious modes appearing in DGTD is a remarkable difference with respect to the continuous formulation of FEMTD, and does not depend on the kind of basis-functions used by the scheme, making both nodal and scalar DGTD spurious-free for penalized fluxes. The application to microwave filters has demonstrated the accuracy and stability of the proposed approach.

Chapter 3

A Nodal Hybrid Continuous-Discontinuous Galerkin Time Domain Method for Maxwell's Equations

L. D. Angulo, J. Alvarez, F. L. Teixeira, M. F. Pantoja, and S. G. Garcia. A nodal hybrid continuous-discontinuous galerkin time domain method for maxwell's equations. *IEEE Transactions On Microwave Theory And Techniques*, Submitted

Abstract

A new nodal hybrid Continuous-Discontinuous Galerkin Time Domain (CDGTD) method for the solution of Maxwell's curl equations is proposed and analyzed. This hybridization is made by clustering small collections of elements with a Continuous Galerkin (CG) formalism. These clusters exchange information with their exterior through a Discontinuous Galerkin (DG) numerical flux. This scheme shows reduced numerical dispersion error with respect to classical DG formulations for certain orders and numbers of clustered elements. The spectral radius of the clustered semi-discretized operator is smaller than its DG counterpart allowing for larger time steps in explicit time integrators. Additionally, the continuity across the element boundaries allows us a reduction of the number of Degrees Of Freedom (DOF) of up to about 80% for a low-order three-dimensional implementation.

3.1 Introduction

Galerkin finite element (FEM) techniques are a very flexible class of numerical methods to solve partial differential equations (PDEs). For electromagnetic problems in linear media, they can be implemented either in the frequency domain (FD) and in the time domain (TD). Continuous Galerkin (CG) [82, 83] formulations are more prevalent in FD, either in nodal [87, 88] or in vector formulations [84, 95, 96], though they can also be found in TD [44]. However, Discontinuous Galerkin (DG) formulations are most often found in TD, also either in nodal [27] or in vector forms [92]. Space-time Galerkin methods treat the time variable in a similar setting to the spatial variables [8, 24, 117, 119, 132]. However, the most popular approach is to evolve the semi-discrete spatial equations by means of explicit time-integration schemes such as the second-order leap-frog (LF2) [34, 77, 93, 122] or the fourth-order low-storage explicit Runge-Kutta (LSERK4) [23, 27, 30, 113, 199]. The maximum time step allowed for stability by these schemes is constrained by the spectral radius of the spatial operator, which in turns depend on the inverse square of the polynomial order P , and on the minimum edge length h used for the spatial discretization. This makes the use of p -refinement in DGTD, not common beyond intermediate-orders of $3 \sim 5$ [122, 200, 201], though higher order implementations are reported to be more parallelizable in GPU-based machines [184]. The use of h -refinement in DGTD, also becomes problematic in multiscale problems, since (local) smaller elements enforce reduced (global) time-steps to ensure stability. Strategies to mitigate this exist, like local time-stepping techniques [23, 77, 122], and implicit-explicit (IMEX) time-integration schemes [120, 121].

Generally speaking, DGTD requires larger number of DOFs and smaller time-steps for stability, however it provides a number of advantages over CGTD [44, 80]. Among them: simpler treatment of discontinuities at interfaces [68, 171], spurious modes control through modification of the numerical flux [13, 62], and block-diagonal mass matrices [27], trivially invertible by frontal methods. DG algorithms thus become explicit, unlike CG for which the solution of linear systems of equations at each time-step is required. Consequently DGTD allows us a straightforward MPI/GPU parallelization [122, 184]. Motivated by these advantages, considerable efforts have been made at improving several aspects of DGTD. Some of them follow.

In [35] different continuity constraints are imposed to the electric and magnetic fields alternately, leading to energy conservation, optimal convergence, and reduced number of DOFs. Hybridizable discontinuous Galerkin (HDG) techniques [167, 202, 203], with a reduced number of DOF, successfully applied in FD, and more recently in

TD [117] by using a space-time Galerkin formalism. Reduction on the spectral radius has been achieved using co-volume filtering [203] and mapping techniques [204], though effective only for higher orders. Reduction of algebraic complexity and DOFs has also been addressed by multi-element approaches exploiting the advantages of, mainly, tetrahedral and hexahedral mesh elements. In three-dimensional problems this forces the use of non-conforming interfaces [109, 110], or the use of pyramidal elements [111], for the transitions between elements of different types.

CGTD schemes present also interesting features. CG methods use significantly less DOF than DG methods. They do not introduce dissipation if a symplectic time integrator is used. Moreover, the spectral radius of the assembled system is smaller than when a DG formalism is used [80], thus allowing the use larger time-steps.

In this work, we explore the topic of the hybridization of CG and DG schemes. The motivation is to exploit the advantages of both formulations in a computationally affordable manner. This topic is present in the context of elliptic problems arising to a family of methods known as Mortar methods [205–210], hybridizing Mixed Finite Element (MFE) or HDG methods in different regions of the mesh that have certain homogeneity, while the DG method is used to handle discontinuities on the material properties or at non-conforming interfaces. Among some other benefits, the resulting methods achieve a reduction, of DOF and offer the possibility of using a model reduction in different regions. For non-electromagnetic problems, another approach was explored in [4, 211] to approximate the shallow water equations using DG for the primitive continuity equation and CG for the momentum equation.

In this paper we present a new nodal hybrid Continuous-Discontinuous Galerkin (CDG) method for the solution of the time-domain first-order coupled Maxwell's curl equations. The proposed method is aimed at taking advantage of a reduced number of DOF and smaller spectral radius in CG while benefiting from the spurious-free and block-diagonal properties of DG. Previous attempts exist [212], employing a 2D multi-element hybrid Continuous-Discontinuous scheme: CG in a structured grid of square elements, and DG in a unstructured triangular grid. In our approach, rather than applying a CG formalism over large regions, we apply it only on small clusters of elements, thus maintaining the easily invertible block-diagonal nature of the global system of linear equations. Thus resulting in an important difference in terms of computational cost.

Although we will focus on a nodal CG method, a similar approach could be followed with HDG techniques and for other hyperbolic problems. Thus, an added value of the methodology described in this paper, is to show a possible way of taking profit of other implicit techniques that, due to their computational efficiency, cannot be

effectively used in TD. Consequently, this work can potentially be an initial step to connect two branches of numerical methods: spatially implicit and explicit methods.

The rest of this paper is organized as follows. In the next section, we will briefly revisit the classical nodal CG and DG methods. Next, we will introduce the proposed CDG method and present a numerical study of its numerical-dispersion properties and spectral characteristics in 1D. Next a numerical test-case consisting in a 2D PEC cavity serves to further analyze its spectral properties and to provide a L^2 -norm analysis of its h -convergence, for different numerical fluxes and spatial basis orders. The following section will show an analysis of the computational costs of this technique. In a final section, we will present some conclusions from this study and provide an assessment of its benefits in different scenarios.

3.2 Nodal Galerkin TD Formulations for Maxwell Equations

Maxwell's curl equations in sourceless and homogeneous lossless media are¹

$$\begin{aligned}\vec{\nabla} \times \vec{E} &= -\mu \partial_t \vec{H} \\ \vec{\nabla} \times \vec{H} &= \varepsilon \partial_t \vec{E}\end{aligned}\tag{3.1}$$

with \vec{E} , \vec{H} , ε , μ being, respectively: the electric field, magnetic field, permittivity and permeability. For simplicity, we will assume that ε and μ do not vary in the computational domain Ω and use a system of units where $\varepsilon = \mu = 1$.

Let us begin our discussion by briefly recalling the fundamentals of the continuous (CG) and discontinuous (DG) Galerkin techniques that can be used to solve (3.1). Both approaches start by tessellating the computational domain with $k = 1, \dots, K$ non-overlapping elements. On each of these elements, the solution is approximated by a projection of the analytical solution onto a finite expansion basis of functions. In this work we will use classical Lagrange interpolation polynomials, i.e. a nodal basis such as the one described in [82]. The Galerkin problem consists on nullifying the inner product of the approximated fields with respect to the same basis of functions, leading to a system of linear equations [80]. However, CG and DG approaches differ since the first one imposes continuity directly on the fields while the second imposes it on a different quantity so-called numerical flux. Once the spatial semi-discretization has been obtained, either scheme can be evolved using a time integration technique.

¹The lossy media formulation can be straightforwardly derived [213].

As mentioned before, the two most popular are the LF2 and LSERK4 schemes [23]. In brief, LSERK4 has a higher accuracy at the expense of a higher computational cost than LF2. LSERK4 also introduces some numerical dissipation while the LF2 scheme is symplectic.

3.2.1 Continuous Galerkin

The CG formulation imposes the continuity of the fields across element interfaces [80, 82]. This can be expressed succinctly in matrix form as

$$\begin{aligned}\mathcal{Z}\mathcal{M}\mathcal{Z}^T\partial_t\mathbf{E}_g(t) + \mathcal{Z}\mathcal{S}\mathcal{Z}^T\mathbf{H}_g(t) &= 0 \\ \mathcal{Z}\mathcal{M}\mathcal{Z}^T\partial_t\mathbf{H}_g(t) - \mathcal{Z}\mathcal{S}\mathcal{Z}^T\mathbf{E}_g(t) &= 0\end{aligned}\tag{3.2}$$

where \mathcal{M} is the mass matrix and \mathcal{S} is the stiffness matrix, both built independently for each element and assembled-together using an operator that we will denote by \mathcal{Z} that collapses each pair of associated nodes on the element boundaries into a single one. \mathbf{E}_g and \mathbf{H}_g are column vectors containing all the degrees of freedom in the computational domain for the electric and magnetic fields respectively.

3.2.2 Discontinuous Galerkin

DG formalism introduces the concept of numerical fluxes as the quantity for which continuity is enforced across element interfaces [72], rather than the fields themselves [27]. Applying this concept, we obtain the following system of equations for each element k ,

$$\begin{aligned}\mathcal{M}_k\partial_t\mathbf{E}_k(t) + \mathcal{S}_k\mathbf{H}_k(t) - \sum_f^{N_f}\mathcal{F}_{kf}\mathbf{H}_{kf}^*(t) &= 0 \\ \mathcal{M}_k\partial_t\mathbf{H}_k(t) - \mathcal{S}_k\mathbf{E}_k(t) + \sum_f^{N_f}\mathcal{F}_{kf}\mathbf{E}_{kf}^*(t) &= 0\end{aligned}\tag{3.3}$$

with \mathcal{F}_{kf} being the lift operator [27] for face f and vectors \mathbf{E}_{kf}^* and \mathbf{H}_{kf}^* are the numerical fluxes in that face [72]. The DG method can be formulated with different types of numerical fluxes, the centered and upwind fluxes, which are the most commonly used ones [62, 75]. The dispersive and dissipative properties of the solution will greatly depend on the flux choice, allowing for some tuning capability according to the application.

3.3 CGTD vs DGTD: the CDGTD method

From the computational point of view, the main disadvantage of CGTD is that it requires a global linear solver, containing all the degrees of freedom, to be solved on each time-step. DGTD, in turn, when used in conjunction with an explicit time integration technique, allows for each element to be solved independently, thus drastically reducing the computational burden with respect to CG, making it comparable even to that of classical FDTD [10, 21].

However, there are pros and cons of both methods that make sense trying to build hybrid approaches by taking the best of each one. Namely:

- A well-known drawback of nodal FEM is the presence of spurious modes [82]. These are commonly attributed to a variety of reasons, including an inexact representation of the underlying de Rham complex² [214–218]. Spurious nodes are present both in nodal DGTD and CGTD. However, for DGTD they can be easily mitigated, with a slight increase in computational cost, by using upwind or penalized fluxes instead of centered fluxes, at the cost of introducing some dissipation. This dissipation especially affects spurious modes which are much further attenuated than physical ones [13], thus resulting in a cleaner spectrum and better convergence properties³ [74, 77, 113].
- Regarding dissipation, if a symplectic time integrator is used for (3.2), CG methods are not dissipative, while DG becomes dissipative when combined to upwind/penalized fluxes to remove spurious solutions, as mentioned above.
- CG presents more relaxed stability constraints in the time-step than DG, thanks to the fact that the spectral radius of the assembled system (CG) is smaller than that of the unassembled one (DG) [80]. This is a consequence of the better representation of long-range interactions [219].
- Regarding the number of DOFs, CG presents advantages due to the fact that the nodes on the interface between two elements do not need to be duplicated, as in DG, since CG collapses them to enforce continuity. Furthermore DG also

²One way of removing this source of spurious modes, is to resort to vector-based formulations [83–85]. Comparing vector and nodal FEM is out of the scope of this work; advantages and disadvantages of both of them have been reported in literature [86, 87] and would deserve a full work to be further analyzed. Another approach to mitigate spurious modes is by introducing penalty terms associated with the divergence of \mathbf{E} [62, 88], at the cost of adding extra terms, and DOFs, that are to be evolved at each time step [62].

³Centered flux can also be proven to be spurious-free in highly regular meshes [62], though this is not a realistic situation found in a general problem.

needs to compute one matrix-vector product for each face of the element at each iteration.

- Finally, the continuous nature of CGTD also makes necessary a special treatment in regions where the electromagnetic properties of the media exhibit abrupt changes [44], while DGTD naturally implements these conditions thanks to the use of fluxes [68, 169].

The discussion above begs the question as to whether one could formulate a hybrid CDG technique that exploits the advantages of both formulations. In [212] a hybrid method is formulated in 2D. For it, the CG formalism is applied in a large structured region formed of squares, coupled to a DG scheme applied to another region consisting on an unstructured mesh of triangles. The use of a continuous formalism in the large region, thus requires the solution of a large global system of equations that reduces the performance of such approach, specially for large problems.

In contrast, we propose here a new method based on a CG formulation only on multiple, small clusters of elements. As usual in CG, the elements within the cluster remove duplicate DOFs on their boundaries, and they exchange information with adjacent clusters, or single elements, through classical numerical fluxes in a DG manner. As a result, CG clusters are decoupled among them, and the whole domain can be solved by an explicit marching-on-in-time algorithm. In this work, we will analyze the trade-offs of using these CG clusters, which have to be small enough, both to keep the system of equations frontally invertible, and to avoid spurious modes; and as large as possible to reduce the DOFs, enhance the dissipation, and increase the time-step for stability. If upwind numerical fluxes are employed for the DG connection, the CDG method is expected to be spurious-free, partially inheriting from CG the aforementioned advantages.

In the rest of the paper, we will assume a translational symmetry, by meshing regions with clusters that are identical to each other. Though this is not strictly necessary, in general, it is actually a desirable property, since it allows us to compute the semi-discretized operators for a single cluster and reuse it for the rest thus saving memory. Hence, the kind of meshes that would benefit most of this clustering would be structured or semi-structured, as further discussed in the Conclusions. This is also true of multi-element approaches [109–111] in which a reduction of DOFs and increased time-step can be likewise achieved [91]. In the rest of the mesh we apply the usual unstructured DG formalism. We can write the final scheme in matrix

notation as

$$\begin{aligned}\mathcal{M}_c \partial_t \mathbf{E}_c(t) + \mathcal{S}_c \mathbf{H}_c(t) - \sum_f^{N_{fc}} \mathcal{F}_{cf} \mathbf{H}_{cf}^*(t) &= 0 \\ \mathcal{M}_c \partial_t \mathbf{H}_c(t) - \mathcal{S}_c \mathbf{E}_c(t) + \sum_f^{N_{fc}} \mathcal{F}_{cf} \mathbf{E}_{cf}^*(t) &= 0\end{aligned}\quad (3.4)$$

where $\mathcal{M}_c = \mathcal{Z}_c \mathcal{M}_{k_c} \mathcal{Z}_c^T$ and $\mathcal{S}_c = \mathcal{Z}_c \mathcal{S}_{k_c} \mathcal{Z}_c^T$ are the mass and stiffness operators assembled as in the CG method but using only the elements k_c belonging to the cluster c . The operators \mathcal{F}_{cf} are constructed in the same way as for the DG method but considering only the N_{fc} external faces of the cluster.

3.4 Numerical properties

In order to perform a semi-analytical study of CDGTD we will follow a similar approach to [27, 75, 80] for analyzing the dispersive properties of our method in 1D. To do so, we seek spatially periodic solutions of the form

$$\begin{aligned}E(t, x) &= E_0 e^{i(lx - \omega t)} \\ H(t, x) &= H_0 e^{i(lx - \omega t)}\end{aligned}\quad (3.5)$$

that are supported by the spatial semi-discretization. The computational domain Ω is split into K_c elements of equal length h . These K_c elements are assembled in the same way as indicated by equation (3.4). We also define a state vector $\mathbf{q}_c = [\mathbf{E}_c, \mathbf{H}_c]^T$ containing all the N_c degrees of freedom in a cluster c . The elements at the end positions of the computational domain are connected assuming periodic solutions of the form

$$\begin{aligned}\mathbf{e}_0^T \mathbf{q}_{c+1} &= e^{ilhK_c} \mathbf{e}_{N_c}^T \mathbf{q}_c \\ \mathbf{e}_{N_c}^T \mathbf{q}_{c-1} &= e^{-ilhK_c} \mathbf{e}_0^T \mathbf{q}_c\end{aligned}\quad (3.6)$$

and using the DG numerical flux formalism to treat the boundaries of the cluster as if they were neighboring other clusters. We will use the factor $L = lh$ as the normalized numerical wavenumber. With these assumptions, we can reformulate (3.4) as

$$\partial_t \mathbf{q}_c(t) = (\mathcal{M}_c^q)^{-1} (\mathcal{S}_c^q - \sum_f \mathcal{F}_{cf}^q \bar{\mathcal{E}}_{cf}(L)) \mathbf{q}_c(t) \quad (3.7)$$

A diagonal operator \mathcal{W} containing the spectrum of eigenfrequencies is obtained by a similarity transformation via an invertible operator \mathcal{P} to get

$$\mathcal{W} = i \mathcal{P}^{-1} (\mathcal{M}_c^q)^{-1} (\mathcal{S}_c^q - \sum_f \mathcal{F}_f^q \bar{\mathcal{E}}_{cf}(L)) \mathcal{P} \quad (3.8)$$

We can also define the eigenstates of the system as

$$\mathbf{p}_c = \mathcal{P}^{-1} \mathbf{q}_c \quad (3.9)$$

This change of basis let us write equation (3.7) in the following compact form

$$\partial_t \mathbf{p}_c(t) = -i \mathcal{W}(L) \mathbf{p}_c(t) \quad (3.10)$$

with semi-discrete solutions of the form

$$\mathbf{p}_c(t) = e^{-i\mathcal{W}(L)t} \mathbf{p}_c(0) \quad (3.11)$$

The $j = 0, \dots, N_c$ eigenvalues ω_j of \mathcal{W} correspond to the eigenfrequencies of the discrete periodic problem.

The real part $\Re[\omega_j]$ corresponds to the oscillating frequency and the imaginary part $\Im[\omega_j]$ corresponds to the numerical dissipation or amplification of eigenstate j , if any. For all Galerkin methods studied here, we have $\Im[\omega_j] \leq 0$, which is a necessary condition for stability. The phase-velocities supported by the scheme are $c_j(L) = \omega_j h / L$. As in our system of units the speed of light is 1 we will consider that the mode with phase velocity closest to one is one is the free-space mode. Therefore we expect that

$$\lim_{L \rightarrow 0} c_{(\text{fs})}(L) = 1 \quad (3.12)$$

The study of the full spectrum of \mathcal{W} is also useful as its properties impose limitations in regards to the time-integration. The LF2 method [123] has the following stability requirement on its time step h_t

$$h_t \leq 1 / \Re[\omega_j] \quad \forall j \quad (3.13)$$

and therefore will be constrained by the largest real part among all eigenvalues. LSERK methods comprise irregular closed loci in the complex plane [113, 127] in which the eigenvalues must lie to ensure stability. So, to warranty stability, the following condition must be enforced for each cluster

$$\max |\omega_j| \leq \rho(h_t) \quad \forall j \quad (3.14)$$

ρ being the spectral radius of the LSERK method.

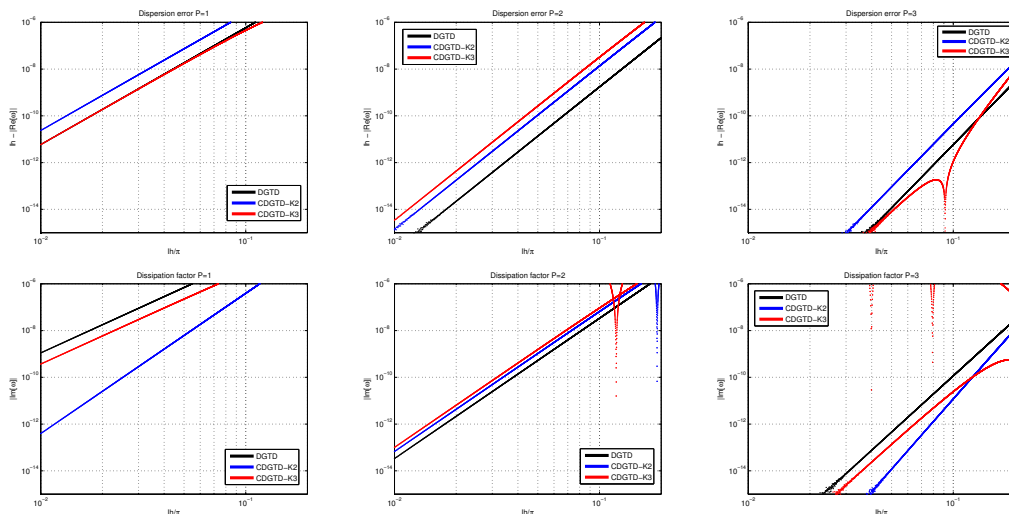


FIGURE 3.1: Convergence rates for DGTD and CDGTD schemes with upwind fluxes. Non-aligned values correspond to other modes also supported by the solutions but that do not correspond to the free-space mode.

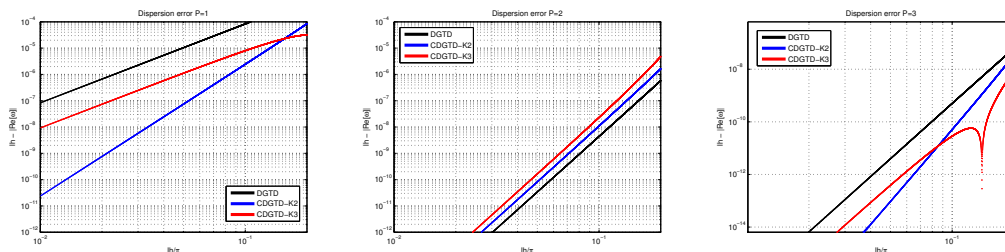


FIGURE 3.2: Convergence rates for DGTD and CDGTD schemes with centered fluxes.

3.4.1 Convergence

Figs. 3.1 and 3.2 show a comparison of the convergence rates on the dispersion curves for the DG and CDG schemes with clusters of 2 and 3 elements, and for upwind and centered fluxes, found with the procedure described above. These convergence rates have been calculated for orders ranging from $P = 1$ to 3. Table 3.1 summarizes the convergence rates where the component dominating in the global error has been highlighted. In agreement with what is found for P refinements of centered DG schemes [75], the convergence rate of CDG depends on the number of elements assembled with an even-odd pattern. With an odd number of elements, CDG with upwind and centered fluxes have the same convergence rates as classical DG methods. For upwind CDG schemes with an even number of elements we see an alternating dominance of the error showing that CDG has a better global convergence for odd orders⁴ of P .

⁴Convergence rates depending on even/odd parameters has been previously in DG analysis [75].

The case of centered CDG with an even number of elements shows that it has the same $2P+3$ convergence as the upwind DG scheme, therefore improving significantly versus its centered DG counterpart. Note that for upwind fluxes (Fig 3.5), spurious modes are also rapidly attenuated in CDG and therefore should not impact the time-domain solution, similarly as observed in [13, 27] for the DG case. Fig. 3.5 also shows that the free-space mode observed is much less attenuated than any other supported mode.

TABLE 3.1: Convergence rates using upwind and centered fluxes. Highlighted cells indicate the dominant term.

	P	DGTD		CDGTD K_c even		CDGTD K_c odd	
		$\Re[\tilde{\omega}]$	$\Im[\tilde{\omega}]$	$\Re[\tilde{\omega}]$	$\Im[\tilde{\omega}]$	$\Re[\tilde{\omega}]$	$\Im[\tilde{\omega}]$
Upwind	1	5	4	5	6	5	4
	2	7	6	7	6	7	6
	3	9	8	9	10	9	8
	4	11	10	11	10	11	10
Centered	1	3	—	5	—	3	—
	2	7	—	7	—	7	—
	3	7	—	9	—	7	—
	4	11	—	11	—	11	—

3.4.2 Spectral properties

Fig. 3.3 shows the full spectrum of DG and CDG operators with 2 and 3 elements and upwind fluxes. Fig. 3.4 shows the effect in the spectrum of increasing the number of elements. The maximum real part, and the spectral radii of the different schemes are presented in Table 3.2. We note that the CDG assembling, even for a moderate number of elements, reduces significantly the spectral radius, to approximately one half of that of the DG. As mentioned above, this allows for a larger time step to be used.

3.5 Computational cost

This section presents some estimates about the number of DOF and computational operations needed for several configurations (Fig. 3.6) in which we can apply the aforementioned translational symmetry.

The number of clustered elements and their order have a critical impact on the number of operations required to evaluate the semi-discretized operators in CDG. For this reason, only relatively small clusters with low orders are studied. Moreover,

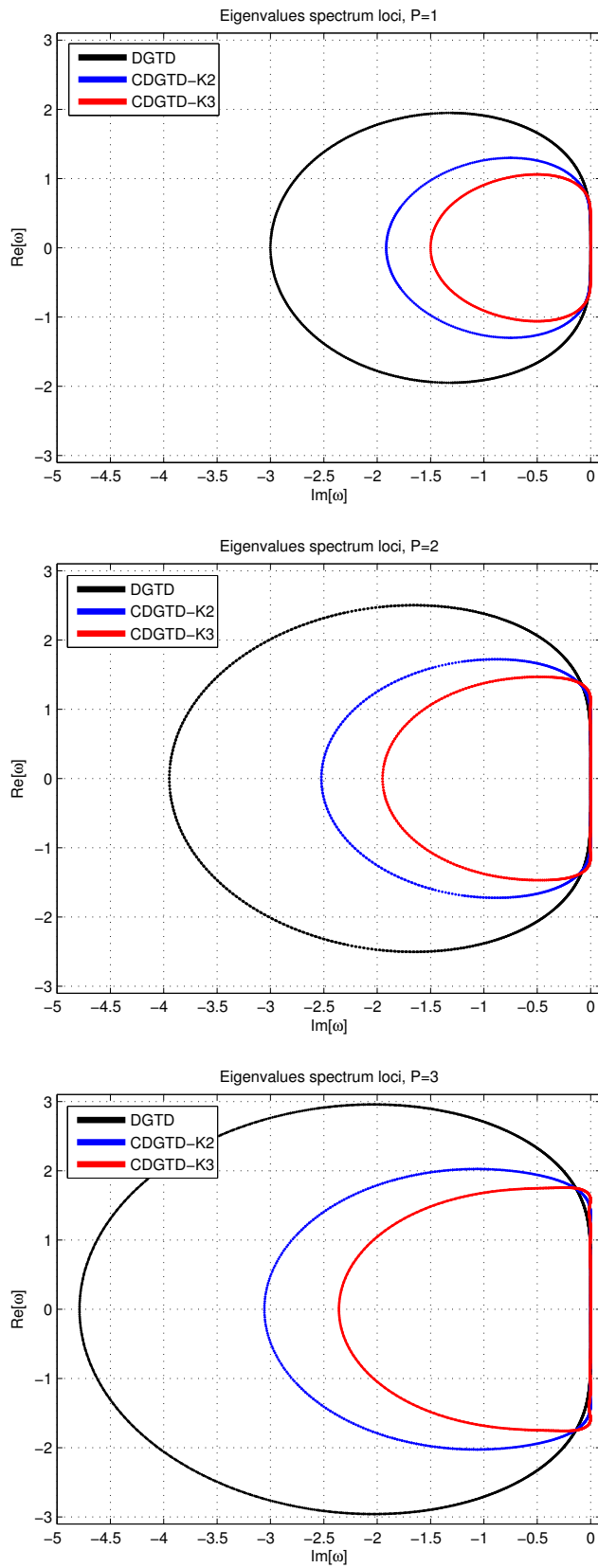


FIGURE 3.3: Eigenvalues spectrum loci for upwind fluxes schemes with polynomial basis up to order 3.

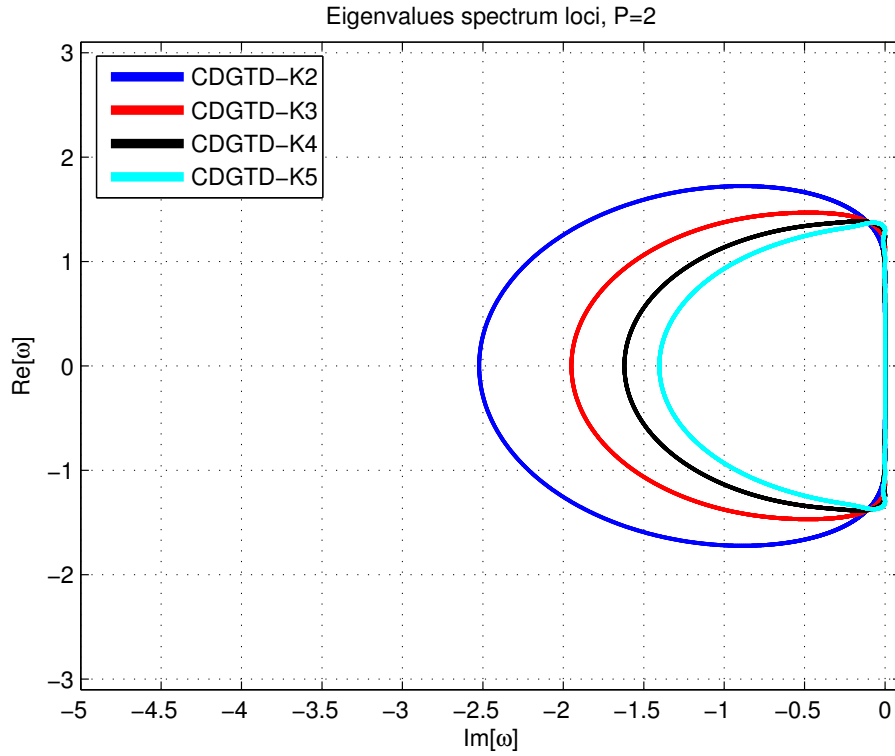


FIGURE 3.4: Eigenvalues spectrum loci for upwind fluxes schemes with polynomial basis of order $P = 2$, for different number of elements clustered.

TABLE 3.2: Maximum real parts and spectral radius. The increase on clustered elements allow the use of larger time steps. Note that for centered fluxes the real part is always zero up to machine precision and therefore the spectral radius is equal to the maximum real value.

	P	DGTD		CDGTD $K_c = 2$		CDGTD $K_c = 3$		CDGTD $K_c = 4$	
		$\max \Re[\tilde{\omega}] $	$\rho[\tilde{\omega}]$						
Upwind	1	1.95	3.00	1.30	1.92	1.06	1.50	0.94	1.25
	2	2.50	3.95	1.72	2.52	1.47	1.95	1.39	1.62
	3	2.96	4.79	2.03	3.06	1.76	2.36	1.74	1.96
	4	3.37	5.57	2.29	3.54	2.03	2.73	2.05	2.27
Centered	1	2.00		1.50		1.35		1.29	
	2	2.69		2.18		1.06		2.02	
	3	3.32		2.79		2.68		2.66	
	4	3.94		3.38		3.30		3.28	

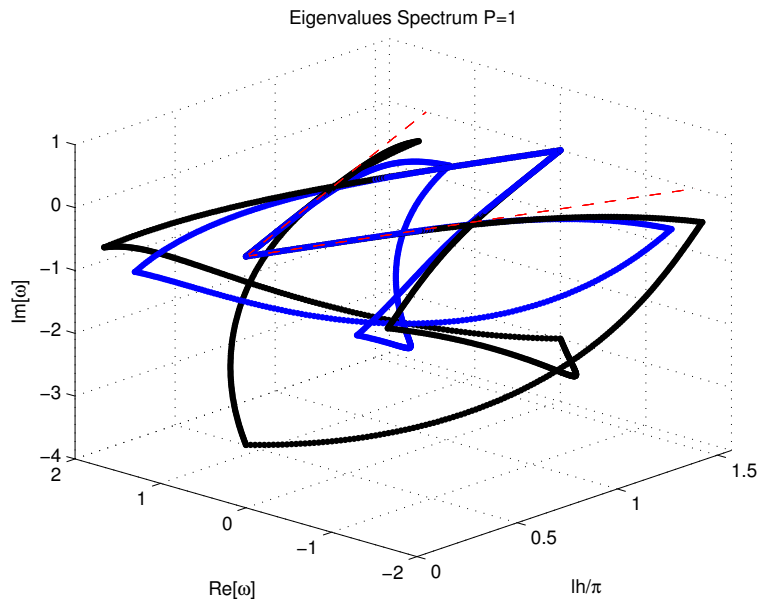
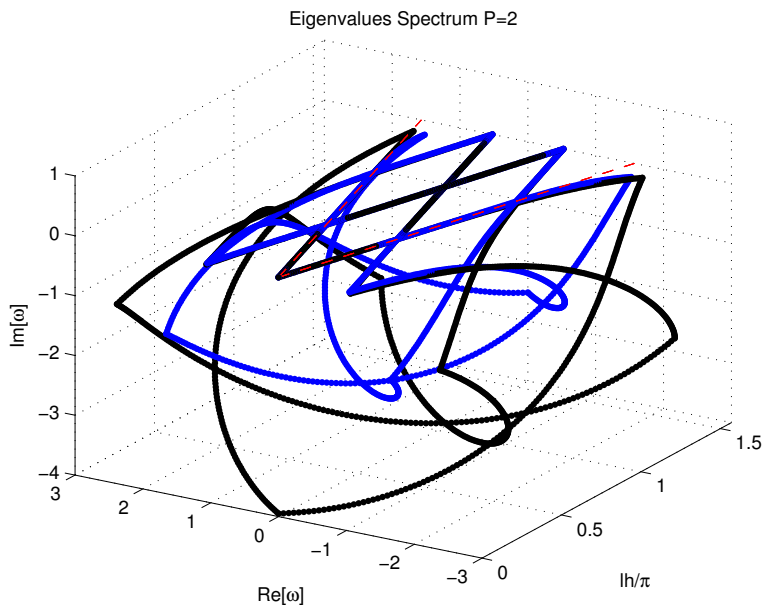
(A) $P = 1$ (B) $P = 2$

FIGURE 3.5: Eigenvalues spectrum loci for upwind fluxes schemes with polynomial basis of different order for DGTD (black) and CDGTD with $K_c = 2$ (blue) schemes. As it can be seen, modes that do not belong to the physical eigenspectrum (dashed red) have large imaginary parts and are therefore quickly attenuated.

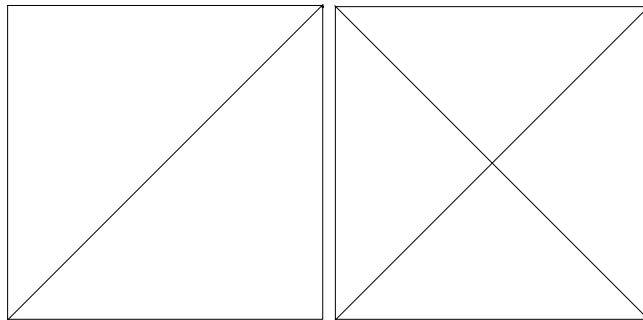
the greater the number of inner faces the cluster has, the greater the number of DOFs and numerical fluxes eliminated. Fig. 3.6 shows the two- and three-dimensional clusters studied in this work that exemplify such properties.

Tables 3.3 and 3.4 show a comparison of the CDG and DG methods for different kinds of elements and cluster configurations. We observe that the clustering always causes a reduction in the DOF by eliminating the need of having duplicated nodes at the interfaces within the cluster. In 3D, the reduction is more significant, e.g. for the cross-hatch cluster with $P = 1$ we have a reduction of about 80%. The number of operations for the lift operations scale as $KN_f N_p N_{fp}$ and for the curl operations as $2KN_p^2$. The cost of computing the numerical fluxes \mathbf{E}^* and \mathbf{H}^* has not been included as it encompasses only vector-vector operations. For $P \leq 2$ the estimates show that the number of operations needed per time step is similar for both methods. For higher orders, the term N_p starts to dominate and the CDGTD method becomes less attractive compared with the classical DGTD approach. However, it should be noted that CDG operators have a reduced spectral radius that allows for a larger time step, as will be shown in Section 3.6. Moreover, in many cases the bottleneck in speed is related to the memory bandwidth and data locality. Therefore, having a reduced number of DOF that are also contiguous in memory may result in additional speed-up, as discussed in [184]. The use of the same spatial operators also alleviates the memory bandwidth, additionally ideally they can remain in the CPU cache during the evaluation of the whole clusters. Finally, the fact that the operator spectrum has a smaller imaginary part when upwind fluxes are used suggests that the scheme can further benefit from the use of different LSERK schemes [113] that allow for a larger time step.

Another question that may arise regarding computational efficiency is how the configurations under study compare with the use of a single element covering the same space, *i.e.* quadrilaterals (quads) in 2D or hexahedrons (hex) in 3D. Tables 3.3 and 3.4 show a comparison of the estimated numbers of operations for different orders and dimensions. As it may be appreciated, for the 3D case, the simple-hatch configuration has the same number of DOFs and needs the same amount of operations to calculate the curl than a hex cell of the same order. There is an increase in the number of operations needed to calculate the LIFT because the increased number of faces, but this is partially compensated with a reduced N_{fp} . The cross-hatch clusters have a similar number of DOFs and need a similar number of operations than a hex cell of one order higher.

TABLE 3.3: DOF and a estimation of the computational costs of the DGTD and CDGTD schemes for a 2D cross-hatch cluster.

P	Quad cell			Cross-hatch						Simple-hatch			
	DGTD2D			DGTD2D			CDGTD2D			DGTD2D		CDGTD2D	
	1	2	3	1	2	3	1	2	3	1	2	1	2
DOF	4	9	16	12	24	40	5	13	25	6	12	4	9
LIFT	32	108	256	72	216	480	24	156	400	36	108	32	108
Curl	32	162	512	72	288	800	50	338	1250	36	144	32	162
Total	64	270	768	144	504	1280	64	494	1650	72	262	64	270



(A) Simple-hatch.

(B) Cross-hatch.

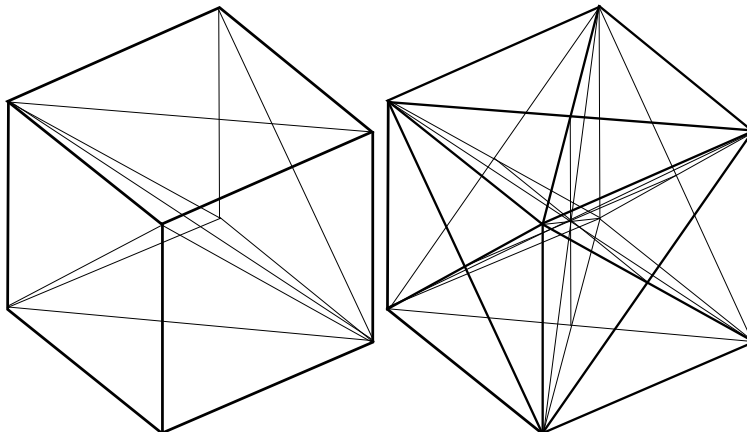
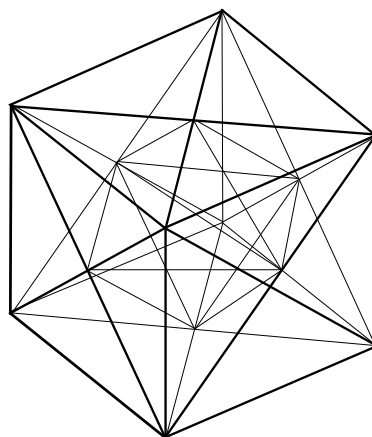
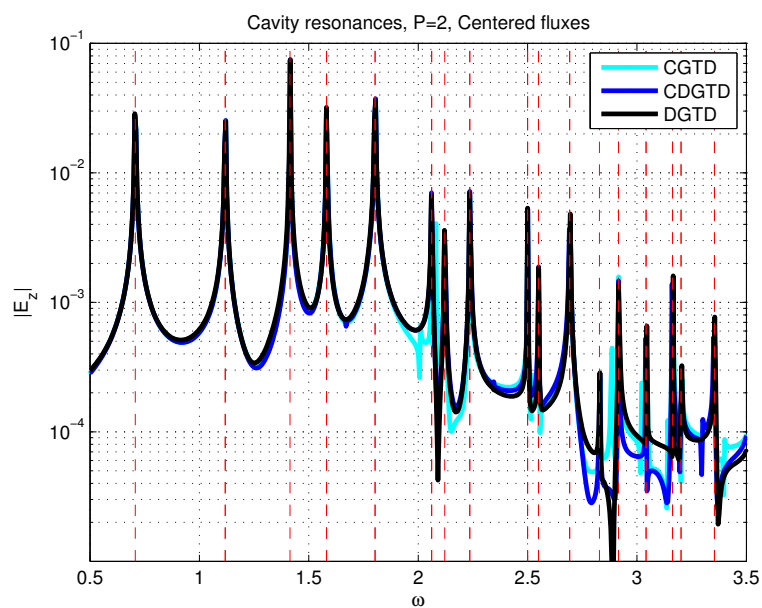
(C) Simple-hatch in 3D, 6 tetra- (D) Cross-hatch in 3D, 24 tetra-
hedrons. hedrons.(E) Anisotropic Cross-hatch in
3D, 24 tetrahedrons.

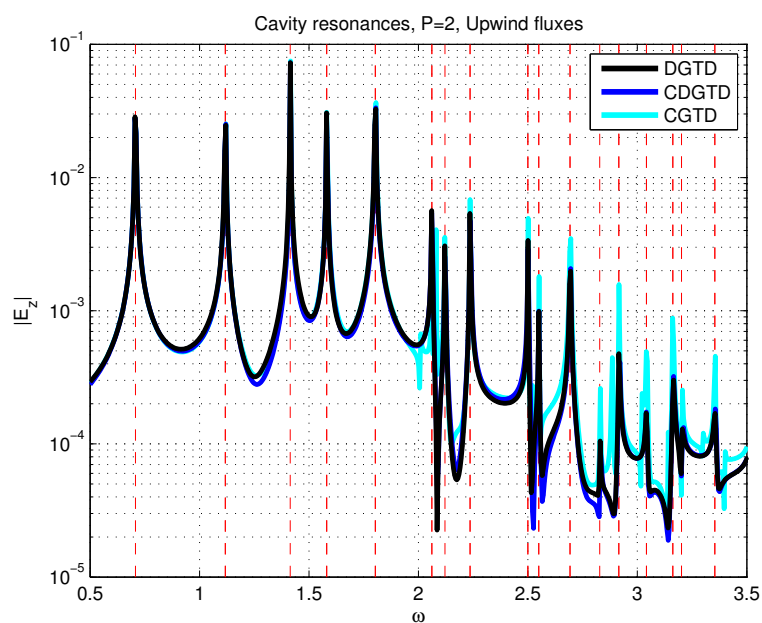
FIGURE 3.6: Different clusters assemblies considered for 2D and 3D CDG.

TABLE 3.4: DOF and a estimation of the computational costs of the DGTD and CDGTD schemes for a 3D cross-hatch cluster.

P	Hex cell		Cross-hatch				Anisotropic cross-hatch		Simple-hatch				
	1	2	DGTD3D	DGTD3D	CDGTD3D	CDGTD3D	1	2	DGTD3D	DGTD3D	CDGTD3D		
DOF	8	27	64	96	240	15	65	14	63	24	60	8	27
LIFT	192	1458	6144	1152	5760	1080	9360	1008	4536	288	1440	288	1944
Curl	128	1458	8192	768	4800	450	8450	392	7938	192	1200	128	1458
Total	320	2916	14336	1920	10560	1530	17810	1400	12474	480	2640	416	3402



(A) Centered flux.



(B) Upwind flux.

FIGURE 3.7: Resonances in a unit square PEC cavity for different methods. The simulations run up to a final time $T = 200$. The basis order is $P = 2$ and the mesh is a cross-hatch grid with $h = 1/8$. The CDGTD results have been obtained by clustering all cross-hatch cells. With centered fluxes, the CGTD and CDGTD method have some visible spurious modes polluting the spectrum at $\omega \simeq 1.7, 2.2, 2.8 \dots$

3.6 Numerical test: 2D cavity

3.6.1 Resonances

Fig. 3.7 shows the results of simulating a unit square cavity using CGTD, DGTD, and CDGTD using a cross-hatch clustering. The simulation runs up to a final time $T = 200$, with a basis order of $P = 2$ and a cross-hatch grid mesh with $h = 1/8$. The time integration was performed with the same LSERK4 scheme used in the previous section. The cavity was excited with a white noise similarly as in [23, 34]. As discussed in the Introduction, CGTD presents spurious modes that pollute the spectrum, the most important being visible at $\omega \simeq 2$ and 2.2 . When centered fluxes are used, CDGTD also exhibits some pollution of the spectrum. A small spurious mode appears at $\omega \simeq 1.7$ and a larger one appears in $\omega \simeq 3.3$. The use of upwind fluxes eliminates this problem at all frequencies considered, as expected from our previous discussion.

3.6.2 Convergence with respect to h-refinement

Table 3.5 shows the results of calculating the L^2 error norm in a square cavity using

$$\|E - E_h\|_{\Omega_h} = \left(\sum_k \int_{\Omega_k} \|E_e - E_h\|^2 d\Omega_k \right)^{1/2} \quad (3.15)$$

where E_e is the exact (analytical) solution, and E_h is the numerical solution. The L^2 error norm is calculated after exciting the first mode of the cavity as initial condition in square meshes of sizes $[0, 1] \times [0, 1]$ with different cell sizes and evolving the scheme up to a final time $T = 4/\sqrt{2}$ (2 cycles). Two of the meshes used for these computations are shown in Fig. 3.8, where the pattern followed for the refinement can be inferred from. The computations have been carried out with upwind and centered fluxes using spatial basis with P from 1 to 3. For CDGTD the clustering has been done using the cross-hatch configuration. For upwind and centered fluxes, we see a clear improvement for $P = 1$ in the convergence rate of the L^2 error norm as it improves from ~ 2.4 to ~ 3.2 . For higher orders the results present a similar convergence rate with the exception of $P = 2$ for centered flux in which CDG produce a considerably higher error. The time integration was done using an LSERK4 scheme where h_t has been set heuristically and we find that for upwind fluxes the h_t for CDGTD can be set $\sim 50\%$ larger than for DGTD. With centered fluxes the gain is more moderate ($\sim 20\%$). As expected, CDGTD used much less DOF, varying from ~ 40 to $\sim 60\%$ less depending on P .

Note that although some improvements are achieved with CDGTD, if we compare results between different orders the DGTD method shows that better results can be achieved with DGTD for a similar number of DOFs by increasing the basis order. For example if we compare the upwind cases of DGTD with $P = 3$ and $h = 1/8$ and, CDGTD with $P = 2$ and $h = 1/16$ we observe that DGTD achieves a smaller error than CDGTD using less DOFs. However, CDGTD allows a larger h_t for stability, and needs less number of operations, according to table 3.3.

TABLE 3.5: L^2 error norm for different resolutions of the first mode of a unit square cavity after a simulated time of $4/\sqrt{2}$ (2 cycles). For all CDGTD cases, the time steps can be larger than those for DGTD, with smaller improvements for centered than for upwind flux. The number of DOFs with the CDGTD cross-hatch configuration are 40 ~ 60% less depending on the spatial order. Convergence ratios remain similar for all cases, except for the case $P = 1$, where a clear improvement is observed.

	P	h	DGTD				CDGTD Cross-hatch			
			L^2 Error	Order	h_t	DOF	L^2 Error	Order	h_t	DOF
Upwind	1	1/2	4.6E-2	-	120E-3	48	3.7E-2	-	197E-3	20
		1/4	1.2E-3	2.5	60E-3	192	1.5E-4	3.8	98E-3	80
		1/8	3.0E-5	2.6	30E-3	768	1.2E-6	3.3	49E-3	320
		1/16	1.1E-6	2.3	15E-3	3072	1.7E-8	3.0	25E-3	3072
		1/32	5.9E-8	2.0	7E-3	12288	2.6E-10	2.9	12E-3	5120
	2	1/2	1.2E-4	-	595E-4	96	1.7E-4	-	984E-4	52
		1/4	1.5E-6	3.0	298E-4	384	1.9E-6	3.1	492E-4	208
		1/8	2.3E-8	2.9	149E-4	1536	2.3E-8	3.1	246E-4	832
		1/16	3.6E-10	2.9	74E-4	6144	3.4E-10	2.9	123E-4	3328
		1/32	5.6E-12	2.9	37E-4	24576	5.2E-12	2.9	61E-4	13312
	3	1/2	1.2E-6	-	397E-4	160	2.8E-6	-	656E-4	100
		1/4	5.2E-9	3.8	198E-4	640	7.5E-9	4.1	328E-4	400
		1/8	2.1E-11	3.8	99E-4	2560	2.0E-11	4.1	164E-4	1600
		1/16	8.2E-14	3.8	50E-4	6400	8.6E-14	3.8	82E-4	6400
		1/32	3.2E-16	3.8	25E-4	40960	2.8E-16	4.0	41E-4	25600
Centered	1	1/2	2.4E-2	-	166E-3	48	4.3E-3	-	197E-3	20
		1/4	9.6E-4	2.2	83E-3	192	9.4E-4	1.1	98E-3	80
		1/8	5.6E-5	2.0	41E-3	768	1.5E-6	4.5	49E-3	320
		1/16	3.5E-6	1.9	21E-3	3072	1.7E-8	3.1	25E-3	3072
		1/32	2.2E-7	1.9	10E-3	12288	2.6E-10	2.9	12E-3	5120
	2	1/2	1.7E-4	-	776E-4	96	1.2E-4	-	984E-4	52
		1/4	2.8E-6	2.8	388E-4	384	4.6E-5	0.7	492E-4	208
		1/8	4.2E-8	2.9	194E-4	1536	2.3E-6	2.1	246E-4	832
		1/16	6.6E-10	2.9	97E-4	6144	9.4E-8	2.2	123E-4	3328
		1/32	1.0E-11	2.9	49E-4	24576	5.2E-9	2.0	61E-4	13312
	3	1/2	1.8E-6	-	518E-4	160	7.9E-6	-	656E-4	100
		1/4	7.1E-9	3.8	259E-4	640	5.3E-9	5.1	328E-4	400
		1/8	2.1E-11	4.0	129E-4	2560	1.3E-10	2.6	164E-4	1600
		1/16	1.2E-13	3.6	65E-4	6400	4.0E-13	4.0	82E-4	6400
		1/32	3.4E-16	4.1	32E-4	40960	1.4E-15	3.9	41E-4	25600

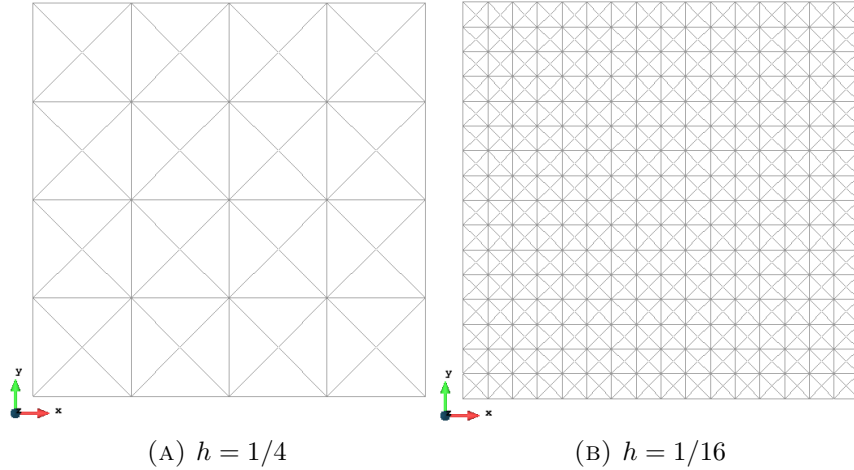


FIGURE 3.8: $h = 1/4$ and $h = 1/16$ meshes used to compute the resonant cavity results. Each of the cross-hatch elements is assembled to form a cluster.

3.7 Conclusions

In this work we have introduced a new hybrid CDG method for Maxwell's curl equations and studied some of its numerical properties. The CDG method facilitates the use of implicit techniques in TD, requires less DOF than conventional DG and allows for larger time-steps. The overall number of operations needed is also reduced for certain configurations and for low orders. Combined with improvements in memory locality leaves open the possibility that the method is computationally more affordable than pure DG, at least up to order $P = 2$. From the analysis performed in this paper, some applicability scenarios can be devised where the use of CDGTD in certain parts of the mesh may be of interest:

1. **DOF reduction in structured regions:** The discussion carried out in Section 3.5 shows that using semi-structured arrangements of CDG clusters can drastically reduce the number of DOFs for any P . Fig. 3.9 shows a situation in which the use of the CDGTD method could improve performance. When used in this way, an added advantage of the CDGTD formulation with respect to multi-element meshes is that the clusters can exist in many different configurations, it suffices for them to have translational symmetry to fully cover a region of the space. If we compare with the costs associated to hex cells we see that we can have benefits similar to the use of hybrid meshes using exclusively tetrahedral meshes while we retain their geometric flexibility. Note also that obtain and operate with a mesh formed exclusively of tetrahedrons is significantly simpler than with hybrid meshes.

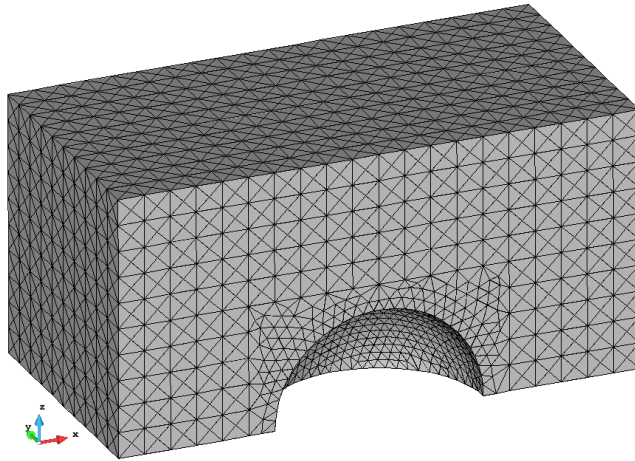


FIGURE 3.9: A suitable partially structured mesh in which the CDGTD formalism would preferably be used only in cross-hatch regular tetrahedron clusters.

2. **Buffering between element types:** Multi-element approaches exploit the advantages of, mainly, tetrahedral and hexahedral mesh elements. In three-dimensional problems this forces the use of non-conforming interfaces [109, 110] or the use of pyramidal elements [111] for the transitions between elements of different types. CDGTD can offer a solution to do these transitions by using a simple-hatch cluster (Fig. 3.6c) between tetrahedral and hexahedral regions (Fig. 3.10). When using nodal functions, the interfacing is simplified because rather than having multivalued nodes at the diagonal of the tetrahedral region, we have a single one. This avoids the need of performing an interpolation or use a non-conformal boundary. We can directly use the DOFs belonging to the nodes in contact in order to compute the fluxes.

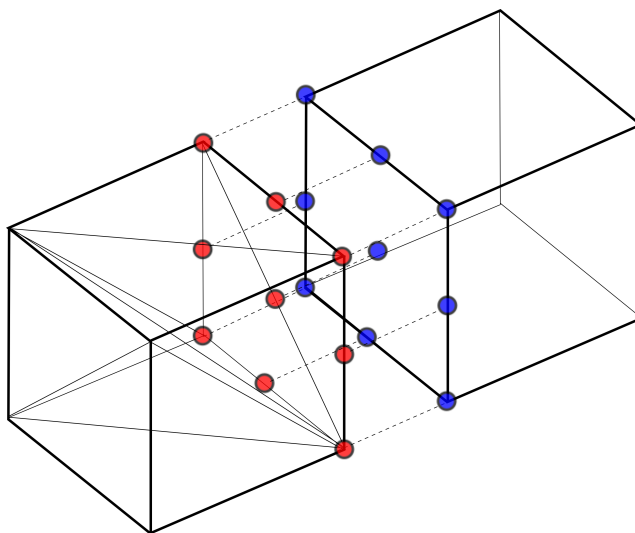


FIGURE 3.10: Interfacing between the simple-hatch cluster and a hex cell for $P = 2$.

3. Reduction of high stiffness time constraints: CDGTD formalism can also be used to assemble stiff elements to alleviate their time step constraints. As shown in Section 3.6 the assembling produces a significant reduction of the size of the spectrum letting us to increase the time step used. This can drive to a significant gain in certain situations (Fig. 3.11) because the maximum time step is constrained by the maximum allowed time step of the smallest element.

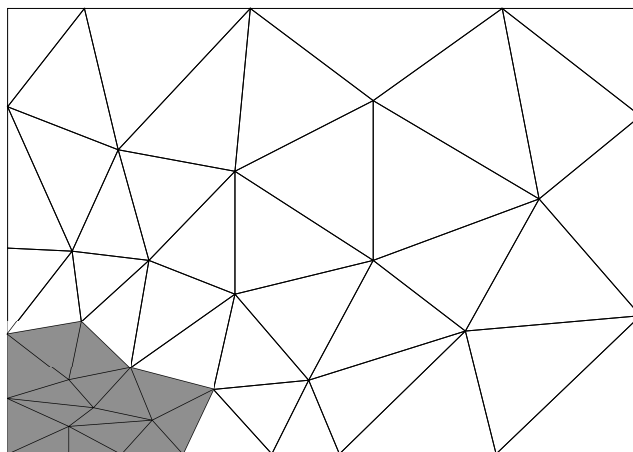


FIGURE 3.11: A region with high stiffness (grayed) can be assembled into a CDG cluster to improve the maximum time step allowed. The rest of the mesh can be evolved using a classical DGTD scheme.

Chapter 4

An analysis of the Leap-Frog Discontinuous Galerkin method for Maxwell's equations

J. Alvarez, L. D. Angulo, M.R. Cabello, A. R. Bretones, and S. G. Garcia. An analysis of the leap-frog discontinuous galerkin method for maxwell's equations. *IEEE Transactions on Microwave Theory and Techniques*, 62(2):197–207, February 2014

Abstract

In this paper, we explore the accuracy limits of a Finite-Element Time-Domain method applied to the Maxwell equations, based on a Discontinuous Galerkin scheme in space, and a Leap-Frog temporal integration. The dispersion and dissipation properties of the method are investigated, as well as the anisotropy of the errors. The results of this novel analysis are represented in a practical and comprehensible manner, useful for the application of the method, and for the understanding of the behavior of the errors in Discontinuous Galerkin Time-Domain methods. A comparison with the Finite-Difference Time-Domain method, in terms of computational cost, is also included.

4.1 Introduction

Since the FDTD method was firstly proposed by Yee in 1966 [37] for solving Maxwell equations, it has become undoubtedly the most widespread method among physicists and engineers, due to its simplicity and flexibility to deal with real problems. However, its inability to effectively handle complex geometries, due to stair-casing error, and the limitations in the accuracy (second order in space and time $O(h^2, \Delta t^2)$), prompted some scientists to search for alternatives long ago, with Finite Element (FE) the obvious alternative. Considering all the schemes based on FE in the literature, Discontinuous Galerkin Time Domain (DGTD) approaches have most of the advantages of FDTD; spatial explicit algorithm, simplicity, easy parallelization, and memory and computational cost growing linearly with the number of elements. Besides, DGTD schemes retain most of the benefits of FE, adaptability of the unstructured meshes and spatial super-convergence, allowing to deal with problems where the required precision varies over the entire domain, or when the solution lacks smoothness.

The performances of the Yee algorithm is very well described in a broad literature [36]. Analytical expressions can be easily derived to analyze the numerical dispersion, stability and anisotropy of the error, due to the use of structured meshes, which enables to find close and general relations. In FETD methods, where unstructured meshes are used, the relations between order of the basis functions (p), element size (h), and time step (Δt) with dispersion, dissipation, and anisotropy, are problem-dependent. The typical approach to analyze the performance of these methods are based on eigenvalue problems [75, 76, 91, 190] or in solving specific numerical problems [193]. An anisotropic analysis in 2D of the DG TD method for wave propagation problems appears in [166]. Some analyses also include the effect of the time-integration scheme [74].

In this paper, we present an analysis of the accuracy and computational cost of the Leap-Frog Discontinuous Galerkin (LFDG) algorithm, finding practical criteria for its application to general problems. We begin by summarizing the LFDG algorithm. We next analyze the convergence and anisotropy of the algorithm, comparing to the semi-discrete DG space operator. For this, we find the solutions of the eigenvalue problem for a canonical geometry, which can be easily used to also compare to the well-known FDTD method. Finally, a computational cost versus accuracy analysis of the LFDG method is performed and compared to the FDTD method.

4.2 LFDG algorithm

4.2.1 Semi-discrete DG formulation

Let us divide the space into M non-overlapping elements V^m , each bounded by ∂V^m , and define element-by-element a set of Q local continuous basis of vector test functions ($\mathcal{B}^m = \{\vec{\Phi}_1^m, \vec{\Phi}_2^m, \dots, \vec{\Phi}_Q^m\}$). In this work, vector basis has been used and more specifically, hierarchical high-order vector-basis functions, [85, 220], which present some implementation advantages in order to reduce computation and memory requirements [92]. Now, assume Maxwell's symmetric curl equations for linear isotropic homogeneous media in Cartesian coordinates. Enforcing the residual of Maxwell's curl time-domain (TD) equations to be orthogonal to each basis function element-by-element, we find

$$\left\langle \vec{\Phi}_{q'}^m, \varepsilon \partial_t \vec{E}^m - \nabla \times \vec{H}^m \right\rangle_{V^m} = 0 \quad (4.1)$$

$$\left\langle \vec{\Phi}_{q'}^m, \mu \partial_t \vec{H}^m + \nabla \times \vec{E}^m \right\rangle_{V^m} = 0 \quad (4.2)$$

$$\forall q' = (1, \dots, Q) \ , \ m = (1, \dots, M)$$

with \vec{E} , \vec{H} , ε , μ being, respectively: electric field, magnetic field, permittivity, and permeability. After some algebra, we can write Eqs. (4.1)(and similarly for Eq. (4.2)) as

$$\int_{V^m} (\vec{\Phi}_{q'}^m \cdot (\varepsilon \partial_t \vec{E}^m + \nabla \times \vec{\Phi}_{q'}^m \cdot \vec{H}^m)) dV = \oint_{\partial V^m} \vec{\Phi}_{q'}^m \cdot (\hat{\mathbf{n}}^m \times \vec{H}^m) dS \quad (4.3)$$

which relate the volume integral of the LHS to a flux integral in the RHS. DGTD defines continuous numerical fluxes of the tangential field components $\hat{\mathbf{n}}^m \times \vec{H}^{m*}$ to be used instead of $\hat{\mathbf{n}}^m \times \vec{H}^m$ at the RHS, at each side of ∂V^m . A robust and efficient choice of the numerical flux is the so-called partially penalized flux [14, 27, 62, 77, 113] which has been proved to provide accurate and free of spurious mode solutions [13],

$$\hat{\mathbf{n}}^m \times \vec{H}^{m*} = \hat{\mathbf{n}}^m \times \vec{H}^m + \kappa_h^m \left[\hat{\mathbf{n}}^m \times (\vec{H}^{m+} - \vec{H}^m) \right] - \nu_e^m \left[\hat{\mathbf{n}}^m \times (\hat{\mathbf{n}}^m \times (\vec{E}^{m+} - \vec{E}^m)) \right] \quad (4.4)$$

with,

$$\kappa_h^m = \frac{Z^{m+}}{Z^m + Z^{m+}}, \quad \nu_e^m = \frac{\tau}{Z^m + Z^{m+}} \quad (4.5)$$

τ being a stabilization parameter which penalizes the discontinuities in the tangential components, $Z^m = \sqrt{\frac{\mu^m}{\varepsilon^m}}$ the intrinsic impedance of the element m , and Z^{m+} the

intrinsic impedance of the adjacent one. An upwind-flux scheme is obtained with $\tau = 1$, and centered with $\tau = 0$.

Using a Faedo-Galerkin method

$$\vec{E}^m = \sum_{q=1}^Q e_q^m(t) \vec{\Phi}_q^m(\vec{r}), \quad \vec{H}^m = \sum_{q=1}^Q h_q^m(t) \vec{\Phi}_q^m(\vec{r}) \quad (4.6)$$

a final spatial semi-discrete operator is found

$$\mu \mathbb{M} d_t H^m - \mathbb{F}_{\nu h} H^m + \mathbb{F}_{\nu h}^+ H^{m+} = -(\mathbb{S} - \mathbb{F}_{\kappa e}) E^m - \mathbb{F}_{\kappa e}^+ E^{m+} \quad (4.7a)$$

$$\varepsilon \mathbb{M} d_t E^m - \mathbb{F}_{\nu e} E^m + \mathbb{F}_{\nu e}^+ E^{m+} = (\mathbb{S} - \mathbb{F}_{\kappa h}) H^m + \mathbb{F}_{\kappa h}^+ H^{m+} \quad (4.7b)$$

where H^m and E^m are column vectors with the degrees of freedom (dofs), and H^{m+} and E^{m+} the dofs of the adjacent elements, and \mathbb{M} is the mass, \mathbb{S} the stiffness, and \mathbb{F} the flux matrices given in [13].

4.2.2 Leap-Frog time integration formulation

For the time integration, we employ the 2^{nd} -order leap-frog (LF) scheme, which is described in the FDTD literature [36]. It samples the unknown fields in a staggered way: the electric field at $t_n = n\Delta t$, and the magnetic field at $t_{n+\frac{1}{2}} = (n + \frac{1}{2}) \Delta t$. The staggered sampling yields an explicit marching-on-in-time algorithm, assuming that

- The time derivatives in (4.7) are replaced by 2^{nd} -order accurate central differences¹

$$(d_t H^m)_n = \frac{H_{n+\frac{1}{2}}^m - H_{n-\frac{1}{2}}^m}{\Delta t} + O(\Delta t^2) \quad (d_t E^m)_{n+\frac{1}{2}} = \frac{E_{n+1}^m - E_n^m}{\Delta t} + O(\Delta t^2) \quad (4.8)$$

- The two extra dissipative terms arising from the upwind/penalized flux formulation, are approximated by a backwards formula

$$H_n^m \simeq H_{n-\frac{1}{2}}^m, \quad E_{n+\frac{1}{2}}^m \simeq E_n^m \quad (4.9)$$

Note that if we also employed an average for these terms, a globally implicit scheme would arise (due to the coupling between E and H DoF coming from adjacent elements). As discussed in [13, 77] this backward approximation for

¹If there were conductivity terms, these would require a 2^{nd} -order accurate average approximation[18].

the flux terms is enough to attenuate spurious modes in space more strongly than physical modes, which is the only aim of these terms.

Inserting the above approximations in (4.7), we find a fully explicit scheme

$$H_{n+\frac{1}{2}}^m = H_{n-\frac{1}{2}}^m + \frac{\Delta t}{\mu} \mathbb{M}^{-1} \left[-(\mathbb{S} - \mathbb{F}_{\kappa e}) E_n^m - \mathbb{F}_{\kappa e}^+ E_n^{m+} + \mathbb{F}_{\nu h} H_{n-\frac{1}{2}}^m - \mathbb{F}_{\nu h}^+ H_{n-\frac{1}{2}}^{m+} \right] \quad (4.10a)$$

$$E_{n+1}^m = E_n^m + \frac{\Delta t}{\varepsilon} \mathbb{M}^{-1} \left[(\mathbb{S} - \mathbb{F}_{\kappa h}) H_{n+\frac{1}{2}}^m + \mathbb{F}_{\kappa h}^+ H_{n+\frac{1}{2}}^{m+} + \mathbb{F}_{\nu e} E_n^m - \mathbb{F}_{\nu e}^+ E_n^{m+} \right] \quad (4.10b)$$

4.3 Description of the eigenvalue problems

In this work, we first formulate the eigenvalue problem for the DG semi-discrete scheme and for the fully discrete LFDG algorithm. Then, we solve this problem for a simple cubic spatial domain in different conditions, in order to study the dispersion and dissipation properties of the schemes, and the anisotropic behavior of the error, as well as being able to directly compare to FDTD.

4.3.1 DG semi-discrete scheme

Let us define a column-vector with all the *DoF* of a given problem

$$\mathbf{U} = [(h_1^1, \dots, h_Q^1), \dots, \dots, (e_1^M, \dots, e_Q^M)]^T$$

The semi-discrete DG equations (4.7) (in free-space) can be expressed for plane-wave solutions as the following eigen-problem

$$j\omega \vec{U} = \mathcal{A}_{DG} \vec{U} \quad (4.11)$$

with \mathcal{A}_{DG} the semi-discrete DG operator under analysis.

We now consider a cubic spatial domain meshed in a non-symmetrical way into 24 tetrahedrons (Fig. 4.1), and we assume that Periodic Boundary Conditions (PBC) conditions are enforced at the box faces by setting

$$\begin{aligned} \hat{\mathbf{n}}^m \times \mathbf{H}^{m+} \Big|_{i+\Delta i} &= \hat{\mathbf{n}}^m \times \mathbf{H}^m \Big|_i e^{-j\alpha_i}, \\ \hat{\mathbf{n}}^m \times \mathbf{E}^{m+} \Big|_{i+\Delta i} &= \hat{\mathbf{n}}^m \times \mathbf{E}^m \Big|_i e^{-j\alpha_i} \quad i = \{x, y, z\} \end{aligned} \quad (4.12)$$

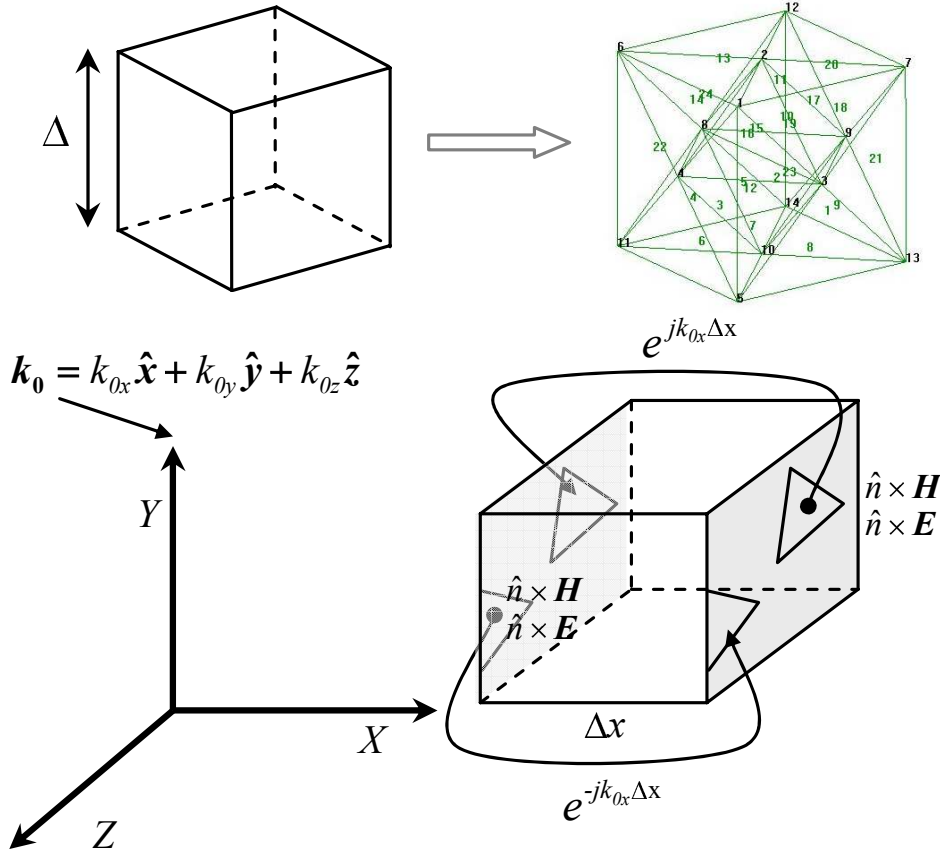


FIGURE 4.1: Geometry under analysis for the eigenvalue problem (top). Application of the PBC between contour faces from elements located at opposite sides.

where α_i is the phase shift in each direction of the space here taken as $\alpha_i = k_{0i}\Delta_i$, with $\vec{k}_0 = k_{0x}\hat{x} + k_{0y}\hat{y} + k_{0z}\hat{z}$ the analytical wave-vector. We have defined h (a measure for the size of the elements) equal to the dimension of the cube $\Delta \equiv h$.

The eigen-problem (4.11) is numerically solved for different \vec{k}_0 to study anisotropy or h for convergence, finding the numerical eigenvalue \tilde{k}_m . For the error analysis, we retain only the \tilde{k}_m closest to the analytical one $\vec{k}_0 = \omega\sqrt{\mu_0\epsilon_0}$ (the rest can be considered spurious in the sense discussed in [13]), referred to here as $\tilde{k}_0 = \tilde{k}_{real} + j\tilde{k}_{imag}$.

Three different Root Mean Square (RMS) error functions per wavelength ($\lambda = 2\pi/k_0$) can be defined:

$$\text{RMS error per } \lambda \text{ (dispersion): } \left| e^{-jk_0\lambda} - e^{-j\tilde{k}_{real}\lambda} \right| \quad (4.13a)$$

$$\text{RMS error per } \lambda \text{ (dissipation): } \left| 1 - e^{\tilde{k}_{imag}\lambda} \right| \quad (4.13b)$$

$$\text{RMS error per } \lambda \text{ (global): } \left| e^{-jk_0\lambda} - e^{-j\tilde{k}_0\lambda} \right| \quad (4.13c)$$

The first one measures the dispersion error (phase delay), depending on the real part of the numerical eigen-value (\tilde{k}_{real}); the second one measures the dissipation error (decrease in amplitude), depending on its imaginary part (\tilde{k}_{imag}); and the third one measures the global combination of both errors.

4.3.2 Fully discrete LFDG algorithm

In this sub-section, we formulate the fully discrete LFDG scheme (temporal integration plus spatial discretization) eigenvalue problem. For this, let us define three column vectors staggered in time

$$\begin{aligned}\mathbf{H}_{n-\frac{1}{2}} &= \left[\left(H_{n-\frac{1}{2}}^1 \right)^T, \dots, \left(H_{n-\frac{1}{2}}^M \right)^T \right]^T \\ \mathbf{E}_n &= \left[\left(E_n^1 \right)^T, \dots, \left(E_n^M \right)^T \right]^T \\ \mathbf{U}_n &= \left[\left(\mathbf{H}_{n-\frac{1}{2}} \right)^T, \left(\mathbf{E}_n \right)^T \right]^T\end{aligned}$$

Eqs. (4.10) (in free-space) can be expressed in a compact manner for the whole spatial domain as

$$\mathbf{H}_{n+\frac{1}{2}} = \left(\mathbb{I}_{MQ} + \frac{\Delta t}{\mu} \mathbb{M}_{\nu h} \right) \mathbf{H}_{n-\frac{1}{2}} + \frac{\Delta t}{\mu} \mathbb{M}_{S\kappa e} \mathbf{E}_n \quad (4.15a)$$

$$\mathbf{E}_{n+1} = \left(\mathbb{I}_{MQ} + \frac{\Delta t}{\varepsilon} \mathbb{M}_{\nu e} \right) \mathbf{E}_n + \frac{\Delta t}{\varepsilon} \mathbb{M}_{S\kappa h} \mathbf{H}_{n+\frac{1}{2}} \quad (4.15b)$$

where \mathbb{I}_{MQ} is the $MQ \times MQ$ identity matrix, and $\mathbb{M}_{\nu h}$, $\mathbb{M}_{S\kappa e}$, $\mathbb{M}_{\nu e}$ and $\mathbb{M}_{S\kappa h}$ are $MQ \times MQ$ matrices, which are the result of assembling the element-matrices of (4.10). Inserting (4.15a) into (4.15b), the following fully explicit system is obtained

$$\mathbf{U}_{n+1} = \mathcal{A}_{LFDG} \mathbf{U}_n \quad (4.16)$$

where the matrix \mathcal{A}_{LFDG} is the Discontinuous Galerkin operator with the Leap-Frog algorithm. It is the result of assembling all the element-matrices of (4.10) into a $2MQ \times 2MQ$ matrix. The matrix \mathcal{A}_{LFDG} depends on the DG spatial discretization features (mesh size (h), penalization factor (τ), order of the basis functions (p)), and on the time-step (Δt).

Seeking, again, for plane-wave solutions, the relationship between \mathbf{U}_{n+1} and \mathbf{U}_n is

$$\mathbf{U}_{n+1} = e^{j\omega\Delta t} \mathbf{U}_n \quad (4.17)$$

with $e^{j\omega\Delta t}$ so-called the amplification factor, which is found after solving the following eigen-problem,

$$e^{j\omega\Delta t}\mathbf{U}_n = \mathcal{A}_{LFDG}\mathbf{U}_n \quad (4.18)$$

Finding the $2MQ$ eigenvalues ($\lambda_{\mathcal{A}_{LFDG}}^m, m = 1, \dots, 2MQ$), we obtain the complex-valued numerical wave-vectors ($\tilde{k}^m = \tilde{k}_{real}^m + j\tilde{k}_{imag}^m, m = 1, \dots, 2MQ$), related to the eigenvalues by

$$\tilde{k}^m = j \frac{\ln\left(\lambda_{\mathcal{A}_{LFDG}}^m\right)}{c\Delta t}, \quad m = 1, \dots, 2MQ \quad (4.19)$$

Using the same PBC cubic problem (Fig. 4.1), and focusing again [13] on the mode closest to the analytical one $\tilde{k}^m = \tilde{k}_0$, we can reproduce the error estimation of Eqs. (4.13). Notice that \mathcal{A}_{LFDG} is a function of Δt . In the following analyses (except for a specific analysis where we have made Δt variable), we have fixed this parameter to $\Delta t = 0.7\Delta t_{max}$, with Δt_{max} the upper limit for stability of the LFDG scheme. This is our typical choice to address complex simulations. [10, 13, 14, 18, 221].

Concerning the evaluation of Δt_{max} , heuristic sufficient stability closed conditions can be found in the literature [77, 90, 92, 124]. However, for the small problem of this paper, we can afford to use a numerical strategy in order to find the least restrictive necessary stability condition case-by-case. For this, we solve the eigenvalue problem (4.18) for different Δt until we find a maximum value of Δt_{max} , which keeps all the complex-valued \tilde{k}^m with a negative imaginary part ($\tilde{k}_{imag}^m < 0, m = 1, \dots, 2MQ$).

4.4 Convergence analysis

In this section, we estimate the convergence rates of the semi-discrete DG operator and the fully discrete LFDG algorithm, also studying the influence of the τ penalization parameter, and Δt . The convergence of DG methods has been dealt with in a number of works [75, 76, 190]. In this paper, we follow the strategy used previously by the authors in [13] for the study of the spurious modes, and the numerical spectrum. We analyze the convergence by searching for numeric plane-wave solutions $e^{j(\omega t - \vec{k}\vec{r})}$ of real frequency ω and complex wave-vector \vec{k} , for the simple problem of Fig. 4.1 with PBC, described in the previous section. The numerical wavevector compared to the analytical one will provide a measure for the error of the numerical scheme.

For this analysis, we have taken $\alpha_z = 2\pi\Delta$, and no phase-shift for the other directions $\alpha_x = \alpha_y = 0$ ($\vec{k}_0 = k_0\hat{\mathbf{z}}$), since the convergence rates do not depend on the

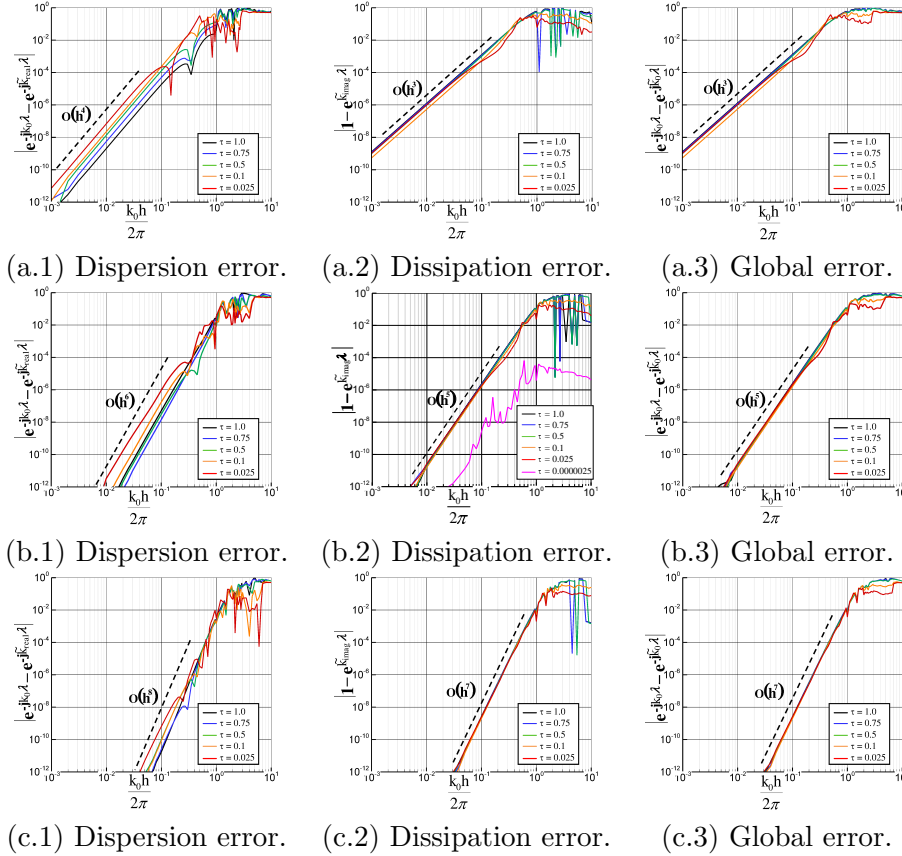


FIGURE 4.2: Convergence and influence of the τ parameter in the error of the DG operator for different p orders. (a) $p = 1$, (b) $p = 2$ and (c) $p = 3$. The dissipation error with a very small value of τ has been computed for $p = 2$ and included in (b.2).

In case of $\tau = 0$ (centered flux) the dissipation error would be zero.

illumination direction. The eigen-problem (4.11) is numerically solved for different h to find the numerical eigenvalue \tilde{k}_m .

For the DG semi-discrete scheme, the RMS for basis orders $p = 1, 2, 3$ and for five values of τ penalization parameter (from upwind $\tau = 1$, to $\tau = 0.025$) are shown in Fig. 4.2 as a function of the spatial resolution ($h/\lambda = k_0 h/(2\pi)$).

From Fig. 4.2, we can derive the following conclusions:

- Super-convergence of the error is found in all cases. The phase error increases as $O(h^{2p+2})$ and the amplitude error follows $O(h^{2p+1})$, p being the order of the polynomial space for the vector-basis functions [75, 76, 190].
- Since the convergence rate for the dissipation error is worse than for the dispersion error ($2p + 2 > 2p + 1$), dissipation places higher constraints on the scheme resolution (h/λ) than does the dispersion error. This fact should be

considered when choosing the time integration scheme, to avoid the introduction of more dissipation, keeping dispersion under control. For instance, Runge-Kutta schemes optimize the stability region, while holding dispersion and dissipation fixed. It is found [222] that maximizing dispersion minimizes dissipation, and *vice versa*. LF, as shown below, does not add dissipation error, but only dispersion.

- The parameter τ has little influence in the dispersion and dissipation error of the physical mode, considered here. Only for very low values of τ the dissipation error decreases, as it should be since $\tau = 0$ (centered) has zero dissipation. Fig. 4.2(b.2) shows results for a very small value of τ showing this fact. However, it bears noting that the dissipation of the spurious modes is strongly affected by the τ parameter, as demonstrated in [13], and also in the stability condition [77, 113].

Let us now analyze the fully discrete LFDG scheme to compare it with the previous results of the spatial DG operator alone and with the well-known FDTD method. Since the influence of the τ parameter on the accuracy of the physical mode has been seen to be negligible for the semi-discrete case, we have fixed a value of $\tau = 0.1$. This value has been chosen as a trade-off between stability and spurious-mode reduction [13].

Results for RMS errors are shown in Fig. 4.3 for different orders p , taking $\Delta t = 0.7\Delta t_{max}$. Fig. 4.4 also shows results for different $\Delta t < \Delta t_{max}$ (for $p = 2$).

We can conclude from Figs. 4.3 and 4.4:

- The super-convergence property of the DG spatial operator is maintained up to an error limit where the convergence of the error becomes $O(h^2)$ dominated by the LF time integration scheme (only 2^{nd} -order). This fact depends neither on the order of functions p , nor on Δt , and coincides with that found for the FDTD method. Higher order Leap-Frog (LF_N) schemes have been proposed to improve this [224].
- Since LF is non-dissipative, only the dispersion error is affected. The dissipation error coincides with that of the semi-discrete case.
- The limit between the zones where the error is dominated by the spatial discretization and by the temporal integration methods depends on Δt , as shown in Fig. 4.4. This limit can be improved by reducing Δt , at the cost of increasing the computational cost.

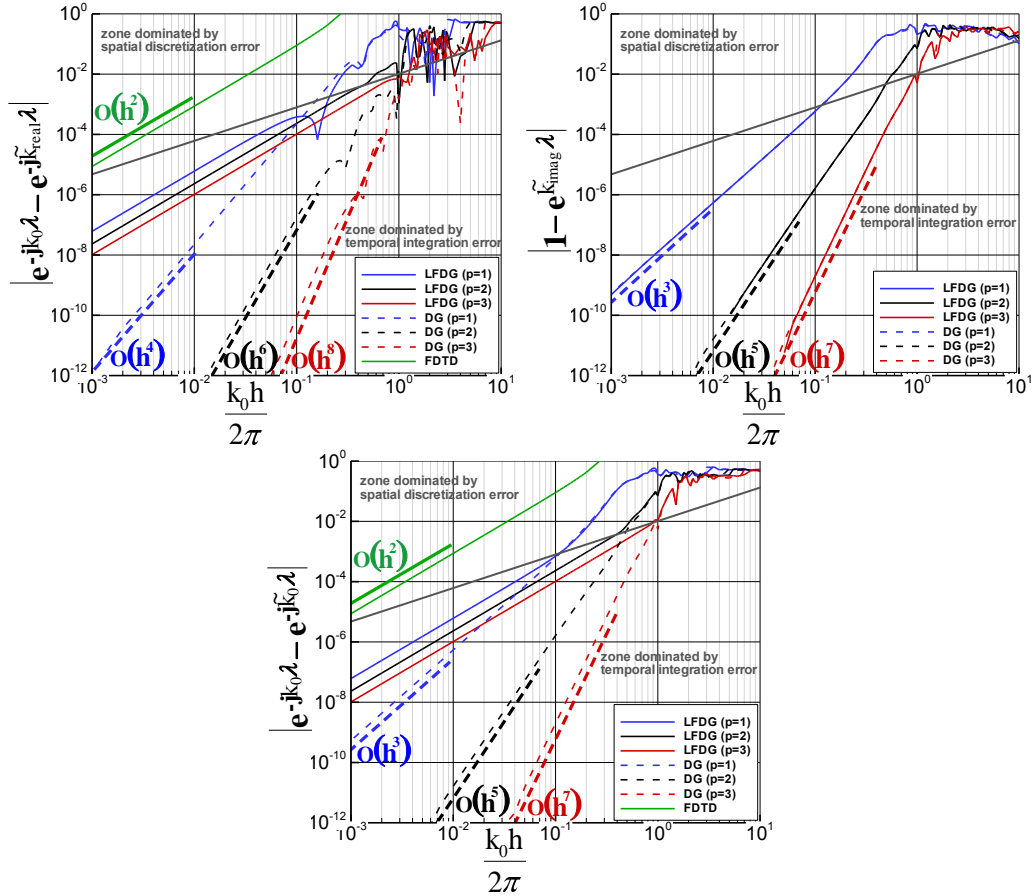


FIGURE 4.3: Convergence of the physical mode for the LFDG algorithm with $\tau = 0.1$ and $\Delta t = 0.7\Delta t_{max}$. Analogous curves for the DG operator and FDTD[223] have been included for comparison ($\tilde{k}_0 = \frac{2}{h} \arcsin(\frac{h}{c\Delta t} \sin(\frac{k_0 c \Delta t}{2}))$, $\Delta t_{max} = \frac{h}{c\sqrt{3}}$). In the case of the dissipation error, FDTD curve has been omitted, since the error is zero, and notice that the LFDG and DG curves are superposed. A limit (grey line) has been included in the graphs to separate two zones, one (upper) dominated by the spatial discretization and other (lower) by the temporal integration.

- The typical 10^{-2} accuracy value is in the zone dominated by the spatial discretization error for the LFDG method, for $p = 1$, $p = 2$ and $p = 3$ and $\Delta t = 0.7\Delta t_{max}$ with resolutions ranging from $\sim \frac{\lambda}{4.5}$, $\sim \frac{\lambda}{1.9}$ and $\sim \frac{\lambda}{1.1}$, respectively. This characteristic is not expected to be fulfilled by higher orders than $p = 3$. In FDTD a resolution of $\sim \frac{\lambda}{28.5}$ can be found from its dispersion relationship[223] to be required to reach a 10^{-2} accuracy² for propagation along the cube edge³.

²Notice that the resolution for FDTD, is that of the cubic spatial domain of Fig. 4.1, meshed with one cell, while for LFDG, the same domain is meshed into 24 tetrahedrons. The influence of the resolution is taken into account in Section 4.6 to compare in terms of computational cost.

³Propagation along the Cartesian axes is the worst-case of dispersion in FDTD (no phase error occurs along the diagonals at the stability limit). However in a real problem, no control over the propagation direction exists, and a resolution of 28.5 cells/wavelength is reasonable in many FDTD situations.

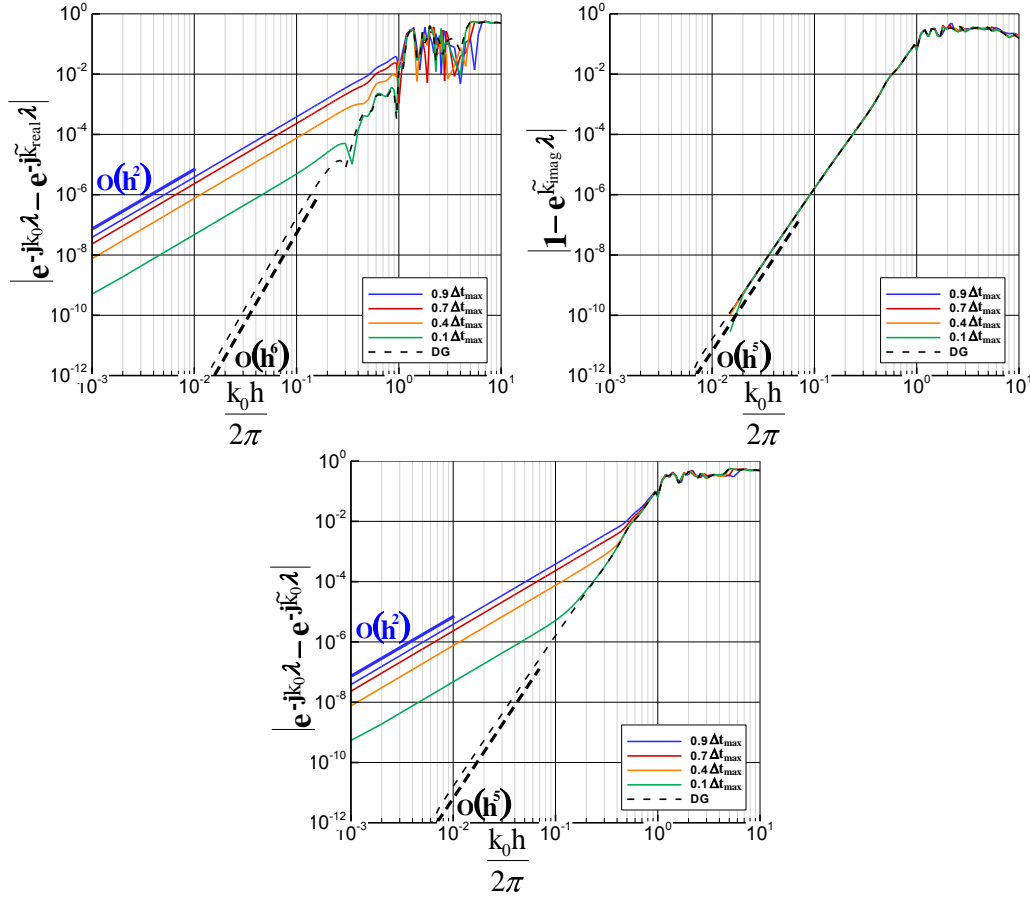


FIGURE 4.4: Influence of Δt in the dispersion (upper), dissipation (middle) and global (lower) errors of the LFDG algorithm with $\tau = 0.1$ and $p = 2$. Analogous curves for the DG operator have been included.

A simple numerical experiment has been performed in order to reproduce some results from the previous analysis. A region of $(0.6 \times 0.6 \times 12)$ m. has been meshed into $(3 \times 3 \times 60)$ cubes, each one equal to that used for the previous eigenvalue analysis (Fig. 4.1, with $\Delta = 0.2$ m.). A y -polarized plane wave, propagating along the z -axis, has been excited at the lower z -plane by using perfect electric conductor (PEC) at the y -boundaries and perfect magnetic conductor (PMC) at the x -boundaries (which support the plane wave propagation). Silver-Müller absorbing (impedance) boundary conditions [10] have been taken at the z -boundaries.

Two probes separated by $L = 10$ m. along z have been taken to estimate the error in the propagation of the y -component of the electric field ($e_0(t), e_L(t)$). The RMS dissipation error per wavelength has been computed in the frequency domain ($E_0(f), E_L(f)$) by

$$\left| 1 - \left[\frac{|E_L(f)|}{|E_0(f)|} \right]^{\frac{\lambda}{L}} \right| \quad (4.20)$$

where we have taken into account the multiplicative effect along the propagation path in order to express it in terms of a per-wavelength error and compare to Eq. (4.13b). For the RMS dispersion error per wavelength, we have computed the numerical phase error with respect to the analytical phase $(-\frac{2\pi L}{\lambda})$ and normalized by the wavelengths traveled by the wave $(\frac{L}{\lambda})$ to compare with Eq. (4.13a). Fig. 4.5 shows this comparison for two different Δt . A good agreement is found for errors above 10^{-7} . Errors below this level happen at very low frequency and are due to truncation of the signals and the presence of spurious modes (a further study of these has been performed in [13]),

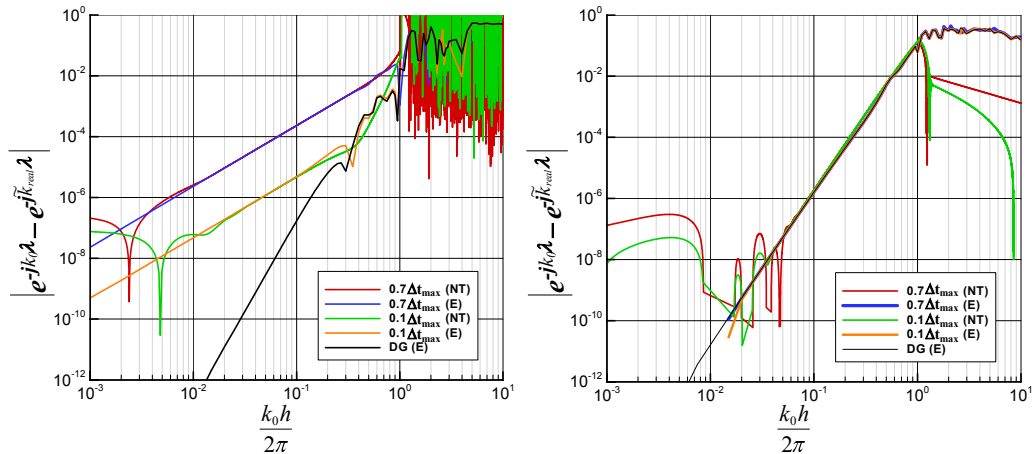


FIGURE 4.5: Convergence of the dispersion (up) and dissipation (down) errors of the LFDG algorithm computed with the numerical test (NT) and with the eigenvalue analysis (E). We have used in both cases $\tau = 0.1$, and $p = 2$. Analogous curves for the DG operator have been included for comparison.

4.5 Anisotropy analysis

In this section, we analyze the 3D anisotropic behavior of the errors for the semi-discrete DG operator and for the fully discrete LFDG algorithm in 3D (a 2D analysis for the wave propagation problem appears in [166]). In this case, we follow the same strategy used for the convergence analysis. Again, we take $\tau = 0.1$ and $\Delta t = 0.7\Delta t_{max}$ for LFDG. The anisotropic behavior of the error is analyzed by solving the eigenvalue problems for different \vec{k}_0 .

Figs. 4.6 and 4.7 show 2D plots of the anisotropic errors for different illumination angles (due to the symmetry of problems $\theta = [0^\circ, 90^\circ]$ and $\phi = [0^\circ, 90^\circ]$ include all the possible illuminations), and basis orders $p = 1, 2, 3$, respectively. 3D representations of the normalized real part of the numerical eigen-value $(e^{-j(\tilde{k}_{real}-k_0)\lambda})$ referred to as dispersion rate, and dissipation rates $(e^{\tilde{k}_{imag}\lambda})$ have been included to show the

shape of the anisotropy⁴. Fig. 4.8 also shows cuts along the θ angle of the dispersion error for $\phi = 45^\circ$, comparing the DG operator and the LFDG algorithm for different orders p .

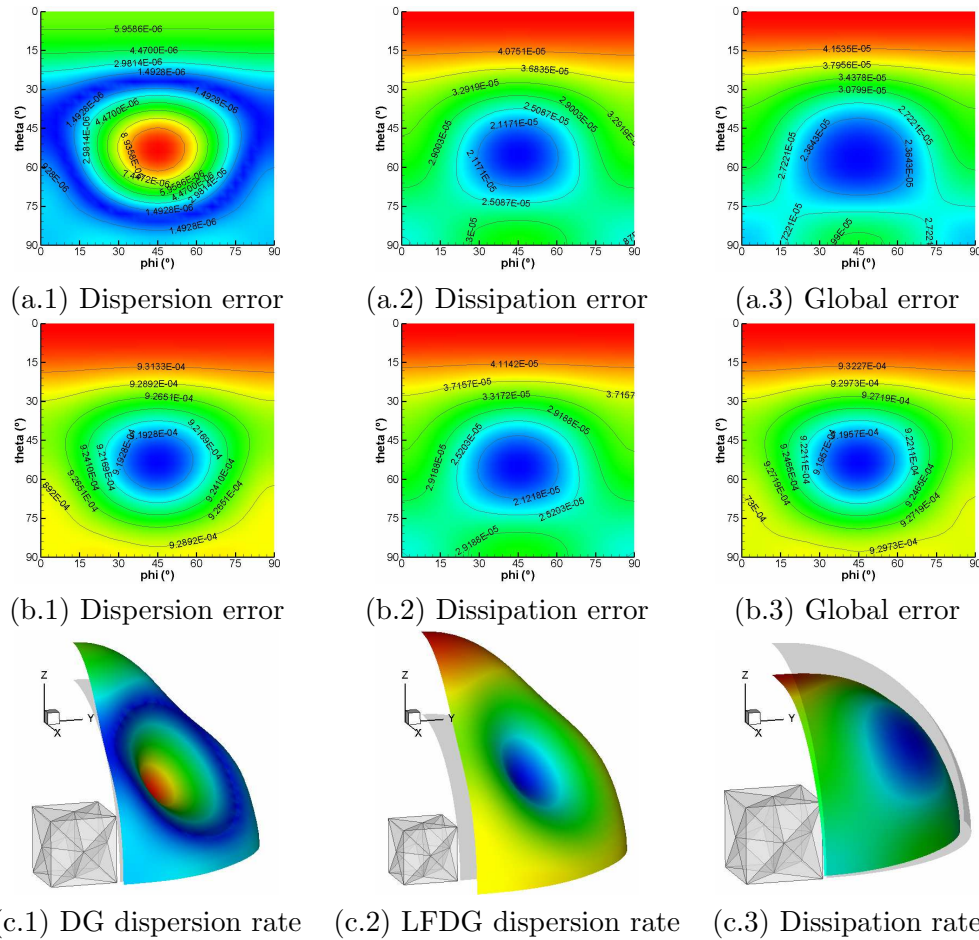


FIGURE 4.6: Anisotropy of the error for $\tau = 0.1$, $p = 2$ and $h = 0.2$. (a) DG semi-discrete scheme, (b) LFDG scheme with $\Delta t = 0.7\Delta t_{max}$ (c) 3D representation. The error has been amplified in order to represent the shape of the anisotropy. The analytical solution has been represented in grey (sphere of radio 1).

From this analysis, we can derive the following conclusions:

- The anisotropy of the error, both dispersive and dissipative, is given by the spatial discretization. The LF temporal integration only introduces an offset in the dispersion error in all directions, and no dissipation error (as expected).
- For conciseness, plots for different values of h and p have been omitted, but we have observed, in general, that the shape of the anisotropy of the error (both

⁴Notice that the rate magnitudes, represented in the 3D figures, gives different information than the 2D plots. The rates are accumulative factors per wavelength, having the dispersion rate information of the phase error sign, which changes if the numerical phase speed is larger or smaller than the analytical one.

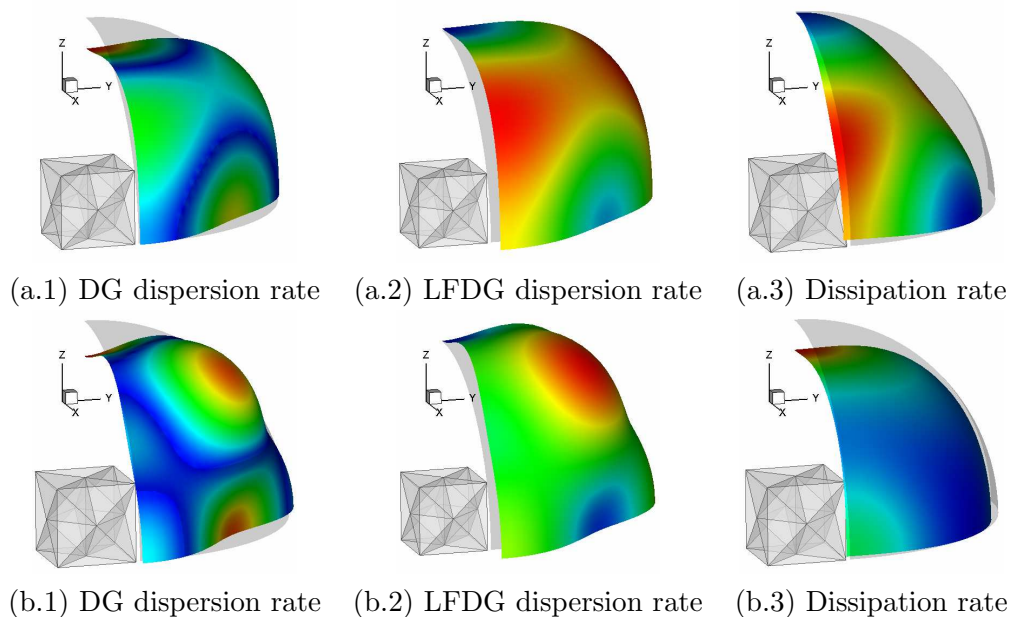


FIGURE 4.7: 3D representations of the anisotropy of the error for $\tau = 0.1$, $h = 0.25$, (a) $p = 1$ and (b) $p = 3$. The error has been amplified in order to represent the shape of the anisotropy. The analytical solution has been represented in grey (sphere of radius 1).

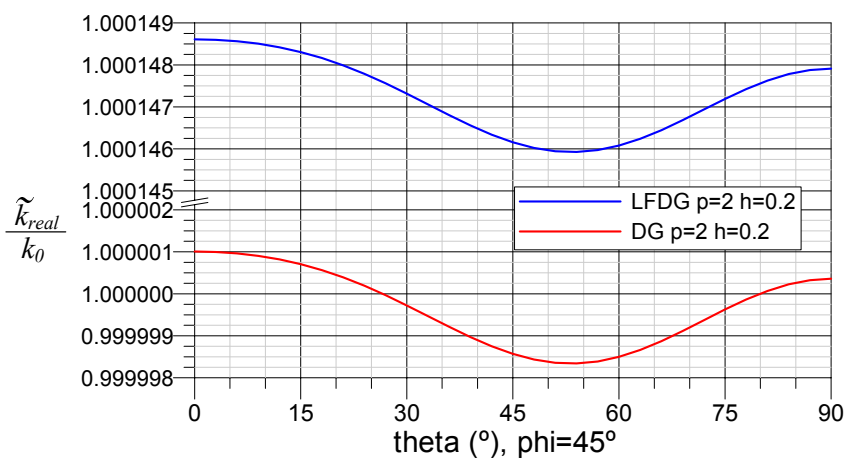


FIGURE 4.8: Cuts of the dispersion error comparing the DG operator and the LFDG algorithm for order $p = 2$ and $h = 0.2$. The Y axes have been broken in all cases, maintaining the same spacing, in order to show the offset in the dispersion error.

dispersive and dissipative) only depends on the order of the basis functions (p), while the h -parameter mainly affects to the error amplitude.

- For the semi-discrete DG operator the numerical phase speed is higher than 1.0 for some directions, and lower for some others. That implies that the semi-discrete DG operator has dispersion-free propagation directions.

4.6 Computational cost vs. accuracy

The differences in accuracy between LFDG and FDTD (apparently high from Fig. 4.3) should be analyzed with both methods under fair comparison conditions. In this section, we study the computational cost vs. accuracy in order to draw an effective application of the proposed scheme in real problems and explore the limitations and the efficiency of the method. The main trade-off involves the order of the basis functions p , the mesh resolution h , and accuracy, with the aim of minimizing the computational cost. We must take into account that:

- Increasing p improves accuracy but requires shorter Δt for stability, and the computational cost per element is higher.
- Decreasing h improves accuracy but requires shorter Δt for stability for smaller elements, and the number of elements increases.

To compare the different configurations of the method, a computational cost per λ^3 and picosecond (psec) has been defined. The computational cost for one element of a DG scheme is proportional to the square of the number of basis functions Q in that element

$$C_{element} \propto Q^2 \quad (4.21)$$

The cost for one time step per λ^3 , will be approximately the number of elements M per λ^3 multiplied by the cost per element,

$$\frac{C_{time\ step}}{\lambda^3} \approx \frac{M}{\lambda^3} C_{element} \quad (4.22)$$

Finally, we can define the following figure of merit (CC) to measure the global cost of the method, also including the effect of the Δt taken for stability

$$CC = K \frac{M}{\lambda^3} Q^2 \frac{1}{\Delta t(\text{in psec.})} \quad (4.23)$$

with K being a factor that has been considered equal to 1 for the FDTD case, and equal to 2 for the LFDG method (heuristically taken into account for the additional

LFDG terms). This simple estimation is based on the fact that FDTD can be seen as a kind of FVTD method, which in turn is equivalent to a $p = 0$ LFDG, where the elements are cubes instead of tetrahedrons [195] (we will not consider here specific architecture-based computer-optimized FDTD codes that might render $K < 1$).

The CC magnitude has been computed for the results of the convergence analysis of Fig. 4.3, and shown in Fig. 4.9, where CC is on the X-axis and accuracy is on the Y-axis on the upper side of the plot and the resolution of the mesh, h , on the lower side.

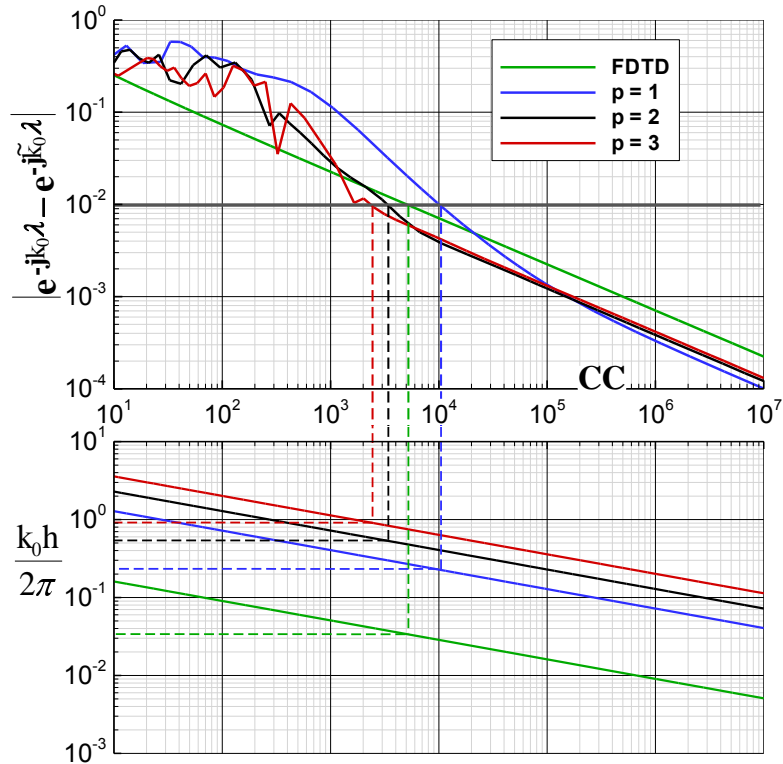


FIGURE 4.9: Computational cost of the LFDG algorithm for $\tau = 0.1$, $\Delta t = 0.7\Delta t_{max}$ and different order of the basis functions p . CC is on the X-axis and, accuracy is on the Y-axis, on the upper side of the plot, and the resolution of the mesh, h , on the lower side. A similar curve of the FDTD method has been included for comparison.

The numerical values of CC for the 10^{-2} accuracy case appear in Table 4.1. As expected, for higher orders p , the number of elements per wavelength ($\frac{\lambda}{h}$) to reach this accuracy can be decreased and larger Δt are allowable. Thus, the overall computational cost decreases with higher order p . However, if we require higher accuracies ($> 10^{-3}$), this is no longer true, as seen in Fig. 4.9, because the global error is dominated by the 2^{nd} -order temporal integration method, and the super-convergence behavior is lost. The same reasoning explains that the gain for using $p = 3$ instead

of $p = 2$ is not as high as the gain from $p = 1$ to $p = 2$. The convergence of the dispersion error for order $p = 4$ of the spatial discretization is 10, since the convergence of the simple LF is just 2, going to higher orders in the spatial discretization is not efficient. For all these reasons, we conclude that orders $p > 3$ are not efficient in practical problems in the LFDG algorithm. This is a major limitation of the method, which prevents us from taking full advantage of p refinement techniques. On the other hand, the method has a comparable computational cost to FDTD for practical applications (from the plane-wave analysis standpoint), but preserving most of the advantages of finite-element methods (e.g. the conformal meshing or h-refinement in regions with strong spatial variations of the fields, where time integration errors are negligible).

TABLE 4.1: Results of the computational cost analysis for an accuracy of 10^{-2} per wavelength.

	Q	$\frac{\lambda}{h}$	$\frac{M}{\lambda^3}$	$\frac{MQ^{(1)}}{\lambda^3}$	$c \Delta t 10^3$	CC	Gain ⁽²⁾
FDTD	3	28.5	23149	69447	14.1	4430	–
$p = 1$	12	4.5	2187	26244	17.6	9660	–
$p = 2$	30	1.9	165	4950	85.3	3270	2.95
$p = 3$	60	1.1	32	1920	97.1	2260	1.45

⁽¹⁾ MQ is the number of basis functions. The number of DoF will be $2MQ$
⁽²⁾ The gain has been defined as $\left(\frac{CC(p-1)}{CC(p)}\right)$

We can summarize the results given in Fig. 4.9 and Table 4.1 as:

- The computational cost of the LFDG method is of the same order of magnitude as the traditional FDTD method. Therefore, it is expected that LFDG has all the advantages of finite-element methods as a similar computational cost of the FDTD method.
- Due to the limitations of using a 2^{nd} -order accurate time integration scheme, it will not be worthwhile to use basis functions of order p higher than 3.
- LFDG method is an efficient algorithm for an accuracy of 10^{-2} to 10^{-3} global error per wavelength⁵. For higher accuracies, higher-order time integration methods are required to take greater advantage of the super-convergence property of the DG operator.

⁵In case of FDTD, for an accuracy of 10^{-2} we need a 30 samples per wavelength and 100 for 10^{-3} .

4.7 Conclusions

In this paper, we have used a semi-analytical eigenvalue analysis to study the convergence of the DG semi-discrete scheme and compared it with the fully discrete LFDG method.

We have shown that the semi-discrete DG method with penalized flux exhibits a super-convergence behavior, with a dissipative error increasing with the basis order p more rapidly than the dispersive one. When it is combined with a 2^{nd} order LF time integration scheme (LFDG), dispersion is added (not dissipation) and corruption of the super-convergence behavior occurs. The anisotropy of the semi-discrete DG and the LFDG scheme has also been analyzed. A numerical plane-wave propagation experiment has been employed to corroborate the results found with the eigenvalue approach and illustrate the appearance of other numerical artifacts.

The accuracy limits and computational cost of the LFDG method have been explored, providing efficient criteria to tune the simulation parameters. We have shown that, for the typical accuracies required in practical problems, the LFDG method is efficient for orders $p \leq 3$. Higher accuracies could be achieved for $p > 3$ if combined with higher-order time-integration methods. We have also seen that, even for simple plane-wave propagation, the computational costs of the LFDG method are in the same order of magnitude of the traditional FDTD method, with a similar accuracy. This makes of LFDG an especially attractive alternative to FDTD for realistic problems because of its superior accuracy when dealing with curved objects and the adaptability of the unstructured meshes.

Part III

On Time Integration techniques

Chapter 5

Causal-Path Local Time-Stepping in the Discontinuous Galerkin Method for Maxwell's equations

L. D. Angulo, J. Alvarez, F.L. Teixeira, M.F. Pantoja, and S.G. Garcia. Causal-path local time-stepping in the discontinuous galerkin method for maxwell's equations. *Journal of Computational Physics*, 256:678 – 695, 2014

Abstract

We introduce a novel local time-stepping technique for marching-in-time algorithms. The technique is denoted as Causal-Path Local Time-Stepping (CPLTS) and it is applied for two time integration techniques: fourth order low-storage explicit Runge-Kutta (LSERK4) and second order Leapfrog (LF2). The CPLTS method is applied to evolve Maxwell's curl equations using a Discontinuous Galerkin (DG) scheme for the spatial discretization. Numerical results for LF2 and LSERK4 are compared with analytical solutions and the Montseny's LF2 technique. The results show that the CPLTS technique improves the dispersive and dissipative properties of LF2-LTS scheme.

5.1 Introduction

Many time-stepping algorithms have been proposed in order to improve the performance of Discontinuous Galerkin (DG) based schemes by increasing the maximum time step while preserving stability. There are usually two kinds of strategies used for this purpose: to use implicit schemes [93, 120] or, to use an explicit local time-stepping (LTS) technique [13, 64, 67, 77, 93, 225–227]. An advantage of LTS schemes versus implicit strategies is that the former can be used recursively and easily parallelized. Moreover, highly disparate mesh element sizes can lead to ill-conditioning problems in implicit schemes which are obviated by explicit schemes. Additionally, time integration algorithms may have other constraints on the time-step arising from accuracy considerations and other inherent time scales such as in dispersive media [125] or when hybridized with network/lumped elements models [171], LTS techniques can also contribute to mitigate these problems in a simple and straightforward way.

When a second order convergent spatial discretization is used, the most commonly used time integration method is the second-order leapfrog (LF2) algorithm. Several authors [64, 67] use a LF2-LTS scheme proposed by Montseny [77] consisting of using the last known values of the fields on the larger time stepped region each time that the smaller one needs a field value. Piperno [93] adopts a similar approach based on a Verlet scheme. Alvarez [13, 17, 221] contributed with a novel approach to perform LTS in LF2 schemes whereby an interpolation between the fields is used in an interface between the larger and smaller time-stepped regions. A rigorous demonstration of the stability and dispersive properties of these schemes is still an open problem.

Diaz and Grote [225, 226] implemented a rigorous study on the stability and dispersion of LF-LTS high-order schemes applied to the second-order wave equation by means of an eigenvalue analysis. They found that the LTS introduces numerical dispersion and can produce instabilities if the global time step is not slightly reduced with respect to a classic implementation. The authors also found that the global stability could be improved by enlarging the smaller time-stepped region.

For higher order methods, explicit Runge-Kutta (RK) algorithms [10, 12, 27, 74, 113, 200] seem to be preferred with respect to LF schemes [107]. Despite of their popularity, there are less works in the literature related to RK-LTS than to LF-LTS. In [128] we find an RK-LTS scheme in which all elements are integrated with the least restrictive time step and then the interface with the region where the polluted solution has not been able to affect is used as a boundary condition for the regions

which require substepping. Specifically for Maxwell's equations, RK-LTS algorithms usually rely on interpolations at the interfaces using previously computed solutions [27] or arbitrary high-order derivatives (ADER) schemes [129, 227, 228].

In this paper we present a novel LTS technique that can be applied to a large variety of time integration algorithms. It does not need interpolation between computed solutions and nor directly uses any previously known values. Numerical results showing comparisons with analytical solutions for applications on a second-order Leap-Frog (LF2) and on a fourth-order Low Storage Explicit Runge-Kutta scheme (LSERK4) are shown to demonstrate the advantages of the proposed LTS technique.

5.2 Discontinuous Galerkin Semidiscretization

Maxwell's curl equations for source-less homogeneous media can be written as

$$\begin{aligned}\vec{\nabla} \times \vec{E} &= -\mu \partial_t \vec{H} \\ \vec{\nabla} \times \vec{H} &= \varepsilon \partial_t \vec{E}\end{aligned}\tag{5.1}$$

For simplicity, in our discussion we will assume that ε and μ do not vary in the computational domain, and use a system of units where $\varepsilon = \mu = 1$.

We tessellate the computational domain with $k = 1, \dots, K$ non-overlapping tetrahedrons. In each of those, we apply the Discontinuous Galerkin's formalism [10, 12, 27] to obtain

$$\begin{aligned}\mathcal{M}_k \partial_t \mathbf{E}_k(t) + \mathcal{S}_k \mathbf{H}_k(t) - \sum_f \mathcal{F}_{kf} \mathbf{H}_{kf}^*(t) &= 0 \\ \mathcal{M}_k \partial_t \mathbf{H}_k(t) + \mathcal{S}_k \mathbf{E}_k(t) - \sum_f \mathcal{F}_{kf} \mathbf{E}_{kf}^*(t) &= 0\end{aligned}\tag{5.2}$$

With \mathcal{M} being the mass matrix, \mathcal{S} the spatial semidiscretization of the curl operator and \mathcal{F}_f the lift operator for face f . \mathbf{E} and \mathbf{H} are column vectors containing all the degrees of freedom for the electric and magnetic field respectively. \mathbf{E}^* and \mathbf{H}^* are the numerical fluxes.

We define a state vector $\mathbf{q}_k = [\mathbf{E}_k \ \mathbf{H}_k]^T$ containing all the N_k degrees of freedom of element k . With this definition, we can rewrite system (5.2) as a single equation that governs the time evolution of the system,

$$\partial_t \mathbf{q}_k(t) = -(\mathcal{M}_k^q)^{-1} \left(\mathcal{S}_k^q \mathbf{q}_k(t) - \sum_f \mathcal{F}_{kf}^q (\bar{\mathcal{E}}_{kf} \mathbf{q}_k(t) - \bar{\mathcal{E}}_{kf+} \mathbf{q}_{kf+}(t)) \right)\tag{5.3}$$

The DG method gives us some freedom in the selection of the operators $\bar{\mathcal{E}}_{kf}$ and $\bar{\mathcal{E}}_{kf+}$ as long as it respects the properties of consistency, continuity, and monotonicity needed for the numerical flux [72]. If this operator is block diagonal with all its components being 1/2, we will say that the semi-discrete scheme is using a centered flux and therefore is numerically non-dissipative [13, 80]. On the other hand, if these operators are non-block diagonal we will say that the flux is being penalized and therefore the semi-discrete scheme is numerically dissipative. We will mostly focus on a particular case of penalized flux: the upwind flux [10, 14], coming from the solution of the Riemann problem.

When using penalized fluxes some dissipation is introduced and more operations are needed to compute the flux terms. However, introducing such penalization is known to improve numerical dispersion and suppress spurious modes [10, 13, 27, 62, 77]. Although the contribution to dissipation coming from penalized fluxes may be negligible at well-resolved frequencies, it may become important at higher frequencies for sufficiently long integration times; therefore, care should be exercised by the user depending on the application.

To simplify the discussion further we will change the basis of the vector space using an invertible operator \mathcal{P}_k on equation (5.3) that diagonalizes only the locally applied operators,

$$\mathcal{W}_k = -\mathcal{P}_k^{-1}(\mathcal{M}_k^q)^{-1}(\mathcal{S}_k^q - \sum_f \mathcal{F}_{kf}^q \bar{\mathcal{E}}_{kf})\mathcal{P}_k \quad (5.4)$$

We can also define the eigenmodes as

$$\mathbf{p}_k = \mathcal{P}_k^{-1} \mathbf{q}_k \quad (5.5)$$

and the external operators as

$$\mathcal{V}_{kf} = -\mathcal{P}_k^{-1}(\mathcal{M}_k^q)^{-1} \mathcal{F}_{kf}^q \bar{\mathcal{E}}_{kf+} \mathcal{P}_k \quad (5.6)$$

This change of basis let us write equation (5.3) in the following compact form

$$\partial_t \mathbf{p}_k(t) = \mathcal{W}_k \mathbf{p}_k(t) + \sum_f \mathcal{V}_{kf} \mathbf{p}_{kf+}(t) \quad (5.7)$$

5.3 Time integration

In the following discussion, we will focus on two time integration methods that are also the most popular choices in conjunction with DG semidiscretizations.

5.3.1 Second-order Leap-Frog (LF2)

The second-order leap-frog method [122] is applied by alternately evolving the \mathbf{E}^n and $\mathbf{H}^{n+1/2}$ fields, arbitrarily defined at times t_n and $t_n + \Delta t/2$ respectively. This implies that we do not have a fully defined state vector in the sense of eq. (5.3) for a given time t . To obtain the future values from a present state the following algorithm is applied

$$\begin{aligned}\mathbf{E}^{n+1} &= \mathbf{E}^n + \Delta t \mathcal{L}_h \left(\mathbf{H}^{n+1/2}, \mathbf{E}^n \right) \\ \mathbf{H}^{n+3/2} &= \mathbf{H}^{n+1/2} + \Delta t \mathcal{L}_h \left(\mathbf{E}^n, \mathbf{H}^{n+1/2} \right)\end{aligned}\quad (5.8)$$

With \mathcal{L}_h being a function representing the result of applying the spatial semi-discretization. When centered fluxes are used, the operator \mathcal{L}_h only uses $\mathbf{H}^{n+1/2}$ or \mathbf{E}^n as arguments. This implies that the scheme is reversible in time and will preserve energy as long as the time step used is below a maximum value Δt_k set by a CFL-like condition [93, 120, 122].

5.3.2 Low-Storage Explicit Runge–Kutta (LSERK4)

The second method that we will use in our discussion is the five-stage fourth-order Explicit Runge-Kutta method (LSERK4) [27, 113, 126]. This method states that for a given vector representing the state of the system, i.e. $\mathbf{p}_k(t) = \mathbf{p}_k^n$ we can find an approximate solution state $\mathbf{p}_k(t + \Delta t) = \mathbf{p}_k^{n+1}$ applying the following algorithm

$$\begin{aligned}\mathbf{p}_k^{(0)} &= \mathbf{p}_k^n, \\ \mathbf{r}^{(i)} &= a_i \mathbf{r}^{(i-1)} + \Delta t \left(\mathcal{W}_k \mathbf{p}_k^{(i-1)} + \sum_f \mathcal{V}_{kf} \mathbf{p}_{kf+}^{(i-1)} \right), \\ \mathbf{p}_k^{(i)} &= \mathbf{p}_k^{(i-1)} + b_i \mathbf{r}^{(i)}, \\ \mathbf{p}_k^{(n+1)} &= \mathbf{p}_k^{(5)}\end{aligned}\quad (5.9)$$

with $i \in [1, \dots, 5]$ and the coefficients a_i , b_i and c_i taking the values indicated in Table 5.1. The LSERK4 scheme is one of the most used methods in high-order Discontinuous Galerkin semi-discretizations, because it introduces low dispersion and dissipation. Contrary to other RK implementations, the low-storage version requires the storage of only two times the number of degrees of freedom in the scheme at the expense of one additional stage. RK methods are constrained by the spectra of the operator \mathcal{W}_k , i.e. all the eigenvalues of \mathcal{W}_k must lie inside of the stability region of the RK scheme. Consequently, the time step must be chosen

sufficiently small, e.g. for a nodal basis the following inequality must hold [27]

$$\Delta t_k \leq \frac{C}{c_k} \min_i \frac{\Delta r_{ki}}{2} \quad (5.10)$$

where $\min_i \Delta r_{ki}$ indicates the minimum distance between nodes in element k and c_k is the maximum speed of light in the element k .

Despite its many advantages, LSERK4 has a high computational cost and the numerical dissipation it introduces can be a factor depending on the application.

TABLE 5.1: Coefficients for the low-storage five-stages fourth-order Explicit Runge–Kutta method (LSERK4)

s	a_s	b_s	c_s
1	0	$\frac{1432997174477}{9575080441755}$	0
2	$-\frac{567301805773}{1357537059087}$	$\frac{5161836677717}{13612068292357}$	$\frac{13612068292357}{9575080441755}$
3	$-\frac{2404267990393}{2016746695238}$	$\frac{1720146321549}{2090206949498}$	$\frac{22526269341429}{6820363962896}$
4	$-\frac{3550918686646}{2091501179385}$	$\frac{3134564353537}{4481467310338}$	$\frac{2006345519317}{3224310063776}$
5	$-\frac{1275806237668}{842570457699}$	$\frac{2277821191437}{14882151754819}$	$\frac{28032321613138}{2924317926251}$

5.4 The Causal–Path LTS technique

In this section we introduce the Causal–Path technique as a novel way of performing LTS in different time integration techniques. We require two basic properties for the time integration technique:

1. It has to provide a fully defined state $\mathbf{q}_k(t)$ for each element.
2. The next state $\mathbf{q}_k(t + \Delta t)$ can be explicitly computed from a neighbourhood of elements.

As a first step we will organize the elements in different groups, called tiers, according to their time steps denoted as Δt^m . An element k will belong to a tier $m = [0, \dots, N_m - 1]$ if its maximum time step Δt_k is such that

$$\Delta t^m \leq \Delta t_k < \Delta t^{m+1} \quad (5.11)$$

In order to compute the next time step, we need to use the field values at local and neighbor elements, $\mathbf{p}_k^{(m,i-1)}$ and $\mathbf{p}_{kf_+}^{(m,i-1)}$. If there is no connection with other elements belonging to a lower tier, we can evolve all the elements in m using their Δt^m . However, in the border between a tier m and $m + 1$ we can not apply the direct algorithm because the value $\mathbf{p}_{k^m f_+}^{(m,i-1)} = \mathbf{p}_{k^{m+1}}^{(m,i-1)}$ has not been computed.

The strategy that we propose is to compute the values $\mathbf{p}_{k^{m+1}}^{(m,i-1)}$ using $\Delta t^{m-1} = h_{i-1} \Delta t^m$ as time step wherever they are necessary. If to do that, we need additional neighbour values that have not been computed, we recursively apply this idea until a known value is found. Thus, starting from $m = 0$ we can compute all the stages needed to evolve it before starting with the tier $m = 1$ and so on. Finally, the values $\mathbf{p}_{k^{m+1}}^{(m,i-1)}$ are casted aside and the upper tier uses the original values from the lower tier.

To compute the next time step values in each of the N_m tiers we may need to compute N_s stages in all the elements of tier m . We will also need to compute intermediate stages between the stages in the $m + 1$ tier. So, in order to avoid a possible interleaving with other higher tiers, we impose that the $(N_s - 1)$ -depth neighbourhood of a tier m is only composed of elements belonging to tier $m + 1$ or $m - 1$. This additional condition for the tier assortment is illustrated in Figure 5.1.

The implementation of this algorithm may seem difficult at a first glance; however, the recursive nature of the algorithm allows us to make use of recursive calls to the function used to evolve the system. Every time the function is called, we pass the information about the tier in which this is being computed and the time step that has to be applied. So starting from a call to evolve the N_m tier for a given time step Δt , the function will recursively call itself on each of the stages of the algorithm passing $N_m - 1$ and $h_i \Delta t$ as arguments and evolving its corresponding tier elements. This technique also requires that the degrees of freedom in the region being interfaced are saved in the higher tier. Note that no interpolation of field values is necessary and only past field values generated by the discretization itself are utilized. This is a desirable property because schemes that perform interpolation are not reversible in time and thus dissipative. However, the fact that we are casting away values used in the intermediate states of lower tiers makes our scheme also non-reversible. Although the idea of creating a discrete domain-of-dependence is not new, our technique differs from the one presented in [128] because we are not interpolating at the interface with a non polluted solution to obtain the values that would be needed by the lower tier. Rather than that, the lower tier evolves using the values obtained from applying the same integration technique with its maximum time step. In the next sections we

describe two examples of the CPLTS technique, applied to the LF2 and LSERK4 algorithms, together with illustrations to clarify the concepts.

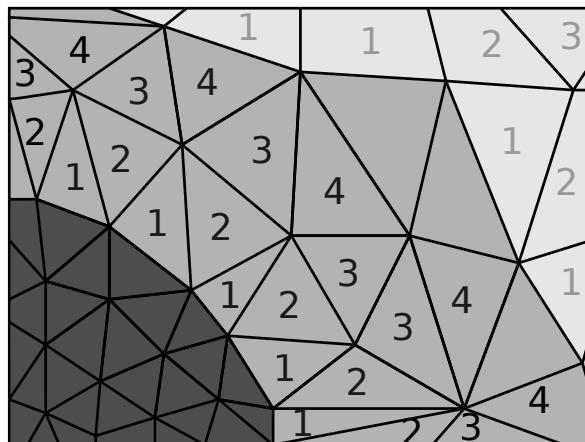


FIGURE 5.1: This figure illustrates the concept of 4–depth neighbourhood of two different regions. The darker colors indicate elements belonging to a lower temporal tier and thus having a smaller time step.

5.4.1 LF2-CPLTS

Since the LF2 performs iterations using a single stage we can create any distribution of N_s intermediate stages in the higher tiers to fit the evaluations needed by the smaller tiers. The time–steps of the intermediate stages would then be $h_i \Delta t^{m+1, i} = \Delta t^m$, with $h_i > 0$ and the restriction $\sum_i^{N_s} h_i = 1$. The choice of $h_i = 1/N_s$ would be the most favourable in terms of computational cost. Figure 5.2 and Algorithm 1 show an schematic view of this scheme applied to the case $h_1 = h_2 = 1/2$. Note that this freedom in choosing h_i is an improvement compared with the Montseny’s scheme [77], which is constrained due to the field interleaving of the LF2 scheme by the condition $\Delta t^m = \Delta t^{m-1}(1 + 2k)$, where k is a positive integer number. This is also an improvement with respect to the Verlet–Piperno’s scheme [93] in which $\Delta t^{m+1} = 2\Delta t^m$, and it allows our scheme to adapt to the different transitions as necessary; however, for the sake of simplicity we will not consider these cases here.

On the other hand, we need both values of \mathbf{E} and \mathbf{H} at same time instants in order to find a fully–defined state of the system at any given stage $\mathbf{p}^{(m, i)}$. In other words, we can not apply this LTS technique computing only $\mathbf{E}(t_n)$ and $\mathbf{H}(t_n + \Delta t/2)$ because to compute the intermediate value of a lower tier, let us say $\mathbf{E}^{m-1}(t_n + \Delta t^m/2)$ we would need the values of the magnetic field $\mathbf{H}^m(t_n)$. To overcome this issue we need to apply LF2 twice, doubling the computational costs with respect to the conventional approach.

When we apply this scheme to a non-dissipative semi-discretization (e.g. DG with centered flux) we find that the scheme is unstable showing growing high-frequency numerical modes. The introduction of a penalized flux solves this problem through higher frequency damping [74, 80].

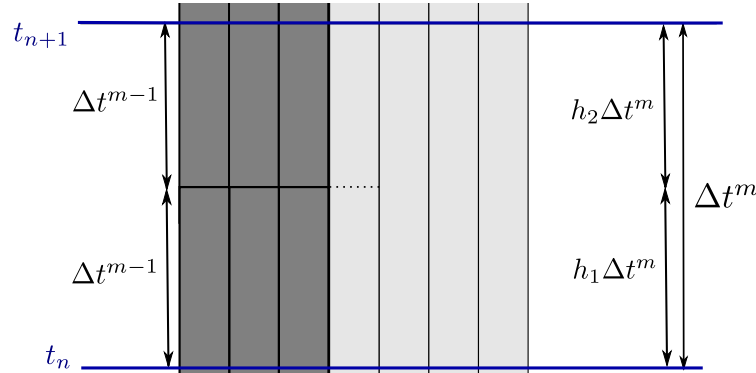


FIGURE 5.2: Schematic view of the LF2-CPLTS algorithm for the case $h_1 = h_2 = 1/2$. Vertical lines indicate boundaries between elements. At t_n all the field values are known. With a maximum time step Δt^{m-1} , the darker region needs to apply twice the time integration algorithm to reach t_{n+1} . The LF2-CPLTS approach applies the first integration also in the elements of the neighbourhood of the darker region (marked with a dashed line). With those values at $t_n + \Delta t^{m-1}$ we can apply the algorithm again to reach t_{n+1} . The lighter region t_{n+1} values are obtained using the original values in t_n with a Δt^m time integration.

Algorithm 1: LF2-CPLTS algorithm with two stages and $h_1 = h_2 = 1/2$. To evolve from $\mathbf{q}(t_n)$ to $\mathbf{q}(t_{n+1})$ this algorithm is called twice using (t_n) , $(\Delta t^{N_m-1}/2)$ and $(N_m - 1)$ as input arguments. The superscript RHS refers to Right Hand Side.

Data: Inputs: $t, \Delta t, m$

Result: $\mathbf{q}_k(t)$ is evolved to $\mathbf{q}_k(t + \Delta t)$

if $m = N_m - 1$ **then**

 | k are all the elements in tier m .

else

 | k are all the elements in tier m and its 1-neighbourhood.

end

$\mathbf{q}_k^{\text{RHS}} \leftarrow \mathcal{L}_h(\mathbf{q}_k)$

if $m > 0$ **then**

 | k^* are the elements in the 1-neighbourhood of $m - 1$.

$\mathbf{q}_{k^*}^{\text{Saved}} \leftarrow \mathbf{q}_{k^*}$

 Calls this algorithm with $(t + c_s \Delta t)$, $(h_s \Delta t)$ and $(m - 1)$ as inputs.

$\mathbf{q}_{k^*} \leftarrow \mathbf{q}_{k^*}^{\text{Saved}}$

end

$\mathbf{q}_k \leftarrow \mathbf{q}_k + \mathbf{q}_k^{\text{RHS}} \Delta t$

5.4.2 LSERK4-CPLTS

When the CPLTS technique is applied to an LSERK4 (Algorithm 2) we note that the stages are not evenly distributed in time. As a result, we apply a variable time

step in the lower tiers (Figure 5.3). The values for Δt^m and Δt^{m-1} are chosen such that equation (5.10) is always enforced and therefore

$$\max_i(h_i)\Delta t^m = \Delta t^{m-1} \quad (5.12)$$

with $\max_i(h_i)$ being the maximum stage size (for LSERK4 $\max_i(h_i) = h_4 = c_5 - c_4 = 0.336026 \simeq 1/3$). Whenever we compute intermediate stages in higher tiers we satisfy this condition because in higher tiers this condition is less restrictive. However, every time we apply this division, N_s times more computational operations are needed to get a speed-up of about three times in the higher tier region. So, if the largest tier region is not at least $5/3$ times larger than the smallest we would not see any appreciable global speed-up.

For this reason it seems preferable to organize the time tiers with $\Delta t^{m-1} = \Delta t^m / N_s$ rather than with the maximum stage size criteria. By doing this, we are computing an stage in the lower tier region with a time-step bigger than is strictly allowed based on a conventional CFL-like criterion for the associated direct algorithm, which could be a source of potential instability. On the other hand, the smaller stages in the lower tier compute the solution using a time-step smaller than the maximum allowed and thus introducing an additional numerical dissipation. We may then wonder if the additional dissipation introduced by the smaller stages offsets the potential for instability introduced by the larger. Note that as long as these effects are mostly kept limited to high frequency components (which are under-resolved anyway) the solution accuracy should not be impacted. In the next sections we perform some tests to assess the practical validity of this approach.

5.5 Numerical Results

In this section we present comparisons between results using the proposed CPLTS technique, the LF2-LTS technique introduced by Montseny [77], classical implementations of the algorithms, and analytical solutions.

For all cases we use nodal basis of order $P = 2$ and numerical upwind fluxes as described in [10, 12, 27, 87]. This implies that we are using 60 degrees of freedom per element. The implementation has been performed with an in-house C++ code¹ with OpenMP parallelization². GiD was used to obtain meshes and for pre and

¹Compiled with GNU C++ v4.6.3 using -O3 -ffast-math flags

²For more information visit: <http://www.ugrfdtd.es>

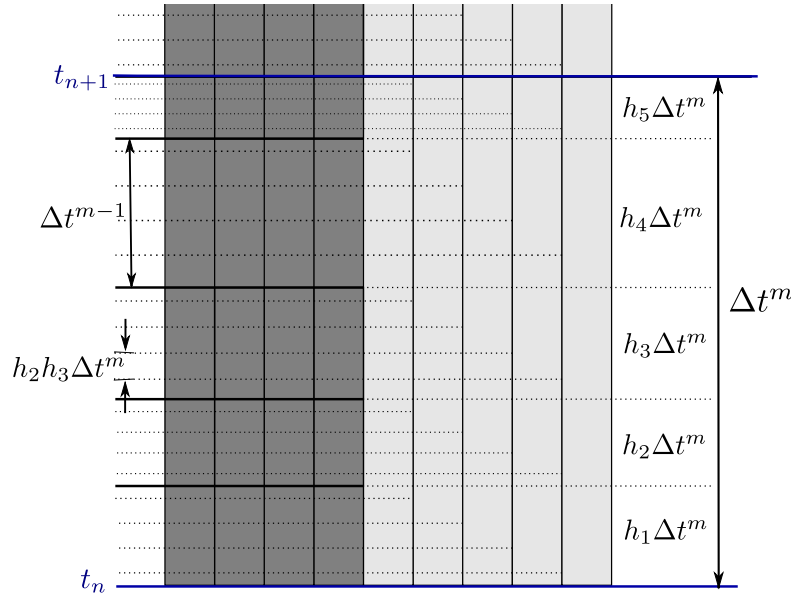


FIGURE 5.3: LSERK4-CPLTS sketch. Additional operations are made only in the 4-depth neighbourhood of the smaller tier region (darker). In this sketch the darker region has a maximum time step $\Delta t^{m-1} = h_4 \Delta t^m$ corresponding to the largest stage of the LSERK4 scheme. As with the LF2-CPLTS case, the darker region is evolved first to reach $t_n + h_1 \Delta t^m$. To do so, the field values marked with a dashed line will be needed for the different stages of the LSERK4 algorithm applied for a time step $h_1 \Delta t^m$. Once the darker region has evolved to $t_n + \Delta t^m$, the lighter one computes its first stage from the original values in t_n . The process continues in a similar fashion until all the stages of the lighter region are computed and both regions are in the state t_{n+1} . Note that the darker region never uses a time step bigger than its maximum, Δt^{m-1}

post-processing³. Simulations for the reflection and resonance problems were performed using a single processor laptop with Intel(R) Core(TM)2 Duo CPU T9400 @ 2.53GHz processor and running Ubuntu 12.04 LTS. The RCS problem were run in a desktop computer with an Intel(R) Core(TM) i7-3960X CPU @ 3.30GHz processor with 12 cores and Ubuntu 10.04 LTS.

5.5.1 Reflection caused by a non-homogeneous mesh

The first example we present is an study of the numerical reflection caused by differences in the mesh size, a similar type of analysis can be found in [59, 229]. This type of analysis is important for LTS because it quantifies a source of additive noise on the results. Figure 5.4 shows the meshes used, together with an isometric view of the boundary conditions employed. A plane wave excitation with z -polarization is introduced in one of the ends of the computational domain and the other end is backed by an Silver-Mueller absorbing (SMA) boundary condition. The side-walls of the domain are Perfect Electric Conducting (PEC) and Perfect Magnetic

³For more information visit: <http://www.gidhome.com>

Algorithm 2: LSERK4-CPLTS algorithm. To evolve from $\mathbf{q}(t_n)$ to $\mathbf{q}(t_{n+1})$ this algorithm is called using (t_n) , (Δt^{N_m-1}) and $(N_m - 1)$ as input arguments. The superscripts RHS and Res refer to Right Hand Side and Residue respectively. For the LSERK4, we have that $N_s = 5$, and the constants a_s , b_s and c_s are those shown in table 5.1.

Data: Inputs: t , Δt , m

Result: $\mathbf{q}_k(t)$ is evolved to $\mathbf{q}_k(t + \Delta t)$

$s \leftarrow 2$

while $s \leq N_s$ **do**

if $m = N_m - 1$ **then**

k are all the elements in tier m .

else

k are all the elements in tier m and its $N_s - s$ neighbourhood.

end

$\mathbf{q}_k^{\text{RHS}} \leftarrow \mathcal{L}_h(\mathbf{q}_k)$

if $m > 0$ **then**

k^* are the elements in the 4-neighbourhood of $m - 1$.

$\mathbf{q}_{k^*}^{\text{Saved}} \leftarrow \mathbf{q}_{k^*}$

 Calls this algorithm with $(t + c_s \Delta t)$, $(h_s \Delta t)$ and $(m - 1)$ as inputs.

$\mathbf{q}_{k^*} \leftarrow \mathbf{q}_{k^*}^{\text{Saved}}$

end

$\mathbf{q}_k^{\text{Res}} \leftarrow a_s \mathbf{q}_k^{\text{Res}} + \mathbf{q}_k^{\text{RHS}} \Delta t$

$\mathbf{q}_k \leftarrow \mathbf{q}_k + b_s \mathbf{q}_k^{\text{Res}}$

$s \leftarrow s + 1$

end

Conducting (PMC) boundary conditions at the xy and xz planes respectively. The mesh is 1 m long from one end to the other. The coarse cell size is 7.5 cm and the cell sizes in the finer region vary from 0.1 to 0.5 cm.

Figures 5.5, 5.6 and 5.7 show the reflection coefficient in a range of frequencies. The closer the values are to zero the better are the properties of the scheme. When LF2 integration techniques are used, we observe two asymptotic regions, the steeper region corresponds to the range of frequency where the spatial error is dominating over the error coming from the order of the time integration. That is why no differences are observed between the different techniques used. At lower frequencies the time integration error dominates and different behaviours arise depending on the technique. We observe that for this case the LF2 with a fully defined state (LF2full) exhibits slightly better properties than the classic LF2 scheme. A possible explanation for this is that the incident wave is resolved using more time steps. In LF2-LTS and LF2-CPLTS, we observe some additional degradation when compared to the classic LF2 schemes. The CPLTS exhibits less reflection than the Montseny's LTS, the difference growing with the ratio between the coarser and finer mesh. With LSERK4 we observe that the spatial error dominates for the range of frequencies

studied and the differences observed at lower frequencies can be attributed to errors coming from illumination or poor absorption properties of the SMA boundary. The three LSERK4 figures exhibit a better behaviour than the LF2, as expected due to the higher order of the time integration technique, and for the cases studied, the different LSERK4 CPLTS implementations do not show a time integration error dominating over the spatial. When the maximum stage is used for the tier assortment, we observe a higher degradation in the low-frequency regime, probably because more time-stepping operations are being performed. The results for the LSERK4-CPLTS are very encouraging as we see little differences between the use the LSERK4-CPLTS technique and the classic LSERK4. Table 5.2 shows data corresponding to the tier assortment and computational times. As expected, the LF2-CPLTS is able of create more tiers than LF2-LTS because it only needs a ratio of two between maximum time step sizes. The CPU times for this simulation are listed for reference only and are not quite representative because the time employed to compute the excitation at the boundaries and the initialization is significant when compared with the operations performed to evolve the elements.

TABLE 5.2: Element Tier assorting for LTS in the plane wave reflection.

	Integrator	Tier	Number of Elements							Δt^m [ps]	CPU [s]
			0	1	2	3	4	5	6		
PW-Ref-r15-SInt	LSERK4-CPLTS		120	312	-	-	-	-	-	0.624	226
	LSERK4-CPLTS-mS		120	24	288	-	-	-	-	0.624	485
	LSERK4		432	-	-	-	-	-	-	0.624	468
	LF2-LTS		120	8	304	-	-	-	-	0.281	78
	LF2		432	-	-	-	-	-	-	0.281	211
	LF2full-CPLTS		80	48	12	292	-	-	-	0.281	173
	LF2full		432	-	-	-	-	-	-	0.281	1799
PW-Ref-r75-SInt	LSERK4-LTS		600	24	288	-	-	-	-	0.12	3148
	LSERK4-CPLTS-mS		600	24	24	264	-	-	-	0.12	15097
	LSERK4		912	-	-	-	-	-	-	0.12	4700
	LF2-LTS		600	8	12	292	-	-	-	0.06	1444
	LF2		912	-	-	-	-	-	-	0.06	2296
	LF2full-CPLTS		400	208	12	8	12	184	88	0.06	3524
	LF2full		912	-	-	-	-	-	-	0.06	7211
PW-Ref-r7.5-Slab	LSERK4-CPLTS		240	288	-	-	-	-	-	1.24	190
	LSERK4-CPLTS-mS		240	288	-	-	-	-	-	1.24	342
	LSERK4		528	-	-	-	-	-	-	1.24	325
	LF2-LTS		240	288	-	-	-	-	-	0.55	158
	LF2		528	-	-	-	-	-	-	0.55	151
	LF2full-CPLTS		160	96	272	-	-	-	-	0.55	157
	LF2full		528	-	-	-	-	-	-	0.55	254

5.5.2 PEC cavity resonances

As a second example we show comparisons of evolving a spatially uncorrelated random field (white noise) to study the resonances of a 1 m PEC cavity, in a similar

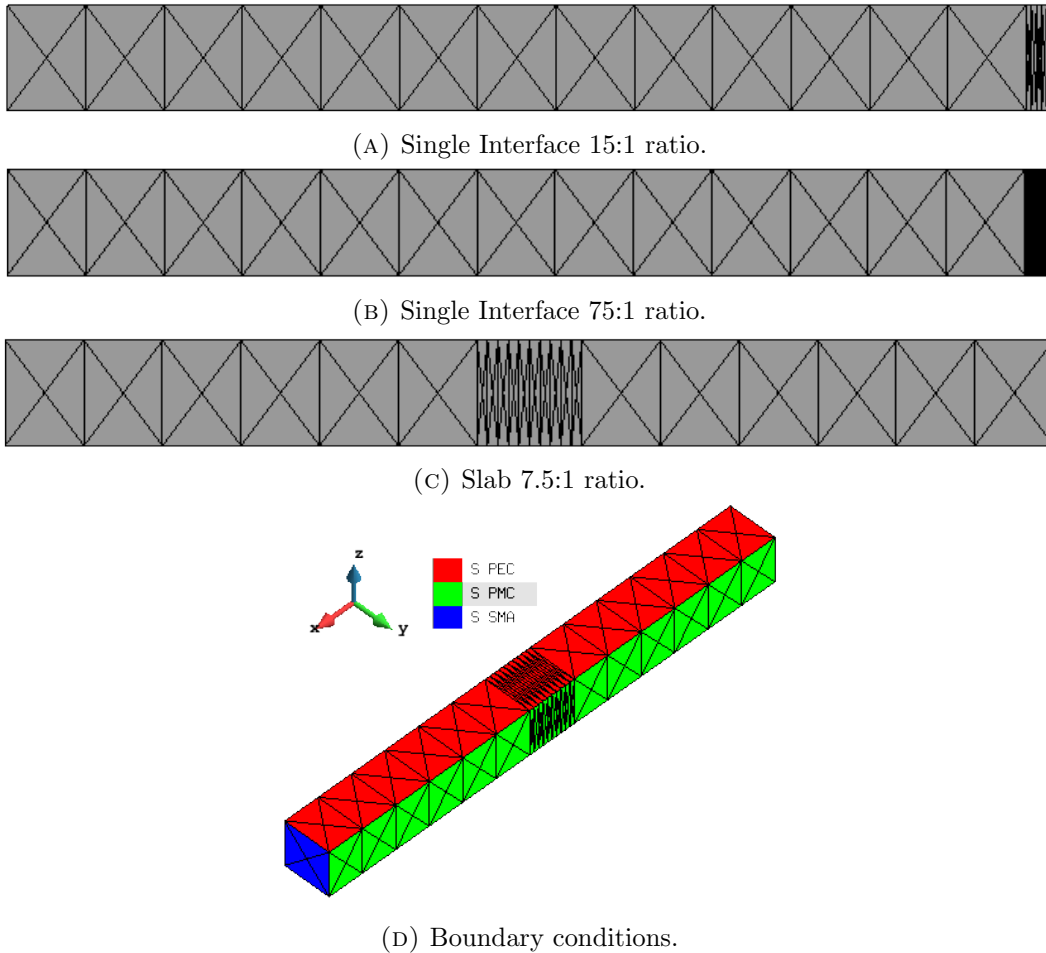
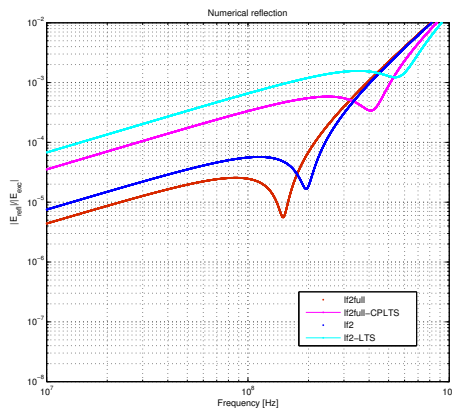
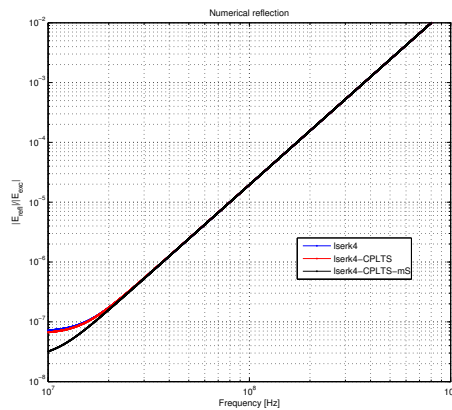


FIGURE 5.4: Meshes used for the study numerical reflections by an inhomogeneous mesh.

way as done in [34]. The mesh used is depicted in Figure 5.4c with PEC boundaries at the ends rather than SMA. The resonance frequencies are obtained by performing the Fourier transform of the electric field evolution after 250 ns at a point separated 0.3m from one of the boundaries. Figure 5.8 show the eigenfrequencies obtained by the simulations together with the exact ones (black dashed vertical lines). The LF2 schemes do not show any particular difference with respect to their dispersive properties. The differences in amplitude between LF2 and LF2full can be attributed to the different initial treatment of fields. The LSERK4 schemes exhibit a similar behaviour in frequency but we observe additional attenuation when the CPLTS is used. When the tiers are assorted using the maximum stage criteria the attenuation is reduced. No late time stabilities were observed in any of the simulations. Figure 5.9 shows the discrete energy computed for both schemes. As we see, all the schemes present some dissipation coming from the upwinding. When the LSERK4-CPLTS technique is used we observe more dissipation if we do not use the max stage criteria for tier assortment. Figure 5.10 shows the error evolution at for an initial condition

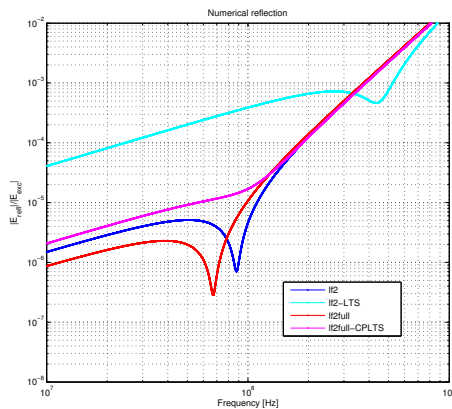


(A) LF2

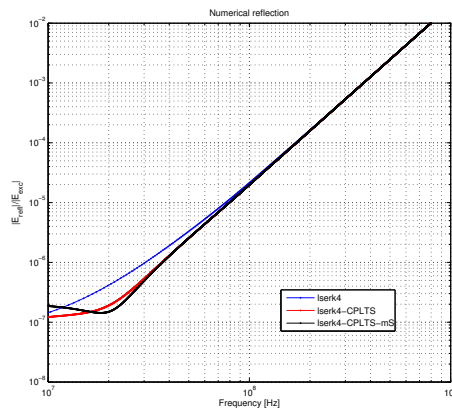


(B) LSERK4

FIGURE 5.5: Numerical reflection from a single interface with ratio of 15:1

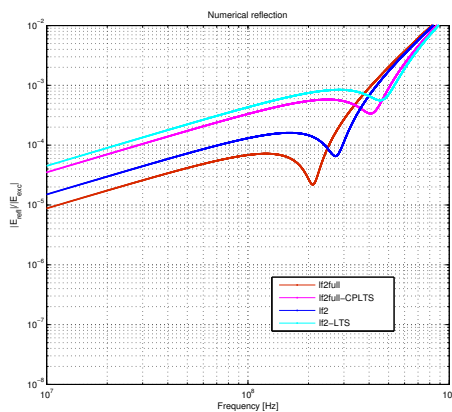


(A) LF2

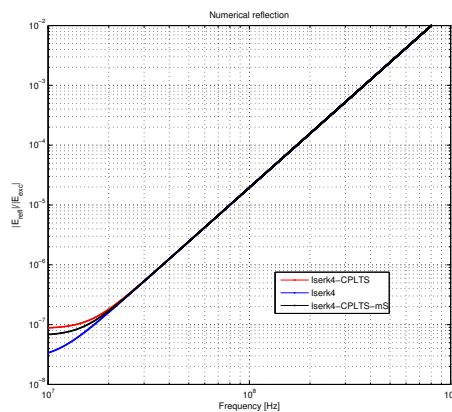


(B) LSERK4

FIGURE 5.6: Numerical reflection from a single interface with ratio of 75:1

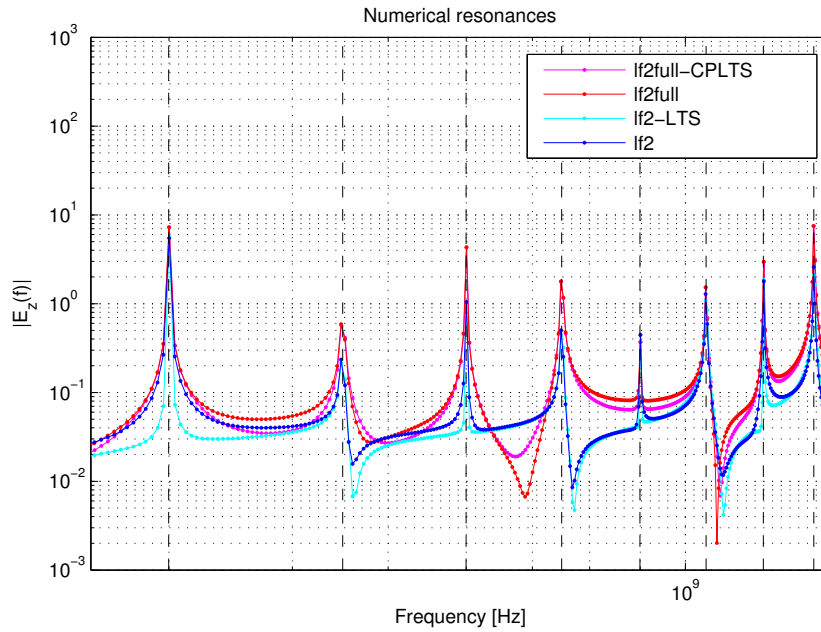


(A) LF2

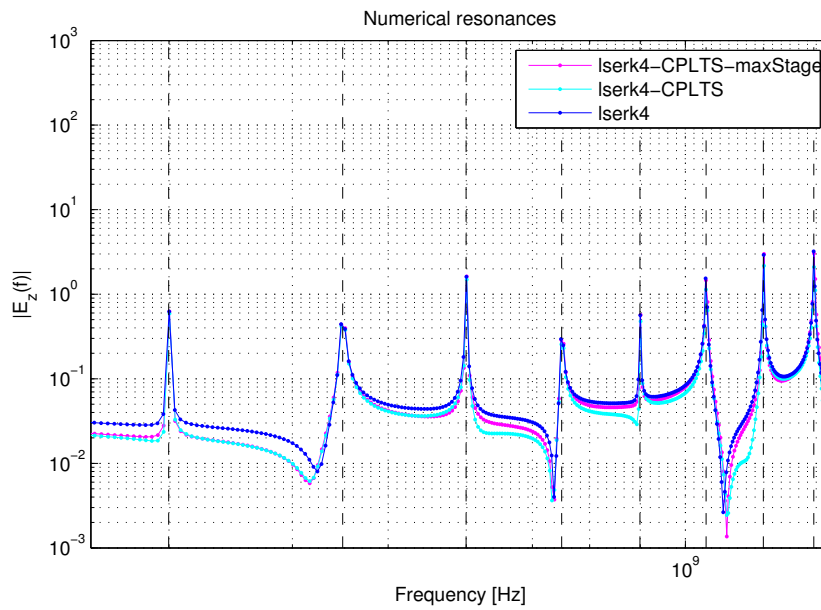


(B) LSERK4

FIGURE 5.7: Numerical reflection from a slab with ratio of 7.5:1.



(A) LF2



(B) LSERK4

FIGURE 5.8: Resonances in a 1 m PEC cavity with slab meshing. Vertical dashed lines represent exact eigenfrequencies.

of three harmonics. In all cases we observe that the CPLTS introduces additional error when compared with the non LTS approaches. Table 5.3 shows data corresponding to the tier assortment and computational times. The CPU times show a clear improvement with the LSERK4-CPLTS algorithm while the gains for the LF2-LTS are more moderate. LF2-CPLTS does not perform better than the LF2.

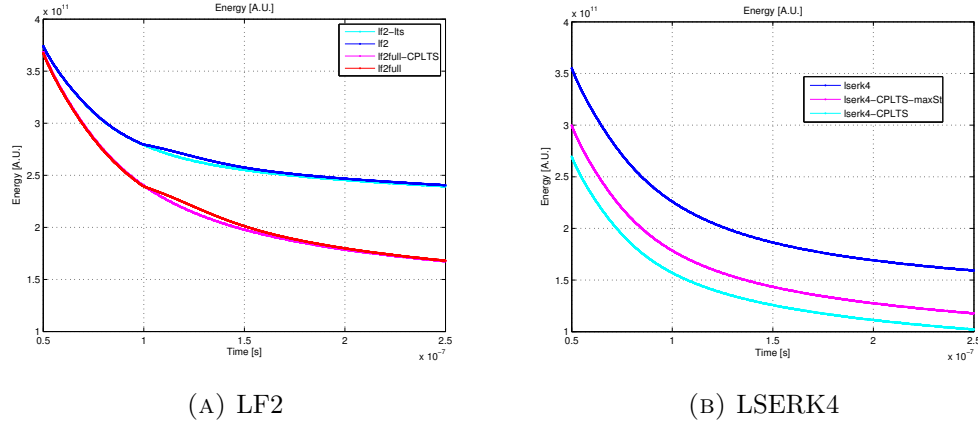


FIGURE 5.9: Energy evolution in a 1 m PEC cavity with slab meshing.

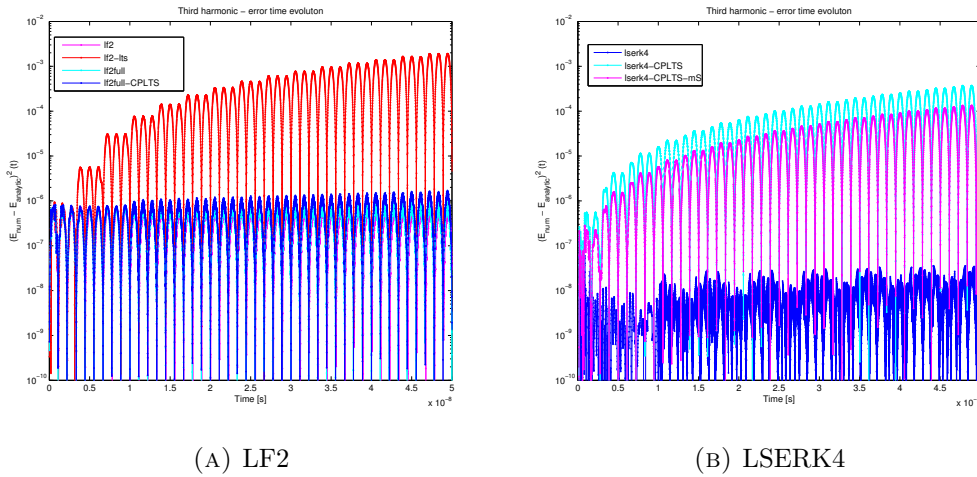


FIGURE 5.10: Evolution of the $(E_{\text{analytical}} - E_{\text{numerical}})^2$ error at the center of the 1 m PEC cavity with slab meshing for a three harmonics initial condition.

5.5.3 RCS Analysis of a PEC Sphere

As a last test case we present a bi-static Radar Cross Section (RCS) analysis [10]. Figure 5.11 show the boundary conditions used. Symmetry conditions were used to reduce the computational domain and the 1 m radius sphere was modelled using a PEC boundary condition. SMA boundary conditions were used to terminate the domain 3 m away from the surface of the sphere. The illumination was done using a Total Field/Scattered Field boundary condition in a spherical surface located 1 m away from the sphere using a Gaussian wave with 1 ns spread, y -polarization and propagating along the x axis. The typical element size of the mesh was 25 cm everywhere except in the PEC spherical surface modelling the sphere in which was set to 5 cm.

Figure 5.12 shows the results of the analysis for the various LF2 and LSERK4

TABLE 5.3: Element Tier assorting for LTS in the resonant cavity and RCS problems.

	Integrator	Number of Elements					Δt^m [ps]	CPU [s]	
		Tier	0	1	2	3			4
reson-r7-5-Slab	LSERK4-CPLTS		240	288	-	-	-	1.24	2403
	LSERK4-CPLTS-mS		240	288	-	-	-	1.24	4051
	LSERK4		528	-	-	-	-	1.24	4013
	LF2-LTS		240	288	-	-	-	0.55	1207
	LF2		528	-	-	-	-	0.55	1917
	LF2full-CPLTS		160	96	272	-	-	0.55	2381
	LF2full		528	-	-	-	-	0.55	3615
rCS-1m	LSERK4-CPLTS		4535	57279	157	-	-	2.1	3733
	LSERK4		61971	-	-	-	-	2.1	8613
	LF2-LTS		522	8614	52798	37	-	0.95	963
	LF2		61971	-	-	-	-	0.95	4348
	LF2full-CPLTS		114	2155	7411	34521	17770	0.95	1851
	LF2full		61971	-	-	-	-	0.95	8642

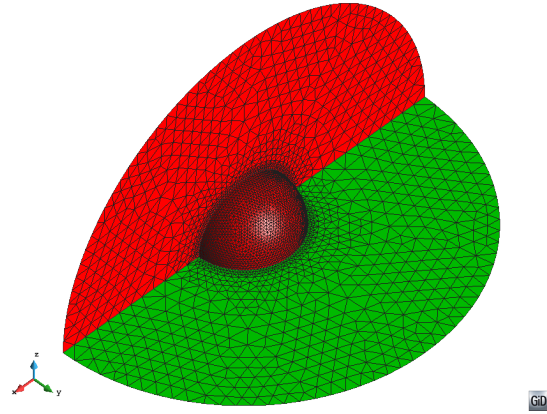
schemes under study. At 450 MHz we see that the LF2 methods fit the Mie’s analytical solution but the LF2 using Montseny’s approach exhibits an angular offset caused by an appreciable difference in the dispersion relation. At 600MHz all methods present a higher deviation, caused by a poorer resolution of the spatial grid.

The LSERK4 results exhibit a better behaviour than the LF2, capturing the main features of the analytical solution. The application of CPLTS seems to better preserve the dispersion relation and thus the position of the peaks. However, at 600 MHz we can observe an appreciable numerical dissipation being introduced.

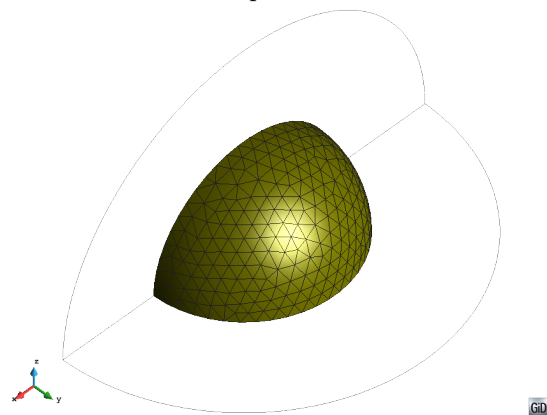
Table 5.3 shows data corresponding to the tier assortment and computational times. In this case, the LSERK4-CPLTS is able to provide a considerable speed up, reducing the CPU time from 8613 to 3733 s (~ 2). The LF2 LTS techniques yield a speed-up of about four times the non-LTS counterparts. The CPLTS speeds up the classic LF2 by a factor about two.

5.6 Tier assortment

In practice, an automated meshing process may produce a quite random tier assortment having an important impact in performance and accuracy. This occurs because we let the LTS algorithm and the tier-assortment to span the entire mesh. Notice that in practice this may not be necessary an optimal approach. Figures 5.13, 5.15, 5.16, 5.17, 5.18 and 5.19 illustrate this phenomenon. For the 1 m PEC sphere (Fig. 5.13, 5.15, 5.16), after imposing a constraint in the element size of 5 cm and leaving the rest with 25 cm we observe that there is an appreciable amount of



(A) PEC (red) and PMC (green). SMA is not depicted.

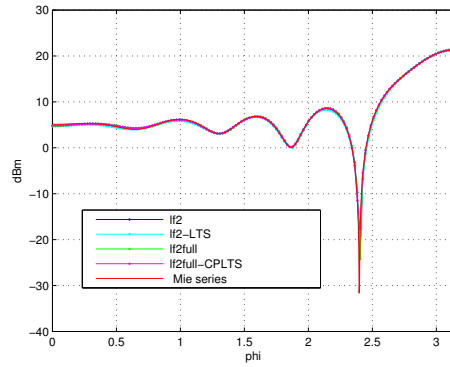


(B) Total Field region

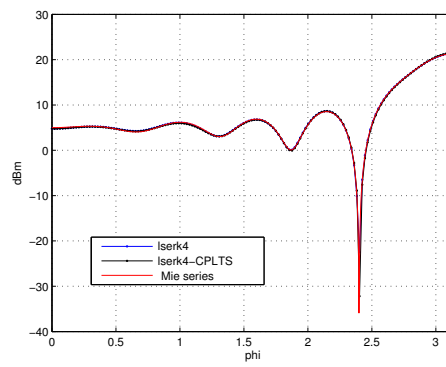
FIGURE 5.11: Boundary conditions for the RCS case.

scattered elements in the mesh belonging to a lower tier. The meshing algorithm is able to respect the sizes imposed to the elements in the regions closer to the surfaces but not in the inner part. Figures 5.17, 5.18 and 5.19 represent a variation of the 1m PEC sphere case in which a small cylinder representing a small scale feature has been appended to the sphere. In this example we observe that the presence of scattered lower tiers happens also in problems exhibiting disparate scales, unless the user pre-sets a given maximum number of tiers.

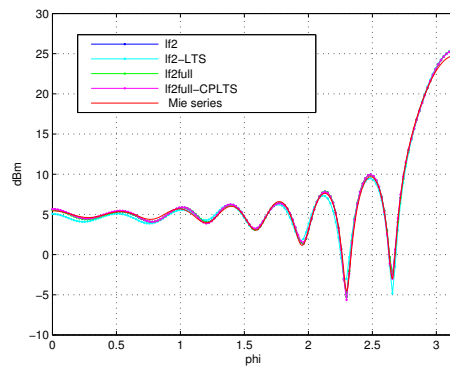
For the LSERK4 algorithm, scattered lower tiers degrade performance because, as depicted in Figure 5.14, many elements in the neighbourhood of lower tiers have to perform additional operations. Additionally, the CPLTS technique requires the storage of the elements in the neighbourhood of smaller tiers, increasing the memory consumption. Often the meshing and tier assorting processes result in the highest tier having a very small amount of elements (see Table 5.3), so it is up to the user whether to preserve those tiers or not. In the LF2-CPLTS case, we observe in Figures 5.15 and 5.18 that the assorting is able to create more tiers than in the LF2-LTS



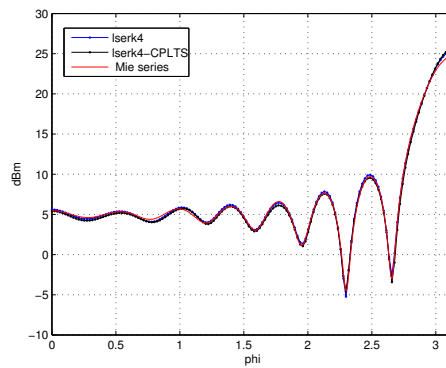
(A) LF2



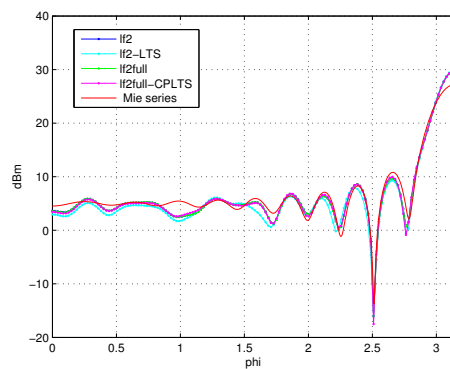
(B) LSERK4



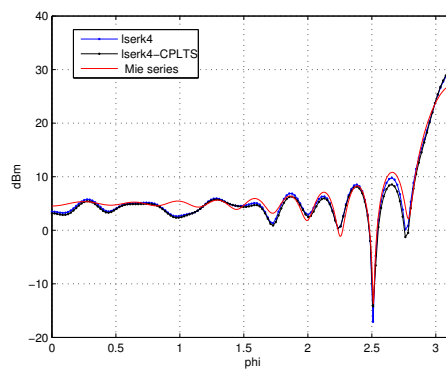
(C) LF2



(D) LSERK4



(E) LF2



(F) LSERK4

FIGURE 5.12: Bi-static RCS at 300 MHz (top row), 450 MHz (middle row) and 600 MHz (bottom row). Continuous red line represents the analytical solution obtained through Mie's series.

case. This has a positive impact in performance, which is specially relevant in cases with disparate spatial scales such as the presented in Figure 5.18.

5.7 Conclusions

In this work, we have introduced the Causal-Path concept as a way to perform LTS on explicit marching-in-time algorithms. We have applied this concept to the DG discretization under two different time integration techniques: LSERK4 and LF2.

When applied to LSERK4, the CPLTS implementation in which the tier assortment is done using the number of stages criterium has improved the performance by a factor of about two. For the case in which the assortment is done using the maximum stage size, no computational performance improvement has been observed but the numerical dissipation is reduced. For both cases the dispersive properties of the scheme do not seem to be significantly affected.

For LF2 the performance is also improved by a factor of about two for a bi-static RCS analysis case. In contrast, the commonly used Montseny's technique provides an speed up of about four. The CPLTS technique however seems to present better dispersive properties than the Montseny's approach and has better adaptivity to multiscale problems.

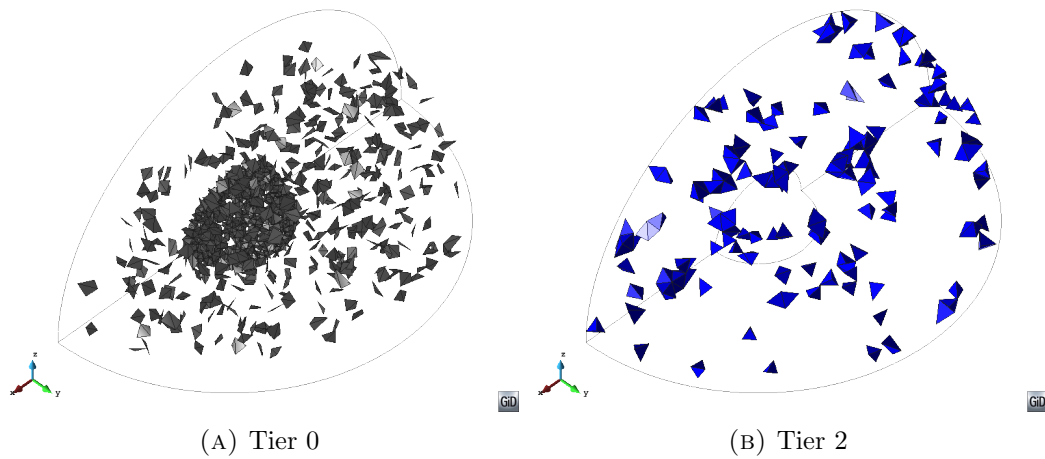


FIGURE 5.13: Tier assortment for LSERK4. Tier 1 is not represented.

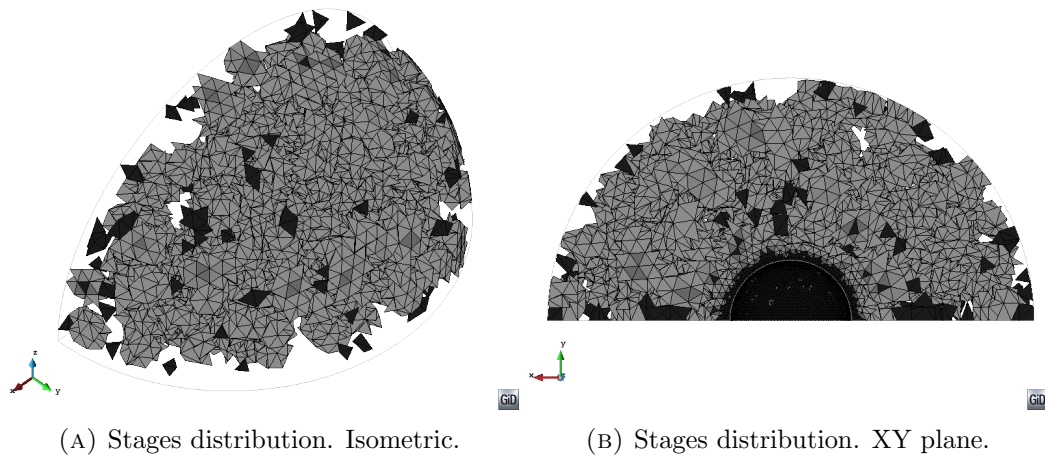


FIGURE 5.14: Elements in LSERK4 where some operations are required by the smaller tiers. Darker colour means more operations (closer to a smaller tier). The degrees of freedom belonging to the elements represented need to be stored when the smaller tier is solved. Elements that do not require additional operations and storage are not represented.

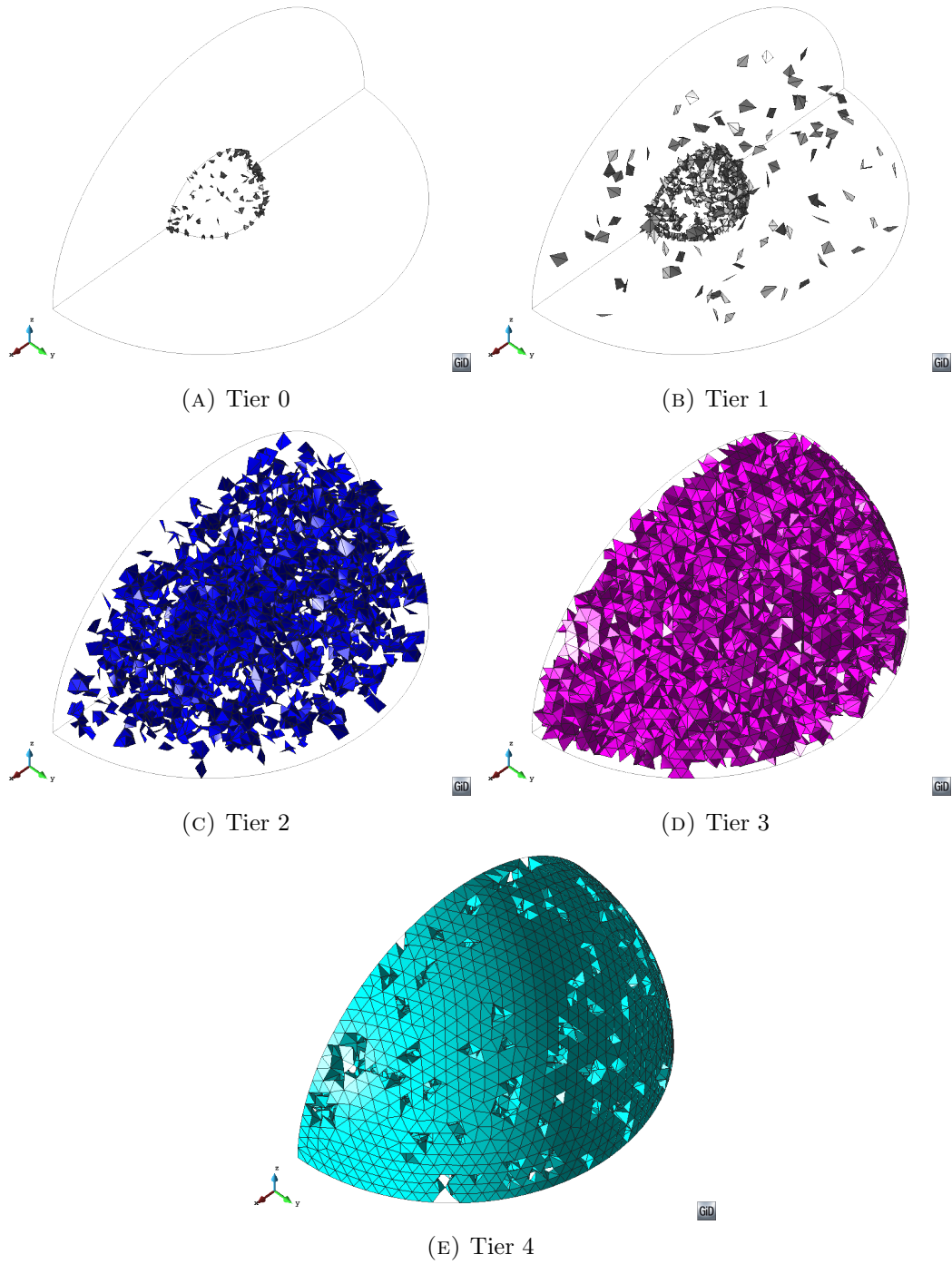


FIGURE 5.15: Tier assortment for LF2-CPLTS.

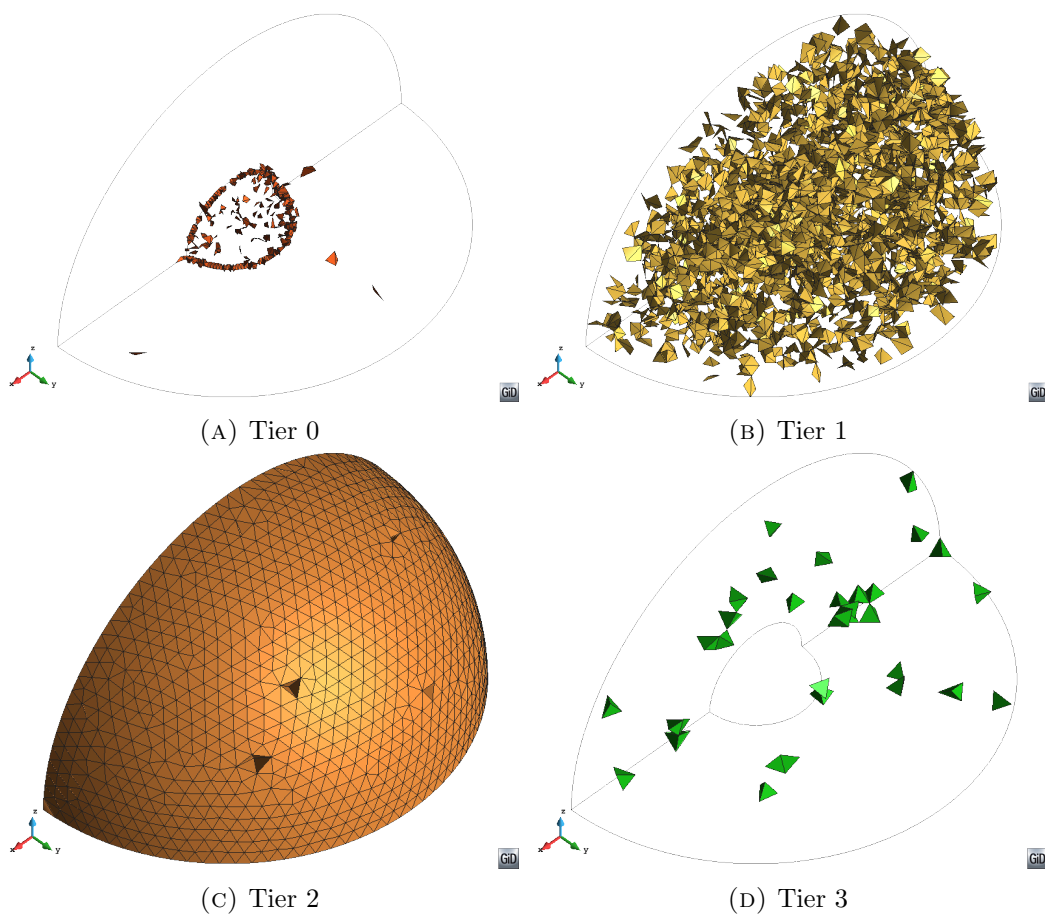


FIGURE 5.16: Tier assortment for LF2-LTS.

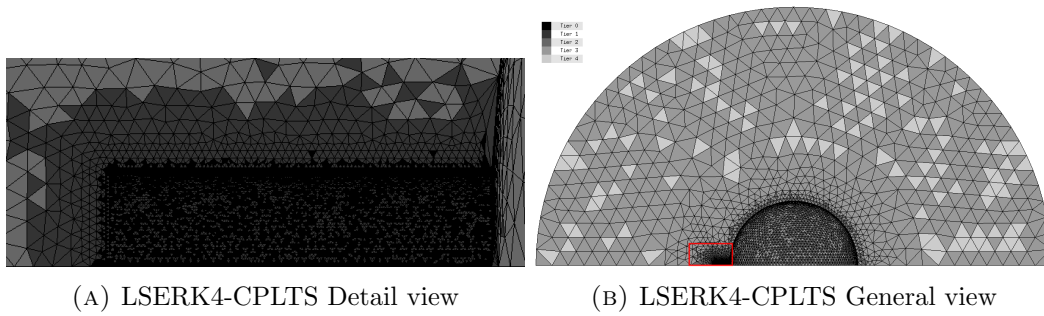


FIGURE 5.17: Tier assortment for LSERK4-CPLTS

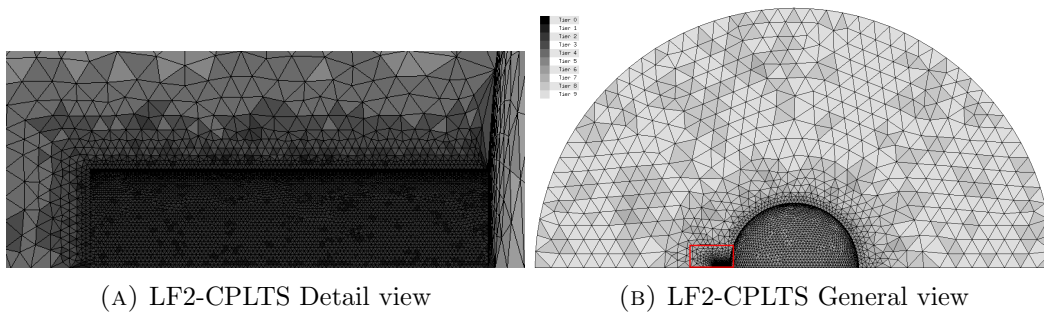


FIGURE 5.18: Tier assortment for LF2-CPLTS

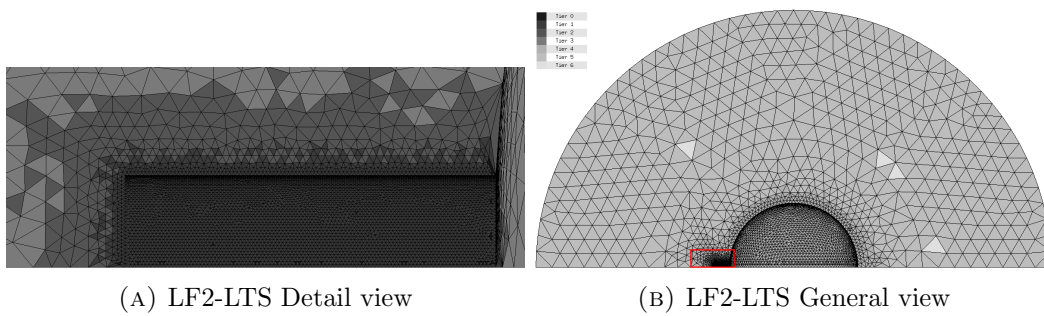


FIGURE 5.19: Tier assortment for LF2-LTS

Chapter 6

Space-Time Discontinuous Galerkin

L. D. Angulo, J. Alvarez, M. F. Pantoja, and S. G. Garcia. An explicit nodal space-time discontinuous galerkin method for maxwell's equations. *IEEE Microwave and Wireless Components Letters*, Accepted

Abstract

A novel implicit nodal Space-Time Discontinuous Galerkin (STDG) method is proposed in this paper. An eigenvalue analysis is performed and compared with that for a DG scheme solved with a 4th-Order Runge-Kutta time integrator. We show that STDG offers a significant improvement of dissipative and dispersive properties and allows larger time steps, regardless of the spatial hp-refinement. A domain-decomposition technique is used to introduce an explicit formulation of the method in order to render it computationally efficient.

6.1 Introduction

A common approach for Discontinuous Galerkin (DG) time-domain (TD) methods, is to treat the time and space variables separately [27], often using an explicit time-integrating schemes such as the 4th-Order Low-Storage Runge-Kutta LSERK4, which prevents the full exploitation of the higher-order spatial convergence. Although works to cope with this limitation [130] exist, a noteworthy alternative is to use Space-Time DG (STDG) methods, already used in other fields of Physics [8, 230], and in Electromagnetics [119, 132]. A major drawback of STDG resides in its implicit nature, though semi-explicit approaches also exist [119, 132] (tent-pitching technique).

In this work, we present a novel STDG formulation combined with a causal domain-decomposition technique [231] to render it explicit (E-STDG). This letter is organized as follows: we first formulate a nodal[27] STDG scheme, with a new spurious-free upwind-in-space flux, combined with a centered-in-time flux. Next, we study the properties of the resulting implicit STDG scheme with an eigenvalue analysis, comparing with a DG-LSERK4 one. Next, we describe the explicit causal formulation E-STDG, and validate it with a simple resonant problem. We finally conclude that the use a nodal approach, together with the domain-decomposition technique provides an affordable solution to the problem.

6.2 Implicit Formulation

Let us start by defining a 2D space-time region tessellated with $k = 1, \dots, K_x$ elements. With $\zeta \in V$ defined as a space-time coordinate within each element, and with $\hat{n} = (n_t, n_x)$ normal vectors pointing outwards from its boundary. The weak form of 1D Maxwell's curl equations is found by multiplying by weighting functions $\alpha_{ij}(\zeta)$, integrating over V , and enforcing the residual to vanish. For instance, the free-space Ampère's law (taking for simplicity the permittivity and permeability both equal to 1) becomes

$$\int_V (\partial_t E(\zeta) + \partial_x H(\zeta)) \alpha_{ij}(\zeta) d\zeta = 0 \quad (6.1)$$

with E and H being the electric and magnetic fields. Integrating by parts in (6.1) and replacing the boundary flux-integral by a numerical flux, as usual in DGTD, we find

$$\int_V \partial_x H \alpha_{ij} d\zeta = \int_T dt \left[\int_{\partial X} \hat{n} \cdot H^* \alpha_{ij} dx - \int_X H \partial_x \alpha_{ij} dx \right] \quad (6.2)$$

with H^* (and similarly E^*) being the usual numerical fluxes [27]. Next, following the Galerkin procedure, we expand the fields in series using the weighting functions also as basis functions, and assuming that their space-time dependence can be separated in polynomials of orders P^t and P^x for the temporal and spatial parts, respectively

$$H^h(\zeta) = \sum_{i=0}^{P^t} \sum_{j=0}^{P^x} \alpha_{ij}(\zeta) H_{ij} = \sum_{i=0}^{P^t} \sum_{j=0}^{P^x} \alpha_i^t(t) \alpha_j^x(x) H_{ij} \quad (6.3)$$

and similarly for E . Substituting (6.3) into (6.2), the spatial-stiffness term becomes,

$$\int_V H^h \partial_x \alpha_{mn} d\zeta = \sum_{i=0}^{P^t} \sum_{j=0}^{P^x} H_{ij} \int_T \alpha_i^t \alpha_m^t dt \int_X \alpha_j^x \partial_x \alpha_n^x dx \quad (6.4)$$

And the spatial-flux term,

$$\begin{aligned} & \int_T (H^*(t, x_R) \alpha_{mn}(t, x_R) - H^*(t, x_L) \alpha_{mn}(t, x_L)) dt = \\ & \sum_{i=0}^{P^t} \sum_{j=0}^{P^x} H_{ij}^* (\alpha_n^x(x_R) - \alpha_n^x(x_L)) \int_T \alpha_i^t \alpha_m^t dt \end{aligned} \quad (6.5)$$

Flux evaluations are highly simplified by using a nodal approach based on Lagrange interpolating polynomials[27], since the flux in a space-time node requires only the degrees of freedom (DOFs) at the nodes occupying the same position in the neighboring elements. To determine the space-time flux, let us define

$$[[H_{ij}]]^t = \frac{H_{ij} - H_{ij}^{t,+}}{2} \quad [[H_{ij}]]^x = \frac{H_{ij} - H_{ij}^{x,+}}{2} \quad (6.6)$$

and similarly for the E-field. There, the upper subscript $x, +$ refers to the neighboring node along the spatial boundary (see Fig. 6.1). First, we find the centered version of the numerical fluxes, as the average with the contiguous-space/earlier-time border values

$$H_{ij}^\diamond = \delta_{i0} [[H_{0j}]]^t - \delta_{0j} [[H_{i0}]]^x + \delta_{jP^x} [[H_{iP^x}]]^x \quad (6.7)$$

and, secondly, we complete them with the lacking terms to obtain upwind fluxes in space, keeping centered fluxes in time

$$H_{ij}^\bullet = H_{ij}^\diamond - \delta_{0j} [[E_{i0}]]^x Z^{-1} + \delta_{jP^x} [[E_{iP^x}]]^x Z^{-1} \quad (6.8)$$

where δ_{ij} refers to the usual Kronecker-delta, and Z, Y the medium impedance and admittance, respectively (both unity in our case).

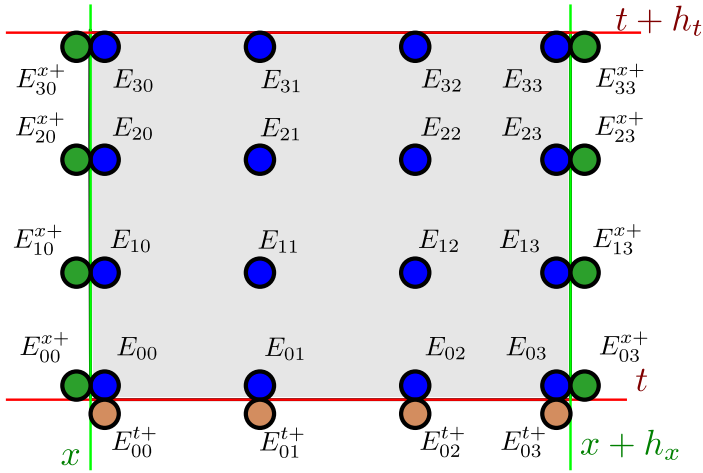


FIGURE 6.1: Notation: a space-time element (in gray) with $P^t = P^x = 3$.

A compact matrix formulation can be written by arranging the E and H field coefficients (DOFs) in an ordered column-vector, e.g.

$$\mathbf{E} \doteq [E_{0,0}, \dots, E_{0,P^x} \dots E_{P^t,0}, \dots, E_{P^t,P^x}]^T$$

. Eq. (6.4), with the usual tensor product \otimes , becomes

$$\int_V H^h(\zeta) \partial_x \alpha(\zeta) d\zeta \doteq \mathcal{M}^t \otimes \mathcal{C}^x \mathbf{H} \quad (6.9)$$

with \mathcal{M} and \mathcal{C} being the mass and stiffness matrices, respectively. The spatial-flux term (6.5) can be expressed as

$$\begin{aligned} \int_T \left(H^{h,*}(t, x_R) \alpha(t, x_R) - H^{h,*}(t, x_L) \alpha(t, x_L) \right) dt \\ \doteq \mathcal{M}^t \otimes (\mathcal{R}_L^x - \mathcal{R}_R^x) \mathbf{H}^* \end{aligned} \quad (6.10)$$

with $\mathcal{R}_L^t = \mathbf{e}_0^{P^t} \mathbf{e}_0^{P^t, T}$ and $\mathcal{R}_R^t = \mathbf{e}_{P^t}^{P^t} \mathbf{e}_{P^t}^{P^t, T}$ where \mathbf{e}_i^N is a $N + 1$ long zero vector with 1 in entry i . Operating similarly for the rest of terms and the Ampere's equation, we can express the scheme locally as

$$\begin{aligned} \varepsilon \mathcal{C}^t \otimes \mathcal{M}^x \mathbf{E} + \mathcal{M}^t \otimes \mathcal{C}^x \mathbf{H} \\ = \mathcal{M}^t \otimes (\mathcal{R}_L^x - \mathcal{R}_R^x) \mathbf{H}^* + (\mathcal{R}_L^t - \mathcal{R}_R^t) \otimes \mathcal{M}^x \mathbf{E}^* \end{aligned} \quad (6.11)$$

Let us now assume that our computational domain is divided by K_x space-time elements and let us define

$$\mathcal{F}_{R,L}^t = \mathcal{I}_{K_x} \otimes \mathcal{I}_2 \otimes \mathcal{R}_{R,L}^t \otimes \mathcal{M}^x, \quad \mathcal{F}_{R,L}^x = \mathcal{I}_{K_x} \otimes \mathcal{V} \otimes \mathcal{M}^t \otimes \mathcal{R}_{R,L}^x$$

$$\mathcal{S}^t = \mathcal{I}_{K_x} \otimes \mathcal{I}_2 \otimes \mathcal{C}^t \otimes \mathcal{M}^x, \quad \mathcal{S}^x = \mathcal{I}_{K_x} \otimes \mathcal{V} \otimes \mathcal{M}^t \otimes \mathcal{C}^x \quad (6.12)$$

with $\mathcal{I}_N = \sum_{n=0}^{N-1} \mathbf{e}_n^{N-1} \mathbf{e}_n^{N-1,T}$ and $\mathcal{V} = \mathbf{e}_0^1 \mathbf{e}_1^{1,T} + \mathbf{e}_1^1 \mathbf{e}_0^{1,T}$. We can write the following compact expression

$$(\mathcal{S}^t + \mathcal{S}^x) \mathbf{q} = (\mathcal{F}_L^t - \mathcal{F}_R^t + \mathcal{F}_L^x - \mathcal{F}_R^x) \mathbf{q}^* \quad (6.13)$$

where \mathbf{q} represents all the field coefficients in a given space-time element. The upwind-in-space centered-in-time numerical flux (6.8) can be expressed as

$$\mathbf{q}_{\text{upwind}}^* = \underbrace{-\mathcal{E}_R^t \mathbf{q}' + (\mathcal{E}_L^t + \mathcal{E}_L^x - \mathcal{E}_R^x) \mathbf{q}}_{q_{\text{centered}}^*} + (\mathcal{E}_L^x - \mathcal{E}_R^x) \tilde{\mathcal{V}} \mathbf{q} \quad (6.14)$$

with \mathbf{q}' being the state vector of the previous space-time element. The operators \mathcal{E} perform the operations needed to assemble the unknowns associated with the fluxes in the global system of equations. The superscripts t and x and subscripts L and R indicate the boundary at which they are operating. The operator $\tilde{\mathcal{V}} = \mathcal{I}_{K_x} \otimes \mathcal{V} \otimes \mathcal{I}_{P^t} \otimes \mathcal{I}_{P^x}$ indicates the operation on the dual field. Note that $\mathcal{F}^x \mathcal{E}^t \mathbf{q}' = \mathcal{F}^t \mathcal{E}^x \mathbf{q} = \mathbf{0}$ because \mathcal{E} is defined to extract only the unknowns needed by the flux acting on the boundary indicated by its superscript. Replacing the centered part of (6.14) into (6.13)

$$\underbrace{(\mathcal{S}^t + \mathcal{S}^x - \mathcal{F}_L^x \mathcal{E}_L^x + \mathcal{F}_R^x \mathcal{E}_R^x + \mathcal{F}_L^t \mathcal{E}_L^t)^{-1}}_{\mathcal{H}} (-\mathcal{F}_L^t \mathcal{E}_R^t) \mathbf{q}' = \mathbf{q} \quad (6.15)$$

and a similar expression can be formulated for upwind flux. Eq. (6.15) enables us to find the current state, \mathbf{q} , from the previous state, \mathbf{q}' , in a marching-in-time way. A major limitation of this scheme is its spatial implicitness, requiring matrix inversion (or solving a linear system at each time step) of operators scaling as $\mathcal{O}(K_x^2)$ (only tentatively efficient for problems where the space and time scales are very dissimilar).

6.3 An explicit scheme

Semi-explicit formulations of STDG exist [119, 132], and in this section we present a new explicit alternative simpler than those, in terms of the needed mesh, and using a reduced number of DOFs. A domain-decomposition technique [231] will be used to formulate an explicit variant of the scheme in (6.15), at the cost of adding a CFL-like causality condition. Rather than solving the whole domain Ω , we divide the problem into smaller regions Ω_d such that $\bigcup_d \Omega_d = \Omega$. Then, we enlarge each region Ω_d to include the elements that are causally connected with it for a given h_t , we will denote this enlarged region with Ω'_d . An element is considered to be causally

connected with another one if any of its fields at t can propagate to Ω_d at $t + h_t$. i. e. if it contains a point within a distance $d \leq ch_t$ to any point in Ω_d , with c being the numerical speed of light. The border of Ω'_d ends in a zero-flux boundary condition that decouples it from the rest of the computational domain. Finally, the problem is solved in each Ω'_d using the implicit method described above but passing only the values in Ω_d to the next step. The values in $\Omega'_d \setminus \Omega_d$ are discarded as they are corrupted by the artificial boundary condition. This approach reduces the computational cost from $\mathcal{O}(K_x^2)$ to $\sum_d^{N_d} \mathcal{O}(K_{x,d}^2)$ with $K_{x,d} < K_x$. The region sizes Ω_d can be chosen as a trade-off taking into account the computational cost in determining the initial \mathcal{H}_d , the cost to evolve the scheme, and the size of the time step.

6.4 Numerical Analysis

A PEC-terminated spatial domain has been discretized with $K_x = 4$ elements of size $h_x = 0.25$ and order $P^x = 4$ using the spatial upwind flux (6.8), as a simple proof-of-concept test-case. The eigenvalues of \mathcal{H} have been numerically found to investigate dispersion and dissipation independently (rather than using error norms such as in [8, 119, 132, 230]). We have conducted studies for different h_t , which have not exhibited eigenvalues with positive real parts, thus implying that the scheme is unconditionally stable for any h_t .

Fig. 6.2 shows the dispersion and dissipation properties of the scheme for the first resonant modes to the closest analytical mode $k_a = \pi$ with $\omega_a = \pi$ for different STDG schemes and a classical DG evolved using LSERK4 and the same upwind spatial fluxes. The accuracy of the scheme presents high-order convergence with h_t , following the relationship $(h_t^{2P_t+1})$ for the dissipation, and $(h_t^{2P_t+2})$ for the dispersion, in agreement with [22] for the spatial DG semi-discrete scheme. Therefore we can conclude that the spatial and temporal convergences of the scheme coincide. Note that, although the LSERK4 physical eigenvalue can be computed and represented, it is unstable for approx. $h_t \geq 0.05$ because of the presence of other eigenvalues lying outside its stability region, thus limiting with $h_{t,\max} \propto (P^x)^{-2} \min h_x^k$. We also find that we have higher convergence for $P^t \geq 2$, which is a significant improvement over LSERK4, especially when combined with a higher P^x .

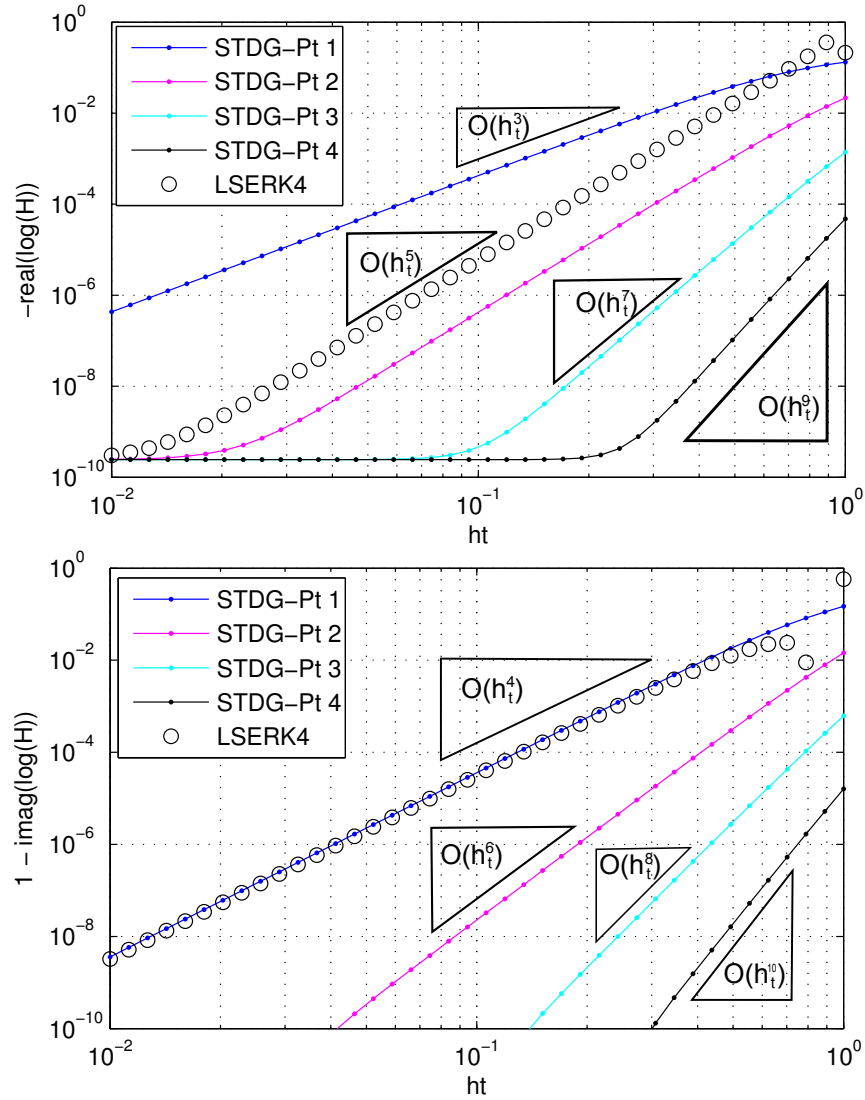


FIGURE 6.2: Dissipative (up)/dispersive (down) convergence rates of the eigenvalues of the evolution operator \mathcal{H} for different orders & h_t .

6.5 Numerical Results

For validation, we have simulated the above problem using a discretization of $K_x = 8$, $h_x = 0.125$, $h_t = 0.1$, and $P^t = P^x = 4$ and upwind fluxes up to a time $T = 10000$ (note that all quantities are dimensionless in our system of units). Also, we have computed the same problem with the explicit implementation of the scheme. The STDG scheme has a single evolution operator with 6400 non-zero entries. The E-STDG works with a split domain having 8 different evolution operators totaling 4800 non-zero entries, indicating a significant reduction in the computational complexity. Fig. 6.3 shows the resonances and the error for the first modes.

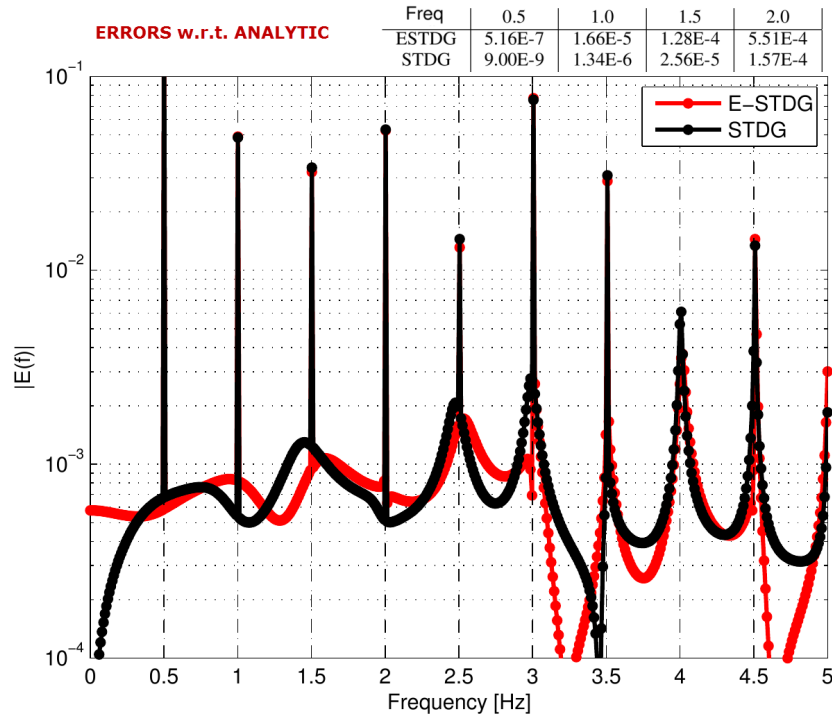


FIGURE 6.3: Response to a white noise in the E-STDG and STDG schemes with $P^t = 4$, $h_t = 0.1$, $P^x = 4$, $K_x = 8$, $h_x = 0.125$ after a time of 100. Vertical dashed lines represent the analytical modes.

6.6 Conclusions

In this work, we have introduced and analyzed a novel implicit and stable nodal STDG technique, and compared it with the classic DG-LSERK4 scheme. This nodal formulation needs to store twice the DOFs of the LSERK4 formulations, but it is suitable to be used in high-order-in-space schemes, taking full advantage of the convergence of the spatial DG semi-discretization. To overcome its implicitness, we have proposed a new explicit implementation, showing that the scheme can be computationally affordable, allowing certain freedom in choosing the size of the time step and evolution operators.

Part IV

On modeling

Chapter 7

Source and boundary implementation in vector and scalar DGTD

J. Alvarez, L.D. Angulo, M. Fernandez Pantoja, A. Rubio Bretones, and S.G. Garcia. Source and boundary implementation in vector and scalar dgtd. *Antennas and Propagation, IEEE Transactions on*, 58(6):1997–2003, 2010. ISSN 0018-926X. doi: 10.1109/TAP.2010.2046857

Abstract

In this paper we summarize the boundary and source implementation for the several formulations of the Discontinuous Galerkin Time Domain method (DGTD). Since DGTD with 0th-order scalar basis functions using the upwind flux, coincides with the Finite Volume Time Domain (FVTD), many of the concepts developed for FVTD can be ported to DGTD in any of its different formulations (scalar/vector basis, upwind/centered flux). Numerical examples illustrate the different alternatives.

7.1 Introduction

The Discontinuous Galerkin Time Domain (DGTD) method is a rapidly emerging technique in computational electromagnetics in the time domain [67, 92, 189, 192, 193, 195, 213], which provides an alternative to Finite Elements Time domain (FETD), Finite Volume Time Domain (FVTD) and Finite Difference Time Domain (FDTD) methods.

Like FETD, DGTD employs a variational formulation (discontinuous Galerkin) to integrate the spatial part of time-domain Maxwell's curl equations, with a differential integration scheme for the time part. The space is divided into M non-overlapping elements, in each of which the solution is expanded in a set of local scalar [194] or vector [92] basis functions of arbitrary order. The weak form of Maxwell's curl equations are found element by element by employing a Galerkin test procedure.

Unlike FETD, the solution is not enforced to be continuous at the boundaries between adjacent elements. Instead, continuous numerical fluxes are defined at the interface in order to connect the solution between them in the manner used in FVTD methods. Two common flux conditions are found in the literature: the centered flux [189], and the upwind flux [188]. The latter is the one actually employed in FVTD, and in fact, FVTD can be regarded as a special case of DGTD with this flux, and 0^{th} order (constant) scalar basis functions [232].

The main advantage of DGTD over FVTD is its higher order in space, while over FETD, the advantage resides in the fact that DGTD needs only the inversion of M square matrices of $Q \times Q$ elements (with Q the number of basis functions), while larger matrices ($\simeq MQ \times MQ$) are involved in FETD.

In this paper, we take advantage of the resemblances of FVTD and DGTD to derive simple boundary conditions and to implement sources into DGTD for the different formulations: vector/scalar, centered/upwind flux approximation (this idea was successfully employed in [195] to derive a hybrid FDTD/DGTD algorithm). Here, we use the numerical flux to: a) incorporate wave sources directly by using the total field/scattered field formulation [223], b) implement Perfect Electric/Magnetic Conducting (PEC/PMC) surfaces, and c) incorporate Silver-Müller Absorbing Boundary conditions (SM-ABCs) [78] into DGTD. Though some of those ideas are well-known in FVTD, we think it may be useful to extend everything under a common framework for the different formulations of the DGTD method.

This paper is organized as follows. In Section II we summarize the DGTD fundamentals in 3D with vector/scalar basis and the centered/upwind flux. Section III shows the implementation of boundary conditions, wave sources and SM-ABC into DGTD, and Section IV presents some results.

7.2 DGTD fundamentals

7.2.1 Scalar basis formulation

Let us assume Maxwell's symmetric curl equations for linear isotropic homogeneous media in Cartesian coordinates. Now, let us divide the space in M non-overlapping elements V_m , each bounded by ∂V_m and enforce the inner product of each equation with a set of local continuous scalar test functions, to nullify element by element

$$\begin{aligned} \int_{V^m} \Phi_{q'}^{e^m} (\varepsilon \partial_t \vec{E}^m + \sigma \vec{E}^m + \vec{J} - \nabla \times \vec{H}^m) dV &= 0 \\ \int_{V^m} \Phi_{q'}^{h^m} (\mu \partial_t \vec{H}^m + \sigma^* \vec{H}^m + \vec{M} + \nabla \times \vec{E}^m) dV &= 0 \end{aligned} \quad (7.1)$$

$$\Phi_{q'}^{e,h} \in \mathcal{B}^{e,h^m} = \{\Phi_1^{e,h^m}, \Phi_2^{e,h^m}, \dots, \Phi_Q^{e,h^m}\} \quad (7.2)$$

With $\vec{E}, \vec{H}, \vec{J}, \vec{M}, \sigma, \sigma^*, \varepsilon, \mu$ being, respectively: electric field, magnetic field, electric current density, magnetic current density, electric conductivity, magnetic conductivity, permittivity and permeability.

After some algebra we can write Eqs. (7.1) as

$$\int_{V^m} (\Phi_{q'}^{e^m} (\varepsilon \partial_t \vec{E}^m + \sigma \vec{E}^m + \vec{J}) + \nabla \Phi_{q'}^{e^m} \times \vec{H}^m) dV = \oint_{\partial V^m} \Phi_{q'}^{e^m} (\hat{n}^m \times \vec{H}^m) dS \quad (7.3)$$

$$\int_{V^m} (\Phi_{q'}^{h^m} (\mu \partial_t \vec{H}^m + \sigma^* \vec{H}^m + \vec{M}) - \nabla \Phi_{q'}^{h^m} \times \vec{E}^m) dV = - \oint_{\partial V^m} \Phi_{q'}^{h^m} (\hat{n}^m \times \vec{E}^m) dS \quad (7.4)$$

Eqs. (7.3)(7.4) together with a tangential field continuity¹ condition between adjacent elements leads to a FETD method [44]. Namely, adding the superscript + to the fields at ∂V_m calculated in the element adjacent to m , the continuity on the tangential field components on the common face ∂V^m of two adjacent elements requires

¹Let us assume at the moment that no PEC/PMC are present. We will show later how to handle these.

for FETD that

$$\hat{n}^m \times \vec{E}^{m+} = \hat{n}^m \times \vec{E}^m, \quad \hat{n}^m \times \vec{H}^{m+} = \hat{n}^m \times \vec{H}^m \quad (7.5)$$

The main drawback of the resulting algorithm resides in its implicit nature, which requires the solution of large matrix equations[82]. The core idea of DGTD is to relax the continuity conditions to yield a quasi-explicit algorithm. Namely, instead of plugging (7.5) into (7.3)(7.4), DGTD defines numerical values of the tangential fields on ∂V_m , henceforth called numerical fluxes ($\hat{n}^m \times \vec{E}^{m*}$ and $\hat{n}^m \times \vec{H}^{m*}$), which do not coincide with any of the values of the tangential fields at any side of ∂V_m but depend on them

$$\begin{aligned} \hat{n}^m \times \vec{E}^{m*} &= \hat{n}^m \times \left(\vec{f}_E^-(\vec{E}^m, \vec{H}^m) + \vec{f}_E^+(\vec{E}^{m+}, \vec{H}^{m+}) \right) \\ \hat{n}^m \times \vec{H}^{m*} &= \hat{n}^m \times \left(\vec{f}_H^-(\vec{E}^m, \vec{H}^m) + \vec{f}_H^+(\vec{E}^{m+}, \vec{H}^{m+}) \right) \end{aligned} \quad (7.6)$$

This numerical flux is the one actually employed by any pair of adjacent elements to calculate the surface (flux) integrals in the RHS of (7.3)(7.4), instead of $\hat{n}^m \times \vec{E}^m$ and $\hat{n}^m \times \vec{H}^m$.

Two common choices of the numerical flux are reported in the literature:

1. A centered flux [194] found by averaging the solutions at both sides of the interface

$$\begin{aligned} \hat{n}^m \times \vec{E}^{m*} &= \hat{n}^m \times \frac{\vec{E}^m + \vec{E}^{m+}}{2} \\ \hat{n}^m \times \vec{H}^{m*} &= \hat{n}^m \times \frac{\vec{H}^m + \vec{H}^{m+}}{2} \end{aligned} \quad (7.7)$$

2. The upwind flux usually employed in FVTD [188] arising from the solution of the advection equations with discontinuous initial values (Riemann problem) [189]

$$\begin{aligned} \hat{n}^m \times \vec{E}^{m*} &= \hat{n}^m \times \frac{(Y^m \vec{E}^m - \hat{n}^m \times \vec{H}^m) + (Y^{m+} \vec{E}^{m+} + \hat{n}^m \times \vec{H}^{m+})}{Y^m + Y^{m+}} \\ \hat{n}^m \times \vec{H}^{m*} &= \hat{n}^m \times \frac{(Z^m \vec{H}^m + \hat{n}^m \times \vec{E}^m) + (Z^{m+} \vec{H}^{m+} - \hat{n}^m \times \vec{E}^{m+})}{Z^m + Z^{m+}} \end{aligned} \quad (7.8)$$

with $Z^m = \sqrt{\frac{\mu^m}{\epsilon^m}} = \frac{1}{Y^m}$ being the intrinsic impedance of the element m , and $Z^{m+} = \frac{1}{Y^{m+}}$ being that of the adjacent one.

The semi-discrete algorithm is found by assuming that the space and time dependencies of the fields can be separated, and that the spatial part is expanded within

each element in a set of basis functions equal to the set of test functions (Galerkin method)

$$\vec{E}^m = \sum_{q=1}^Q \vec{E}_q^m(t) \Phi_q^{e^m}(\vec{r}), \quad \vec{H}^m = \sum_{q=1}^Q \vec{H}_q^m(t) \Phi_q^{h^m}(\vec{r}) \quad (7.9)$$

The final form of the semi-discrete algorithm at the element m is

$$\varepsilon \widetilde{M}^{ee} \partial_t \bar{\bar{E}} + (\sigma \widetilde{M}^{ee} - \widetilde{F}^{ee}) \bar{\bar{E}} = -\bar{\bar{J}} - \widetilde{S}^{eh} \bar{\bar{H}} + \widetilde{F}^{eh} \bar{\bar{H}} + \widetilde{F}^{eh^+} \bar{\bar{H}}^+ - \widetilde{F}^{ee^+} \bar{\bar{E}}^+ \quad (7.10)$$

$$\mu \widetilde{M}^{hh} \partial_t \bar{\bar{H}} + (\sigma^* \widetilde{M}^{hh} - \widetilde{F}^{hh}) \bar{\bar{H}} = -\bar{\bar{M}} + \widetilde{S}^{he} \bar{\bar{E}} - \widetilde{F}^{he} \bar{\bar{E}} - \widetilde{F}^{he^+} \bar{\bar{E}}^+ - \widetilde{F}^{hh^+} \bar{\bar{H}}^+ \quad (7.11)$$

where

- $\bar{\bar{E}}$ and $\bar{\bar{H}}$ are the field coefficients

$$\bar{\bar{E}} = \left(\vec{E}_1^m(t), \dots, \vec{E}_Q^m(t) \right)^T \quad (7.12)$$

$$\bar{\bar{H}} = \left(\vec{H}_1^m(t), \dots, \vec{H}_Q^m(t) \right)^T \quad (7.13)$$

- $\bar{\bar{J}}$ and $\bar{\bar{M}}$ are the weak form of the source terms

$$\bar{\bar{J}} = \int_{V^m} \left(\vec{J}(\vec{r}, t) \Phi_1^{h^m}, \dots, \vec{J}(\vec{r}, t) \right)^T \Phi_Q^{h^m} dV \quad (7.14)$$

$$\bar{\bar{M}} = \int_{V^m} \left(\vec{M}(\vec{r}, t) \Phi_1^{h^m}, \dots, \vec{M}(\vec{r}, t) \right)^T \Phi_Q^{h^m} dV \quad (7.15)$$

- \widetilde{M} is the mass matrix

$$[\widetilde{M}^{\alpha\alpha}]_{q'q} = \int_{V^m} \Phi_{q'}^{\alpha^m} \Phi_q^{\alpha^m} dV \quad (7.16)$$

- \widetilde{S} is the stiffness matrix

$$[\widetilde{S}^{\alpha\beta}]_{q'q} = \left(\int_{V^m} \nabla \Phi_{q'}^{\alpha^m} \Phi_q^{\beta^m} dV \right) \times \quad (7.17)$$

- \tilde{F} are the flux matrices

$$\begin{aligned} [\tilde{F}^{\alpha\alpha}]_{q'q} &= \kappa^{\alpha\alpha} \left(\int_{\partial V^m} \Phi_q^{\alpha m} \Phi_q^{\alpha m} dS \right) \hat{n}^m \times \hat{n}^m \times \\ [\tilde{F}^{\alpha\beta}]_{q'q} &= \nu^{\alpha\beta} \left(\int_{\partial V^m} \Phi_q^{\alpha m} \Phi_q^{\beta m} dS \right) \hat{n}^m \times, \quad \alpha \neq \beta \end{aligned} \quad (7.18)$$

where, for the centered flux

$$\begin{aligned} \kappa^{hh} &= \kappa^{hh+} = \kappa^{ee} = \kappa^{ee+} = 0 \\ \nu^{eh} &= \nu^{eh+} = \nu^{he} = \nu^{he+} = 1/2 \end{aligned} \quad (7.19)$$

and for the upwind flux

$$\begin{aligned} \kappa^{hh} &= \kappa^{hh+} = \frac{1}{Y^m + Y^{m+}}, \quad \kappa^{ee} = \kappa^{ee+} = \frac{1}{Z^m + Z^{m+}} \\ \nu^{he} &= \kappa^{hh} Y^m, \quad \nu^{he+} = \kappa^{hh+} Y^{m+} \\ \nu^{eh} &= \kappa^{ee} Z^m, \quad \nu^{eh+} = \kappa^{ee+} Z^{m+} \end{aligned} \quad (7.20)$$

Notice that the flux terms $\tilde{F}^{\alpha\alpha}$ on the LHS of Eqs. (7.10)(7.11) are factors appearing only when the upwind flux is employed.

A common choice for the basis functions [189], is the set 3D Lagrange interpolating n^{th} order polynomials (Legendre polynomial basis can be found in[213]) with equal set of electric and magnetic basis functions $\Phi_q^{em} = \Phi_q^{hm} \equiv \Phi_q^m$. They are first defined in a standard reference element [82] as a function of the simplex coordinates (ξ, η, ζ) by

$$\Phi_q(\xi, \eta, \zeta) \in P_n^3 = \text{span}\{\xi^i \eta^j \zeta^k; \substack{i,j,k \geq 0 \\ i+j+k \leq n}\} \quad (7.21)$$

requiring $(n+1)(n+2)(n+3)/6$ nodal points in the element to form a complete basis. The local basis for each element is found by computing the mapping of the transformation from the reference element to the actual one. The case $n=0$ leads to the classical FVTD algorithm[188].

The resulting system of ordinary differential equations in time can be solved in a number of ways: second-order leapfrog (LF)[195], 4th order Runge-Kutta[92], implicit Crank-Nicolson[232], symplectic[233], etc.

7.2.2 Vector–basis formulation

The fundamentals of the vector formulation are similar to those of the scalar one. Now the basis and test functions are chosen to be vectorial:

$$\mathcal{B}^{e,h^m} = \{\vec{\Phi}_1^{e,h^m}, \vec{\Phi}_2^{e,h^m}, \dots, \vec{\Phi}_Q^{e,h^m}\}, \quad m = 1, \dots, M$$

The weak form of Maxwell's equations is found by using the scalar product of the vector test–functions and the fields

$$\int_{V^m} (\vec{\Phi}_{q'}^{e^m} \cdot (\varepsilon \partial_t \vec{E}^m + \sigma \vec{E}^m + \vec{J}) - \nabla \times \vec{\Phi}_{q'}^{e^m} \cdot \vec{H}^m) dV = \oint_{\partial V^m} \vec{\Phi}_{q'}^{e^m} \cdot (\hat{n}^m \times \vec{H}^{m*}) dS \quad (7.22)$$

$$\int_{V^m} (\vec{\Phi}_{q'}^{h^m} \cdot (\mu \partial_t \vec{H}^m + \sigma^* \vec{H}^m + \vec{M}) + \nabla \times \vec{\Phi}_{q'}^{h^m} \cdot \vec{E}^m) dV = - \oint_{\partial V^m} \vec{\Phi}_{q'}^{h^m} \cdot (\hat{n}^m \times \vec{E}^{m*}) dS \quad (7.23)$$

where we already assumed the fluxes in the RHS to be the numerical ones.

Comparing Eqs. (7.3)(7.4) and Eqs. (7.22)(7.23) we find similar flux–density integrals in their RHSs. Thus the same upwind and centered fluxes of the scalar case can be used here.

For vector–basis functions the expansion (7.9) now becomes

$$\vec{E}^m = \sum_{q=1}^Q E_q^m(t) \vec{\Phi}_q^{e^m}(\vec{r}), \quad \vec{H}^m = \sum_{q=1}^Q H_q^m(t) \vec{\Phi}_q^{h^m}(\vec{r}) \quad (7.24)$$

The semi–discrete algorithm is formulated by plugging (7.24) into (7.22)(7.23). The resulting equations are formally equal to (7.10)(7.11), now with

$$\overline{\vec{E}} = \left(E_1^m(t), \dots, E_Q^m(t) \right)^T \quad (7.25)$$

$$\overline{\vec{H}} = \left(H_1^m(t), \dots, H_Q^m(t) \right)^T \quad (7.26)$$

$$\overline{\vec{J}} = \left(\int_{V^m} \vec{J}(\vec{r}, t) \cdot \vec{\Phi}_1^{e^m}, \dots, \int_{V^m} \vec{J}(\vec{r}, t) \cdot \vec{\Phi}_Q^{e^m} dV \right)^T \quad (7.27)$$

$$\overline{\vec{M}} = \left(\int_{V^m} \vec{M}(\vec{r}, t) \cdot \vec{\Phi}_1^{h^m}, \dots, \int_{V^m} \vec{M}(\vec{r}, t) \cdot \vec{\Phi}_Q^{h^m} dV \right)^T \quad (7.28)$$

$$[\widetilde{M}^{\alpha\alpha}]_{q'q} = \int_{V^m} \vec{\Phi}_{q'}^{\alpha^m} \cdot \vec{\Phi}_q^{\alpha^m} dV \quad (7.29)$$

$$[\widetilde{S}^{\alpha\beta}]_{q'q} = - \int_{V^m} (\nabla \times \vec{\Phi}_{q'}^{\beta^m}) \cdot \vec{\Phi}_q^{\alpha^m} dV \quad (7.30)$$

$$[\tilde{F}^{\alpha\alpha}]_{q'q} = \kappa^{\alpha\alpha} \int_{\partial V^m} \vec{\Phi}_q^{\alpha m} \cdot (\hat{n}^m \times \hat{n}^m \times \vec{\Phi}_q^{\alpha m}) dS \quad (7.31)$$

$$[\tilde{F}^{\alpha\beta}]_{q'q} = \nu^{\alpha\beta} \int_{\partial V^m} \vec{\Phi}_q^{\alpha m} \cdot (\hat{n}^m \times \vec{\Phi}_q^{\beta m}) dS, \quad \alpha \neq \beta \quad (7.32)$$

A common election of the basis functions is the hierarchical high-order vector–basis functions, widely used in finite elements methods [85, 92], which present some implementation advantages in order to reduce computation and memory requirements. Namely, since only the edge– and face–basis functions associated with the face ∂V^m have non-zero tangential components, the flux matrices \tilde{F} are sparse. Furthermore, the \mathcal{B}^{e,h^m} function space is separated in the gradient space (\mathcal{G}^{e,h^m}) and the rotational space (\mathcal{R}^{e,h^m}) [85], and only the functions belonging to the rotational space have non-zero $\nabla \times \vec{\Phi}_q^{e,h^m} \neq 0$, leading \tilde{S} to be also sparse. Finally, the $\tilde{F}^{\alpha\beta}$ and \tilde{S} matrices do not depend on geometrical information (this does not apply to $\tilde{F}^{\alpha\alpha}$) and can be shared by all V^m , only needing one storage when an explicit time integration scheme is used.

7.3 Boundary conditions

The flux conditions which serve to connect adjacent fields, also serve to implement boundary conditions.

1. The interface of two elements with different ε and μ is handled in an indirect manner in the DGTD formulation, thanks to taking the same tangential components of the fields $\hat{n}^m \times \vec{E}^{m*}$ and $\hat{n}^m \times \vec{H}^{m*}$ in the flux integrals for two adjacent elements.
2. PEC boundary conditions on a face of an element m require the setting of the tangential electric field employed in the flux integrals to be null, and the tangential magnetic field to be continuous

$$\begin{aligned} \hat{n}^m \times \vec{E}^{m+} &= -\hat{n}^m \times \vec{E}^m \\ \hat{n}^m \times \vec{H}^{m+} &= \hat{n}^m \times \vec{H}^m \end{aligned} \quad (7.33)$$

3. PMC conditions are reciprocal of PEC

$$\begin{aligned} \hat{n}^m \times \vec{H}^{m+} &= -\hat{n}^m \times \vec{H}^m \\ \hat{n}^m \times \vec{E}^{m+} &= \hat{n}^m \times \vec{E}^m \end{aligned} \quad (7.34)$$

Let us note that for the upwind flux, both for PEC and PMC, we must also assume $Y^{m+} = Y^m$ and $Z^{m+} = Z^m$.

4. Regarding the ABCs, the straightest ones are the so-called first-order Silver-Müller (SM-ABC) [78] which are based on considering that outside the computation domain, the fields propagate as plane waves normally to the interface $\hat{n}^m \times \vec{E}^{m+} = Z^m \vec{H}^{m+}$, $\hat{n}^m \times \vec{H}^{m+} = -Y^m \vec{E}^{m+}$. For the upwind flux, this is directly implemented since it is equivalent to assuming that there is no contribution to the flux from outside the region of solution, only remaining $\vec{f}_{E,H}^-$ in Eq. (7.6).

$$\begin{aligned}\hat{n}^m \times \vec{f}_E^+ &= 0 = \hat{n}^m \times \frac{Y^m \vec{E}^{m+} + \hat{n}^m \times \vec{H}^{m+}}{Y^m + Y^{m+}} \\ \hat{n}^m \times \vec{f}_H^+ &= 0 = \hat{n}^m \times \frac{Z^m \vec{H}^{m+} - \hat{n}^m \times \vec{E}^{m+}}{Z^m + Z^{m+}}\end{aligned}\quad (7.35)$$

SM-ABC for the upwind flux provide a reflection coefficient of up to -50 dB for normal incidence, this rapidly degrading when the angle of incidence increases[79]. For the centered flux, SM-ABC conditions can also be employed [124], but, in this paper, we have implemented instead PML (Perfectly Matched Layer) ABCs [213][191].

5. Incident-wave conditions can also be generated in a straightforward way. Let us consider that, inside a total-field zone (TFZ), a known wave is propagating, while outside it (scattered-field zone (SFZ)) the field is null. If \vec{E}^{inc} , \vec{H}^{inc} denote the wave fields at each point of the TFZ/SFZ interface (Fig. 7.1), the flux across the face of an element m in the TFZ (with this face lying on the TFZ/SFZ interface) needs to be modified according to

$$\begin{aligned}\hat{n}^m \times \vec{E}^{m+} &= \hat{n}^m \times (\vec{E}^{m+} + \vec{E}^{inc}) \\ \hat{n}^m \times \vec{H}^{m+} &= \hat{n}^m \times (\vec{H}^{m+} + \vec{H}^{inc})\end{aligned}\quad (7.36)$$

and if m is in the scattered field zone

$$\begin{aligned}\hat{n}^m \times \vec{E}^{m+} &= \hat{n}^m \times (\vec{E}^{m+} - \vec{E}^{inc}) \\ \hat{n}^m \times \vec{H}^{m+} &= \hat{n}^m \times (\vec{H}^{m+} - \vec{H}^{inc})\end{aligned}\quad (7.37)$$

This technique can also be applied in a *reverse* way to incorporate the fields created by other sources (Hertzian dipoles, wire antennas, etc.). Let us assume that the sources are inside the SFZ, while the TFZ is outside. If we know the fields on the SFZ/TFZ interface, we can use them as incident fields in (7.36)(7.37), to get null fields inside SFZ and the original ones in the TFZ.

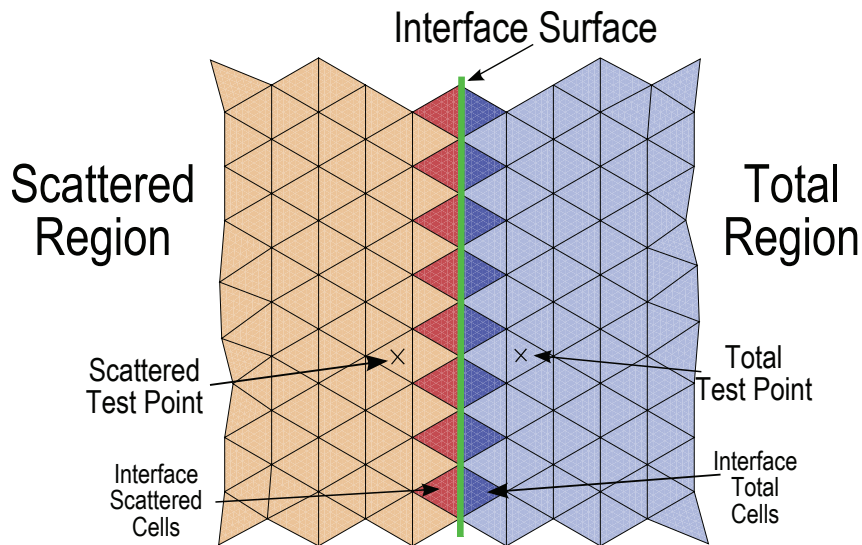


FIGURE 7.1: Total Field/Scattered Field decomposition.

This form of the Huygen's principle was successfully employed in [234] in a hybrid method implementation.

7.4 Results

We have implemented 3D codes, both with the scalar and vector-basis functions, and with the upwind and centered numerical fluxes, incorporating sources and ABCs (SM-ABC and PML). Second-order accurate centered differences (LF2) as well as fourth-order Runge-Kutta (RK4) schemes, have been used for the time integration. The study of the stability (and dispersion) of the resulting schemes will not be addressed here, and we have limited ourselves to derive heuristic estimations[124, 189] for the maximum time steps, yielding stable schemes in each case.

To validate the ideas presented in this paper, three simple examples are shown. Exhaustive side-by-side comparisons of the accuracy of scalar- and vector-DGTD are beyond the scope of this work, and they are left to a forthcoming publication.

7.4.1 Plane-wave generation

In order to test the TFZ/SFZ formulation, we have generated a known field inside the total field zone, and we have measured the field that escapes to the scattered field zone due to numerical errors. The TF zone consists of a 1m-side cube where a plane-wave is traveling with $\theta = 45^\circ$, $\Phi = 0^\circ$, and \vec{E} polarized along \hat{y} . The time

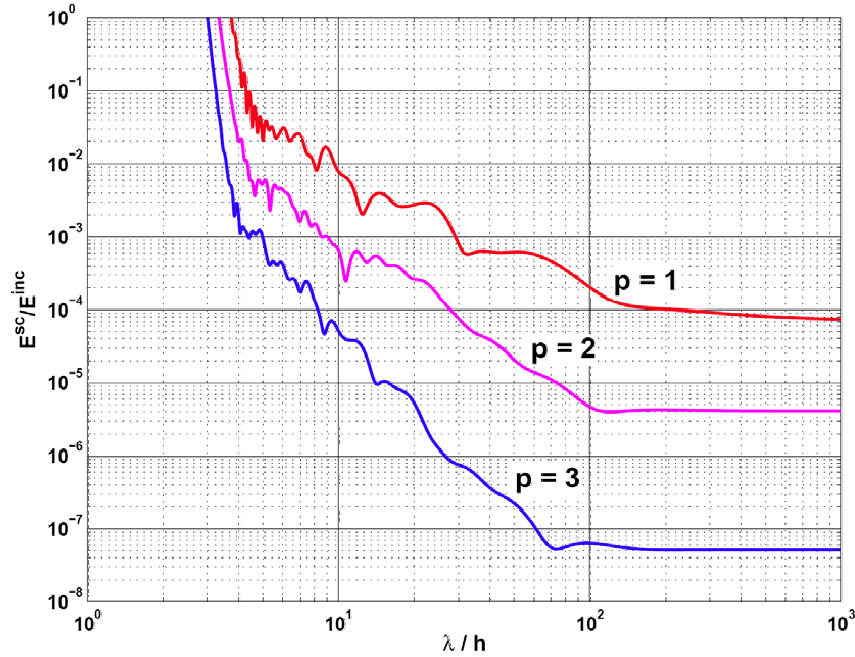


FIGURE 7.2: Scattered field error as a function of the minimum space resolution: $\frac{\lambda}{h}$. Vector centered–flux approximation. LF2.

variation is chosen to be a sine modulated by a Gaussian pulse

$$f(t) = e^{-\frac{t^2}{2\sigma^2}} \sin(2\pi ft) \text{ with } \sigma = 2\text{ns.}, f = 300\text{MHz} \quad (7.38)$$

Fig.7.2 shows the normalized field in a scattered–field point near the TFZ/SFZ interface (Fig.7.1) as a function of the minimum space resolution (minimum wavelength normalized to the maximum edge length), for different orders of the basis functions (1,2,3), using a hierarchal vector–basis DGTD, with the centered flux, and with a LF2–scheme in time. As in FDTD [235], the field that escapes from the TF zone, due to dispersion errors, decreases with the space resolution.

7.4.2 ABCs

To test the ABC performance, we have measured the energy decay with time in a cubic region (side=1m), with a Hertzian dipole at its center with the time variation given by (7.38). Fig. 7.3 shows results for the SM–ABCs, placed in a sphere (radius=0.5m) that is concentric with the dipole, found with scalar basis (Lagrange polynomials) of orders $p = 1, 2, 3$, upwind flux approximation, and with RK4–scheme in time. In this case the absorption of SM-ABCs is especially efficient because of the spherical nature of the waves impinging on the truncation boundary, which satisfies

the SM-ABCs principle. The Hertzian dipole illumination has been incorporated into DGTD using the reverse TFZ/SFZ formulation described above.

Finally, let us show in Fig. 7.4 results of the RCS in the E-plane of a 1m radius PEC sphere in a UPML-truncated region. We compare results found by FDTD (under conditions similar to those of DGTD) and Mie series solution, with DGTD results found with the centered flux approximation together with hierarchal vector-basis of orders $(\mathcal{G}_0, \mathcal{R}_1)$ and $(\mathcal{G}_1, \mathcal{R}_2)$ (with \mathcal{G}_n and \mathcal{R}_n being the n^{th} order gradient and rotational spaces), and with a LF2-scheme in time. We have used quadratic curvilinear tetrahedra (not detailed in the inset of Fig. 7.4) to further remove discretization errors. The sphere is illuminated with the TFZ/SFZ formulation described in this paper, by a plane wave with time variation (7.38). The UPML for the DGTD method is chosen to be a spherical crown (see inset of Fig. 7.4), with parabolic conductivity, and a theoretical reflection coefficient of -80 dB. For the FDTD method a parallelepiped crown with similar characteristics is chosen.

It bears noting from Figs. 7.4,7.5 that to achieve the accuracy of DGTD with $(\mathcal{G}_1, \mathcal{R}_2)$ (less than 1 dBsm almost everywhere), we needed to employ FDTD resolutions over 90 cells/ λ , requiring the solution of over $160 \cdot 10^6$ unknowns, while DGTD only needs $7.5 \cdot 10^6$ unknowns².

7.5 Conclusions

In this paper, we have described the implementation of boundary conditions and total field/scattered field zone separation into the DGTD method. We have made use of the concept of numerical flux to generate them, taking advantage of the similarities between FDTD and DGTD. A common framework to incorporate them into the different formulations of DGTD (vector/scalar basis, centered/upwind flux) has been described. These concepts have been numerically tested in canonical examples, and validated in RCS prediction, with extremely accurate results.

²Computational requirements in a 1.66Ghz Core 2 Duo T5500: FDTD \rightarrow Calculation speed= $14 \cdot 10^{-12}$, Memory=1104 Mb. DGTD $(\mathcal{G}_1, \mathcal{R}_2) \rightarrow$ Calculation speed= $126 \cdot 10^{-12}$, Memory= 300Mb. DGTD $(\mathcal{G}_0, \mathcal{R}_1) \rightarrow$ Calculation speed= $728 \cdot 10^{-12}$, Memory=60Mb. Calculation speed is given in terms of physical time normalized to the CPU time (e.g. a calculation speed of 10^{-12} implies that 1s is needed by the CPU to simulate a physical time of 1ps).

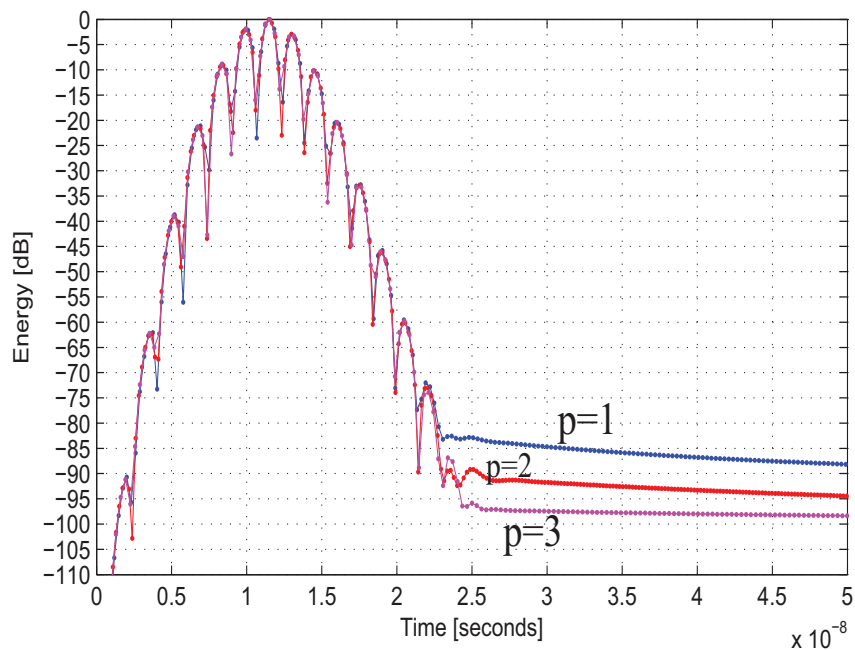


FIGURE 7.3: Energy decay with time in the simulation region. A centered dipole fed with a 300 MHz continuous wave modulated by a Gaussian pulse ($\sigma = 2\text{ns.}$) is placed at its center. Scalar upwind-flux formulation. SM-ABCs. RK4.

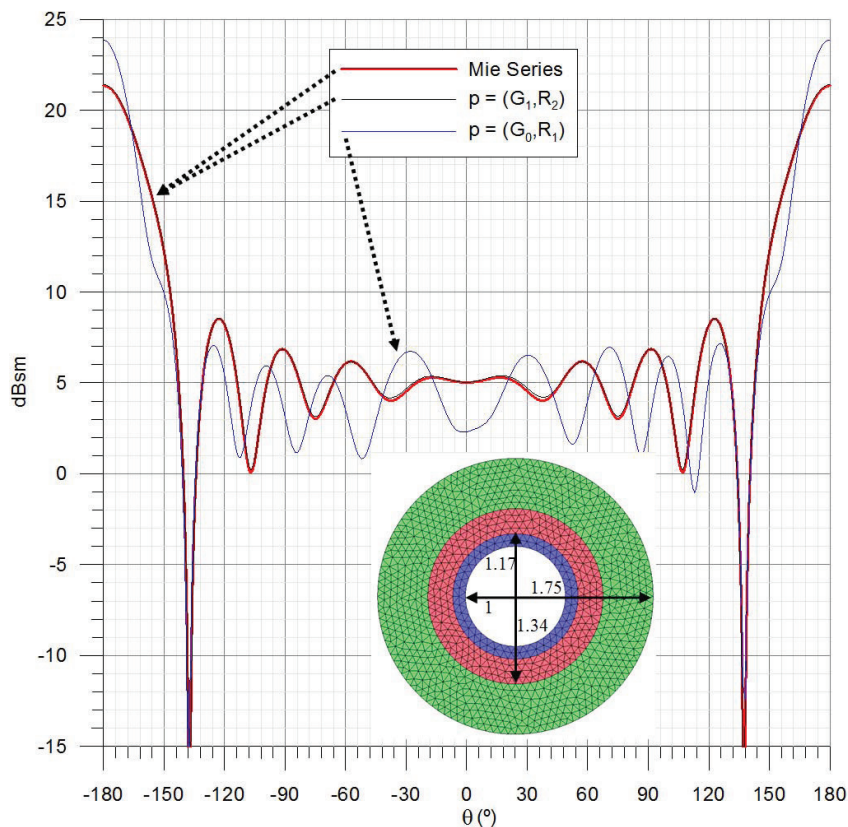


FIGURE 7.4: Bi-static RCS in the E-plane of a 1m radius PEC sphere at 300 MHz illuminated with a 300 MHz continuous wave modulated by a Gaussian pulse ($\sigma = 2\text{ns.}$). DGTD results. Vector centered-flux approximation. UPML, LF2. White sphere: PEC (1 m. radius). Blue crown: TF zone (1.17 m. ext. radius). Red crown: Maxwellian zone (1.34 m ext. radius). Green crown: UPML (1.75m ext. radius).

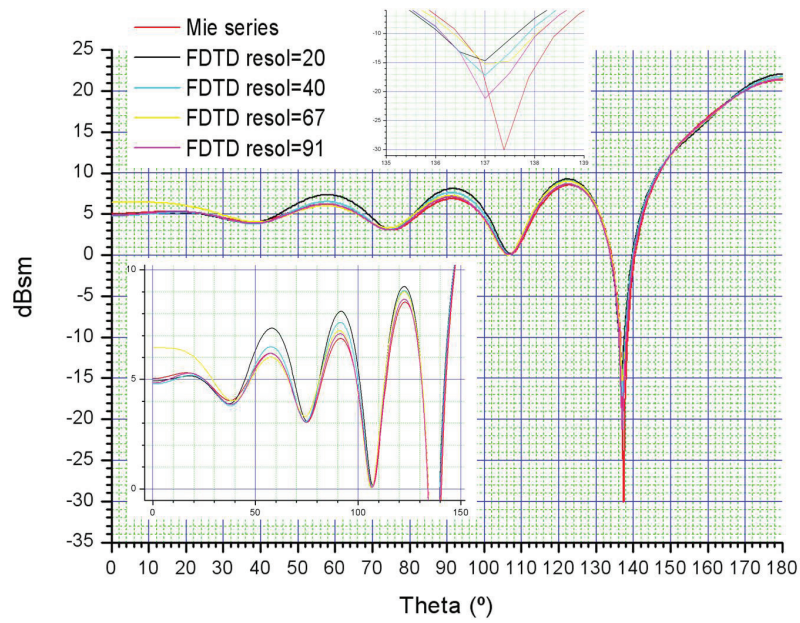


FIGURE 7.5: Bistatic RCS in the E-plane of a 1m radius PEC sphere at 300 MHz illuminated with a 300 MHz continuous wave modulated by a Gaussian pulse ($\sigma = 2\text{ns}$). FDTD results. UPML.

Acknowledgments

The authors wish to thank SPEAG for providing us the software SEMCAD X, employed in the FDTD simulations of this paper.

Chapter 8

3-D Discontinuous Galerkin Time-Domain Method for Anisotropic Materials

J. Alvarez, L. D. Angulo, A. Rubio Bretones, and S. Gonzalez Garcia. 3d discontinuous galerkin time-domain method for anisotropic materials. *Antennas and Wireless Propagation Letters, IEEE*, 11:1182–1185, 2012

Abstract

Discontinuous Galerkin, applied to time-dependent Maxwell equations (DGTD), offers attractive properties when compared to other numerical methods. This method is flexible and accurate, like the finite-elements method, and efficient as well as scalable like finite-difference time-domain algorithms. In this paper, a new rigorous treatment of anisotropic materials in three dimensions is described and validated for the upwind-flux DGTD method.

8.1 Introduction

The Discontinuous Galerkin Time Domain method (DGTD) is a variational numerical technique which is attracting attention in time-domain (TD) computational electromagnetics [10, 13, 27, 99, 157, 168, 191, 192, 195, 213]. Like the Finite Elements Methods (FEM), it employs a Galerkin test procedure to enforce a weak form of Maxwell's curl equations element by element, combined with a explicit differential integration scheme (e. g. leap-frog, Runge-Kutta,...) for the time part. Unlike in FEM, the solution is allowed to be fully discontinuous across the boundaries between adjacent elements, not requiring costly matrix inversions, but keeping FEM convergence properties. The result is an affordable marching-on-in-time algorithm, competitive with FDTD [10] (in terms of the ratio accuracy-to-computational burden), and easily parallelizable and highly scalable.

To connect the solution between elements sharing a common surface, continuous numerical fluxes of the tangential field components are defined at each interface, like in finite volume time domain (FVTD) methods [188, 236]. The most widely used flux condition is the upwind flux [27] found from the solution of the Riemann discontinuous initial value problem, which has been proven [13, 62] to yield spurious-free solutions.

In this paper, we describe and validate a new 3D upwind-flux DGTD method for lossy anisotropic media. Up to now, most formulations of the DGTD method have been restricted to isotropic and in some cases dispersive materials [157, 158, 213]. The treatment of anisotropic materials within a DGTD approach has been discussed in [99], where the authors employed the simple central flux, for which the limitations are well known [13, 62]. Recently, upwind flux conditions were found in [168] for 2D problems. In the present paper, new generalized upwind flux expressions in 3D are formulated, from which the [168] scheme can be regarded as a particular case.

8.2 DGTD fundamentals

As in FEM, we start by dividing the space into M non-overlapping elements V^m , bounded by a surface ∂V^m , in which a set of local continuous basis of vector test functions and two inner products (volume and surface) can be defined

$$\begin{aligned} \langle \vec{u}, \vec{w} \rangle_{V^m} &= \int_{V^m} (\vec{u} \cdot \vec{w}) dV, \quad \langle \vec{u}, \vec{w} \rangle_{\partial V^m} = \oint_{\partial V^m} (\vec{u} \cdot \vec{w}) dS \\ \mathcal{B}^m &= \{\vec{\Phi}_1^m, \vec{\Phi}_2^m, \dots, \vec{\Phi}_Q^m\}, \quad m = 1 \dots M \end{aligned} \quad (8.1)$$

Let us assume source-free TD Maxwell's curl equations for linear lossy anisotropic media in Cartesian coordinates¹, and let us enforce their residue to be orthogonal to each basis function element-by-element $\forall q = (1, \dots, Q)$

$$\left\langle \vec{\Phi}_q^m, \bar{\epsilon} \partial_t \vec{E}^m + \bar{\sigma}_e \vec{E}^m - \nabla \times \vec{H}^m \right\rangle_{V^m} = 0 \quad (8.2a)$$

$$\left\langle \vec{\Phi}_q^m, \bar{\mu} \partial_t \vec{H}^m + \bar{\sigma}_m \vec{H}^m + \nabla \times \vec{E}^m \right\rangle_{V^m} = 0 \quad (8.2b)$$

With \vec{E}, \vec{H} , electric and magnetic fields, and $\bar{\sigma}_e, \bar{\sigma}_m, \bar{\epsilon}$ and $\bar{\mu}$ being, respectively: electric conductivity, magnetic conductivity, permittivity and permeability tensors, varying in space. After some well-known algebra[13, 27] we can write, for instance, Eq. (8.2a) (and similarly Eq. (8.2b)) as

$$\int_{V^m} (\vec{\Phi}_q^m \cdot (\bar{\epsilon} \partial_t \vec{E}^m + \bar{\sigma}_e \vec{E}^m) + \nabla \times \vec{\Phi}_q^m \cdot \vec{H}^m) dV = \oint_{\partial V^m} \vec{\Phi}_q^m \cdot (\hat{\mathbf{n}}^m \times \vec{H}^{m*}) dS \quad (8.3)$$

This equation relates the volume integral of the LHS to a (surface) flux integral in the RHS of the tangential field of some intermediate value \vec{H}^{m*} (instead of \vec{H}^m as in continuous FEM), which permits the interchange of information between elements. \vec{H}^{m*} , as seen in the next section, depends on the electromagnetic field solutions at both sides of the interface. A common choice for this flux is the upwind one, taken from FVTD [188, 236], which is the solution of the one-dimensional Riemann problem in the normal direction to the discontinuity surface.

8.3 Riemann problem (isotropic case)

Let us first define a local set of coordinates on the interface (Fig. 8.1) between two adjacent elements (t_1, t_2, n) , and its associated orthonormal vector basis $(\hat{\mathbf{t}}_1, \hat{\mathbf{t}}_2, \hat{\mathbf{n}})$ at each position of the interface characterized by a vector \mathbf{r}

$$\hat{\mathbf{t}}_1 = \frac{\partial \mathbf{r}}{\partial t_1} \left| \frac{\partial \mathbf{r}}{\partial t_1} \right|^{-1}, \quad \hat{\mathbf{t}}_2 = \frac{\partial \mathbf{r}}{\partial t_2} \left| \frac{\partial \mathbf{r}}{\partial t_2} \right|^{-1}, \quad \hat{\mathbf{n}} = \hat{\mathbf{t}}_1 \times \hat{\mathbf{t}}_2 \quad (8.4)$$

The first two vectors are tangential to $\partial \mathcal{T}_m$, and the last one normal to it. The Maxwell-Ampere law, for instance, for isotropic lossy media can be written in this

¹Surface currents (for instance to generate plane-waves[10]) will be later taken into account by appropriate discontinuity conditions.

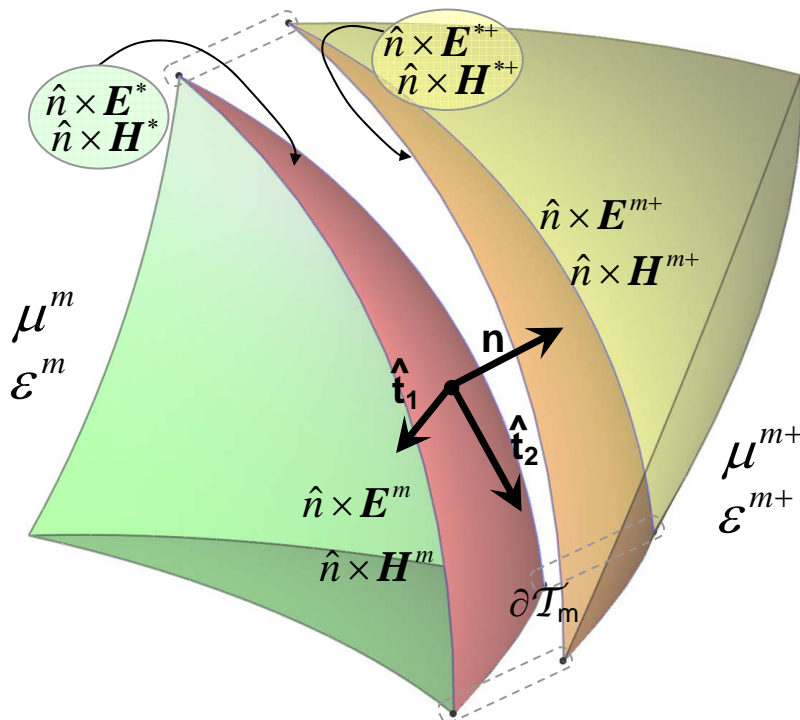


FIGURE 8.1: Surface interface $\partial\mathcal{T}_m$ between two elements containing different materials. Both tetrahedrons (physically in contact), have been represented as separate just for clarification.

basis as

$$\begin{aligned} \frac{\partial \mathbf{E}}{\partial t} - \frac{1}{\varepsilon} \frac{\partial}{\partial n} \hat{\mathbf{n}} \times \mathbf{H} - \frac{1}{\varepsilon} \nabla_S \times \mathbf{H} + \frac{\sigma_e}{\varepsilon} \mathbf{E} &= 0 \\ \nabla_S \times \mathbf{H} &= \partial_{t_2} H_n \hat{\mathbf{t}}_1 - \partial_{t_1} H_n \hat{\mathbf{t}}_2 + (\partial_{t_1} H_{t_2} - \partial_{t_2} H_{t_1}) \hat{\mathbf{n}} \end{aligned} \quad (8.5)$$

A common approach to find numerical schemes for multidimensional and/or hyperbolic problems with source terms², is to use an operation-splitting method [73, 237]. The idea is to split the problem into subproblems, so that different methods can be used to solve each of them. Let us split Eq. (8.5) into

$$\text{Problem A: } \frac{\partial \mathbf{E}}{\partial t} - \frac{1}{\varepsilon} \frac{\partial}{\partial n} \hat{\mathbf{n}} \times \mathbf{H} = 0 \quad (8.6a)$$

$$\text{Problem B: } \frac{\partial \mathbf{E}}{\partial t} - \frac{1}{\varepsilon} \nabla_S \times \mathbf{H} + \frac{\sigma_e}{\varepsilon} \mathbf{E} = 0 \quad (8.6b)$$

Observe that only Eq. (8.6a) involves (normal) derivatives, which are discontinuous at the surface, and Eq. (8.6b) involves element-wise continuous derivatives. Upwind flux is found by solving only the discontinuous (Riemann) problem [73] given by Eq. (8.6a), which can be rewritten at element m (and similarly at the adjacent one

²In the sense of [73], source terms are those not strictly belonging to the hyperbolic conservative problem: dissipative, terms to deal with dispersive or PML media, etc.

henceforth noted with the superindex $^+$)

$$\partial_t \bar{q}^m + \bar{\mathbb{A}}_n^m \partial_n \bar{q}^m = 0, \quad \bar{q}^m = (H_{t_1}^m, H_{t_2}^m, E_{t_1}^m, E_{t_2}^m)^T \quad (8.7)$$

$$\bar{\mathbb{A}}_n^m = \begin{pmatrix} 0 & 0 & 0 & -\frac{1}{\mu^m} \\ 0 & 0 & \frac{1}{\mu^m} & 0 \\ 0 & \frac{1}{\varepsilon^m} & 0 & 0 \\ -\frac{1}{\varepsilon^m} & 0 & 0 & 0 \end{pmatrix} \quad (8.8)$$

The system (8.7) is hyperbolic: $\bar{\mathbb{A}}_n$ is diagonalizable with four real eigenvalues (λ_p), and four linearly independent right eigenvectors (r_p) forming a basis. Eigenvalues have multiplicity two, and are opposite in sign (minus sign accounts for waves coming into the element, and plus sign for outgoing ones)

$$\begin{aligned} \lambda_1 = \lambda_2 &= \frac{-1}{\sqrt{\mu\varepsilon}}; r_1 = (0, -Y, 1, 0)^T, r_2 = (Y, 0, 0, 1)^T \\ \lambda_3 = \lambda_4 &= \frac{1}{\sqrt{\mu\varepsilon}}; r_3 = (0, Y, 1, 0)^T, r_4 = (-Y, 0, 0, 1)^T \end{aligned} \quad (8.9)$$

where $Z = \sqrt{\frac{\mu}{\varepsilon}} = \frac{1}{Y}$.

The Rankine-Hugoniot condition [73] states that the jump in the solution when crossing a characteristic (Fig. 8.1) is a linear combination of the eigenvectors associated with that characteristic; that is,

$$\bar{q}^* - \bar{q}^m = \alpha_1^m r_1^m + \alpha_2^m r_2^m \quad (8.10a)$$

$$\bar{q}^{m+} - \bar{q}^{*+} = \alpha_3^{m+} r_3^{m+} + \alpha_4^{m+} r_4^{m+} \quad (8.10b)$$

which can be solved for the α unknowns, assuming some relationship between \bar{q}^* , \bar{q}^{*+} . If no surface currents exist, we can assume $\bar{q}^* = \bar{q}^{*+}$; otherwise $\bar{q}^* \neq \bar{q}^{*+}$ and (8.10) must be solved jointly with

$$\hat{\mathbf{n}} \times (\mathbf{E}^{*+} - \mathbf{E}^*) = -\mathbf{M}_s, \quad \hat{\mathbf{n}} \times (\mathbf{H}^{*+} - \mathbf{H}^*) = \mathbf{J}_s \quad (8.11)$$

After some algebra we finally find

$$\hat{\mathbf{n}} \times \mathbf{E}^* = \frac{\hat{\mathbf{n}} \times (Y^m \mathbf{E}^m + Y^{m+} \mathbf{E}^{m+}) + Y^{m+} \mathbf{M}_s}{Y^m + Y^{m+}} - \tau \frac{\hat{\mathbf{n}} \times [\hat{\mathbf{n}} \times (\mathbf{H}^m - \mathbf{H}^{m+}) + \mathbf{J}_s]}{Y^m + Y^{m+}} \quad (8.12a)$$

$$\hat{\mathbf{n}} \times \mathbf{H}^* = \frac{\hat{\mathbf{n}} \times (Z^m \mathbf{H}^m + Z^{m+} \mathbf{H}^{m+}) - Z^{m+} \mathbf{J}_s}{Z^m + Z^{m+}} + \tau \frac{\hat{\mathbf{n}} \times [\hat{\mathbf{n}} \times (\mathbf{E}^m - \mathbf{E}^{m+}) - \mathbf{M}_s]}{Z^m + Z^{m+}} \quad (8.13a)$$

where $\bar{\varepsilon}$ and $\bar{\mu}$ and their inverse ($\bar{\varepsilon}' = \bar{\varepsilon}^{-1}$ and $\bar{\mu}' = \bar{\mu}^{-1}$, respectively) are expressed in the local vectorial basis (8.4).

To express the right eigenvectors of \bar{A}_n and compute the four eigenvalues

$$\det(\bar{A}_n - \lambda \mathbb{I}_4) = 0$$

, we need to define a new diagonalizable matrix \mathbb{M}_2 , whose eigenvalues (c_1^2 and c_2^2) are the square of the eigenvalues of the \bar{A}_n matrix ($-c_1$, $-c_2$, c_1 and c_2), according to

$$\mathbb{C}_2 = \begin{pmatrix} c_1 & 0 \\ 0 & c_2 \end{pmatrix}, \mathbb{M}_2 = \bar{\varepsilon}_2^{-1} \mathbb{D}_2^{-1} \bar{\mu}_2^{-1} \mathbb{D}_2 = \mathbb{R}_{\mathbb{M}_2} \mathbb{C}_2 \mathbb{C}_2^{-1} \mathbb{R}_{\mathbb{M}_2}^{-1} \quad (8.18)$$

where matrix $\mathbb{R}_{\mathbb{M}_2}$ contains its right eigenvectors as columns.

Now, we can diagonalize \bar{A}_n with its right eigenvectors and eigenvalues with the following expression,

$$\bar{A}_n = \frac{1}{\sqrt{2}} \begin{pmatrix} -Y_2 \mathbb{D}_2 \mathbb{R}_{\mathbb{M}_2} & Y_2 \mathbb{D}_2 \mathbb{R}_{\mathbb{M}_2} \\ \mathbb{R}_{\mathbb{M}_2} & \mathbb{R}_{\mathbb{M}_2} \end{pmatrix} \begin{pmatrix} -\mathbb{C}_2 & \mathbb{O}_2 \\ \mathbb{O}_2 & \mathbb{C}_2 \end{pmatrix} \frac{1}{\sqrt{2}} \begin{pmatrix} -\mathbb{R}_{\mathbb{M}_2}^{-1} \mathbb{Z}_2 \mathbb{D}_2^{-1} & \mathbb{R}_{\mathbb{M}_2}^{-1} \\ \mathbb{R}_{\mathbb{M}_2}^{-1} \mathbb{Z}_2 \mathbb{D}_2^{-1} & \mathbb{R}_{\mathbb{M}_2}^{-1} \end{pmatrix} \quad (8.19)$$

where we make use of two matrices, referred-to as "impedance" (\mathbb{Z}_2) and "admittance" (\mathbb{Y}_2), which are the anisotropic counterparts of the Z, Y isotropic magnitudes

$$\mathbb{Y}_2 = \bar{\mu}_2^{-1} \mathbb{D}_2 \mathbb{R}_{\mathbb{M}_2} \mathbb{C}_2^{-1} \mathbb{R}_{\mathbb{M}_2}^{-1} \mathbb{D}_2^{-1}, \mathbb{Z}_2 = \mathbb{R}_{\mathbb{M}_2} \mathbb{C}_2^{-1} \mathbb{R}_{\mathbb{M}_2}^{-1} \bar{\varepsilon}_2^{-1}$$

The Rankine–Hugoniot condition now requires the solution of four equations to account for the jumps across the four characteristics depicted in Fig. 8.3, each jump being a linear combination of the eigenvectors associated with that characteristic. After some algebra we find (for the source-free case, for writing simplicity) an expression formally similar to the isotropic case

$$\begin{aligned} \hat{\mathbf{n}} \times \mathbf{E}^* &= \left(\bar{Y}^m + \bar{Y}^{m+} \right)^{-1} \left[\bar{Y}^m \hat{\mathbf{n}} \times \mathbf{E}^m + \bar{Y}^{m+} \hat{\mathbf{n}} \times \mathbf{E}^{m+} + \hat{\mathbf{n}} \times \hat{\mathbf{n}} \times (\mathbf{H}^{m+} - \mathbf{H}^m) \right] \\ \hat{\mathbf{n}} \times \mathbf{H}^* &= \left(\bar{Z}^m + \bar{Z}^{m+} \right)^{-1} \left[\bar{Z}^m \hat{\mathbf{n}} \times \mathbf{H}^m + \bar{Z}^{m+} \hat{\mathbf{n}} \times \mathbf{H}^{m+} - \hat{\mathbf{n}} \times \hat{\mathbf{n}} \times (\mathbf{E}^{m+} - \mathbf{E}^m) \right] \end{aligned} \quad (8.20a)$$

where the \bar{Z}, \bar{Y} are tensors of dimension 3, completed from those of dimension 2. For instance for \bar{Z}

$$\bar{Z} = \begin{pmatrix} & & 0 \\ \mathbb{Z}_2 & & 0 \\ 0 & 0 & 1 \end{pmatrix} \quad (8.21)$$

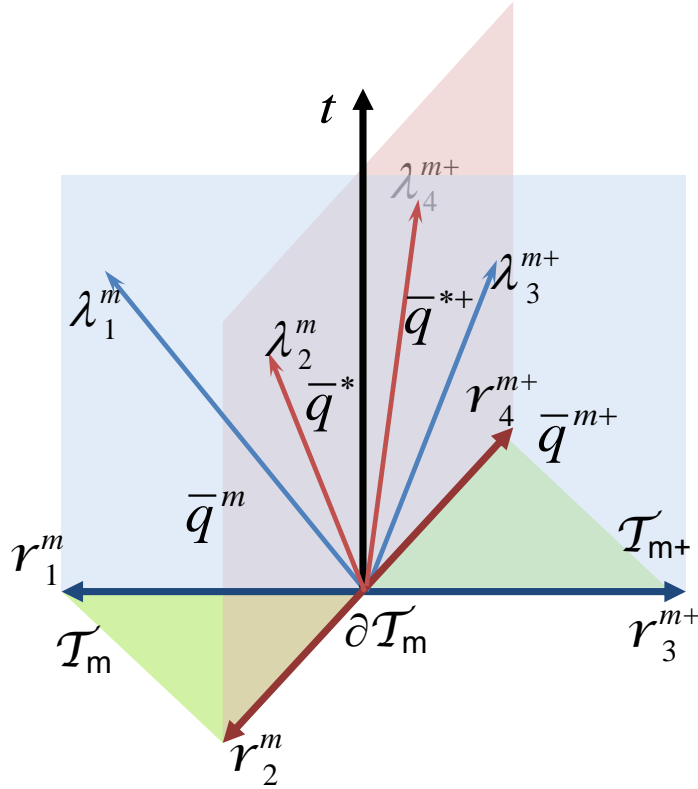


FIGURE 8.3: Space–time structure of the anisotropic Riemann problem.

8.5 Semi-Discrete Scheme

The final semi-discrete algorithm with the upwind flux at the element m for anisotropic materials (source-free and lossless for concise writing) becomes

$$\begin{aligned} \mathbb{M}_{\bar{\mu}} d_t H^m - \mathbb{F}_{\nu h} H^m + \mathbb{F}_{\nu h}^+ H^{m+} &= (\mathbb{F}_{\kappa e} - \mathbb{S}) E^m - \mathbb{F}_{\kappa e}^+ E^{m+} \\ \mathbb{M}_{\bar{\varepsilon}} d_t E^m - \mathbb{F}_{\nu e} E^m + \mathbb{F}_{\nu e}^+ E^{m+} &= (\mathbb{S} - \mathbb{F}_{\kappa h}) H^m + \mathbb{F}_{\kappa h}^+ H^{m+} \end{aligned}$$

- H^m , H^{m+} , E^m , and E^{m+} are column vectors holding all the time-dependent degrees of freedom.
- $\mathbb{M}_{\bar{\mu}}$ and $\mathbb{M}_{\bar{\varepsilon}}$ are the mass matrices,

$$[\mathbb{M}_{\bar{\mu}}]_{q'q} = \langle \phi_{q'}^m, \bar{\mu} \phi_q^m \rangle_{\mathcal{T}_m}, [\mathbb{M}_{\bar{\varepsilon}}]_{q'q} = \langle \phi_{q'}^m, \bar{\varepsilon} \phi_q^m \rangle_{\mathcal{T}_m}$$

- \mathbb{S} is the stiffness matrix (equal to the isotropic one)

$$[\mathbb{S}]_{q'q} = \langle \phi_{q'}^m, \nabla \times \phi_q^m \rangle_{\mathcal{T}_m}$$

- \mathbb{F} are the flux matrices

$$[\mathbb{F}_{\kappa h}]_{q'q} = \left\langle \phi_{q'}^m, \bar{\bar{R}} \bar{\bar{Z}}_s^{-1} \bar{\bar{Z}}^{m+} \bar{\bar{R}}^{-1} (\hat{\mathbf{n}}^m \times \phi_q^m) \right\rangle_{\partial\mathcal{T}_m}$$

$$[\mathbb{F}_{\kappa e}]_{q'q} = \left\langle \phi_{q'}^m, \bar{\bar{R}} \bar{\bar{Y}}_s^{-1} \bar{\bar{Y}}^{m+} \bar{\bar{R}}^{-1} (\hat{\mathbf{n}}^m \times \phi_q^m) \right\rangle_{\partial\mathcal{T}_m}$$

$$[\mathbb{F}_{\nu h}]_{q'q} = \left\langle \phi_{q'}^m, \bar{\bar{R}} \bar{\bar{Y}}_s^{-1} \bar{\bar{R}}^{-1} (\hat{\mathbf{n}}^m \times \hat{\mathbf{n}}^m \times \phi_q^m) \right\rangle_{\partial\mathcal{T}_m}$$

$$[\mathbb{F}_{\nu e}]_{q'q} = \left\langle \phi_{q'}^m, \bar{\bar{R}} \bar{\bar{Z}}_s^{-1} \bar{\bar{R}}^{-1} (\hat{\mathbf{n}}^m \times \hat{\mathbf{n}}^m \times \phi_q^m) \right\rangle_{\partial\mathcal{T}_m}$$

$$[\mathbb{F}_{\kappa h}^+]_{q'q} = \left\langle \phi_{q'}^{m+}, \bar{\bar{R}} \bar{\bar{Z}}_s^{-1} \bar{\bar{Z}}^{m+} \bar{\bar{R}}^{-1} (\hat{\mathbf{n}}^m \times \phi_q^{m+}) \right\rangle_{\partial\mathcal{T}_m}$$

$$[\mathbb{F}_{\kappa e}^+]_{q'q} = \left\langle \phi_{q'}^{m+}, \bar{\bar{R}} \bar{\bar{Y}}_s^{-1} \bar{\bar{Y}}^{m+} \bar{\bar{R}}^{-1} (\hat{\mathbf{n}}^m \times \phi_q^{m+}) \right\rangle_{\partial\mathcal{T}_m}$$

$$[\mathbb{F}_{\nu h}^+]_{q'q} = \left\langle \phi_{q'}^{m+}, \bar{\bar{R}} \bar{\bar{Y}}_s^{-1} \bar{\bar{R}}^{-1} (\hat{\mathbf{n}}^m \times \hat{\mathbf{n}}^m \times \phi_q^{m+}) \right\rangle_{\partial\mathcal{T}_m}$$

$$[\mathbb{F}_{\nu e}^+]_{q'q} = \left\langle \phi_{q'}^{m+}, \bar{\bar{R}} \bar{\bar{Z}}_s^{-1} \bar{\bar{R}}^{-1} (\hat{\mathbf{n}}^m \times \hat{\mathbf{n}}^m \times \phi_q^{m+}) \right\rangle_{\partial\mathcal{T}_m}$$

with $\bar{\bar{Z}}_s = (\bar{\bar{Z}}^m + \bar{\bar{Z}}^{m+})$, $\bar{\bar{Y}}_s = (\bar{\bar{Y}}^m + \bar{\bar{Y}}^{m+})$ and $\bar{\bar{R}}$ the basis-change matrix between the local basis (8.4) and the Cartesian basis.

A simple leap-frog marching-on-time algorithm is finally derived by replacing the time derivatives by second-order centered approximations.

8.6 Validation

For comparison, we have used two simple problems of scattering from a non-magnetic dielectric sphere ($\mu_r = 1$): the first one isotropic with $\varepsilon_r = 3.0$, and the second one anisotropic with

$$\bar{\bar{\varepsilon}}_r^{XYZ} = \begin{pmatrix} 3.0 & 0.0 & 0.0 \\ 0.0 & 3.0 & 0.0 \\ 0.0 & 0.0 & 4.0 \end{pmatrix} \quad (8.22)$$

The sphere is illuminated with a x-polarized plane wave, and the bi-static Radar Cross Section (RCS) is computed at a frequency for which the sphere diameter is $D = 1.2\lambda$, with λ being the wavelength. For reference, results from [2], computed with a Finite Element-Boundary Integral-Multilevel Fast Multipole Algorithm, are used. Figure 8.4 shows a good agreement between results found by both methods.

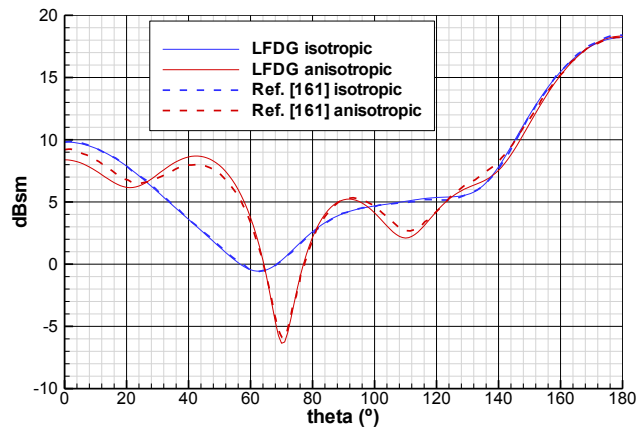


FIGURE 8.4: Bistatic RCS of an anisotropic/isotropic sphere ($D = 1.2\lambda$). Leap-frog DGTD results are compared to those appearing in [2].

8.7 Conclusions

In this paper, we have presented a systematic operation-splitting method for Maxwell curl equations. It has enabled us to split them into a hyperbolic (Riemann) discontinuous problem, and a continuous one. Upwind-flux conditions in DGTD for 3D anisotropic lossy materials, have been found by solving the Riemann problem and imposing the Rankine-Hugoniot jump conditions. Though applied to anisotropic media, the method found so far is general, and can be eventually extended to more complex situations.

Part V

On validation

Chapter 9

A leap-frog discontinuous Galerkin time-domain method for HIRF assessment

J. Alvarez, L. D. Angulo, A.R. Bretones, M.R. Cabello, and S.G. Garcia. A leap-frog discontinuous galerkin time-domain method for hirt assessment. *Electromagnetic Compatibility, IEEE Transactions on*, 55(6):1250–1259, 2013. ISSN 0018-9375. doi: 10.1109/TEMC.2013.2265045

Abstract

In this paper, we demonstrate the computational affordability and accuracy of a leap-frog discontinuous Galerkin (LFDG) time-domain method for HIRF assessment in EMC for aerospace. The conformal truncation of the computational domain is discussed and formulated in the LFDG context. Numerical validations are performed on challenging test cases, in comparison to measurements and to other numerical methods, demonstrating the accuracy, efficiency, and scalability of the algorithm.

9.1 Introduction

The adverse effects caused by High Intensity Radiated Fields (HIRF) in any electronic device or in a very complex system, such as an aircraft, is a challenging topic from the standpoint of computational electromagnetics (CEM). The typical approach to tackle this Electromagnetic Compatibility (EMC) problem is based mainly on testing. The development of efficient algorithms, able to deal with electrically large structures, and accurate methods, capable of estimating transfer functions between incident EM fields and internal fields, or induced currents in bundles, has recently been attracting a great deal of interest in the aerospace industry [16, 238]

Typical frequency-domain methods, such as the method of moments (MoM) or the finite element method (FEM), are able to cope with electrically large structures having electrically small details. However, the analysis of HIRF requires the computation of wideband frequency responses. In this context, frequency domain (FD) methods may become computationally inefficient, since each frequency needs one complete simulation requiring the resolution of a linear system of equations. Time domain (TD) methods are an attractive alternative for these purposes. Some well-known TD methods have been used traditionally in EMC: finite difference in time domain (FDTD) [37], transmission-line-matrix (TLM) method [239] and finite integral technique (FIT) [240]. All of these are based on a cubic space partitioning, which impose a significant constraint on the geometrical discretization of complex objects, having arbitrary curvatures and intricate details. To overcome this limitation, advances in finite elements in the time domain (FEMTD) methods have been made [44], to solve Maxwell's equations in complex geometries by using an unstructured mesh based, for instance, on tetrahedral tessellation. However, classical FEMTD methods are still computationally unaffordable for electrically large problems.

Among all FEMTD-based methods in the literature, discontinuous Galerkin time domain (DGTD) approaches are experiencing a fast development. On one hand, DGTD have most of the advantages of FDTD; spatial explicit algorithm, memory and computational cost only growing linearly with the number of elements, simplicity, and easy parallelization [27]. Furthermore Perfectly Matched Layer (PML) truncation techniques[140] can also be straightforwardly integrated into DGTD. Several formulations of PML exist; in this paper, we employ an auxiliary differential equation (ADE) implementation of the uniaxial PML (UPML) technique[142, 146, 150, 241], in a conformal formulation to achieve an optimum reduction of the computational domain. This conformal capability, with no counterpart in the FDTD context, has been successfully employed in finite-volume time-domain (FVTD) methods [41, 242, 243]

(which is equivalent to a low-order DGTD), and is highly appropriate for DGTD [64, 200, 213, 244].

On the other hand, DGTD schemes retain most of the benefits of FEM: adaptability of the unstructured meshes and spatial super-convergence, thus enabling problems to be met where the required precision varies over the entire domain, or when the solution lacks smoothness.

Regarding the time-integration scheme, two ones are commonly found in the DGTD literature: Runge-Kutta[27, 244] and Leap-Frog (LF)[124]. In this paper, we have chosen a second-order LF for providing a computationally efficient algorithm for which PML can be efficiently formulated.

In this paper, a LF algorithm (hereafter LFDG), including the conformal UPML, is described in some detail. We prove that this method is able to simulate very complex electromagnetic problems in an accurate manner, and validate it with a medium-sized 3D object, compared to measurement, and with an electrically large problem, compared to the well-known FDTD method. We have chosen those two benchmark problems for being available under the HIRF-SE [245] 7PM EU project for the validation of the numerical codes involved in that project [16].

9.2 Formulations

9.2.1 DG formulation

Let us assume Maxwell's symmetric curl equations for linear isotropic homogeneous media. Now, let us divide the space in M non-overlapping elements V^m , each bounded by ∂V^m and element-by-element define a set of local continuous basis of vector test functions and two inner products (volume and surface)

$$\mathcal{B}^m = \{\vec{\Phi}_1^m, \vec{\Phi}_2^m, \dots, \vec{\Phi}_Q^m\} \quad (9.1)$$

$$\langle \vec{u}, \vec{w} \rangle_{V^m} = \int_{V^m} (\vec{u} \cdot \vec{w}) dV, \quad \langle \vec{u}, \vec{w} \rangle_{\partial V^m} = \oint_{\partial V^m} (\vec{u} \cdot \vec{w}) dS \quad (9.2)$$

Enforcing the residue of Maxwell curl TD equations to be orthogonal to each basis function, we find

$$\left\langle \vec{\Phi}_{q'}^m, \varepsilon \partial_t \vec{E}^m + \sigma_e \vec{E}^m - \nabla \times \vec{H}^m \right\rangle_{V^m} = 0 \quad (9.3)$$

$$\left\langle \vec{\Phi}_{q'}^m, \mu \partial_t \vec{H}^m + \sigma_m \vec{H}^m + \nabla \times \vec{E}^m \right\rangle_{V^m} = 0 \quad (9.4)$$

$$\forall q = (1, \dots, Q) \ , \ m = (1, \dots, M)$$

With \vec{E} , \vec{H} , σ_e , σ_m , ε , μ being, respectively: electric and magnetic field in Cartesian coordinates, electric and magnetic conductivity, permittivity and permeability. After some algebra, we can write Eqs. (9.3) (and similarly Eqs. (9.4)) as

$$\begin{aligned} \int_{V^m} (\vec{\Phi}_{q'}^m \cdot (\varepsilon \partial_t \vec{E}^m + \sigma_e \vec{E}^m) + \nabla \times \vec{\Phi}_{q'}^m \cdot \vec{H}^m) dV = \\ \oint_{\partial V^m} \vec{\Phi}_{q'}^m \cdot (\hat{\mathbf{n}}^m \times \vec{H}^m) dS \end{aligned} \quad (9.5)$$

which relate the volume integral of the LHS to a flux integral in the RHS. Classical mixed FEMTD computes the RHS of (9.5) by enforcing the tangential component to be continuous at the interface across adjacent elements $\hat{\mathbf{n}}^m \times \vec{u}^m = \hat{\mathbf{n}}^m \times \vec{u}^{m+}$ (the superscript + denotes magnitudes from adjacent elements, and $\vec{u} = \{\vec{E}, \vec{H}\}$). However, DG defines continuous numerical fluxes of the tangential field components $\hat{\mathbf{n}}^m \times \vec{u}^{m*}$ to be used instead of $\hat{\mathbf{n}}^m \times \vec{u}^m$ at the RHS of (9.5), at each side of ∂V^m . These tangential fields do not coincide with any of the values at any side of ∂V^m , but depend linearly on them, with a general form

$$\begin{aligned} \hat{\mathbf{n}}^m \times \vec{E}^{m*} &= \hat{\mathbf{n}}^m \times \vec{E}^m + \kappa_e^m \left[\hat{\mathbf{n}}^m \times (\vec{E}^{m+} - \vec{E}^m) + \vec{M}_s \right] + \\ &\quad \nu_h^m \left[\hat{\mathbf{n}}^m \times (\hat{\mathbf{n}}^m \times (\vec{H}^{m+} - \vec{H}^m) - \vec{J}_s) \right] \\ \hat{\mathbf{n}}^m \times \vec{H}^{m*} &= \hat{\mathbf{n}}^m \times \vec{H}^m + \kappa_h^m \left[\hat{\mathbf{n}}^m \times (\vec{H}^{m+} - \vec{H}^m) - \vec{J}_s \right] - \\ &\quad \nu_e^m \left[\hat{\mathbf{n}}^m \times (\hat{\mathbf{n}}^m \times (\vec{E}^{m+} - \vec{E}^m) + \vec{M}_s) \right] \end{aligned} \quad (9.6)$$

with κ, ν appropriate coefficients (Table 9.1). In Eq. (9.6), we have included possible surface currents required for the implementation of Huygen's sources [10]. For further details on the general derivation of this numerical flux and the tuning of its parameters to yield spurious-free methods, see [13, 14].

Assuming that the space and time dependencies of the fields can be separated, and that the spatial part is expanded within each element in a set of basis functions

$\frac{\kappa_e^m}{Y^{m+}}$	$\frac{\kappa_h^m}{Z^{m+}}$	$\frac{\nu_h^m}{Y^{m+}Y^{m+}}$	$\frac{\nu_e^m}{Z^{m+}Z^{m+}}$
$\frac{Y^{m+}}{Y^{m+}Y^{m+}}$	$\frac{Z^{m+}}{Z^{m+}Z^{m+}}$	$\frac{\tau}{Y^{m+}Y^{m+}}$	$\frac{\tau}{Z^{m+}Z^{m+}}$

TABLE 9.1: Parameters in Eq. (9.6) functions of τ parameter, used to build a family of fluxes, ranging from the upwind flux ($\tau = 1$), to the centered flux ($\tau = 0$), going through the so-called partially penalized flux ($0 < \tau < 10$) [13, 14, 27, 62, 77, 113].

$Z^m = \sqrt{\frac{\mu^m}{\varepsilon^m}} = \frac{1}{Y^m}$ is the intrinsic impedance of the element m , and $Z^{m+} = \frac{1}{Y^{m+}}$ is that of the adjacent one, and

equal to the set of test functions (Faedo-Galerkin method)

$$\vec{E}^m = \sum_{q=1}^Q e_q^m(t) \vec{\Phi}_q^m(\vec{r}), \quad \vec{H}^m = \sum_{q=1}^Q h_q^m(t) \vec{\Phi}_q^m(\vec{r}) \quad (9.7)$$

a final semi-discrete algorithm is found

$$\begin{aligned} \mu \mathbb{M} d_t H^m + (\sigma_m \mathbb{M} - \mathbb{F}_{\nu h}) H^m + \mathbb{F}_{\nu h}^+ H^{m+} = \\ - (\mathbb{S} - \mathbb{F}_{\kappa e}) E^m - \mathbb{F}_{\kappa e}^+ E^{m+} - M^{s\kappa} + J^{s\nu} \end{aligned} \quad (9.8a)$$

$$\begin{aligned} \varepsilon \mathbb{M} d_t E^m + (\sigma_e \mathbb{M} - \mathbb{F}_{\nu e}) E^m + \mathbb{F}_{\nu e}^+ E^{m+} = \\ (\mathbb{S} - \mathbb{F}_{\kappa h}) H^m + \mathbb{F}_{\kappa h}^+ H^{m+} - J^{s\kappa} - M^{s\nu} \end{aligned} \quad (9.8b)$$

where

- H^m and E^m are column vectors varying in time with the field coefficients (degrees of freedom –dofs–) in the element m , and H^{m+} and E^{m+} with the field coefficients (dofs) of the adjacent elements,

$$H^m = (h_1^m(t), \dots, h_Q^m(t))^T \quad (9.9a)$$

$$E^m = (e_1^m(t), \dots, e_Q^m(t))^T \quad (9.9b)$$

- $M^{s\kappa}$, $M^{s\nu}$, $J^{s\kappa}$ and $J^{s\nu}$ are column vectors varying in time with the weak form of the surface source terms in the element m ,

$$M_{s\kappa} = \left(\left\langle \vec{\Phi}_1^m, \kappa_e^m \vec{M}_s(r, t) \right\rangle_{\partial V^m}, \dots \right)^T \quad (9.10a)$$

$$M_{s\nu} = \left(\left\langle \vec{\Phi}_1^m, \nu_e^m \hat{\mathbf{n}}^m \times \vec{M}_s(r, t) \right\rangle_{\partial V^m}, \dots \right)^T \quad (9.10b)$$

$$J_{s\kappa} = \left(\left\langle \vec{\Phi}_1^m, \kappa_h^m \vec{J}_s(r, t) \right\rangle_{\partial V^m}, \dots \right)^T \quad (9.10c)$$

$$J_{s\nu} = \left(\left\langle \vec{\Phi}_1^m, \nu_h^m \hat{\mathbf{n}}^m \times \vec{J}_s(r, t) \right\rangle_{\partial V^m}, \dots \right)^T \quad (9.10d)$$

- \mathbb{M} is the mass matrix,

$$[\mathbb{M}]_{q'q} = \left\langle \vec{\Phi}_{q'}^m, \vec{\Phi}_q^m \right\rangle_{V^m} \quad (9.11)$$

- \mathbb{S} is the stiffness matrix

$$[\mathbb{S}]_{q'q} = \left\langle \vec{\Phi}_{q'}^m, \nabla \times \vec{\Phi}_q^m \right\rangle_{V^m} \quad (9.12)$$

- \mathbb{F} are the flux matrices

$$[\mathbb{F}_{\kappa h}]_{q'q} = \left\langle \vec{\Phi}_{q'}^m, \kappa_h^m \hat{\mathbf{n}}^m \times \vec{\Phi}_q^m \right\rangle_{\partial V^m}$$

$$[\mathbb{F}_{\kappa e}]_{q'q} = \left\langle \vec{\Phi}_{q'}^m, \kappa_e^m \hat{\mathbf{n}}^m \times \vec{\Phi}_q^m \right\rangle_{\partial V^m} \quad (9.13a)$$

$$[\mathbb{F}_{\nu h}]_{q'q} = \left\langle \vec{\Phi}_{q'}^m, \nu_h^m \hat{\mathbf{n}}^m \times \hat{\mathbf{n}}^m \times \vec{\Phi}_q^m \right\rangle_{\partial V^m}$$

$$[\mathbb{F}_{\nu e}]_{q'q} = \left\langle \vec{\Phi}_{q'}^m, \nu_e^m \hat{\mathbf{n}}^m \times \hat{\mathbf{n}}^m \times \vec{\Phi}_q^m \right\rangle_{\partial V^m} \quad (9.13b)$$

$$[\mathbb{F}_{\kappa h}^+]_{q'q} = \left\langle \vec{\Phi}_{q'}^m, \kappa_h^m \hat{\mathbf{n}}^m \times \vec{\Phi}_q^{m+} \right\rangle_{\partial V^m}$$

$$[\mathbb{F}_{\kappa e}^+]_{q'q} = \left\langle \vec{\Phi}_{q'}^m, \kappa_e^m \hat{\mathbf{n}}^m \times \vec{\Phi}_q^{m+} \right\rangle_{\partial V^m} \quad (9.13c)$$

$$[\mathbb{F}_{\nu h}^+]_{q'q} = \left\langle \vec{\Phi}_{q'}^m, \nu_h^m \hat{\mathbf{n}}^m \times \hat{\mathbf{n}}^m \times \vec{\Phi}_q^{m+} \right\rangle_{\partial V^m}$$

$$[\mathbb{F}_{\nu e}^+]_{q'q} = \left\langle \vec{\Phi}_{q'}^m, \nu_e^m \hat{\mathbf{n}}^m \times \hat{\mathbf{n}}^m \times \vec{\Phi}_q^{m+} \right\rangle_{\partial V^m} \quad (9.13d)$$

9.2.2 LFDG algorithm

For the time-domain integration, several approaches can be chosen. The most commonly employed ones are the 4th-order Runge-Kutta (RK4) [27] and the 2nd-order Leap-Frog (LF) [124] scheme selected in this work. The basis of the LF scheme is to sample the unknown fields in a staggered way: the electric field is evaluated at $t_n = n\Delta t$, while the magnetic field, at $t_{n+\frac{1}{2}} = (n + \frac{1}{2}) \Delta t$. That is, Eq. (9.8a) is evaluated at t_n and Eq. (9.8b) at $t_{n+\frac{1}{2}}$. The first-order time derivatives are approximated by central differences, which are 2nd-order accurate.

$$(d_t H^m)_n = \frac{H_{n+\frac{1}{2}}^m - H_{n-\frac{1}{2}}^m}{\Delta t} + O(\Delta t^2)$$

$$(d_t E^m)_{n+\frac{1}{2}} = \frac{E_{n+1}^m - E_n^m}{\Delta t} + O(\Delta t^2) \quad (9.14)$$

For the terms with the electric and magnetic conductivity, we use an average approximation which is also a 2nd-order approximation of the identity operation.

$$H_n^m = \frac{H_{n+\frac{1}{2}}^m + H_{n-\frac{1}{2}}^m}{2} + O(\Delta t^2)$$

$$E_{n+\frac{1}{2}}^m = \frac{E_{n+1}^m + E_n^m}{2} + O(\Delta t^2) \quad (9.15)$$

For the two extra dissipative terms arising from the upwind flux formulation, we use the backward approximation ($H_n^m \simeq H_{n-\frac{1}{2}}^m$ and $E_{n+\frac{1}{2}}^m \simeq E_n^m$), since an average would yield a globally implicit scheme, due to the coupling terms from the adjacent elements [64]. This fact introduces a slight penalization in stability condition, and considering that purely upwind flux evaluation requires an also smaller time step, the alternative is the use of partially penalized flux evaluation [77]. When we choose an appropriate value of the τ parameter, the effect in the stability of the scheme is very low. In case of centered flux evaluation, these terms are null, but problems arise in relation to spurious modes [13].

When the temporal approximation for the dofs is inserted in (9.16), the resulting fully explicit LFDG algorithm becomes

$$\begin{aligned} H_{n+\frac{1}{2}}^m &= \alpha_m H_{n-\frac{1}{2}}^m \\ &+ \beta_m \mathbb{M}^{-1} \left[-(\mathbb{S} - \mathbb{F}_{\kappa e}) E_n^m - \mathbb{F}_{\kappa e}^+ E_n^{m+} + \mathbb{F}_{\nu h} H_{n-\frac{1}{2}}^m - \mathbb{F}_{\nu h}^+ H_{n-\frac{1}{2}}^{m+} - M_n^{s\kappa} + J_n^{s\nu} \right] \end{aligned} \quad (9.16a)$$

$$\begin{aligned} E_{n+1}^m &= \alpha_e E_n^m \\ &+ \beta_e \mathbb{M}^{-1} \left[(\mathbb{S} - \mathbb{F}_{\kappa h}) H_{n+\frac{1}{2}}^m + \mathbb{F}_{\kappa h}^+ H_{n+\frac{1}{2}}^{m+} + \mathbb{F}_{\nu e} E_n^m - \mathbb{F}_{\nu e}^+ E_n^{m+} - J_{n+\frac{1}{2}}^{s\kappa} - M_{n+\frac{1}{2}}^{s\nu} \right] \end{aligned} \quad (9.16b)$$

where the expressions for the constants are

$$\alpha_m = \frac{1 - \frac{\Delta t \sigma_m}{2\mu}}{1 + \frac{\Delta t \sigma_m}{2\mu}}, \quad \beta_m = \frac{\Delta t}{\mu \left(1 + \frac{\Delta t \sigma_m}{2\mu} \right)} \quad (9.17a)$$

$$\alpha_e = \frac{1 - \frac{\Delta t \sigma_e}{2\varepsilon}}{1 + \frac{\Delta t \sigma_e}{2\varepsilon}}, \quad \beta_e = \frac{\Delta t}{\varepsilon \left(1 + \frac{\Delta t \sigma_e}{2\varepsilon} \right)} \quad (9.17b)$$

9.2.3 Conformal UPML formulation

Let us consider the setup of Fig.9.1 used for the conformal UPML problem. There, the interface of the PML region with the homogeneous medium is the S surface. S' is a surface conformal to S containing the PML internal point P' , where we intend to formulate the UPML. Considering the projection of point P' into point P on S , we can define local coordinates as ξ_1, ξ_2 and ξ_3 , and both surfaces S and S' can be expressed as a functions of these local coordinates,

$$S \equiv f(\xi_1, \xi_2, \xi_3 = 0), \quad S' \equiv f(\xi_1, \xi_2) + \xi_3 \quad (9.18)$$

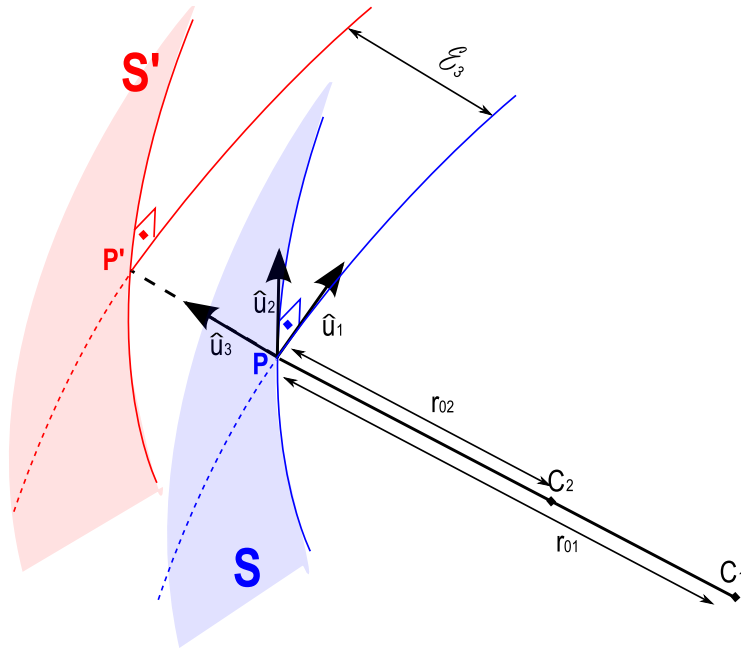


FIGURE 9.1: Conformal UPML setup.

Points of constant ξ_3 lie on parallel surfaces at a distance ξ_3 from S . An orthonormal local vector base can be defined as,

$$\hat{\mathbf{u}}_1 = u_1(\xi_1, \xi_2) = \frac{\partial \mathbf{r}}{\partial \xi_1} \left| \frac{\partial \mathbf{r}}{\partial \xi_1} \right|^{-1} \quad (9.19a)$$

$$\hat{\mathbf{u}}_2 = u_2(\xi_1, \xi_2) = \frac{\partial \mathbf{r}}{\partial \xi_2} \left| \frac{\partial \mathbf{r}}{\partial \xi_2} \right|^{-1} \quad (9.19b)$$

$$\hat{\mathbf{u}}_3 = \hat{\mathbf{u}}_1 \times \hat{\mathbf{u}}_2 \quad (9.19c)$$

related to the Cartesian base through the basis-change matrix $\bar{\bar{R}}$, and the principal radii of curvature of the doubly curved surfaces S and S' are

$$r_{01} = r_{01}(\xi_1, \xi_2), \quad r_{02} = r_{02}(\xi_1, \xi_2) \quad (9.20a)$$

$$r_1 = r_{01} + \xi_3, \quad r_2 = r_{02} + \xi_3 \quad (9.20b)$$

The UPML consists of a change on the metric of the space to the complex space in the vectorial base $(\hat{\mathbf{u}}_1, \hat{\mathbf{u}}_2, \hat{\mathbf{u}}_3)$ of the local coordinate ξ_3 . The spatial coordinates inside the PML are mapped to the complex variables domain as:

$$\xi_3 \longrightarrow \tilde{\xi}_3 = \int_0^{\xi_3} s(\tau) d\tau \quad (9.21)$$

where $s(\tau)$ is the complex stretching variable, which can take different expressions [242, 246]. In this work, the following expression has been used,

$$s(\tau) = 1 + \frac{1}{j\omega} \sigma_{max} \left(\frac{\tau}{\Delta\xi_3} \right)^2 \quad (9.22)$$

where $\Delta\xi_3$ is the PML thickness and σ_{max} the maximum conductivity in the PML. These two parameters characterize the PML layer and determine the rate of decay of the energy of the transmitted wave into the PML. The analytical reflection coefficient depends on the incident angle (θ) according to

$$R_0(\theta) = e^{-\frac{2}{3} \frac{\sigma_{max} \Delta\xi_3}{c} \cos(\theta)} \quad (9.23)$$

where $c = \frac{1}{\sqrt{\mu\varepsilon}}$ is the speed of propagation along $\hat{\mathbf{u}}_3$.

The change of the space metric of (9.21) and (9.22) can be easily implemented as an artificial anisotropic material [146, 150, 241], whose general metric tensor, in local coordinates, can be expressed in terms of three different conductivities, corresponding to each space direction, depending on the curvature radius and the distance to the S surface.

$$\bar{\bar{\Lambda}} = \begin{pmatrix} \frac{(1+\frac{\sigma_3}{j\omega})(1+\frac{\sigma_2}{j\omega})}{(1+\frac{\sigma_1}{j\omega})} & 0 & 0 \\ 0 & \frac{(1+\frac{\sigma_3}{j\omega})(1+\frac{\sigma_1}{j\omega})}{(1+\frac{\sigma_2}{j\omega})} & 0 \\ 0 & 0 & \frac{(1+\frac{\sigma_1}{j\omega})(1+\frac{\sigma_2}{j\omega})}{(1+\frac{\sigma_3}{j\omega})} \end{pmatrix} \quad (9.24)$$

with

$$\sigma_3(\xi_3) = \sigma_{max} \left(\frac{\xi_3}{\Delta\xi_3} \right)^2 \quad (9.25a)$$

$$\sigma_1(\xi_3) = \sigma_3 \frac{\xi_3}{3r_1} \quad (9.25b)$$

$$\sigma_2(\xi_3) = \sigma_3 \frac{\xi_3}{3r_2} \quad (9.25c)$$

The UPML can be expressed in the frequency domain in a Maxwellian form as

$$\nabla \times \mathbf{E} = -j\omega\mu \bar{\bar{R}} \bar{\bar{\Lambda}} \bar{\bar{R}}^{-1} \mathbf{H} \quad (9.26a)$$

$$\nabla \times \mathbf{H} = j\omega\varepsilon \bar{\bar{R}} \bar{\bar{\Lambda}} \bar{\bar{R}}^{-1} \mathbf{E} \quad (9.26b)$$

For simplicity, only one component of (9.26a) is written, and similar results can be found for the other components and (9.26b),

$$\begin{aligned}
(\nabla \times \mathbf{E})|_{\hat{\mathbf{u}}_1} &= -j\omega\mu \frac{\left(1 + \frac{\sigma_3}{j\omega}\right) \left(1 + \frac{\sigma_2}{j\omega}\right)}{\left(1 + \frac{\sigma_1}{j\omega}\right)} \mathbf{H}|_{\hat{\mathbf{u}}_1} \\
&= -j\omega\mu \mathbf{H}|_{\hat{\mathbf{u}}_1} - \mu(\sigma_3 + \sigma_2 - \sigma_1) \mathbf{H}|_{\hat{\mathbf{u}}_1} - \\
&\quad \mu \frac{(\sigma_3 - \sigma_1)(\sigma_2 - \sigma_1)}{j\omega + \sigma_1} \mathbf{H}|_{\hat{\mathbf{u}}_1}
\end{aligned} \tag{9.27}$$

Eq. (9.27) can be solved introducing an auxiliary field and an auxiliary partial differential equation. Fourier transform, using identity $j\omega f(\omega) \rightarrow (\partial/\partial t) f(t)$, is applied to formulate the equivalent differential equations in time-domain,

$$\left. \frac{\partial \mathbf{M}}{\partial t} \right|_{\hat{\mathbf{u}}_1} = -\sigma_1 \mathbf{M}|_{\hat{\mathbf{u}}_1} + \mu(\sigma_3 - \sigma_1)(\sigma_2 - \sigma_1) \mathbf{H}|_{\hat{\mathbf{u}}_1} \tag{9.28a}$$

$$\mu \left. \frac{\partial \mathbf{H}}{\partial t} \right|_{\hat{\mathbf{u}}_1} = -(\nabla \times \mathbf{E})|_{\hat{\mathbf{u}}_1} - \mu(\sigma_3 + \sigma_2 - \sigma_1) \mathbf{H}|_{\hat{\mathbf{u}}_1} - \mathbf{M}|_{\hat{\mathbf{u}}_1} \tag{9.28b}$$

Finally, the set of equation for the PML layer for the fields magnitudes \mathbf{E} , \mathbf{H} and the auxiliary fields (polarization currents) \mathbf{M} and \mathbf{J} , can be written as,

$$\frac{\partial \mathbf{M}}{\partial t} = -\bar{\bar{A}}_2 \mathbf{M} + \mu \bar{\bar{A}}_3 \mathbf{H} \tag{9.29a}$$

$$\mu \frac{\partial \mathbf{H}}{\partial t} = -\nabla \times \mathbf{E} - \mathbf{M} - \mu \bar{\bar{A}}_1 \mathbf{H} \tag{9.29b}$$

$$\frac{\partial \mathbf{J}}{\partial t} = -\bar{\bar{A}}_2 \mathbf{J} + \varepsilon \bar{\bar{A}}_3 \mathbf{E} \tag{9.29c}$$

$$\varepsilon \frac{\partial \mathbf{E}}{\partial t} = \nabla \times \mathbf{H} - \mathbf{J} - \varepsilon \bar{\bar{A}}_1 \mathbf{E} \tag{9.29d}$$

where the tensors $\bar{\bar{A}}_1$, $\bar{\bar{A}}_2$ and $\bar{\bar{A}}_3$ have the form,

$$\bar{\bar{A}}_1 = \bar{\bar{R}} \begin{pmatrix} \sigma_3 + \sigma_2 - \sigma_1 & 0 & 0 \\ 0 & \sigma_1 + \sigma_3 - \sigma_2 & 0 \\ 0 & 0 & \sigma_2 + \sigma_1 - \sigma_3 \end{pmatrix} \bar{\bar{R}}^{-1} \tag{9.30a}$$

$$\bar{\bar{A}}_2 = \bar{\bar{R}} \begin{pmatrix} \sigma_1 & 0 & 0 \\ 0 & \sigma_2 & 0 \\ 0 & 0 & \sigma_3 \end{pmatrix} \bar{\bar{R}}^{-1} \tag{9.30b}$$

$$\bar{\bar{A}}_3 = \bar{\bar{R}} \begin{pmatrix} (\sigma_2 - \sigma_1)(\sigma_3 - \sigma_1) & 0 & 0 \\ 0 & (\sigma_3 - \sigma_2)(\sigma_1 - \sigma_2) & 0 \\ 0 & 0 & (\sigma_1 - \sigma_3)(\sigma_2 - \sigma_3) \end{pmatrix} \bar{\bar{R}}^{-1} \tag{9.30c}$$

9.2.4 The LFDG algorithm in PML regions

The Galerkin procedure jointly with the DG spatial technique can be straightforwardly applied to (9.29), since curl terms in Eq. (9.29b) and (9.29d) do not change from regular Maxwell's equations. Hence, considering that the auxiliary fields are expanded with the same set of basis functions, and auxiliary differential equations are tested following Galerkin procedure, we find the following spatial semi-discrete scheme for the element m located in a PML region,

$$\mathbb{M}d_t M^m + \mathbb{M}_{A_2} M^m = \mu \mathbb{M}_{A_3} H^m \quad (9.31a)$$

$$\begin{aligned} \mu \mathbb{M}d_t H^m + (\mu \mathbb{M}_{A_1} - \mathbb{F}_{\nu h}) H^m + \mathbb{F}_{\nu h}^+ H^{m+} = \\ - (\mathbb{S} - \mathbb{F}_{\kappa e}) E^m - \mathbb{F}_{\kappa e}^+ E^{m+} - \mathbb{M} M^m \end{aligned} \quad (9.31b)$$

$$\mathbb{M}d_t J^m + \mathbb{M}_{A_2} J^m = \varepsilon \mathbb{M}_{A_3} E^m \quad (9.31c)$$

$$\begin{aligned} \varepsilon \mathbb{M}d_t E^m + (\varepsilon \mathbb{M}_{A_1} - \mathbb{F}_{\nu e}) E^m + \mathbb{F}_{\nu e}^+ E^{m+} = \\ (\mathbb{S} - \mathbb{F}_{\kappa h}) H^m + \mathbb{F}_{\kappa h}^+ H^{m+} - \mathbb{M} J^m \end{aligned} \quad (9.31d)$$

where

- $H^m, H^{m+}, E^m, E^{m+}, M^m$ and J^m are column vectors with the dofs varying in time as (9.9).
- \mathbb{M} is the mass matrix defined in (9.11) and $\mathbb{M}_{A_1}, \mathbb{M}_{A_2}$ and \mathbb{M}_{A_3} are mass matrices but affected by the tensors defined previously in (9.30),

$$[\mathbb{M}_{A_i}]_{q'q} = \left\langle \phi_{q'}^m, \bar{A}_i \phi_q^m \right\rangle_{\mathcal{T}_m} \quad \text{with } i = \{1, 2, 3\} \quad (9.32)$$

- \mathbb{S} is the stiffness matrix defined in (9.12).
- \mathbb{F} are the flux matrices defined in (9.13)

The extension of the leap-frog temporal integration scheme to the semi-discrete system of (9.31) is straightforward. The auxiliary unknown field \mathbf{M} must be evaluated at $t_n = n\Delta t$, as the electric field, and the auxiliary unknown field \mathbf{J} , at $t_{n+\frac{1}{2}} = (n + \frac{1}{2}) \Delta t$, as the magnetic field. In the same way, Eq. (9.31c) is tested at t_n , as Eq. (9.31b), and Eq. (9.31a) at $t_{n+\frac{1}{2}}$, as (9.31d).

Making the usual approximations described above (first-order time derivatives replaced by central differences, identity operators by averages for lossy terms, and backward formulas for the dissipative terms of the flux), we find the following fully

explicit algorithm for the PML medium,

$$M_n^m = \mathbb{A}_2 M_{n-1}^m + \mu \Delta t \mathbb{A}_3 H_{n-\frac{1}{2}}^m \quad (9.33a)$$

$$H_{n+\frac{1}{2}}^m = \mathbb{A}_{11} H_{n-\frac{1}{2}}^m + \beta_m \mathbb{A}_{12} \left[-(\mathbb{S} - \mathbb{F}_{\kappa e}) E_n^m - \mathbb{F}_{\kappa e}^+ E_n^{m+} + \mathbb{F}_{\nu h} H_{n-\frac{1}{2}}^m - \mathbb{F}_{\nu h}^+ H_{n-\frac{1}{2}}^{m+} - \mathbb{M} M_n^m \right] \quad (9.33b)$$

$$J_{n+\frac{1}{2}}^m = \mathbb{A}_2 J_{n-\frac{1}{2}}^m + \varepsilon \Delta t \mathbb{A}_3 E_n^m \quad (9.33c)$$

$$E_{n+1}^m = \mathbb{A}_{11} E_n^m + \beta_e \mathbb{A}_{12} \left[(\mathbb{S} - \mathbb{F}_{\kappa h}) H_{n+\frac{1}{2}}^m + \mathbb{F}_{\kappa h}^+ H_{n+\frac{1}{2}}^{m+} + \mathbb{F}_{\nu e} E_{n-1}^m - \mathbb{F}_{\nu e}^+ E_{n-1}^{m+} - \mathbb{M} J_{n+\frac{1}{2}}^m \right] \quad (9.33d)$$

where

$$\mathbb{A}_2 = \left(\mathbb{M} + \frac{\Delta t}{2} \mathbb{M}_{A_2} \right)^{-1} \left(\mathbb{M} - \frac{\Delta t}{2} \mathbb{M}_{A_2} \right) \quad (9.34a)$$

$$\mathbb{A}_3 = \left(\mathbb{M} + \frac{\Delta t}{2} \mathbb{M}_{A_2} \right)^{-1} \mathbb{M}_{A_3} \quad (9.34b)$$

$$\mathbb{A}_{11} = \left(\mathbb{M} + \frac{\Delta t}{2} \mathbb{M}_{A_1} \right)^{-1} \left(\mathbb{M} - \frac{\Delta t}{2} \mathbb{M}_{A_1} \right) \quad (9.34c)$$

$$\mathbb{A}_{12} = \left(\mathbb{M} + \frac{\Delta t}{2} \mathbb{M}_{A_1} \right)^{-1} \quad (9.34d)$$

It is important to note that in DG methods, the simplest absorbing boundary condition, equivalent to a first-order Silver-Müller (SM-ABC), can be applied with no cost, just setting the incoming flux to zero [10]. Hence, both (SM-ABC and C-UPML) can be used together, improving the overall performance [242].

9.3 Numerical Validation in HIRF

9.3.1 Medium size 3D Object

The first validation geometry has been taken from a test-case proposed under the HIRF-SE project [245] for cross-validation with measurements of several numerical solvers. It consists on a $600 \times 500 \times 300$ mm brass box, with the front face open (Fig. 9.2a), with a 30 mm wide flange around the edge. The box has two holes for N-type connectors on the top, labeled A and B in Fig. 9.2a. Between these holes, a curved-wire is connected (Fig. 9.2b), made up of three semi-circles and two vertical straight sections. Its endings are soldered into the N-Type bulkhead connectors A and B.

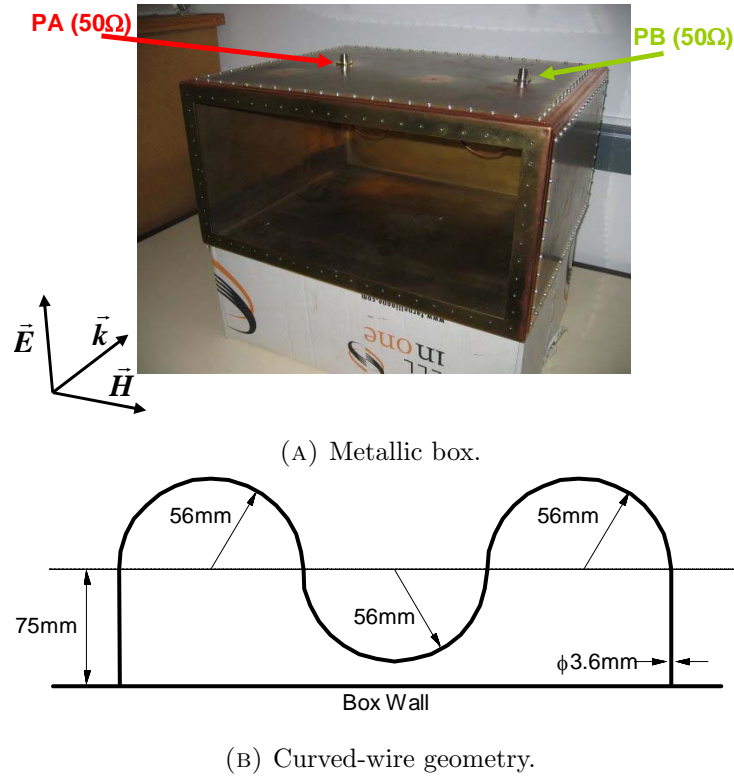


FIGURE 9.2: Setup of the medium size 3D object.

The box is illuminated perpendicularly to the open face using a linearly polarized plane wave, with electric vertical polarization, in the frequency band 1 to 6 GHz. The power received in the load of 50Ω at port A is taken for comparison (port B is grounded through a 50Ω load).

The results found with the LFDG algorithm described in this paper are shown in Fig.9.3. They are compared to measurements and FDTD simulations computed with the parallel UGRFDTD package [247]. Excellent agreement is found for LFDG and measurements.

9.3.2 Aircraft Simulation Case

The second problem consists of a 3D numerical test case based on a modified version of EVEKTOR's EV55 metallic aircraft (Fig.9.4), also taken as a workbench for cross-validation of several simulators under the HIRF-SE project[16]. The aircraft model consists on a PEC skin together with a generic part of the cabling¹. The electrical dimensions at 1 GHz are $53.7 \times 47.4 \times 17.1 \lambda$. The PEC shell is considered with zero thickness, and the cable is modeled as a PEC cylinder of radius 3cm. Some

¹The geometry files (both .igs and .gid format), disclosed by EVEKTOR, are publicly available upon request in the frame of the CEMEMC'13 HIRF-SE dissemination workshop (full info under www.cememc.org).

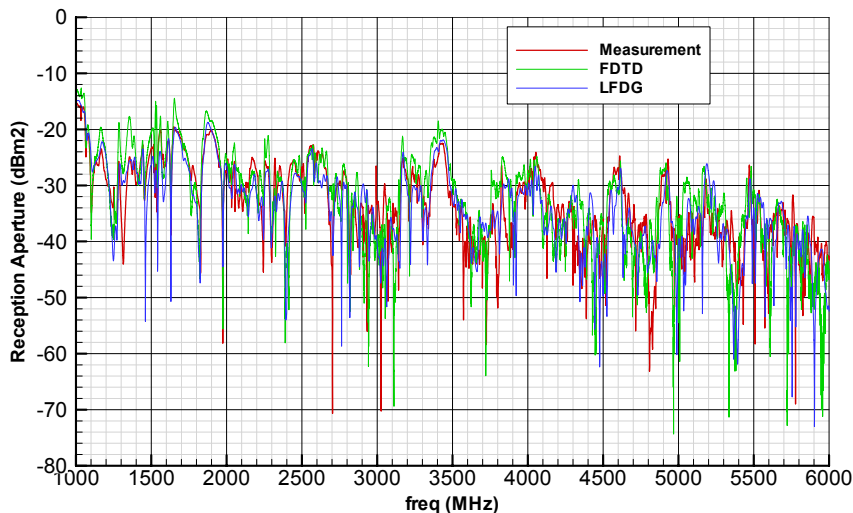


FIGURE 9.3: Reception aperture of the medium size 3D object, the reception aperture being the relation between the power received at port A, and the power density of the plane wave illuminating the box. Measurements are compared with results computed with LFDG and FDTD methods.

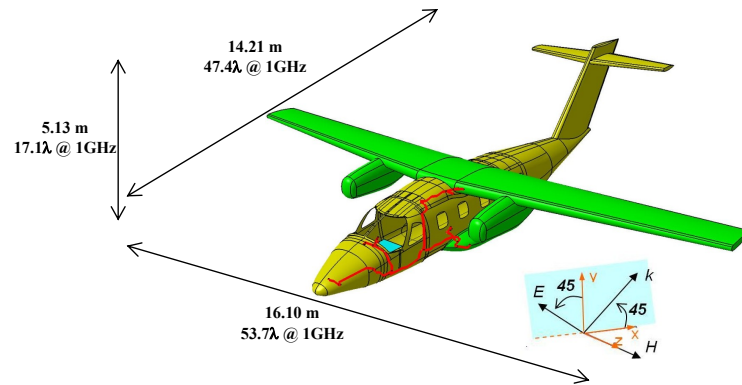
apertures exist in the aircraft shell, cockpit, and fuselage windows, which permit the electromagnetic energy to couple into the airframe, where there are simplified models for some of the systems and cavities. The aircraft is illuminated with a plane wave coming at 45° below its nose, with the magnetic field in the horizontal plane (Fig. 9.4a).

Three probes have been chosen for comparison, for being representative of different coupling scenarios (Fig. 9.4b):

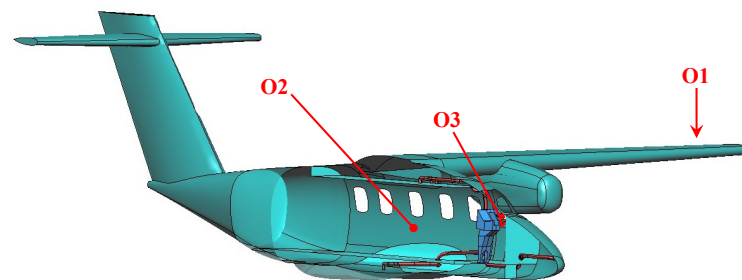
1. **O1.** The electric field at a surface test-point on top of the cockpit hidden from the illumination coming from underneath.
2. **O2.** The magnetic field in a point inside the airframe more weakly coupled to the illumination, and more susceptible to internal resonances.
3. **O3.** The current at the termination of one of the grounded cables.

All these quantities have been found in TD and computed in FD as transfer functions (normalized to the incident field).

The simulation setup is shown in Fig. 9.5. A total-field region is defined directly backed by the conformal PML interface. Thus, the scattered-field region is just the PML, with the subsequent computational saving. The surface at the total-field/PML interface layer is used to introduced the excitation as a Huygen's source, through the flux terms, using the approach in[10].



(A) External view and overall dimensions.



(B) Internal view and observation points.

FIGURE 9.4: External and internal geometry of the aircraft-simulation case. There is a cable modeled as a cylinder. There are some apertures in the aircraft shell, cockpit, and fuselage windows, and also different structures and cavities inside the airframe.

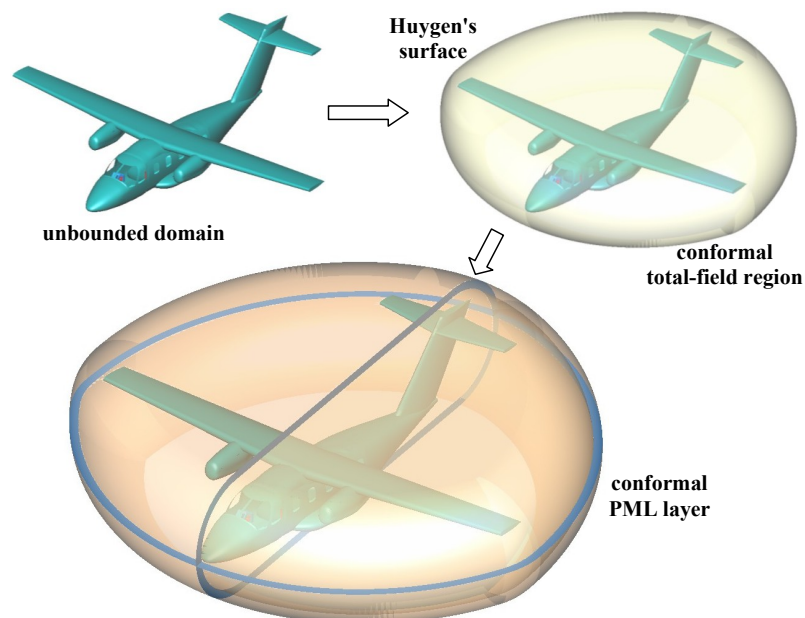


FIGURE 9.5: Simulation setup for the aircraft-simulation case. Starting with the unbounded domain (upper left), a total-field region (with a conformal Huygen's surface) is defined (upper right). Then, from this surface, the conformal PML layer can be created (lower). It should be noted that the scattered-field region is collapsed to the conformal Huygen's surface and is not needed, saving computational space.

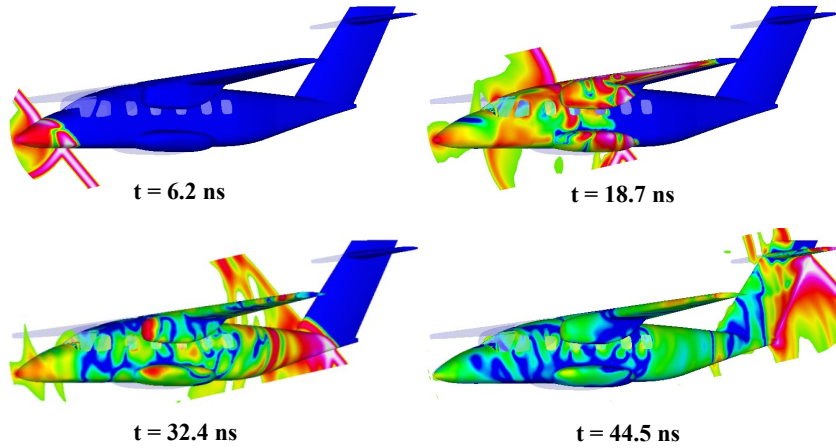


FIGURE 9.6: Screen shots of the aircraft-simulation case.

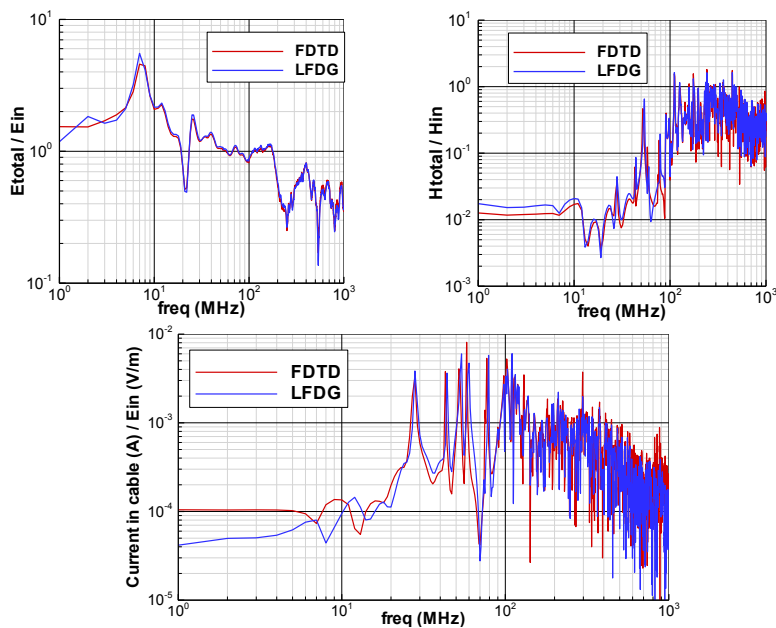


FIGURE 9.7: Computed transfer functions for the aircraft-simulation case. Comparison of results between LFDG and FDTD. Upper left: **O1**, upper right: **O2** and lower: **O3**

The plane-wave source uses a Gaussian pulse time signal, with 14 dB bandwidth at 1 GHz. The problem has been simulated up to a physical time of $1.0 \mu\text{s}$. Some screen shots of the simulation appear in Fig. 9.6, and results are shown in Fig. 9.7, in comparison with those found with FDTD, reflecting very good agreement.

Apart from the features described in this paper, the LFDG implementation makes use of two important techniques briefly described below:

- A *hp*-refinement heuristic strategy to choose the order of the basis function in each tetrahedron, depending on its size. To maintain uniform accuracy throughout the spatial domain, with reasonable computational effort, we used a higher-order basis for larger tetrahedra, and lower orders for smaller ones,

combining gradient spaces of reduced-order $p - 1$, with rotational spaces of complete order p . It is important to note that smaller elements need shorter time steps, but if a lower order is used in these elements, the condition is relaxed. In the same way, longer time-steps can be used for larger elements combined with higher orders. The combination and mixing of different orders of the basis functions depending on element size, makes the time step between all the elements more homogeneous. The numbers of elements and dofs per basis function set are shown in Table 9.2.

- Despite the adaptive hp-refinement described above, large differences in the maximum time steps for stability are found across the geometry. Thus, we have classified the elements according to this limit for the LF-scheme at several levels, and we employed different time-steps for each level. This technique, which is known as local time stepping (LTS) [77, 93, 248], can provide dramatic savings in the CPU time. Details about the LTS for this particular simulation appear in Table 9.3.

In case of the FDTD simulation, the cell size has been constant of 12 mm ($\frac{\lambda}{25}$ at 1 GHz). In both cases, the expected accuracy² is about 10^{-2} per wavelength at 1 GHz. A comparison between LFDG and FDTD computational details is made in Table 9.4.

TABLE 9.2: Number of elements (M) for each set of basis functions for the Aircraft Simulation Case. GxRy stand for x order for the gradient space, y order for the curl space

	G1R1	G1R2	G2R2	G2R3	Total
M	96572	6018789	2729857	59	8845279
M (%)	1.09	68.05	30.86	6.710^{-4}	100.00
dofs(10^3)	3764.1	300665.0	204819.6	6.6	509255.2
dofs (%)	0.74	59.04	40.22	1.310^{-3}	100.00

TABLE 9.3: Local time stepping level distribution for the Aircraft Simulation Case.

	L1	(L1/L2)	L2	(L2/L3)	L3
M	880	980	125602	217506	8500311
M (%)	0.01	0.01	1.42	2.46	96.10
Δt (ps)	1.59	4.77	4.77	14.32	14.32

For this case, the memory and CPU time is about one order of magnitude larger for LFDG than for the UGRFDTD solver used here. In FDTD we use single precision

²Defining the accuracy as the L^2 -norm error per wavelength for a plane wave traveling in free space: $|e^{-jk_0\lambda} - e^{-j\tilde{k}_0\lambda}|$, λ being the wavelength, k_0 the analytical wavenumber, and \tilde{k}_0 the numerical one.

TABLE 9.4: FDTD vs LFDG Comparison.

Method	M(10^6) ¹	dofs(10^6) ²	min. Δt	max. Δt	steps ³	memory	CPU ⁴	M(10^6)/sg ⁵
LFDG	8.845	509.3	1.59 ps	14.32 ps	69837	256.6 GB	114 h	52.2
FDTD	703.704	4394.8	18.00 ps	18.00 ps	55556	36.1 GB	14 h	784

¹ Number of elements (M) are 2^{nd} order tetrahedra for LFDG and Yee-cells for FDTD.

² Double precision (8 bytes per dof) for LFDG. Single precision (4 bytes per dof) for FDTD.

³ Number of steps for the max. Δt . The computed physical time has been 1.0 μs .

⁴ CPU time corresponds to 10 processors Intel Xeon X5680 6 cores, 3.33Ghz.

Hybrid Open MP/MPI implementations are used in both cases.

⁵ Updated mega-elements per second for the highest LTS level.

Different orders p have been used for each cell (Table 9.2) for LFDG.

variables (the use of double precision does not usually improve FDTD performance). However, double precision is needed for LFDG, where we are using high-order functions, LTS and PML, in order to maintain accuracy and avoid instabilities due to round-off errors. Concerning computational costs, three remarks are due:

- The simplicity of the FDTD algorithm makes it easier for the compilers to obtain faster codes. Techniques such as vectorization and the better use of the cache memory are key for speeding up FDTD algorithms. Furthermore the workload balance for MPI-parallelization can be made in an almost perfect way.
- For LFDG, the LTS, PMLs and hp -adaptivity makes the workload prediction more difficult, and the optimization of the MPI-parallelization. For instance, during a complete iteration of the highest LTS level, the workload is not constant across the mesh in the different steps of the LTS algorithm.
- The mesh used in the FDTD is a simple uniform structured mesh. Thus, quite high discretization errors are expected because of the staircasing effect. Moreover, the FDTD mesh parses out details smaller than the cell size, which can be an advantage for electrically irrelevant details, or a source of errors otherwise. In this case, for instance, if a non-uniform mesh had been used, with a smallest cell of 2.0 mm, the CPU time for UGRFDTD would have been very similar to that of the LFDG scheme. In the case of LFDG, where curvilinear 2^{nd} -order tetrahedra have been used, the discretization error is very small. Furthermore, the FEM mesh resolved every detail present in the geometrical model. This fact, concerning accuracy, is clearly appreciated in the first test-case presented above, where we compare with measurements.

9.4 Conclusions

In this paper, we have presented a highly accurate LFDG algorithm. To deal with open problems under HIRF conditions, we formulated the conformal UPML in the DG context. The proposed LTS strategy for the LF time-integration scheme, allows the applicability of the algorithm to electrically large problems. The LFDG scheme, as a FEMTD method, retains most of the goods of FEM, adaptability of the unstructured meshes and spatial super-convergence, considering the use of different order p of the basis functions, which allows us to deal with problems where the required precision varies over the entire domain, or where the solution lacks smoothness. This feature overcomes most of the limitations of FDTD, its inability to effectively handle complex geometries, due to staircasing errors, and the limitations in the accuracy (second order in space and time $O(h^2, \Delta t^2)$). In addition, the LFDG algorithm offers most of the advantages of FDTD: spatial explicit algorithm, simplicity, easy parallelization, and memory and computational cost growing linearly with the number of elements.

Chapter 10

DGTD for a Class of Low-Observable Targets: A Comparison with MoM and (2,2) FDTD

J. Alvarez, J. M. Alonso-Rodriguez, H. Carbajosa-Cobaleda, M. R. Cabello, L. D. Angulo, R. Gomez-Martin, and S. G. Garcia. Dgtd for a class of low-observable targets: A comparison with mom and (2,2) ftdt. *IEEE Antennas and Wireless Propagation Letters*, 13:241–244, 2014. doi: 10.1109/LAWP.2014.2300699

Abstract

The simulation of low-observable targets requires high accuracy, both in the geometrical discretization as well as in the numerical solution of the electromagnetic problem. In this letter, we employ the well-known NASA almond, to illustrate the accuracy of the Leap-Frog Discontinuous Galerkin method, combined with a local time stepping algorithm, comparing it with the MoM and the (2,2) FDTD methods.

10.1 Introduction

The analysis of the electromagnetic scattering by low observable (LO) targets is a challenging problem for numerical solvers. Frequency Domain (FD) methods, like the Method of Moments (MoM) [249], are a common choice to accurately deal with these problems. However, MoM-FD methods become computationally inefficient for wideband computations, since each frequency needs a complete simulation. Time-domain (TD) methods are an attractive alternative, since they employ a marching-on-in-time algorithm that permits to find the whole FD behavior with a single simulation. Among TD methods, the Finite-Difference Time-Domain (FDTD) method [37] has become very popular for its versatility and power, though its staircased nature imposes a significant constraint on the discretization of arbitrary curvatures and intricate details. Finite Element Methods in TD (FEMTD)[44] permit to overcome these limitations, thanks to the use of unstructured meshes to handle geometrical details. Nevertheless, they are computationally intensive because of their implicit nature, which requires the solution of a sparse linear system of equations at each step of the time marching procedure. Explicit FEMTD algorithms have been proposed based on sparse approximate inverses, efficiently implemented on parallel machines [34].

The Discontinuous Galerkin Time Domain (DGTD) methods are currently attracting an increasing attention [27], for combining some of the advantages of FDTD and FEMTD methods. The main difference between DGTD and other FEMTD methods, is that the solution is allowed to be discontinuous across the boundaries between adjacent elements, which communicate by means of numerical fluxes. The result are computationally affordable and accurate TD algorithms.

In this letter, we apply a DGTD method [13, 18] based on the Leap-Frog (LF) time integration scheme (LFDG) and combined with a Local Time Stepping (LTS) strategy, to calculate the RCS of PEC and coated NASA almonds. This geometry has been chosen for being a challenging example of LO target used in the validation of numerical solvers[250]. Results show that the LTS-LFDG method can be competitive with MoM-FD, and the (2,2) FDTD, methods, in terms of accuracy vs. computational time.

10.2 LFDG fundamentals

Let us begin by describing briefly the fundamentals of the DGTD method (further details of the implementation used by the authors can be found in [13, 15, 18,

221]). The DGTD method is based on a finite-element geometrical discretization of the space into M non-overlapping elements V^m , where we define element-by-element a basis of local continuous vector test functions ($\mathcal{B}^m = \{\vec{\Phi}_1^m, \vec{\Phi}_2^m, \dots, \vec{\Phi}_Q^m\}$), used both to expand the electromagnetic field, and as test functions to find a weak form of Maxwell curl equations (Galerkin procedure). For lossless linear isotropic homogeneous media, we have

$$\left\langle \vec{\Phi}_{q'}^m, \mu \partial_t \vec{H}^m + \nabla \times \vec{E}^m + \sigma_m \mathbf{H} \right\rangle_{V^m} = 0 \quad (10.1)$$

$$\left\langle \vec{\Phi}_{q'}^m, \varepsilon \partial_t \vec{E}^m - \nabla \times \vec{H}^m + \sigma_e \mathbf{E} \right\rangle_{V^m} = 0 \quad (10.2)$$

$$\forall q = (1, \dots, Q) \ , \ m = (1, \dots, M)$$

with \vec{E} , \vec{H} , σ_e , σ_m , ε , μ being, respectively: the electric and magnetic field, the electric and magnetic conductivity, permittivity, and permeability. Applying the discontinuous Galerkin method [27] to Eqs. (10.1) and (10.2), we can formulate the following semi-discrete spatial algorithm:

$$\begin{aligned} \mu \mathbb{M} d_t H^m + (\sigma_m \mathbb{M} - \mathbb{F}_{\nu h}) H^m + \mathbb{F}_{\nu h}^+ H^{m+} &= (\mathbb{F}_{\kappa e} - \mathbb{S}) E^m - \mathbb{F}_{\kappa e}^+ E^{m+} \\ \varepsilon \mathbb{M} d_t E^m + (\sigma_e \mathbb{M} - \mathbb{F}_{\nu e}) E^m + \mathbb{F}_{\nu e}^+ E^{m+} &= (\mathbb{S} - \mathbb{F}_{\kappa h}) H^m + \mathbb{F}_{\kappa h}^+ H^{m+} \end{aligned} \quad (10.3)$$

where H^m and E^m are column vectors with the degrees of freedom (dofs) at the element m , and H^{m+} and E^{m+} the dofs at the adjacent elements. \mathbb{M} is the mass matrix, \mathbb{S} is the stiffness matrix, and \mathbb{F} are the flux matrices [10]. The resulting method has a spatial error behaving as $O(h^{2p+1})$, with h a measure of the size of the elements, and p the order of the basis functions [13].

The time integration, can be performed in different manners [27]. In this paper, we use a 2^{nd} -order Leap-Frog (LF) scheme, which employs a centered approximation for the time derivatives $\left(d_t U_n^m \approx \Delta t^{-1} \left(U_{n+\frac{1}{2}}^m - U_{n-\frac{1}{2}}^m \right) \right)$ in (10.3), to yield¹

$$\begin{aligned} H_{n+\frac{1}{2}}^m &= \alpha_m H_{n-\frac{1}{2}}^m + \beta_m \mathbb{M}^{-1} \left[-(\mathbb{S} - \mathbb{F}_{\kappa e}) E_n^m - \mathbb{F}_{\kappa e}^+ E_n^{m+} + \right. \\ &\quad \left. \mathbb{F}_{\nu h} H_{n-\frac{1}{2}}^m - \mathbb{F}_{\nu h}^+ H_{n-\frac{1}{2}}^{m+} - M_n^{s\kappa} + J_n^{s\nu} \right] \end{aligned} \quad (10.4)$$

$$\begin{aligned} E_{n+1}^m &= \alpha_e E_n^m + \beta_e \mathbb{M}^{-1} \left[(\mathbb{S} - \mathbb{F}_{\kappa h}) H_{n+\frac{1}{2}}^m + \mathbb{F}_{\kappa h}^+ H_{n+\frac{1}{2}}^{m+} + \right. \\ &\quad \left. \mathbb{F}_{\nu e} E_n^m - \mathbb{F}_{\nu e}^+ E_n^{m+} - J_{n+\frac{1}{2}}^{s\kappa} - M_{n+\frac{1}{2}}^{s\nu} \right] \end{aligned} \quad (10.5)$$

¹A backward approximation for the terms $H_n^m \approx H_{n-\frac{1}{2}}^m$ and $E_{n+\frac{1}{2}}^m \approx E_n^m$, and an average approximation for the conductive terms $H_n^m \approx \frac{1}{2} (H_{n+\frac{1}{2}}^m + H_{n-\frac{1}{2}}^m)$ and $E_{n+\frac{1}{2}}^m \approx \frac{1}{2} (E_{n+1}^m + E_n^m)$ are also used.

where the expressions for the constants are

$$\alpha_m = \frac{1 - \frac{\Delta t \sigma_m}{2\mu}}{1 + \frac{\Delta t \sigma_m}{2\mu}}, \quad \beta_m = \frac{\Delta t}{\mu \left(1 + \frac{\Delta t \sigma_m}{2\mu}\right)} \quad (10.6)$$

$$\alpha_e = \frac{1 - \frac{\Delta t \sigma_e}{2\varepsilon}}{1 + \frac{\Delta t \sigma_e}{2\varepsilon}}, \quad \beta_e = \frac{\Delta t}{\varepsilon \left(1 + \frac{\Delta t \sigma_e}{2\varepsilon}\right)} \quad (10.7)$$

Local time-stepping strategies have been efficiently incorporated into the LF stepping procedure [77, 248] to alleviate the computational overload driven by the conditional stability of LF in real problems. Here, we use the LTS algorithm described in [15, 221], to arrange the mesh elements in different tiers, according to the maximum time step allowed for stability, so that different time steps can be used for each tier. An interpolation procedure is used at the interface between tiers.

10.3 MoM CCIE fundamentals

The MoM used in this comparison is applied to the Current and Change Integral Equation (CCIE) [251], combined with a Multilevel Fast Multipole Method (MLFMM) [252] to efficiently perform the matrix-vector products. CCIE introduces electric and magnetic surface charges densities, apart from the surface current densities of the Poggio-Miller-Chan-Harrington-Wu-Tsai (PM-CHWT) method [253], and solves a system of four integral equations for all four unknowns. The resulting scheme is well conditioned and leads to fast convergences with iterative solvers on a wide frequency range. Let us briefly summarize its fundamentals.

The time-harmonic ($e^{j\omega t}$) total electric and magnetic fields can be expressed on the surface of a homogeneous body as a function of the electric and magnetic surface charges densities (\vec{J}, \vec{M}) , and the electric and magnetic surface charges densities (ρ_e, ρ_m) as,

$$\vec{E} = \vec{E}^{in} - j\omega\mu\mathcal{S}(\vec{J}) + \frac{\mu}{j\omega\varepsilon}\mathcal{N}(\rho_e) - \mathcal{K}(\vec{M}) \quad (10.8a)$$

$$\vec{H} = \vec{H}^{in} - j\omega\varepsilon\mathcal{S}(\vec{M}) + \frac{\varepsilon}{j\omega\mu}\mathcal{N}(\rho_m) + \mathcal{K}(\vec{J}) \quad (10.8b)$$

with \vec{E}^{in} and \vec{H}^{in} being the incident fields, $\hat{\mathbf{n}}$ the inner unit normal of the surface, and \mathcal{S} , \mathcal{N} and \mathcal{K} the surface integral operators,

$$\mathcal{S}(\vec{f})(\vec{r}) = \int G(\vec{r}, \vec{r}') \vec{f}(\vec{r}') ds(\vec{r}') \quad (10.9a)$$

$$\mathcal{N}(f)(\vec{r}) = \int \nabla G(\vec{r}, \vec{r}') f(\vec{r}') ds(\vec{r}') \quad (10.9b)$$

$$\mathcal{K}(\vec{f})(\vec{r}) = \nabla \times \mathcal{S}(\vec{f})(\vec{r}) \quad (10.9c)$$

$G(\vec{r}, \vec{r}') = \frac{e^{-jkR}}{4\pi R}$, $R = |\vec{r} - \vec{r}'|$, is the usual free-space Green function, with $k = \omega\sqrt{\varepsilon\mu}$.

Considering the usual boundary conditions at the interface between two media (1 and 2),

$$\begin{aligned} \hat{\mathbf{n}}_2 \cdot (\varepsilon_2 \vec{E}_2 - \varepsilon_1 \vec{E}_1) &= \rho_e, \quad \hat{\mathbf{n}}_2 \cdot (\mu_2 \vec{H}_2 - \mu_1 \vec{H}_1) = \rho_m \\ \hat{\mathbf{n}}_2 \times (\vec{H}_2 - \vec{H}_1) &= \vec{J}, \quad \hat{\mathbf{n}}_2 \times (\vec{E}_2 - \vec{E}_1) = -\vec{M} \end{aligned} \quad (10.10a)$$

four surface Fredholm integral equations of the second kind can be formulated for the tangential and normal components of the fields,

$$\begin{pmatrix} \varepsilon \vec{E}_n^{in} \\ \mu \vec{H}_n^{in} \\ \vec{H}_t^{in} \\ -\vec{E}_t^{in} \end{pmatrix} = \begin{pmatrix} \mathcal{I} - \frac{\mu}{j\omega\varepsilon} \mathcal{N}_n & 0 & j\omega\mu \mathcal{S}_n & \mathcal{K}_n \\ 0 & \mathcal{I} - \frac{\varepsilon}{j\omega\mu} \mathcal{N}_n & -\mathcal{K}_n & j\omega\varepsilon \mathcal{S}_n \\ 0 & -\frac{\varepsilon}{j\omega\mu} \mathcal{N}_t & \mathcal{I} - \mathcal{K}_t & j\omega\varepsilon \mathcal{S}_t \\ \frac{\mu}{j\omega\varepsilon} \mathcal{N}_t & 0 & -j\omega\mu \mathcal{S}_t & \mathcal{I} - \mathcal{K}_t \end{pmatrix} \begin{pmatrix} \rho_e \\ \rho_m \\ \vec{J} \\ \vec{M} \end{pmatrix} \quad (10.11)$$

where $\vec{F}_n = \hat{\mathbf{n}} \cdot \vec{F}$ and $\vec{F}_t = \hat{\mathbf{n}} \times \vec{F}$. This set of equations together with the continuity conditions

$$\nabla \cdot \vec{J} + j\omega\rho_e = 0, \quad \nabla \cdot \vec{M} + j\omega\rho_m = 0 \quad (10.12)$$

form the CCIE system, which can be numerically solved by making use of the MoM method. Similarly to the CFIE, which combines EFIE and MFIE, a combined form of the CCIE is formulated, resulting into the CCCIE described in [251]. The continuity equations are taken into account by directly adding a combination of the null (10.12) to ρ_e and ρ_m of (10.8). This combination is crucial for the accurate behavior of the scheme along the whole frequency range [251]. The final algorithm is found by expanding the scalar unknowns (ρ_e, ρ_m) with pulse functions, and the vector unknowns (\vec{J}, \vec{M}) with the classical Rao-Wilton-Glisson (RWG) basis functions. In the same manner, the equations of rows 1 and 2 are tested with pulse functions, and rows 3 and 4 with RWG ones.

10.4 NASA Almond Benchmark

In this section, we find the Radar Cross-Section (RCS) of a typical LO target: the NASA almond. This geometry is a benchmark of the Electromagnetic Code Consortium, used for validation purposes[250]. The LTS-LFDG method[13], the MoM-MLFMM for CCCIE (HPTESP-MAT Cassidian tool, certified for RCS calculation by the Spanish Military Airworthiness Authority INTA [254]), and the well-known (2,2) FDTD method (UGRFDTD MPI/OpenMP parallel code [247], validated under the 7PM EU HIRF-SE project [245]), have been employed for this purpose.

The NASA almond (Fig.10.1) is composed by

$$\begin{aligned} &\text{Half ellipsoid: } -0.416667 < t < 0.0 \text{ and } -\pi < \psi < \pi \\ &\begin{cases} x = dt, \\ y = 0.193333 d \left(\sqrt{1 - \left(\frac{t}{0.416667} \right)^2} \right) \cos \psi, \\ z = 0.06444 d \left(\sqrt{1 - \left(\frac{t}{0.416667} \right)^2} \right) \sin \psi, \end{cases} \end{aligned} \quad (10.13a)$$

$$\begin{aligned} &\text{Half elliptic ogive: } -0.0 < t < 0.583333 \text{ and } -\pi < \psi < \pi \\ &\begin{cases} x = dt, \\ y = 4.833450 d \left(\sqrt{1 - \left(\frac{t}{2.083350} \right)^2} - 0.96 \right) \cos \psi, \\ z = 1.611148 d \left(\sqrt{1 - \left(\frac{t}{2.083350} \right)^2} - 0.96 \right) \sin \psi, \end{cases} \end{aligned} \quad (10.14a)$$

where $d = 2.5$ m, is the length of the structure. Note that this is a complete double curvature geometry, where we can find, both smoothly and sharply curved zones, as well as a singular point, the ogive vertex. Apart from a PEC case, two different coated material cases have been studied: with a perfect dielectric, and with a Radar Absorber Material (RAM), proposed under JINA 2006[255] (see Fig. 1 for details). For the LTS-LFDG method, we have discretized the surface with curvilinear 2^{nd} -order tetrahedrons. Care has been taken for the discretization close to the vertex by defining small elements (low value of h), as an *a priori* level of h-refinement (see Fig. 10.2). Apart from the vertex, we have defined a maximum element size h during the mesh-generation process, corresponding to the value of $\frac{h}{\lambda} = 0.4$ of the maximum frequency, which is efficient in terms of computational and required accuracy. Once we have generated the mesh, the order p in each element is chosen depending on the element size, assigning the minimum p that meets the required accuracy [15]. For instance, in the simplest case (PEC, bistatic RCS at 1 GHz), the mesh was

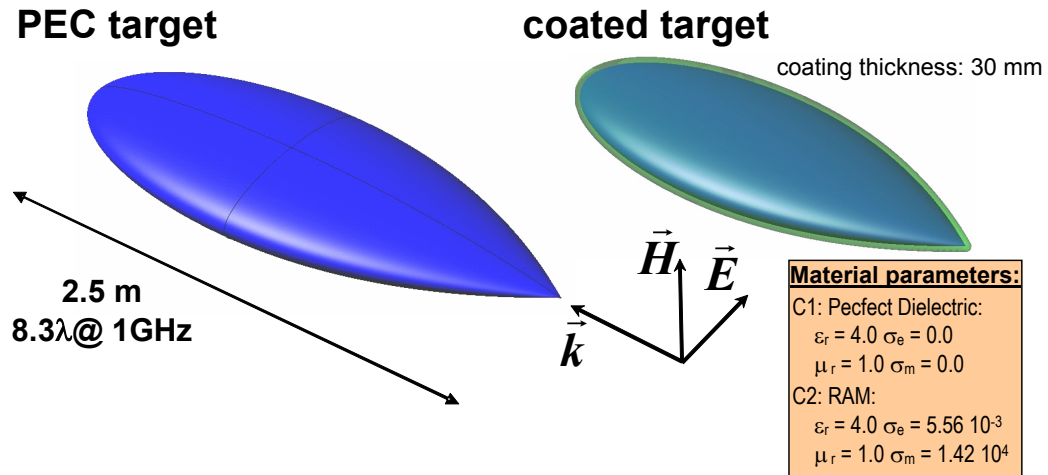


FIGURE 10.1: Geometry of the NASA almond.

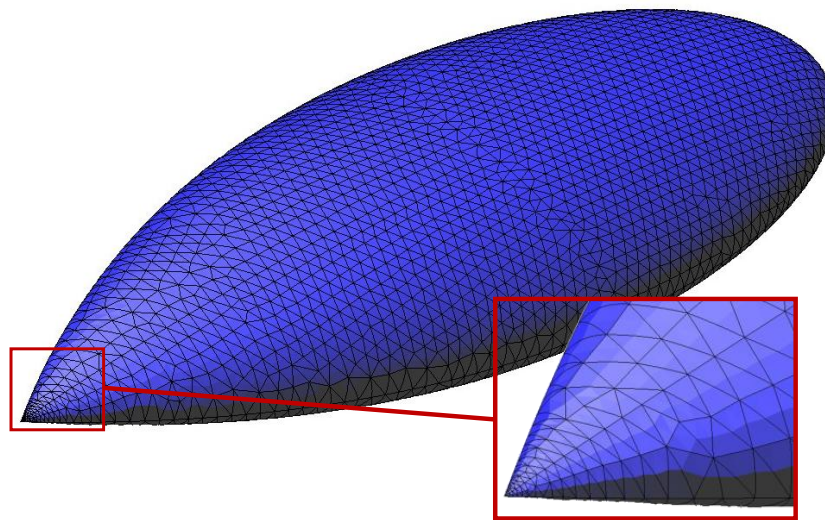


FIGURE 10.2: Snapshot of the mesh used for the PEC case computation. Only the surface mesh is shown.

composed of 2018928 elements: 785678 had $p=1$, 523786 had $p=2$, and 709464 had $p=3$, being the total number of unknowns $187 \cdot 10^6$. We do not use orders p higher than 3 since have been found not to be optimum in terms of computational cost and accuracy [15].

The simulation region is divided into a total-field zone, holding the almond, and a scattered-field zone. The surface between both regions serve to excite the plane-wave by Huygens sources, through the flux terms in a weak way[10]. The same surface is used to compute the near-to-far-field transformation and to calculate the RCS. Conformal PMLs [18, 150] are used to truncate the whole domain.

The structures are illuminated with a horizontally-polarized plane wave, impinging on the almond at the vertex. The resulting copolar bistatic RCS at 1 GHz, computed

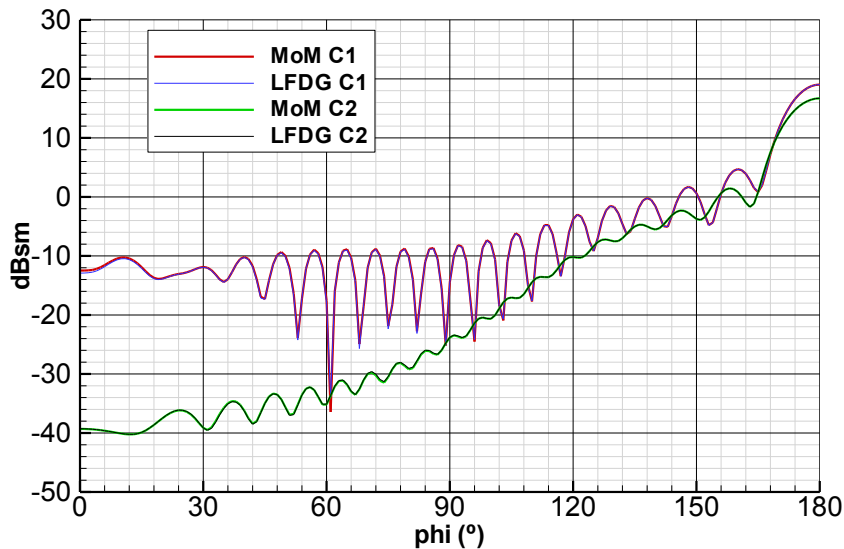


FIGURE 10.3: Bistatic Radar Cross Sections of the NASA almond at 1 GHz. Comparison results between LTS-LFDG and MoM for the coated almond.

with LTS-LFDG and compared the results with MoM, are shown in Fig. 10.3 for the three cases analyzed, with excellent agreement. The monostatic RCS from 500 MHz to 2 GHz is shown in Fig. 10.4. Excellent agreement is again found both for PEC and C2 (RAM material) cases. Minor differences are detected for the C1 (perfect dielectric) case. It is important to note that this is a challenging case for MoM, where the required number of iterations to solve iteratively the MoM linear system is quite high, and the number of unknowns cannot be too high in order to have a solution with affordable computational costs. Notice that the whole frequency band computation requires 301 runs. The minor differences found so far are, in our opinion, due to the use of a coarse mesh in the MoM computations.

In Fig. 10.5, we have also compared the PEC case with uniform-mesh FDTD simulations with a 1.5 mm cell length. A brute-force solution has been obtained with (2,2) FDTD just for comparison purposes (higher-order stencils, uneven meshing, sub-gridding or conformal techniques, combined with FDTD are not used here, though they are well-known to improve the results and reduce the computational costs). Both for FDTD and LTS-LFDG, we use a padding of half a wavelength at 1GHz between the almond and the PML region, and we simulate 50 nsec of the transient response. The FDTD problem employs 750 MCells ($6 \cdot 10^9$ unknowns) and requires a CPU time of 24 hours in a 12 core Intel Xeon X5520 2.26Ghz architecture, while the LTS-LFDG code only requires 18 hours. No computer resources are shown for the HPTESP-MAT, for industrial property rights protection. The reader is referred to [256] for typical figures of MoM methods. Results for the bistatic RCS at 1 GHz

confirm, as also stated by the authors in [10], the superior accuracy of LTS-LFDG especially near the LO (monostatic) zone.

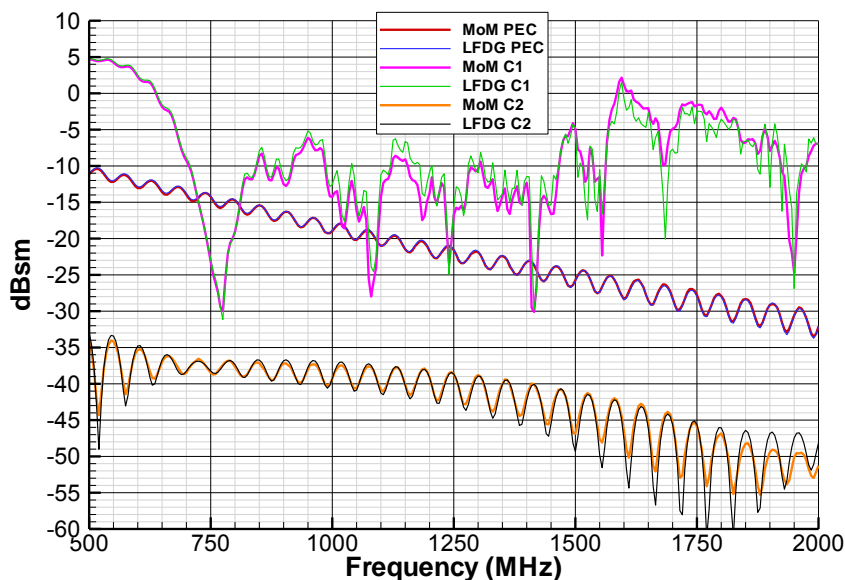


FIGURE 10.4: Monostatic Radar Cross Sections of the NASA almond. Comparison results between LTS-LFDG (1 computation per case) and MoM (301 frequencies/computations per case).

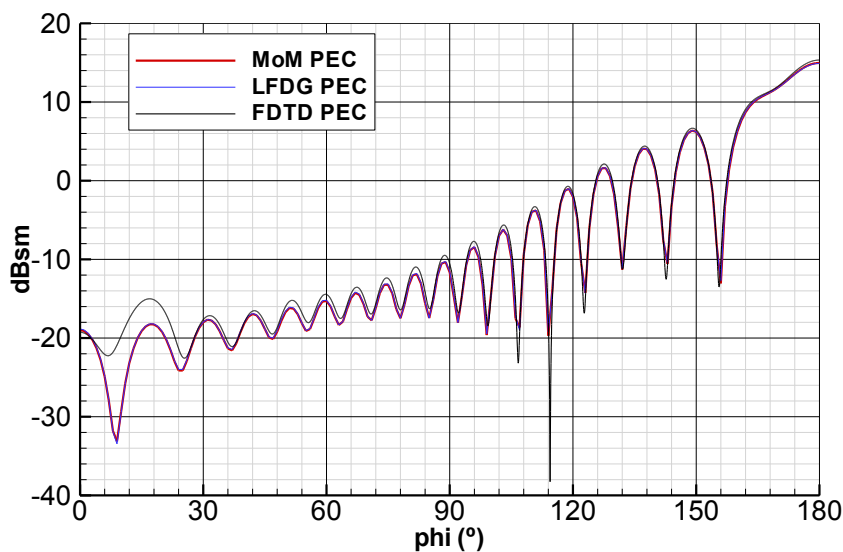


FIGURE 10.5: Bistatic Radar Cross Sections of the NASA almond at 1 GHz. Comparison results between LTS-LFDG, MoM and FDTD for the PEC case.

10.5 Conclusions

In this letter, we have shown the application of three numerical solvers, based on the LTS-LFDG, MoM CCCIE and FDTD methods, to the prediction of the RCS of

a typical LO target: the NASA almond. The accuracy of the LTS-LFDG has been demonstrated to be in the range of that of the MoM CCIE method, outperforming the classical (uniform-mesh, second-order) FDTD method in terms of computational time vs. accuracy.

Chapter 11

Discontinuous Galerkin Time Domain Method for GPR simulation

L. D. Angulo, J. Alvarez, S.G. Garcia, A. Rubio Bretones, and R. Gomez Martin. Discontinuous galerkin time-domain method for gpr simulation of conducting objects. *Near Surface Geophysics*, 9:257–263, 2011

11.1 Introduction

Numerical techniques are an indispensable tool in the analysis and design of all kind of electromagnetic systems. In particular, they have been successfully applied to the simulation and optimization of Ground Penetrating Radar (GPR) systems [257–259]. Among them, time domain methods are especially suitable for GPR simulation, since they are able to provide the full transient response of the system on a single run, allowing the user to analyze the system response in a causal way. The finite difference time domain (FDTD) method has been the most employed one, mainly because of its simplicity, ease of implementation, and simulation speed[260].

However, FDTD has severe drawbacks related to the staircased approximation it employs for curved boundaries. A recent alternative of FDTD is given by the Discontinuous Galerkin Time Domain (DGTD) method which is experiencing an increasing development in computational electromagnetics [10, 67, 92, 189, 195].

DGTD employs a discontinuous Galerkin weighting procedure to handle the spatial part of time-domain Maxwell's curl equations. Like in the finite elements (FETD)

method, the space is divided into M non-overlapping elements (e.g. curvilinear tetrahedra), in each of which the solution is expanded in a set of nodal [194] or vector [92] basis functions of arbitrary order. The temporal part of Maxwell curl equations can be handled by finite differences or by any other finite differentiation technique.

In DGTD the solution is allowed to be discontinuous at the boundaries between adjacent elements (unlike in FETD), and continuous numerical fluxes are employed at the interface to connect the solution between them. The resulting algorithm is quasi-explicit in space, only requiring the inversion of M square matrices of $Q \times Q$ elements (with Q the number of basis functions).

A two-dimensional DGTD approach has been successfully applied to GPR simulations involving buried objects in a lossy half-space [70]. In this paper, we present a general description of a three-dimensional DGTD method including both of nodal and vector formulations and show an application to the simulation of a full GPR scenario. Validations of the method with benchmark problems serve to prove the superior accuracy of this technique compared to the classical FDTD, outperforming the later in the computer requirements.

This paper is organized as follows. In Section II we summarize the DGTD fundamentals in 3D with vector/scalar basis and the centered/upwind flux. Section III shows a validation of this method, and Section IV presents an application to GPR problems.

11.2 DGTD theory

11.2.1 Vector elements formulation

Let us assume Maxwell's curl equations for linear isotropic homogeneous media in Cartesian coordinates. Now, let us divide the space in M non-overlapping elements V_m , each bounded by S_m and enforce a weak form of them by performing the inner product of each equation with a basis of local continuous vector test functions. The term "weak" here means that we no longer require the equation to hold absolutely and we search for "weak" solutions with respect to certain test functions to be defined later [27].

$$\begin{aligned} \int_{V^m} \vec{\Phi}_{q'}^{e^m} \cdot (\varepsilon \partial_t \vec{E}^m + \sigma \vec{E}^m + \vec{J} - \nabla \times \vec{H}^m) dV &= 0 \\ \int_{V^m} \vec{\Phi}_{q'}^{h^m} \cdot (\mu \partial_t \vec{H}^m + \nabla \times \vec{E}^m) dV &= 0 \end{aligned} \quad (11.1)$$

$$\vec{\Phi}_{q'}^{e,h} \in \mathcal{B}^{e,h^m} = \{\vec{\Phi}_1^{e,h^m}, \vec{\Phi}_2^{e,h^m}, \dots, \vec{\Phi}_Q^{e,h^m}\} \quad (11.2)$$

With $\vec{E}, \vec{H}, \vec{J}, \sigma, \varepsilon, \mu$ being, respectively: electric field, magnetic field, electric current density, electric conductivity, permittivity and permeability.

Integrating by parts the curl terms in both equations we can write Eqs. (11.1) as

$$\int_{V^m} (\vec{\Phi}_{q'}^{e^m} \cdot (\varepsilon \partial_t \vec{E}^m + \sigma \vec{E}^m + \vec{J}) - \nabla \times \vec{\Phi}_{q'}^{e^m} \cdot \vec{H}^m) dV = \oint_{\partial V^m} \vec{\Phi}_{q'}^{e^m} \cdot (\hat{n}^m \times \vec{H}^m) dS \quad (11.3)$$

$$\int_{V^m} (\vec{\Phi}_{q'}^{h^m} \cdot (\mu \partial_t \vec{H}^m) + \nabla \times \vec{\Phi}_{q'}^{h^m} \cdot \vec{E}^m) dV = - \oint_{\partial V^m} \vec{\Phi}_{q'}^{h^m} \cdot (\hat{n}^m \times \vec{E}^m) dS \quad (11.4)$$

The core idea of DGTD is to only require the weak form of the tangential fields on the faces of adjacent elements S_m (right hand side of (11.3)(11.4)) to be continuous, instead of requiring full continuity of the solution as in the classical finite elements method. Since the fields are allowed to be different at each side of the interface, a *trade-off* value must be taken to evaluate the right hand side of Eqs.(11.3)(11.4). This *trade-off* value (denoted with an added superscript $*$) can be written, in general, as a function of the fields at each sides interface

$$\begin{aligned} \hat{n}^m \times \vec{E}^{m*} &= \hat{n}^m \times \left(\vec{f}_E^-(\vec{E}^m, \vec{H}^m) + \vec{f}_E^+(\vec{E}^{m+}, \vec{H}^{m+}) \right) \\ \hat{n}^m \times \vec{H}^{m*} &= \hat{n}^m \times \left(\vec{f}_H^-(\vec{E}^m, \vec{H}^m) + \vec{f}_H^+(\vec{E}^{m+}, \vec{H}^{m+}) \right) \end{aligned} \quad (11.5)$$

where we have added the superscript $+$ to the fields at S_m in the element adjacent to m and $-$ to the fields calculated in m . These terms $\hat{n}^m \times \vec{E}^{m*}$ and $\hat{n}^m \times \vec{H}^{m*}$, so-called numerical fluxes, are used in the right hand side of Eqs.(11.21)(11.22)) instead of $\hat{n}^m \times \vec{E}^m$ and $\hat{n}^m \times \vec{H}^m$. The f functions depend on the numerical flux choice. Two common choices of the numerical flux are reported in the literature:

1. A centered flux [194] found by averaging the solutions at both sides of the interface.

$$\begin{aligned}\hat{n}^m \times \vec{E}^{m*} &= \hat{n}^m \times \frac{\vec{E}^m + \vec{E}^{m+}}{2} \\ \hat{n}^m \times \vec{H}^{m*} &= \hat{n}^m \times \frac{\vec{H}^m + \vec{H}^{m+}}{2}\end{aligned}\quad (11.6)$$

2. The upwind flux usually employed in FVTD (Finite Volume Time Domain) [188] arising from the solution of the advection equations with discontinuous initial values (Riemann problem) [189]

$$\begin{aligned}\hat{n}^m \times \vec{E}^{m*} &= \hat{n}^m \times \\ &\frac{(Y^m \vec{E}^m - \hat{n}^m \times \vec{H}^m) + (Y^{m+} \vec{E}^{m+} + \hat{n}^m \times \vec{H}^{m+})}{Y^m + Y^{m+}} \\ \hat{n}^m \times \vec{H}^{m*} &= \hat{n}^m \times \\ &\frac{(Z^m \vec{H}^m + \hat{n}^m \times \vec{E}^m) + (Z^{m+} \vec{H}^{m+} - \hat{n}^m \times \vec{E}^{m+})}{Z^m + Z^{m+}}\end{aligned}\quad (11.7)$$

with $Z^m = \sqrt{\frac{\mu^m}{\epsilon^m}} = \frac{1}{Y^m}$ being the intrinsic impedance of the element m , and $Z^{m+} = \frac{1}{Y^{m+}}$ being that of the adjacent one.

Notice, that boundary conditions between different dielectric/magnetic media are naturally handled in weak manner in the DGTD formulation, thanks to taking the same tangential components of the fields $\hat{n}^m \times \vec{E}^{m*}$ and $\hat{n}^m \times \vec{H}^{m*}$ in the flux integrals for two adjacent elements. PEC boundary conditions are also enforced in a weak manner by requiring the tangential electric field employed in the flux integrals to be null, and the tangential magnetic field to be continuous[10]

$$\hat{n}^m \times \vec{E}^{m+} = -\hat{n}^m \times \vec{E}^m, \quad \hat{n}^m \times \vec{H}^{m+} = \hat{n}^m \times \vec{H}^m \quad (11.8)$$

Regarding the truncation conditions, PML (Perfectly Matched Layer) are successfully implemented in DGTD following the formulation given in [213].

The semi-discrete algorithm¹ is found by assuming that the space and time dependencies of the fields can be separated, and that the spatial part is expanded within each element in a set of basis functions equal to the set of test functions (Galerkin method)

$$\vec{E}^m = \sum_{q=1}^Q E_q^m(t) \vec{\Phi}_q^{e^m}(\vec{r}), \quad \vec{H}^m = \sum_{q=1}^Q H_q^m(t) \vec{\Phi}_q^{h^m}(\vec{r}) \quad (11.9)$$

¹Semi-discrete means that, up to this point, the spatial part is discretized and the temporal part don't.

The final form of the semi-discrete algorithm at the element m is

$$\varepsilon \widetilde{M}^{ee} \partial_t \overline{\overline{E}} + \left(\sigma \widetilde{M}^{ee} - \widetilde{F}^{ee} \right) \overline{\overline{E}} = -\overline{\overline{J}} - \widetilde{S}^{eh} \overline{\overline{H}} + \widetilde{F}^{eh} \overline{\overline{H}} + \widetilde{F}^{eh+} \overline{\overline{H}}^+ - \widetilde{F}^{ee+} \overline{\overline{E}}^+ \quad (11.10)$$

$$\mu \widetilde{M}^{hh} \partial_t \overline{\overline{H}} + \left(-\widetilde{F}^{hh} \right) \overline{\overline{H}} = +\widetilde{S}^{he} \overline{\overline{E}} - \widetilde{F}^{he} \overline{\overline{E}} - \widetilde{F}^{he+} \overline{\overline{E}}^+ - \widetilde{F}^{hh+} \overline{\overline{H}}^+ \quad (11.11)$$

where

- $\overline{\overline{E}}$ and $\overline{\overline{H}}$ are the field coefficients

$$\overline{\overline{E}} = \left(E_1^m(t), \dots, E_Q^m(t) \right)^T \quad (11.12)$$

$$\overline{\overline{H}} = \left(H_1^m(t), \dots, H_Q^m(t) \right)^T \quad (11.13)$$

- $\overline{\overline{J}}$ are the weak form of the source terms

$$\overline{\overline{J}} = \left(\int_{V^m} \vec{J}(\vec{r}, t) \cdot \vec{\Phi}_1^{hm}, \dots, \int_{V^m} \vec{J}(\vec{r}, t) \cdot \vec{\Phi}_Q^{hm} dV \right)^T \quad (11.14)$$

- \widetilde{M} is the mass matrix

$$[\widetilde{M}^{\alpha\alpha}]_{q'q} = \int_{V^m} \vec{\Phi}_{q'}^{\alpha m} \cdot \vec{\Phi}_q^{\alpha m} dV \quad (11.15)$$

- \widetilde{S} is the stiffness matrix

$$[\widetilde{S}^{\alpha\beta}]_{q'q} = - \int_{V^m} (\nabla \times \vec{\Phi}_{q'}^{\beta m}) \cdot \vec{\Phi}_q^{\alpha m} dV \quad (11.16)$$

- \widetilde{F} are the flux matrices

$$[\widetilde{F}^{\alpha\alpha}]_{q'q} = \kappa^{\alpha\alpha} \int_{\partial V^m} \vec{\Phi}_{q'}^{\alpha m} \cdot (\hat{n}^m \times \hat{n}^m \times \vec{\Phi}_q^{\alpha m}) dS \quad (11.17)$$

$$[\widetilde{F}^{\alpha\beta}]_{q'q} = \nu^{\alpha\beta} \int_{\partial V^m} \vec{\Phi}_{q'}^{\alpha m} \cdot (\hat{n}^m \times \vec{\Phi}_q^{\beta m}) dS, \quad \alpha \neq \beta \quad (11.18)$$

where, for the centered flux

$$\begin{aligned} \kappa^{hh} &= \kappa^{hh+} = \kappa^{ee} = \kappa^{ee+} = 0 \\ \nu^{eh} &= \nu^{eh+} = \nu^{he} = \nu^{he+} = 1/2 \end{aligned} \quad (11.19)$$

and for the upwind flux

$$\begin{aligned}
\kappa^{hh} &= \kappa^{hh+} = \frac{1}{Y^m + Y^{m+}}, \quad \kappa^{ee} = \kappa^{ee+} = \frac{1}{Z^m + Z^{m+}} \\
\nu^{he} &= \kappa^{hh} Y^m, \quad \nu^{he+} = \kappa^{hh+} Y^{m+} \\
\nu^{eh} &= \kappa^{ee} Z^m, \quad \nu^{eh+} = \kappa^{ee+} Z^{m+}
\end{aligned} \tag{11.20}$$

A common election of the basis functions is the hierarchical high-order vector–basis functions, widely used in finite elements methods [85, 92] The resulting system of ordinary differential equations in time can be solved in a number of ways: second-order leapfrog (LF)[195], 4th order Runge–Kutta [92], implicit Crank–Nicholson[232], etc.

11.2.2 Nodal elements formulation

The fundamentals of the scalar formulation are similar to those of the vector one. Now the basis and test functions are chosen to be scalar

$$\mathcal{B}^{e,h^m} = \{\Phi_1^{e,h^m}, \Phi_2^{e,h^m}, \dots, \Phi_Q^{e,h^m}\}, \quad m = 1, \dots, M$$

Where \mathcal{B} denotes the space basis and the superscripts e^m and h^m are used to distinguish between the basis employed for the electric and magnetic fields respectively. The weak form of Maxwell curl equations become

$$\int_{V^m} (\Phi_{q'}^{e^m} (\varepsilon \partial_t \vec{E}^m + \sigma \vec{E}^m + \vec{J}) + \nabla \Phi_{q'}^{e^m} \times \vec{H}^m) dV = \oint_{\partial V^m} \Phi_{q'}^{e^m} (\hat{n}^m \times \vec{H}^{m*}) dS \tag{11.21}$$

$$\int_{V^m} (\Phi_{q'}^{h^m} (\mu \partial_t \vec{H}^m) - \nabla \Phi_{q'}^{h^m} \times \vec{E}^m) dV = - \oint_{\partial V^m} \Phi_{q'}^{h^m} (\hat{n}^m \times \vec{E}^{m*}) dS \tag{11.22}$$

where we already assumed the fluxes in the right hand side to be the numerical ones.

Comparing Eqs. (11.21)(11.22) and Eqs. (11.3)(11.4) we find similar flux–density integrals in their right hand sides. Thus the same upwind and centered fluxes of the scalar case can be used here.

For scalar–basis functions the expansion (11.23) now becomes

$$\vec{E}^m = \sum_{q=1}^Q \vec{E}_q^m(t) \Phi_q^{e^m}(\vec{r}), \quad \vec{H}^m = \sum_{q=1}^Q \vec{H}_q^m(t) \Phi_q^{h^m}(\vec{r}) \quad (11.23)$$

The semi-discrete algorithm is formulated by plugging (11.9) into (11.3)(11.4). The resulting equations are formally equal to (11.10)(11.11), now with

$$\overline{\overline{E}} = \left(\vec{E}_1^m(t), \dots, \vec{E}_Q^m(t) \right)^T \quad (11.24)$$

$$\overline{\overline{H}} = \left(\vec{H}_1^m(t), \dots, \vec{H}_Q^m(t) \right)^T \quad (11.25)$$

$$\overline{\overline{J}} = \int_{V^m} \left(\vec{J}(\vec{r}, t) \Phi_1^{h^m}, \dots, \vec{J}(\vec{r}, t) \right)^T \Phi_Q^{h^m} dV \quad (11.26)$$

$$[\widetilde{M}^{\alpha\alpha}]_{q'q} = \int_{V^m} \Phi_{q'}^{\alpha^m} \Phi_q^{\alpha^m} dV \quad (11.27)$$

$$[\widetilde{S}^{\alpha\beta}]_{q'q} = \left(\int_{V^m} \nabla \Phi_{q'}^{\alpha^m} \Phi_q^{\beta^m} dV \right) \times \quad (11.28)$$

$$\begin{aligned} [\widetilde{F}^{\alpha\alpha}]_{q'q} &= \kappa^{\alpha\alpha} \left(\int_{\partial V^m} \Phi_{q'}^{\alpha^m} \Phi_q^{\alpha^m} dS \right) \hat{n}^m \times \hat{n}^m \times \\ [\widetilde{F}^{\alpha\beta}]_{q'q} &= \nu^{\alpha\beta} \left(\int_{\partial V^m} \Phi_{q'}^{\alpha^m} \Phi_q^{\beta^m} dS \right) \hat{n}^m \times, \quad \alpha \neq \beta \end{aligned} \quad (11.29)$$

A common choice for the basis functions [189], is the set 3D Lagrange interpolating n^{th} order polynomials with equal set of electric and magnetic basis functions $\Phi_q^{e^m} = \Phi_q^{h^m} \equiv \Phi_q^m$. They are first defined in a standard reference element [82] as a function of the simplex coordinates (ξ, η, ζ) by

$$\Phi_q(\xi, \eta, \zeta) \in P_n^3 = \text{span}\{\xi^i \eta^j \zeta^k; i, j, k \geq 0, i + j + k \leq n\} \quad (11.30)$$

requiring $Q = (n+1)(n+2)(n+3)/6$ nodal points in the element to form a complete basis. The local basis for each element is found by computing the mapping of the transformation from the reference element to the actual one. The case $n = 0$ leads to the classical FVTD algorithm[188].

11.3 Validation

We have implemented 3D codes, both with the nodal and vector elements, and with the upwind and centered numerical fluxes, incorporating PML boundary conditions.

Second-order accurate centered differences have been used for the time integration (leap-frog). Heuristic estimations[189, 261] for the maximum time steps have been taken. Although the behavior of vector/nodal centered/upwind is comparable for many situations, we will only show here results found with the vector centered-flux algorithm. An exhaustive comparison is beyond the scope of this publication.

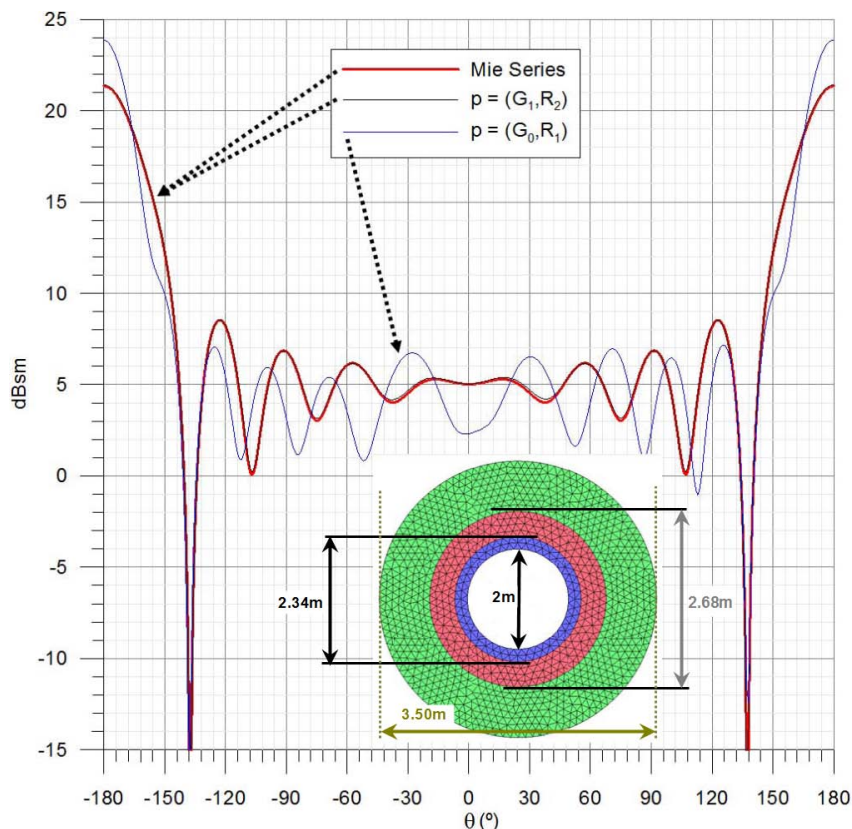


FIGURE 11.1: Bistatic RCS in the E-plane of a 1m radius PEC sphere at 300 MHz illuminated with a 300 MHz continuous wave modulated by a Gaussian pulse ($\sigma = 2\text{ns.}$). DGTD results. Vector centered-flux approximation. PML, LF2. White sphere: PEC (1 m. radius). Blue crown: TF zone (1.17 m. ext. radius). Red crown: Maxwellian zone (1.34 m ext. radius). Green crown: PML (1.75m ext. radius).

In Figs. 11.1,11.2 we validate the DGTD code by calculating the RCS (Radar Cross Section) in the E-plane of a 1m radius PEC sphere and compare with the results found by FDTD (under conditions similar to those of DGTD) and Mie series solution. Results for two set of basis functions are shown: hierarchal vector-basis of orders $(\mathcal{G}_0, \mathcal{R}_1)$ and $(\mathcal{G}_1, \mathcal{R}_2)$ (with \mathcal{G}_n and \mathcal{R}_n being the n^{th} order gradient and rotational spaces). We have used quadratic curvilinear tetrahedra to further remove discretization errors. The sphere is illuminated by a plane wave with a harmonic time variation of 300 MHz. The PML is implemented using a parabolic conductivity profile, and a theoretical reflection coefficient of -80 dB.

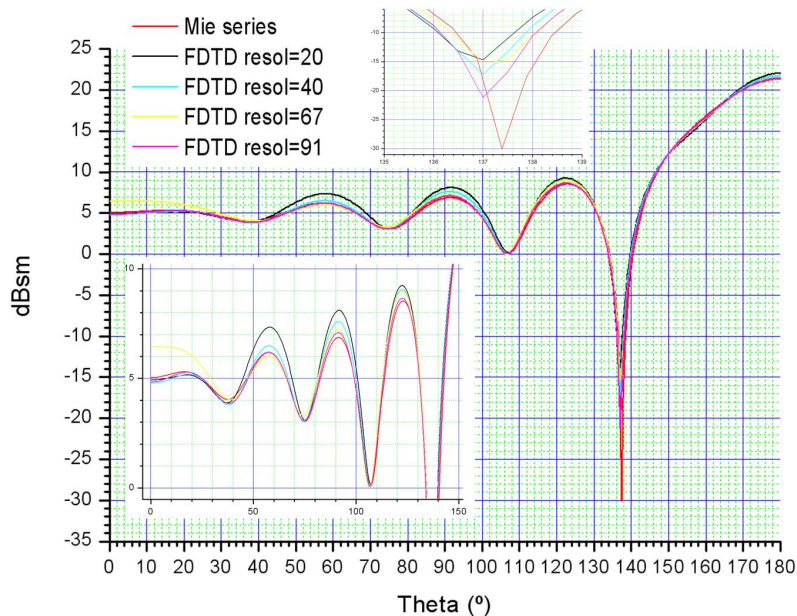


FIGURE 11.2: Bi-static RCS in the E-plane of a 1m radius PEC sphere at 300 MHz illuminated with a 300 MHz continuous wave modulated by a Gaussian pulse ($\sigma = 2\text{ns}$). FDTD results. PML are being used. FDTD resol means number of cells per wavelength.

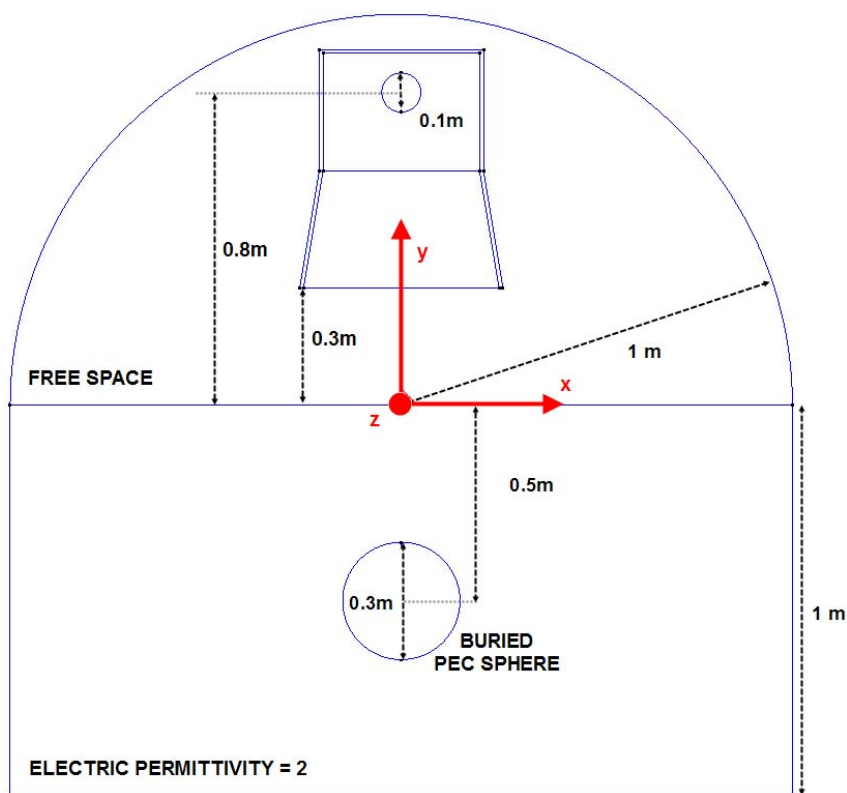


FIGURE 11.3: Computational lay-out of the GPR detection system. PML boundary conditions are placed at the curved/straight boundaries.

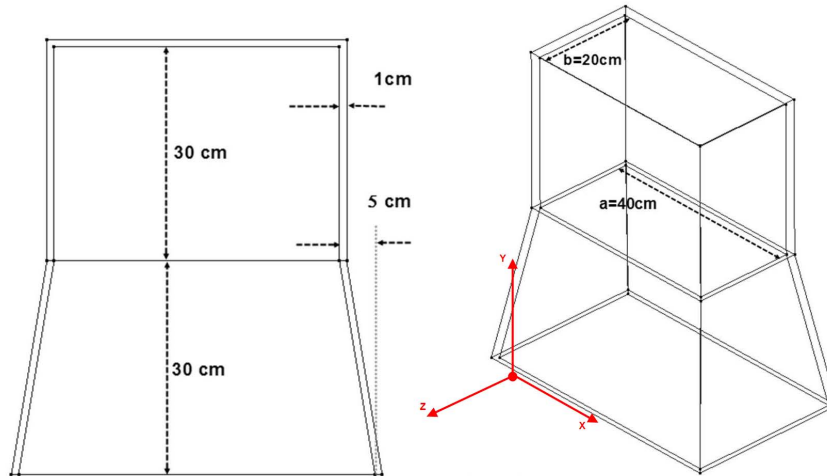


FIGURE 11.4: Geometry of the TEM horn antenna.

Note from Figs. 11.1,11.2 that to achieve the accuracy of DGTD with $(\mathcal{G}_1, \mathcal{R}_2)$ (less than 1 dBsm almost everywhere²), we needed to employ FDTD resolutions over 90 cells/ λ , requiring the solution of over $160 \cdot 10^6$ unknowns, while DGTD only needs $7.5 \cdot 10^6$ unknowns³.

11.4 Application to GPR problems

As demonstrated, DGTD is a numerical technique that achieves a superior accuracy with less computational requirements than FDTD. In this section, as a proof of concept, we show results for the simulation of simple GPR systems.

11.4.1 Object presence discrimination

A TEM horn antenna has been excited with a z -directed gaussian current source near its shortcut wall with a half-width half-amplitude (Fig.11.4) with a -3dB bandwidth of 97.6 MHz and central frequency of 375MHz. The antenna is placed in free-space 0.3m away from a dielectric⁴ soil with electric relative permittivity 2, inside which, a 0.15m-radius PEC sphere is buried at a depth of 0.5m (Fig. 11.3).

Fig. 11.6 shows a snapshot of the E_z field at time step 16.7nsec, computed with a vector DGTD with basis $(\mathcal{G}_1, \mathcal{R}_2)$ and central numerical flux. Fig. 11.5 shows the

²A dBsm is defined as $10 \cdot \log_{10}(s/m^2)$ where s is the effective RCS in squared meters.

³Computational requirements in a 1.66Ghz Core 2 Duo T5500: FDTD \rightarrow Calculation speed= $14 \cdot 10^{-12}$, Memory=1104 Mb. DGTD $(\mathcal{G}_1, \mathcal{R}_2) \rightarrow$ Calculation speed= $126 \cdot 10^{-12}$, Memory= 300Mb. DGTD $(\mathcal{G}_0, \mathcal{R}_1) \rightarrow$ Calculation speed= $728 \cdot 10^{-12}$, Memory=60Mb. Calculation speed is given in terms of physical time normalized to the CPU time (e.g. a calculation speed of 10^{-12} implies that 1s is needed by the CPU to simulate a physical time of 1ps).

⁴No dispersion/losses have been considered in this simplified problem.

time evolution of E_z observed at a point close to the source point inside the antenna (with coordinates $x = 0, y = 0, z = 0$), compared to that in the absence of the buried sphere. The subtraction of both values (magnified by a factor 10) is also shown there to identify the effect of the presence of the sphere. These calibrated E_z field values still show the presence of the air-soil interface through multiple reflections between the soil, the antenna and the buried object.

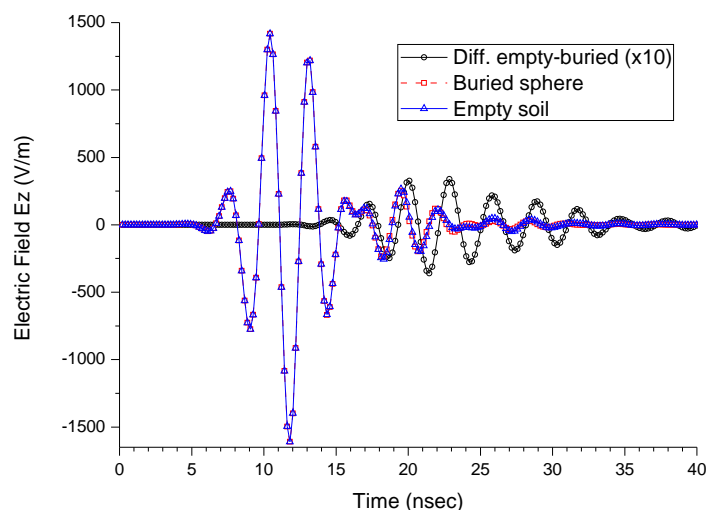


FIGURE 11.5: E_z observed at a point with coordinates $(0,0.5,0)$ meters, both with/without buried sphere. The subtraction of both signals is shown magnified by 10.

11.4.2 Radargram simulation

Next we model the transient response of a metallic landmine buried 5cm in a non-dispersive, non-dissipative medium with relative dielectric permittivity $\epsilon_r = 5$, when a GPR survey is carried out using the TEM-horn antenna shown in fig.11.4. The landmine considered is the TM-62M model and its characteristics are given in [262]. To obtain the synthetic radargram, the TEM-horn antenna is moved along a survey line located 0.3m above the air-soil interface and the z -component of the reflected field is computed approximately at the same antenna location (50cm from the center of the antenna in the \hat{x} direction). Every 5cm the antenna is excited by the same transient pulse used in the previous example and the response at the observation point is recorded. The data obtained are calibrated by subtracting the response of the same configuration but removing the buried landmine. The resulting radargram is plotted in fig.11.7 showing the hyperbola typical of electrically-small objects. Note that, in this example, as the simulation of the radargram required of several runs,

the use of DGTD instead of FDTD resulted in a big reduction in computational time.

11.5 Conclusions

In this paper, we have described and validated a DGTD method, suitable to become an efficient and accurate alternative to FDTD. As a proof of concept, we have simulated a simple GPR scenario with a TEM-horn antenna illuminating soil with an object buried in it. Although formulated for non-dispersive media, DGTD can easily be extended to handle these media using the auxiliary differential equation technique [263], for instance. Actually, DGTD can be extended to handle any type of material for which FDTD is already formulated, in a similar manner since DGTD and FDTD only differ in the treatment of the space variations.

Acknowledgements

The work described in this paper and the research leading to these results has received funding from the European Community's Seventh Framework Programme FP7/2007-2013, under grant agreement no 205294 (HIRF SE project), and from the Spanish National Projects TEC2007-66698-C04-02, CSD2008-00068, DEX-530000-2008-105, and the Junta de Andalucia Project TIC1541.

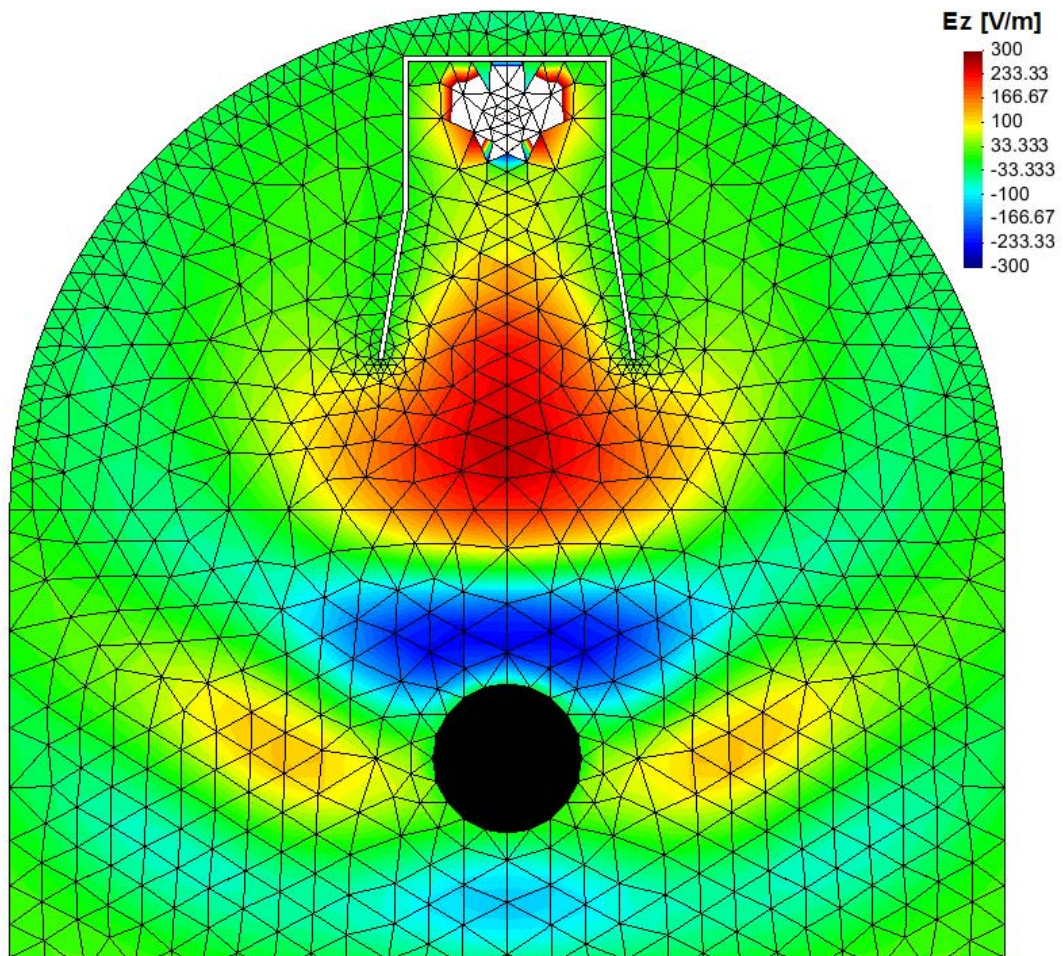


FIGURE 11.6: Snapshot of the E_z field pattern at time step 16.7 ns for the problem presented in figure 11.3. At this time step the wave have traveled through the whole computational domain. White regions inside the TEM-horn are out-of-scale values. Inside the PEC sphere (black) the field is null. The spatial dimensions are the same as in figure 11.3

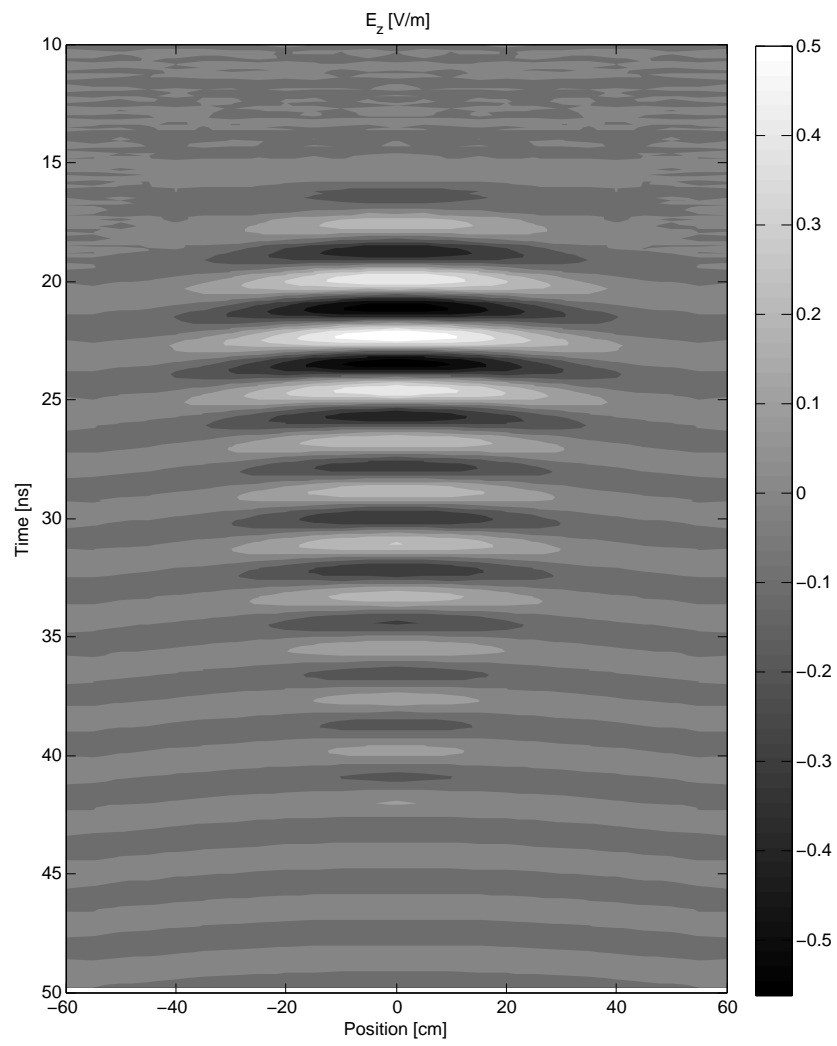


FIGURE 11.7: Synthetic radargram for the landmine case

Part VI

Other works

Chapter 12

FDTD Modeling of Graphene Devices Using Complex Conjugate Dispersion Material Model

H. Lin, M. F. Pantoja, L. D. Angulo, J. Alvarez, R. G. Martin, and S. G. Garcia. FDTD modeling of graphene devices using complex conjugate dispersion material model. *Microwave and Wireless Components Letters, IEEE*, 22(12):612–614, dec. 2012. ISSN 1531-1309. doi: 10.1109/LMWC.2012.2227466

Abstract

Graphene-based devices are becoming an exciting field of research for their extraordinary electromagnetic properties. The incorporation of appropriate models into numerical simulators is a must to take profit of these properties. In this work, we propose a method to incorporate graphene-sheet models into FDTD method. By employing vector-fitting techniques, the permittivity of graphene is expanded into a rational function series, of complex conjugate pole-residue pairs, which is implemented into FDTD by an auxiliary differential equation formulation. Simple waveguiding problems validate our approach.

12.1 Introduction

Graphene, a conjugated sp^2 carbon sheet arranged in a two dimensional (2D) hexagonal lattice, is likely to be the promising candidate plasmonic material used in nanophotonics [264]. Compared with noble metal materials, doped graphene presents unique appealing properties such as tunability, extreme confinement, crystallinity and low losses [265].

Although there are still practical difficulties in exciting and detecting the Surface plasmon-polariton (SPP) waves in graphene, numerous theoretical plasmonic devices have been envisaged in advance [266], and promising transformation optics applications [267] are under study. Via changing the chemical potential using gate electric and/or magnetic fields, the graphene conductivity in the THz and IR frequencies can be tuned. This unique property can be used to construct one atom thick metamaterial cloaking devices. Other researchers have proposed structures of graphene SPP waveguiding devices, which mimic the conventional Metal-Insulator-Metal (MIM) optical waveguide (e.g. Bing Wang and Xiang Zhang theoretically investigate the coupling of far-infrared SPPs between spatially separated graphene sheets.

Due to the difficulties in measuring the SPP field, numerical simulation has been the essential manner to verify the theoretical analysis. Most researchers make use of commercial EM software based on frequency domain method like FDFD and FEM. Yet another popular numerical technique, like the FDTD method [223], is rarely mentioned in solving the Maxwell system containing graphene material. A recent work did RCS analysis of finite graphene sheets through an enhanced frequency-dependent subcell FDTD method [268]. They handle the material dispersion only by including the intraband (Drude) conductivity, while neglecting the interband term. This approximation can obtain reasonable results where the intraband term dominates at the lower frequency band. However, the high frequency dynamic conductivity is dominated by interband conductivity when $|\mu_c| < \hbar\omega/2$, especially for slightly doped graphene. This remedy was improved in [269] through a Pade approximate spectral fit for graphene conductivity, yet this Pade fit method only gives accurate approximation in a restricted spectrum region.

In this paper we propose a new accurate way to describe the equivalent permittivity function of one-atom thick graphene as a sum of multiple complex-conjugate pole-residue pairs obtained through a vector fitting tool [165]. The Auxiliary differential equation (ADE) method described in [161] is used in the parallel UGRFDTD simulator employed in this work [247]. Numerical simulations serve to validate our approach both for low and high frequency applications.

12.2 Formulation of the dispersion model

12.2.1 Graphene conductivity

The graphene can be modeled as an infinitesimally thin surface characterized by a surface conductivity $\sigma(\omega, \mu_c, \Gamma, T)$ [270],

$$\begin{aligned} \sigma(\omega, \mu_c, \Gamma, T) = & \\ & \frac{je^2(\omega - j2\Gamma)}{\pi\hbar^2} \left[\frac{1}{(\omega - j2\Gamma)^2} \int_0^x \varepsilon \left(\frac{\partial f_d(\varepsilon)}{\partial \varepsilon} - \frac{\partial f_d(-\varepsilon)}{\partial \varepsilon} \right) d\varepsilon \right. \\ & \left. - \int_0^x \frac{f_d(-\varepsilon) - f_d(\varepsilon)}{(\omega - j2\Gamma)^2 - 4(\varepsilon/\hbar)^2} d\varepsilon \right] \end{aligned} \quad (12.1)$$

where ω is the angular frequency, μ_c the chemical potential, Γ the scattering rate, T the Kelvin temperature, $-e$ the charge of an electron, $\hbar = h/2\pi$ the reduced Planck's constant, and f_d the Fermi-Dirac distribution. Within the random-phase approximation, the dynamic optical response of graphene can be derived from Kubo formula in a complex form consisting of interband and intraband contributions. The intraband term in Eq. (12.1) can be evaluated as:

$$\sigma_{intra}(\omega, \mu_c, \Gamma, T) = -j \frac{e^2 k_B T}{\pi \hbar^2 (\omega - j2\Gamma)} \left(\frac{\mu_c}{k_B T} + 2 \ln(e^{-\mu_c/k_B T} + 1) \right) \quad (12.2)$$

The interband conductivity can be approximated for $k_B T \ll |\mu_c|, \hbar\omega$ as

$$\sigma_{inter}(\omega, \mu_c, \Gamma, T) = \frac{-je^2}{4\pi\hbar} \ln \frac{2|\mu_c| - (\omega - j2\Gamma)\hbar}{2|\mu_c| + (\omega - j2\Gamma)\hbar} \quad (12.3)$$

From Eq.(12.2) and (12.3), it is obvious that the intraband conductivity takes the form of Drude model while the interband conductivity holds a complex form. (insert figures for the plot of $\sigma \epsilon_{eq}$)

12.2.2 Complex conjugate pole-residue pair model

The 2D conductivity defined can be used to define an equivalent volume conductivity, by using the method proposed in [267]. Assuming the graphene has a very small thickness Δ , the volume conductivity is found by $\sigma_{volume} = \frac{\sigma}{\Delta}$, and the equivalent volume current density can be deduced as $\vec{J} = \sigma_{volume} \vec{E}$. Thus, the equivalent complex permittivity of the Δ -thick graphene layer is $\epsilon_{eq} = \epsilon_0 + \frac{\sigma}{j\omega\Delta}$. When $Re(\epsilon_{eq}) < 0$, the graphene layer acts like a thin metal film, and a TM mode SPP surface wave can be supported.

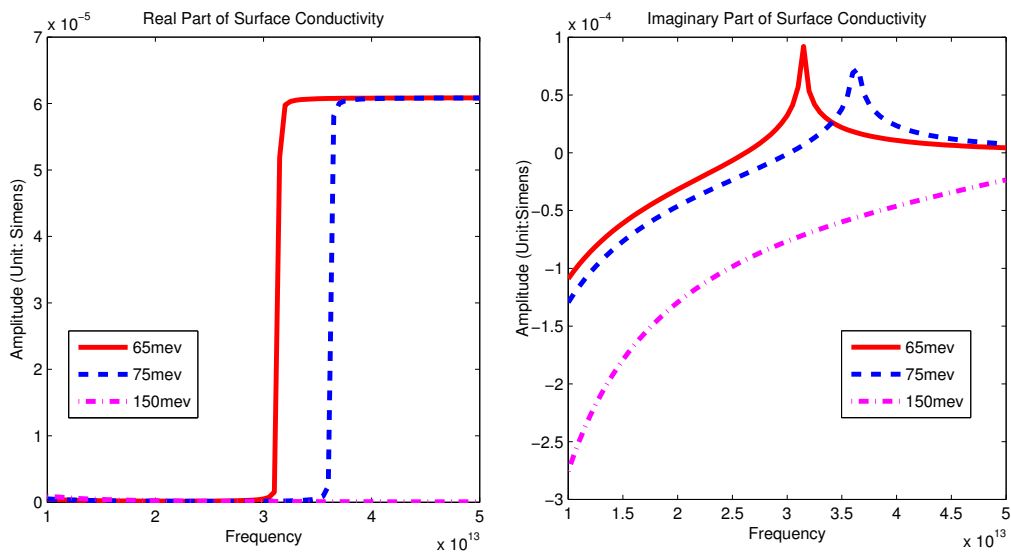


FIGURE 12.1: Surface conductivity of graphene for different μ_c

From the above formula, the complex relative permittivity values at various frequencies can be calculated under different fabrication condition (μ_c, Γ, T). Let us propose that this complex relative permittivity can be described as a sum of partial fractions in terms of complex conjugate pole-residue pairs as follows:

$$\epsilon_{eq} = \epsilon_0 \epsilon_\infty + \epsilon_0 \sum_p \left(\frac{c_p}{j\omega - a_p} + \frac{c_p^*}{j\omega - a_p^*} \right) \quad (12.4)$$

where ϵ_∞ is the relative permittivity at infinite frequency, and a_p and c_p are the p -th pole and residue, respectively.

The complex conjugate pole-residues in Eq.12.4 can be found by vector fitting [165] techniques. The resulting model is both casual (automatically complies with Kramers-Kronig relationships), and stable (poles are in the left complex semi-plane). It can be implemented in time domain either in convolutional or in Auxiliary Differential Equation (ADE) form. In this paper we have chosen the later using the methodology described in [161] implemented into the parallel UGRFDTD simulator [247] partially developed under the HIRF-SE 7PM EU Project [245].

Assuming the thickness of graphene is 1nm, we have listed in Table 12.1 the fitted values of a_p and r_p for the cases used in our numerical simulations. The fitting frequency band ranges from 1 THz to 600 THz which covers the whole interested spectrum region. An 8th order model has been chosen for providing a good enough model without sacrificing the computational time. Fig. 12.2 compares the complex conjugate pole-residue model with the Kubo model, both for the high and low

TABLE 12.1: Fitted pole-residue pairs for $\mu_c = 0.15ev$, $T = 300K$, $\Gamma = 0.5ps$. A value of $\epsilon_\infty = 1.000136193409153$ is found for the infinite-frequency parameter.

p	a_p ($\times 10^{14}$)	c_p ($\times 10^{17}$)
1	-0.000000311990089	9.952097029182077
2	-0.020059641266861	-9.95190402605314
3	$-0.063439734110918 + j4.557315565339019$	$0.000289314063601 + j8.0429178158$
4	$-0.063439734110918 - j4.557315565339019$	$0.000289314063601 - j0.000000310333203$
5	$-0.026877401170715 + j4.557748555290389$	$0.000087819040210 + j0.000000235978050$
6	$-0.026877401170715 - j4.557748555290389$	$0.000087819040210 - j0.000000235978050$
7	$-0.165660164979658 + j4.554918677584330$	$0.000760076976401 - j0.000003424982598$
8	$-0.165660164979658 - j4.554918677584330$	$0.000760076976401 + j0.000003424982598$
9	$-0.42400644448006 + j4.541081141209922$	$0.001880592700406 - j0.000032966348094$
10	$-0.42400644448006 - j4.541081141209922$	$0.001880592700406 + j0.000032966348094$
11	$-1.043659450208929 + j4.459035469999526$	$0.004442370774092 - j0.000180715146878$
12	$-1.043659450208929 - j4.459035469999526$	$0.004442370774092 + j0.000180715146878$
13	$-2.399275629388681 + j3.994855305224047$	$0.009712908060073 - j0.000642521125815$
14	$-2.399275629388681 - j3.994855305224047$	$0.009712908060073 + j0.000642521125815$
15	$-4.430844678567260 + j1.951215718359759$	$0.017090807596325 - j0.000771897787253$
16	$-4.430844678567260 - j1.951215718359759$	$0.017090807596325 + j0.000771897787253$

frequency band.

It can be noticed from Table 12.1 that not all the poles and residues are complex conjugate, the first and second pole-residue pair are real values. In this case, since the first pole is quite small (compared with the second pole), the effect of these two pole-residue pairs can be interpreted as a Drude term, which account for the σ_{intra} at the low frequency band (less than 20THz). The other pole-residue pairs can be interpreted as several small modification terms to the permittivity model. These facts agree with the analysis that σ_{intra} only takes effect in the low frequency band. In the high frequency band, the influence of σ_{inter} should be taken into account.

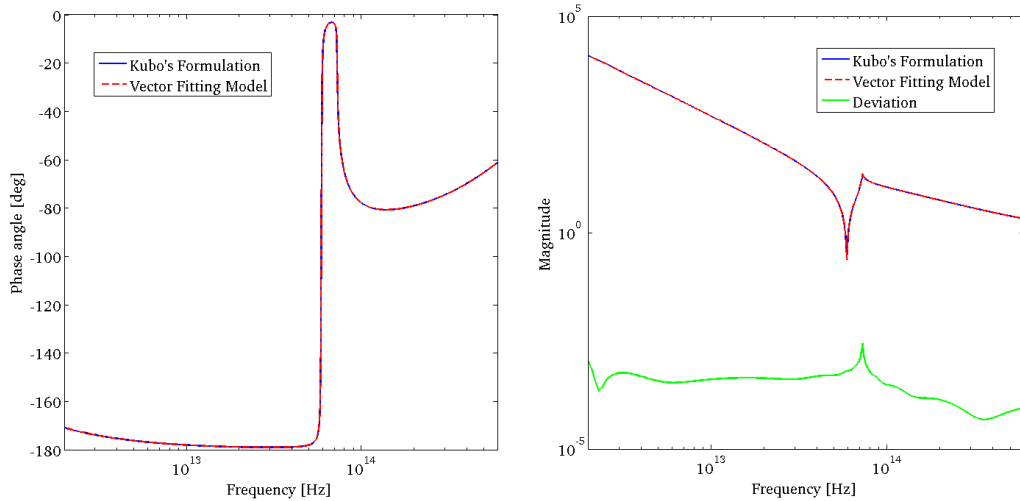


FIGURE 12.2: Comparison of the complex permittivity found by vector fitting to that found from the Kubo model.

12.2.3 FDTD algorithm

Following the strategy of [161], the following FDTD updating equation for the E-field is found (the magnetic field update equation remains unchanged):

$$\vec{E}^{(n+1)} = \vec{E}^{n\Delta t} + \frac{2\Delta t \cdot [\nabla \times \vec{H}^{(n+1/2)\Delta t} - Re \sum_{p=1}^P] (1 + k_p) \vec{J}_p^{n\Delta t}}{2\epsilon_0 \epsilon_\infty + \sum_{p=1}^P 2Re(\beta_p)} \quad (12.5)$$

where J_p is the auxiliary currents introduced by the complex-conjugate pole-residue pairs. These are updated using the following equation after the E-field updating

$$\vec{J}_p^{(n+1)\Delta t} = k_p \vec{J}_p^{n\Delta t} + \beta_p \left(\frac{\vec{E}^{(n+1)} - \vec{E}^{n\Delta t}}{\Delta t} \right) \quad (12.6)$$

the updating coefficients k_p and β_p can be calculated from the given poles and residues as:

$$k_p = \frac{1 + a_p \Delta t / 2}{1 - a_p \Delta t / 2}, \beta_p = \frac{\epsilon_0 c_p \Delta t}{1 - a_p \Delta t / 2} \quad (12.7)$$

12.3 Numerical Validation

To validate the complex-conjugate dispersion model for graphene, we first studied an optical coupling system composed of two parallel free-standing graphene sheets described in Fig.12.3-(b), which has been theoretically investigated in [271] by means of FDFD method. The thickness of graphene is set to $\Delta = 1nm$, which is equivalent to the mesh size along each direction. The equivalent permittivity of the graphene is $\epsilon_{eq} = -45.082 + j0.719$. To meet with the CFL-stability condition, the timestep is set to $1 \times 10^{-18}s$. The Convolutional Perfectly Matched Layer (CPML) technique permits to truncate, both the graphene dispersive layer, and the free-space (an 8-cell layer is used here).

A waveguide mode source with 30THz harmonic wave is illuminated from free-space, exciting either the symmetric or the anti-symmetric surface plasmon waves traveling along the graphene sheets. The normalized E_z field along the width direction of different modes is illustrated In Fig.12.3-(a). It should be noted that, the symmetric and anti-symmetric modes are basic mode of the parallel plate system, while the asymmetric mode can be considered as a hybrid mode of symmetry and asymmetry mode. It can also be viewed as a off-axis excitation results of the input optical field.

When the simulation reaches a steady state, the wavelength can be found from the space field distribution, from which, the propagation constant β can be extracted. For 50nm parallel plate distance, for the symmetric mode, we find $\beta_{sym} = 48.90 + j0.58\mu m^{-1}$, while for anti-symmetric mode $\beta_{antisym} = 38.22 + j0.80\mu m^{-1}$. Thus, the SPP wave for the symmetric mode presents a shorter spatial period compared with anti-symmetric mode. This phenomenon can be easily viewed from the time snapshots shown in Fig.12.3-(b) and Fig.12.3-(d)

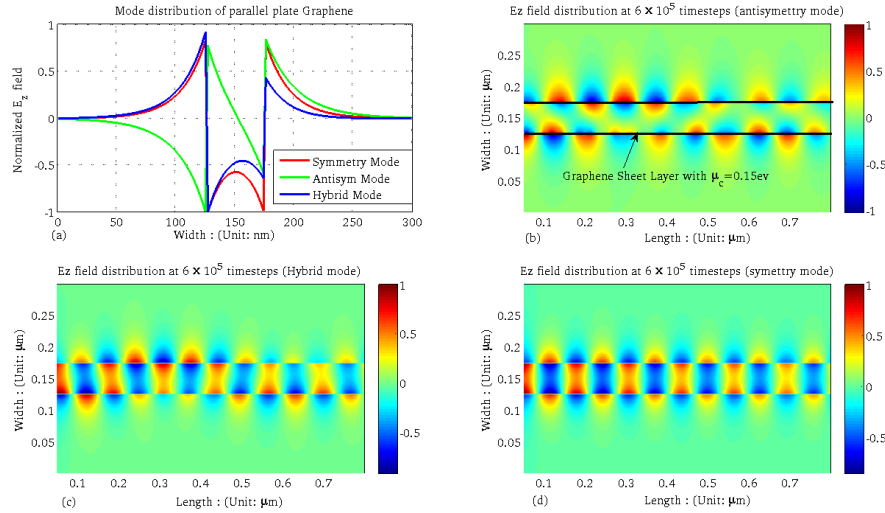


FIGURE 12.3: Ez field of two parallel graphene sheets system excited at three different modes. The distance between two graphene sheet is 50nm

This coupling effect between parallel graphene plates can be used to design splitters. Fig.12.4-(a) and Fig.12.4-(b) show again different snapshots of the electric field in a waveguide splitter. The spaces between the input and two output graphene sheets are both $d=50nm$. The coupling distance is set to 220nm. If we change the chemical potential at the upper/lower coupling arm, the coupling process can be tuned. In Fig.12.4-(c) and Fig.12.4-(d) we show the time evolution of the tuned coupler whose upper arm chemical potential has been changed to 0.05eV (within the coupling distance). Thus, the SPP wave is only coupled to the lower arm.

12.4 Conclusion

In this work, we have proposed a method to incorporate graphene sheet models into the FDTD simulators. Vector-fitting has permitted us to express the permittivity of graphene as a rational function series, with arbitrary order, of complex conjugate pole-residue pairs. An ADE formulation has been employed into the UGRFDTD

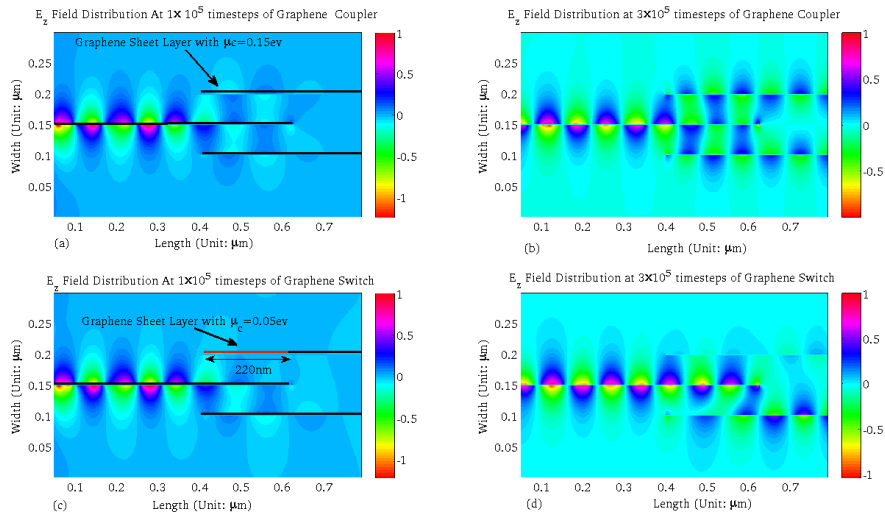


FIGURE 12.4: E_z field of two parallel graphene sheets system excited at anti-symmetric mode. Distance between the two graphene sheet=30nm

solver. Waveguiding structures have served to illustrate and validate the effectiveness of this method.

Chapter 13

Efficient excitation of Waveguides Crank Nicolson FDTD

S. G. Garcia, F. Costen, M. Fernandez Pantoja, L. D. Angulo, and J. Alvarez. Efficient excitation of waveguides in crank-nicolson ftdt. *Progress In Electromagnetics Research Letters*, 17:39–46, 2010. doi: 10.2528/PIERL10072008. URL <http://www.jpier.org/PIERL/pier.php?paper=10072008>

Abstract

In this paper we present a procedure to calculate the discrete modes propagated with Crank–Nicolson FDTD in metallic waveguides. This procedure enables the correct excitation of this kind of waveguides at any resolution. The problem is reduced to solving an eigenvalue equation, which is performed, both in a closed form, for the usual rectangular waveguide, and numerically in the most general case, validated here with a ridged rectangular waveguide.

13.1 Introduction

Two important problems, which have received a broad attention in literature, arise in the simulation of multimode waveguides by time domain methods: on one hand, the correct excitation of the incident modes at the feeding port and, on the other hand, their subtraction at the end of the guide [273–281].

In this paper, we apply some of these techniques to characterize the discrete modes (also known as mode templates [274]) propagating on arbitrarily-shaped conducting waveguides solved by the Crank–Nicolson Finite Difference Time Domain (CN–FDTD) method. For this purpose we find the solution of the eigenvalue problem numerically, for the general case, and analytically, for rectangular waveguides. The numerical procedure is validated here with a simple ridged rectangular waveguide.

The CN–FDTD method [282–284] has been chosen for being a promising alternative to the classical Yee–FDTD method, due to its unconditional stability, which is worth to be extended to include all the features already developed for the classical FDTD method

13.2 Discrete problem

Let us assume a conducting waveguide with arbitrary cross section, filled up with a lossless homogeneous isotropic medium ¹ with electrical parameters ε and μ , and consider its axis in the Z direction. The modes propagating in the waveguide must satisfy Maxwell’s curl equations, together with the boundary conditions at the metallic walls: null tangential components of the \vec{E} field, and null normal components of the \vec{H} field.

In order to solve this problem with Crank–Nicolson FDTD (CN–FDTD) [283, 284] an average-in-time operator is applied to the fields affected by the space derivatives in Maxwell’s curl equations, and all the derivative operators are replaced by the centered difference operator. This results in an unconditionally stable scheme [282], which permits to solve the fields located in the usual Yee-cube spatial disposition with an implicit-in-space marching-on-in-time algorithm

$$\mathcal{D}_u f(u, \dots) = \frac{f(u + \frac{\Delta u}{2}, \dots) - f(u - \frac{\Delta u}{2}, \dots)}{\Delta u} \quad (13.1)$$

¹Although the procedure is shown for simplicity for lossless media, it can be easily formulated for lossy media.

$$\mathcal{P}_t f(t, \dots) = \frac{f(t + \frac{\Delta t}{2}, \dots) + f(t - \frac{\Delta t}{2}, \dots)}{2} \quad (13.2)$$

Placing the field components distributed in the usual Yee's cube [37] $\vec{r}_1 = (i, j + \frac{1}{2}, k + \frac{1}{2})$, $\vec{r}_2 = (i + \frac{1}{2}, j, k + \frac{1}{2})$, $\vec{r}_3 = (i + \frac{1}{2}, j + \frac{1}{2}, k)$, $\vec{r}_4 = (i + \frac{1}{2}, j, k)$, $\vec{r}_5 = (i, j + \frac{1}{2}, k)$, $\vec{r}_6 = (i, j, k + \frac{1}{2})$, we can write CN-FDTD as

$$\begin{aligned} \mu \mathcal{D}_t H_x^n(\vec{r}_1) &= (\mathcal{D}_z \mathcal{P}_t) E_y^n(\vec{r}_1) - (\mathcal{D}_y \mathcal{P}_t) E_z^n(\vec{r}_1) & (13.3) \\ \mu \mathcal{D}_t H_y^n(\vec{r}_2) &= (\mathcal{D}_x \mathcal{P}_t) E_z^n(\vec{r}_2) - (\mathcal{D}_z \mathcal{P}_t) E_x^n(\vec{r}_2) \\ \mu \mathcal{D}_t H_z^n(\vec{r}_3) &= (\mathcal{D}_y \mathcal{P}_t) E_x^n(\vec{r}_3) - (\mathcal{D}_x \mathcal{P}_t) E_y^n(\vec{r}_3) \\ \varepsilon \mathcal{D}_t E_x^{n+\frac{1}{2}}(\vec{r}_4) &= (\mathcal{D}_y \mathcal{P}_t) H_z^{n+\frac{1}{2}}(\vec{r}_4) - (\mathcal{D}_z \mathcal{P}_t) H_y^{n+\frac{1}{2}}(\vec{r}_4) \\ \varepsilon \mathcal{D}_t E_y^{n+\frac{1}{2}}(\vec{r}_5) &= (\mathcal{D}_z \mathcal{P}_t) H_x^{n+\frac{1}{2}}(\vec{r}_5) - (\mathcal{D}_x \mathcal{P}_t) H_z^{n+\frac{1}{2}}(\vec{r}_5) \\ \varepsilon \mathcal{D}_t E_z^{n+\frac{1}{2}}(\vec{r}_6) &= (\mathcal{D}_x \mathcal{P}_t) H_y^{n+\frac{1}{2}}(\vec{r}_6) - (\mathcal{D}_y \mathcal{P}_t) H_x^{n+\frac{1}{2}}(\vec{r}_6) \end{aligned}$$

Following the way employed in the non-discrete case, we will search for discrete solutions of (13.3) with the general form

$$\Psi^{m_t}(m_x, m_y, m_z) = \Psi_o(m_x, m_y) e^{-j\beta_g m_z \Delta z} e^{j\omega m_t \Delta t}$$

with β_g being the propagation constant along the waveguide, and $\Psi_o(m_x, m_y)$ the transversal profile amplitude. For these functions, \mathcal{D}_z , \mathcal{D}_t and \mathcal{P}_t have the following eigenvalues respectively

$$a_z = -2j \frac{\sin(\beta_g \frac{\Delta z}{2})}{\Delta z}, \quad a_t = 2j \frac{\sin(\omega \frac{\Delta t}{2})}{\Delta t}, \quad n_t = \cos(\omega \frac{\Delta t}{2}) \quad (13.4)$$

The general solution of equations (13.3), as in the non-discrete case, can be divided into two basic mode sets: Transverse Magnetic (TM), for which $H_z = 0$, and Transverse Electric (TE), for which $E_z = 0$. It can be seen that for both TM and TE modes, it is sufficient to obtain respectively E_{oz} and H_{oz} , to calculate the remaining components. For instance, for the TM polarization (13.3) is equivalent to

$$E_{ox}(i+\frac{1}{2}, j) = \frac{1}{\kappa^2} (a_z \mathcal{D}_x E_{oz}(i+\frac{1}{2}, j)) \quad (13.5a)$$

$$E_{oy}(i, j+\frac{1}{2}) = \frac{1}{\kappa^2} (a_z \mathcal{D}_y E_{oz}(i, j+\frac{1}{2})) \quad (13.5b)$$

$$H_{ox}(i, j+\frac{1}{2}) = \frac{1}{\kappa^2} (\nu_t \varepsilon \mathcal{D}_y E_{oz}(i, j+\frac{1}{2})) \quad (13.5c)$$

$$H_{oy}(i+\frac{1}{2}, j) = \frac{-1}{\kappa^2} (\nu_t \varepsilon \mathcal{D}_x E_{oz}(i+\frac{1}{2}, j)) \quad (13.5d)$$

$$(\mathcal{D}_x \mathcal{D}_x + \mathcal{D}_y \mathcal{D}_y + \kappa^2) E_{oz}(i, j) = 0 \quad (13.5e)$$

with the dispersion relationship

$$\kappa^2 = a_z^2 - \mu\epsilon\nu_t^2, \quad \nu_t = \frac{a_t}{n_t} = 2j \frac{\tan(\omega \frac{\Delta t}{2})}{\Delta t} \quad (13.6)$$

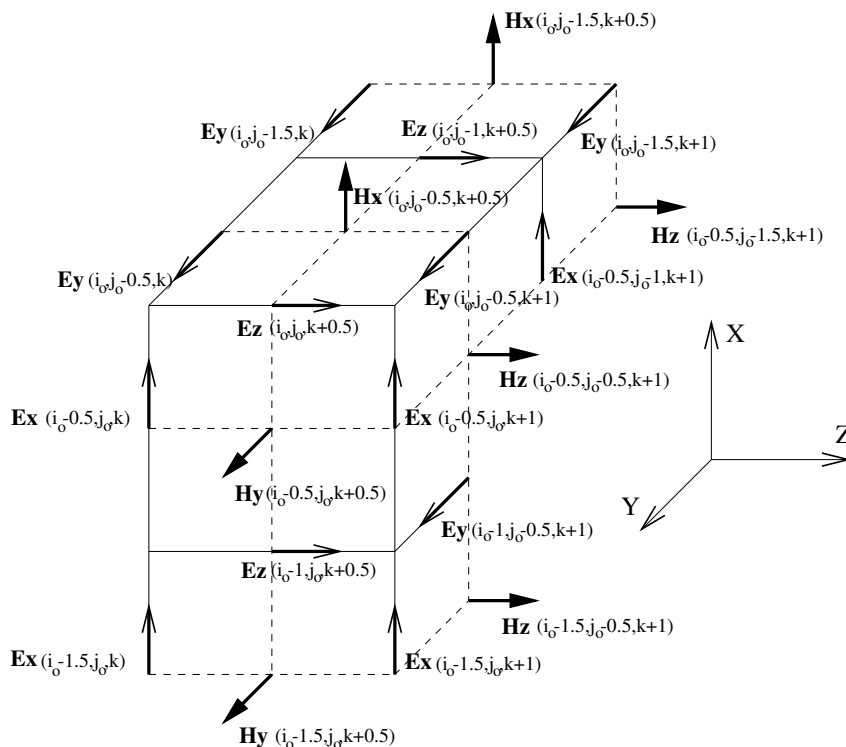


FIGURE 13.1: Arrangement of the fields at an edge of the guide

If we place the staircased conducting walls along the planes of Yee's cube containing the E_z component (Fig. 13.1), the boundary conditions at the planes parallel to XZ are

$$(a) E_{oz}(i_0, j_0) = 0, \quad (b) E_{ox}(i_0 + \frac{1}{2}, j_0) = 0, \quad (c) H_{oy}(i_0 + \frac{1}{2}, j_0) = 0 \quad (13.7)$$

and for the planes parallel to YZ

$$(a) E_{oz}(i_0, j) = 0, \quad (b) E_{oy}(i_0, j + \frac{1}{2}) = 0, \quad (c) H_{ox}(i_0, j + \frac{1}{2}) = 0 \quad (13.8)$$

It can easily be deduced from Eqs. (13.5), that (13.7a) and (13.8a) are enough to satisfy the remaining boundary conditions (13.7b-c) and (13.8b-c) automatically.

Analogously, the eigenvalue equation for the TE polarization is

$$(\mathcal{D}_x \mathcal{D}_x + \mathcal{D}_y \mathcal{D}_y + \kappa^2) H_{oz}(i_0 + \frac{1}{2}, j_0 + \frac{1}{2}) = 0 \quad (13.9)$$

TABLE 13.1: Closed form of the discrete TE and TM modes for a rectangular waveguide of size $a \times b$

TM (p, q non-null integers, E_o arbitrary)		
$E_{ox}(i+\frac{1}{2}, j) = -j \frac{1}{\kappa^2} b_z b_x E_o \cos\left(\frac{p\pi}{a}(i+\frac{1}{2})\Delta x\right) \sin\left(\frac{q\pi}{b} j \Delta y\right)$		
$E_{oy}(i, j+\frac{1}{2}) = -j \frac{1}{\kappa^2} b_z b_y E_o \sin\left(\frac{p\pi}{a} i \Delta x\right) \cos\left(\frac{q\pi}{b}(j+\frac{1}{2})\Delta y\right)$		
$E_{oz}(i, j) = E_o \sin\left(\frac{p\pi}{a} i \Delta x\right) \sin\left(\frac{q\pi}{b} j \Delta y\right)$		
$H_{ox}(i, j+\frac{1}{2}) = j \frac{\epsilon}{\kappa^2} b_t b_y E_o \sin\left(\frac{p\pi}{a} i \Delta x\right) \cos\left(\frac{q\pi}{b}(j+\frac{1}{2})\Delta y\right)$		
$H_{oy}(i+\frac{1}{2}, j) = -j \frac{\epsilon}{\kappa^2} b_t b_x E_o \cos\left(\frac{p\pi}{a}(i+\frac{1}{2})\Delta x\right) \sin\left(\frac{q\pi}{b} j \Delta y\right)$		
$H_{oz}(i+\frac{1}{2}, j+\frac{1}{2}) = 0$		
TE (p, q non simultaneous null integers, H_o arbitrary)		
$E_{ox}(i+\frac{1}{2}, j) = j \frac{\epsilon}{\kappa^2} b_t b_y H_o \cos\left(\frac{p\pi}{a}(i+\frac{1}{2})\Delta x\right) \sin\left(\frac{q\pi}{b} j \Delta y\right)$		
$E_{oy}(i, j+\frac{1}{2}) = -j \frac{\epsilon}{\kappa^2} b_t b_x H_o \sin\left(\frac{p\pi}{a} i \Delta x\right) \cos\left(\frac{q\pi}{b}(j+\frac{1}{2})\Delta y\right)$		
$E_{oz}(i, j) = 0$		
$H_{ox}(i, j+\frac{1}{2}) = j \frac{1}{\kappa^2} b_z b_x H_o \sin\left(\frac{p\pi}{a} i \Delta x\right) \cos\left(\frac{q\pi}{b}(j+\frac{1}{2})\Delta y\right)$		
$H_{oy}(i+\frac{1}{2}, j) = j \frac{1}{\kappa^2} b_z b_y H_o \cos\left(\frac{p\pi}{a}(i+\frac{1}{2})\Delta x\right) \sin\left(\frac{q\pi}{b} j \Delta y\right)$		
$H_{oz}(i+\frac{1}{2}, j+\frac{1}{2}) = H_o \cos\left(\frac{p\pi}{a}(i+\frac{1}{2})\Delta x\right) \cos\left(\frac{q\pi}{b}(j+\frac{1}{2})\Delta y\right)$		
$b_x = \frac{2 \sin(\frac{p\pi}{a} \frac{\Delta x}{2})}{\Delta x}$	$b_y = \frac{2 \sin(\frac{q\pi}{b} \frac{\Delta y}{2})}{\Delta y}$	$b_z = \frac{2 \sin(\beta_g \frac{\Delta z}{2})}{\Delta z}$
$b_t = \frac{2 \tan(\omega \frac{\Delta t}{2})}{\Delta t}$		
$\kappa^2 = 4 \frac{\sin^2(\frac{p\pi}{a} \frac{\Delta x}{2})}{\Delta x^2} + 4 \frac{\sin^2(\frac{q\pi}{b} \frac{\Delta y}{2})}{\Delta y^2} = a_z^2 - \nu_t^2 \mu \epsilon$		
$\omega_{\text{cutoff}} = \frac{2}{\Delta t} \arcsin\left(\sqrt{\frac{\sin^2(\frac{p\pi}{a} \frac{\Delta x}{2})}{(\Delta x/c\Delta t)^2} + \frac{\sin^2(\frac{q\pi}{b} \frac{\Delta y}{2})}{(\Delta y/c\Delta t)^2}}\right)$		

Placing the waveguide walls in the same manner as in the TM case, the boundary conditions reduce to

$$\mathcal{D}_y H_{oz}(i+\frac{1}{2}, j_0) = 0 \text{ (XZ)}, \quad \mathcal{D}_x H_{oz}(i_0, j+\frac{1}{2}) = 0 \text{ (YZ)} \quad (13.10)$$

These eigenvalue problems can be solved by numerical techniques, although an analytical solution can be sought in some simple cases. For instance, for a rectangular waveguide, a closed-form solution is shown in Table I. It should be noticed that the non-discrete solution is obtained from the discrete one by replacing the space discrete variables in Table I by the continuous ones, and b_t by ω , b_x by $\frac{p\pi}{a}$, b_y by $\frac{q\pi}{b}$, and b_z by β_g , which are their respective limits when all the increments tend to 0. The FDTD solution is totally similar just replacing $\tan(\omega \frac{\Delta t}{2})$ by $\sin(\omega \frac{\Delta t}{2})$ wherever it appears.

To obtain a discrete numerical solution, for instance in the TE case, we first arrange the values of $H_{oz}(i+\frac{1}{2}, j+\frac{1}{2})$ for all the discretized points on the waveguide cross section on a single column vector $\vec{\Phi}$, and then, replacing the transverse discrete Laplacian operator $\mathcal{D}_x \mathcal{D}_x + \mathcal{D}_y \mathcal{D}_y$ by (13.1), equations (13.9) and (13.10) can be explicitly written in matrix form as $\tilde{M} \vec{\Phi} = -\kappa^2 \vec{\Phi}$. Since \tilde{M} turns out to be a sparse matrix

(no more than 5 non-null elements per line), this eigenvalue problem can be solved using well known linear algebra numerical techniques.

13.3 Implementation into CN-FDTD

The procedure described in [284] has been followed for the implementation of the CN-FDTD equations (13.3). An iterative Krylov-based solution, employing the BiCGStab solver has been applied. The discrete mode has been fed into the computational space with a total-field/scattered-field formulation implemented by means of an equivalent set of surface currents on two Huygens' planes [36]: one to inject the propagating mode at a plane near one end of waveguide, and the other one close to the other end to suppress it. Simple Mur first order boundary conditions are placed at every end of the waveguide.

13.4 Results

Using the IMSL eigenvalue routines, we have obtained the TE numerical discrete modes supported by an air-filled ridged rectangular waveguide (Fig. 13.2(middle)): a total number of 937 modes can propagate in the waveguide². In order to test the accuracy of the method, we have excited at 3.30 GHz the 9th TE mode, employing for the simulation $\Delta x = \Delta y = 333.3\text{mm}$, $\Delta z = 9.0\text{ mm}$, $\Delta t = 29.70\text{ ps}$. This mode, which has a numerical cutoff frequency of 33.30 MHz, propagates along the Z axis with a low resolution (~ 10 cells/wavelength), and it is poorly sampled in time (~ 10 samples/period). Fig. 13.2 shows the H_{oz} pattern of this mode, together with the propagation of E_x along Z at $y = 38\Delta y$, after 1200 time steps. The null field region beginning at $z = 600\Delta z$ (the mode is excited at $z = 400\Delta z$) corresponds to the scattered field zone. Less than 0.01% of the energy escapes from the total field region, which proves the accuracy of the predicted mode propagation.

We have also excited a 10 mm side air-filled square waveguide, with a discrete TM_{11} mode from Table I at 31 GHz. A coarse space-time sampling has been taken $\Delta x = \Delta y = 1.667\text{ mm}$, $\Delta z = 1.581\text{ mm}$, $\Delta t = 3.12\text{ ps}$, which results in ~ 8 cells/wavelength in the propagation direction, and ~ 10 samples/period. The CN-FDTD cut-off frequency of this mode is $f_c = 20.67\text{GHz}$ ³. Fig. 13.3 shows the E_z profile at $(x = 3\Delta x, y = 3\Delta y)$, from $z = 80\Delta z$ to $z = 120\Delta z$ (the mode is excited

²The actual number of discrete modes is limited by the space discretization.

³Just for comparison: the non-discrete cut-off frequency is $f_c = 21.20\text{GHz}$ while the Yee-FDTD discrete one is 21.11 GHz. The FDTD discrete solution is closer to the non-discrete one, as expected, since the dispersion of CN-FDTD is higher than that of the classical Yee FDTD[285].

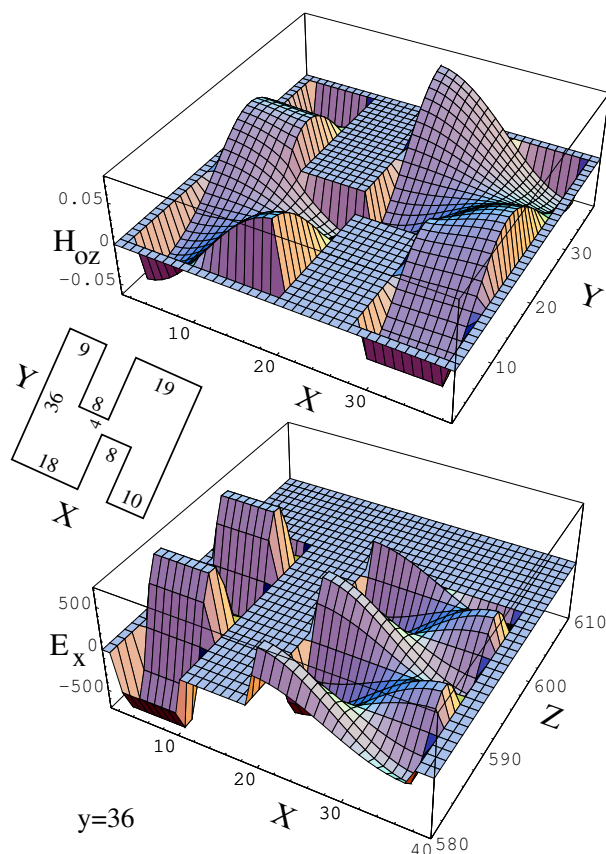


FIGURE 13.2: H_{oz} pattern of the 9th TE mode for a ridged rectangular waveguide (top). Geometry of this guide (middle). Propagation along the Z -axis of the E_x component of the 9th mode, at $y = 38$ cells (bottom). All dimensions are in cells ($\Delta x = \Delta y = 333.3$ mm, $\Delta z = 9.0$ mm, $\Delta t = 29.70$ ps)

at $z = 0$), after 300 time steps. Perfect agreement is shown between the discrete mode propagated with CN-FDTD (dashed line) and its predicted propagation ('+' symbols), while phase differences can be appreciated between the non-discrete mode (sampled in time and in space) propagated with CN-FDTD (continuous line) and its predicted evolution ('◇' symbols).

13.5 Conclusions

In this paper we have presented a procedure to obtain the discrete numerical modes propagated by the CN-FDTD method in arbitrarily-shaped metallic waveguides. We have reduced the problem to the solution of an eigenvalue problem, which has been addressed in the general case by numerical techniques, and in an analytical manner for rectangular waveguides.

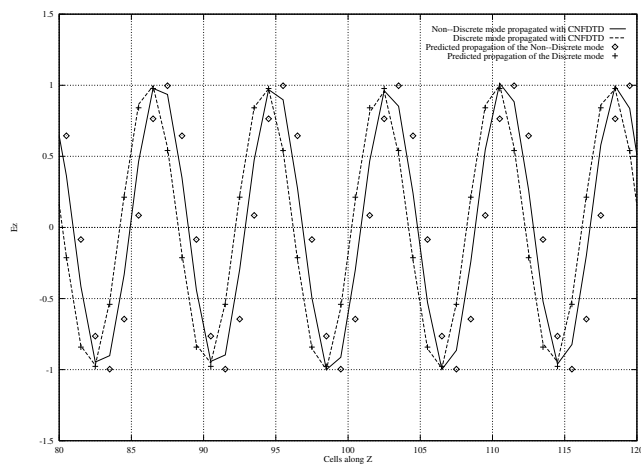


FIGURE 13.3: Propagation along the Z -axis of the E_z component of the TM_{11} mode, at $(x = 3\Delta x, y = 3\Delta y)$, in a 6 cell square waveguide. Comparison between different excitations. ($\Delta x = \Delta y = 1.667$ mm, $\Delta z = 1.581$ mm, $\Delta t = 3.12$ ps).

Chapter 14

Improving the SAR distribution in Petri-dish cell cultures

L.D. Angulo, S.G. Garcia, M.F. Pantoja, C.C. Sanchez, and R.G. Martin. Improving the sar distribution in petri-dish cell cultures. *Journal of Electromagnetic Waves and Applications*, 24:815–826(12), 2010

Abstract

Petri dishes of different types are widely used in bioelectromagnetic experiments for the assessment of the non-thermal biological effects of electromagnetic radiation. Two important qualities required for the experimental setups are to guarantee a sufficiently high level of exposure, and to maintain uniformity of the fields affecting the cell culture under study. In this paper, we apply two novel techniques to improve both parameters: the use of dishes with an elliptical shape, and the addition of metallic patches underneath the Petri dish. Results for plane-wave illumination at 2.45 GHz are shown. This methodology can also be extended to Petri dishes inside waveguide applicators.

14.1 Introduction

In vitro experiments complement epidemiological *in vivo* studies and are essential for the evaluation of biological effects of radio-frequency (RF) electromagnetic radiation. Non-thermal effect studies are becoming a topic of current focus because of the amount of low-power RF devices employed in current devices [287, 288]. Two important requirements are needed in non-thermal effects *in vitro* research: 1) the uniformity of the specific absorption rate (SAR) distribution over the area of cells under observation, and 2) exposures with a sufficiently high level of power (high SAR), so that high-power amplifiers are not needed and the total system cost is not further increased. To fulfill these minimum requirements is not an easy task, making the design and characterization of exposure setups a challenging problem [289–293].

Circular-shaped Petri dishes of different sizes are commonly used to contain the cells under investigation, which are cultured either as a monolayer at the bottom of the dish or in suspension. Several authors have calculated SAR in the volume occupied by the cells, reporting a strong dependence of its value and uniformity on several parameters, such as the amount of liquid contained in the dish, the presence of a meniscus, the polarization of the electromagnetic field, the frequency of operation, the position of the dish inside the exposure chamber, etc. [289, 290, 292–295].

In this paper, we consider monolayer cultures [296, 297] of NB69 human neuroblastoma cells, illuminated by E-polarized traveling plane electromagnetic waves (E-field vector perpendicular to the bottom of the Petri dish), and investigate the influence on the SAR distributions of elongating the Petri dish in an elliptical way, and of adding metallic patches underneath the dish. We show several cases where these techniques improve the homogeneity of the SAR pattern and/or its magnitude with respect to the usual Petri dish. However, although improved setup designs are presented, the objective of this study is not to provide a generally optimum design of a Petri dish, but rather to make the reader aware of the need to perform numerical experiments prior to designing specific Petri containers for cell exposure, bearing in mind that appropriate changes in the shape of the dish¹, and/or attaching metallic patches underneath the dish, increase the SAR and its homogeneity.

Numerical techniques have been successfully employed in bioelectromagnetics over past years, both in time and in frequency domain [298–302]. In this paper, to assess the fields in all the Petri containers considered, the numerical simulations have been

¹Though Petri dishes with uncommon geometries are not commercially available, and they need to be manufactured, we still find it interesting to present this alternative to the Bioelectromagnetic community.

performed using the software package HFSS v11.1 [303]², which is based on the finite element method in the frequency domain, and is appropriate for the narrow band nature of the problems addressed in this paper.

14.2 Circular Petri dish

We start by analyzing the behavior of a circular Petri dish (Nunc 35x10 mm type) commonly used in bioelectromagnetic experiments [296, 297]. It has $R_0 = 16.9\text{mm}$ inner radius, 1 mm–thick walls, and it is made of Polystyrene of measured relative permittivity $\epsilon_r = 3$ with negligible losses ($\tan \delta < 0.0001$) (Figs. 14.1 and 14.2). The device is filled with a Ringer’s solution similar to the D–MEM medium of [305], chemically supplemented in the way described in [297]. Its material properties found from measurements were: dielectric permittivity $\epsilon_r = 77.5$, conductivity $\sigma = 2.3\text{S/m}$ and density $\rho = 1\text{g/cm}^3$. A monolayer culture of NB69 cells is placed at the bottom of the dish, and assumed to span the first $50\mu\text{m}$, with material parameters equal to those of the Ringer’s solution. The dish is illuminated by a harmonic plane-wave of frequency 2.5 GHz, propagating in free space, traveling along the $+\hat{x}$ direction. The average power density of the incoming wave is normalized to 1W/m^2 and it is polarized with the E-field vector along \hat{z} (E polarization). This polarization has been proven to provide the most uniform exposure for monolayer cell cultures [289, 294]. The wavelengths at this frequency are 12.24cm for air, 7.07cm for plastic and 1.38cm in the liquid.

We have conducted numerical simulations of the Petri dish, filled with different amounts of liquid, with the numerical package HFSS³. Since the effect of the meniscus in the SAR values is not negligible [293], the geometry (Fig. 14.2) has been simulated, including a model from [293] for the meniscus shape, with the height of the liquid over the bottom of the dish $h_m(r)$ being an increasing function of the radial coordinate r

$$h_m(r) = h + 2.51 \left(e^{-\frac{R_0-r}{c}} + e^{-\frac{R_0+r}{c}} - 2e^{-\frac{R_0}{c}} \right), \quad |r| \leq R_0 \quad (14.1)$$

²The commercial Finite Difference Time Domain package SEMCAD X [304] was also employed only for validation to get the results of Fig. 14.3.

³2nd–order basis functions together with adaptive h–refinement is employed. Perfect magnetic conductor boundary conditions are placed in the symmetry plane to save computational resources (Fig. 14.2). A total number of 27309 tetrahedra were employed for the full problem. The Ringer solution volume was modeled with 7878 tetrahedra, with a minimum edge length of 0.53 mm., and a maximum one of 6.29 mm.

where h is the height of the liquid at the center, c is a parameter describing the decay of the profile (in our case $c = 2.01\text{mm}$), and $R_0 = 16.9\text{mm}$ is the Petri dish inner radius.

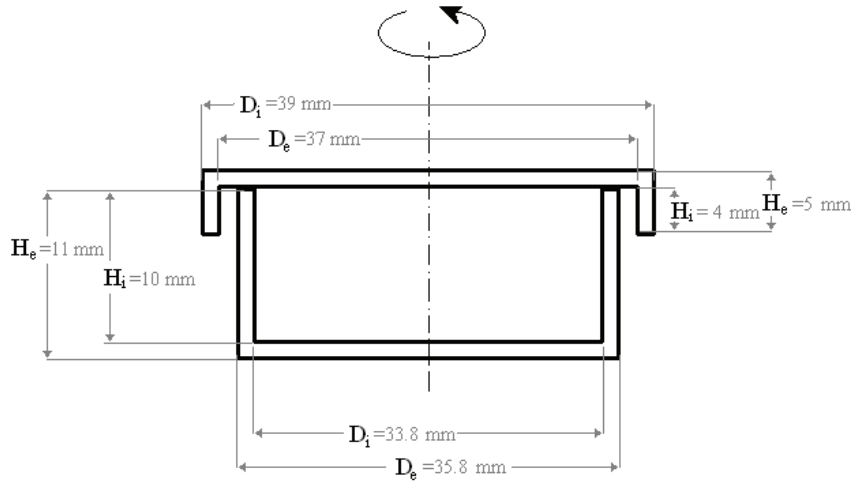


FIGURE 14.1: Petri dish geometry (the thickness of the walls is 1 mm)

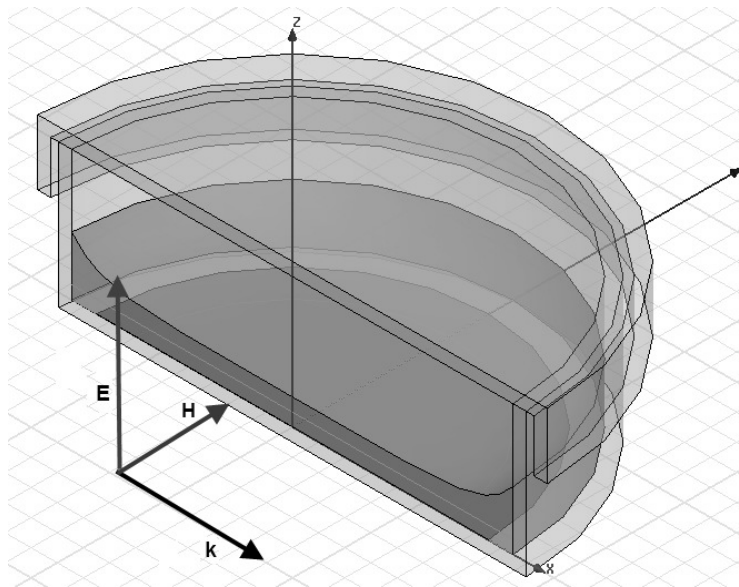


FIGURE 14.2: 3D view of half Petri dish including the liquid and the meniscus (a perfect magnetic conductor boundary condition is used in the simulations on the XZ symmetry plane).

To observe the value of the electromagnetic field and the SAR in a place occupied by the cells, but not too close to the Petri-dish walls, we define for all the simulations in this paper, an observation region S_I given by a circle of radius 15mm placed at $z = 25\mu\text{m}$, which lies approximately in the middle of the monolayer of the cell culture (thus assumed to have a negligible thickness). As suggested in [290], we do not include the whole region (radius 16.9 mm) occupied by the cells to avoid

taking values of SAR in positions near the walls, where SAR is usually strong and inhomogeneous, partly due to the presence of the meniscus⁴.

To evaluate the level and the uniformity of SAR distribution in the S_I region, we define two parameters: the average SAR S_I , μ_S ,

$$\mu_S = \frac{1}{S_I} \int_{S_I} SAR dS \quad (14.2)$$

and an inhomogeneity factor, F_h , which gives a normalized measure of the dispersion of the SAR values, and defined as the coefficient of variation (ratio of the standard deviation to the mean)

$$F_H = \frac{100}{\mu_S} \sqrt{\frac{1}{S_I} \int_{S_I} |SAR - \mu_S|^2 dS} \quad (14.3)$$

Figs. 14.3 and 14.4 show, respectively, that μ_S and F_H depend strongly on h : μ_S increases monotonically with h (greater heights should be taken if we wish to increase the SAR in the cultures), while F_H increases or decreases depending on h , and becomes monotonically decreasing for $h > 2.8mm$. As the height of $h = 5mm$ corresponds to the highest μ_S and almost the lowest F_H of the examples considered, this will be the reference design chosen for comparison in the rest of this paper. Fig. 14.5 shows the SAR pattern for this case.

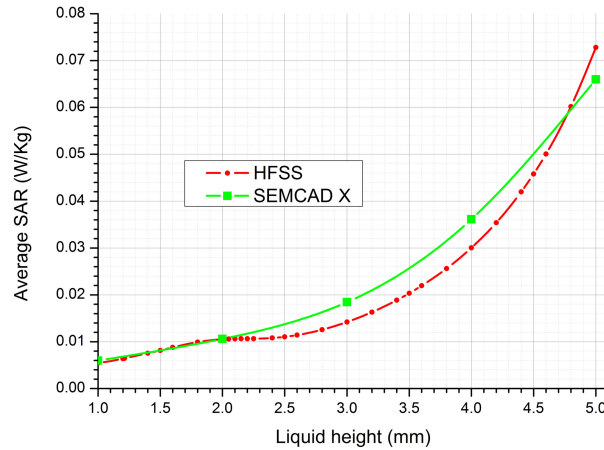


FIGURE 14.3: Average SAR calculated over the S_I region for different heights of the liquid.

⁴The thermal effect of the SAR on these regions cannot be neglected at all, when dealing with thermal biological effects. However, for non-thermal effects studies (maximum temperature rise $< 0.1K$ everywhere in the culture), researchers can exclude the cells near the walls to focus on the biological effects noticed just in the S_I area [296, 297]. In this paper, we do not deal with the thermal study, which needs to be performed on beforehand to assess the adequate illumination powers to be in the non-thermal regime.

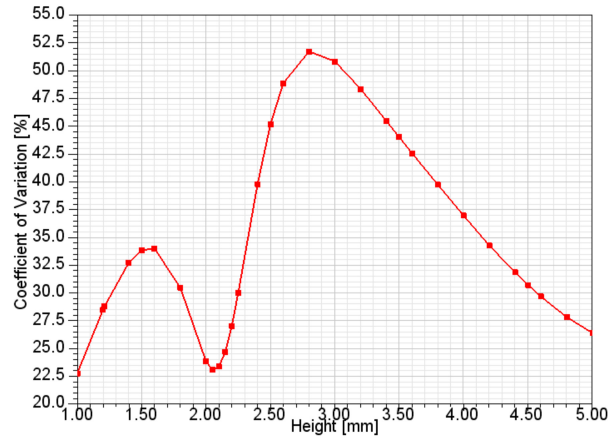


FIGURE 14.4: Coefficient of variation in the S_I region for different heights of the liquid.

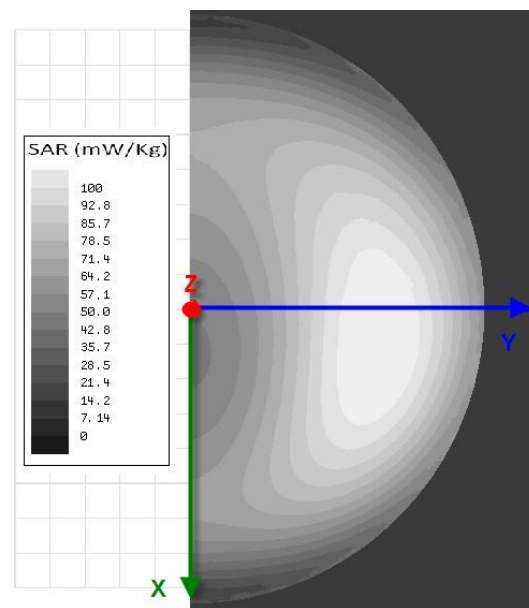


FIGURE 14.5: SAR distribution in the S_I region with a liquid height $h = 5$ mm

14.3 Elliptical Petri dishes

In this section, we explore the effect on the SAR values exerted by changing the shape of the Petri dish, increasing its dimensions in an elliptical way. In particular, the shape is considered to be an ellipse centered at $x = 0$ and $y = 0$ with semi-axes (in mm.) $16.9S_x$ and $16.9S_y$. We seek to improve the homogeneity of the SAR distribution, as well as increasing its level, in the circular region S_I defined in the previous section, by varying S_x and S_y . The idea of distorting the shape emerged after noticing that the SAR patterns usually do not show circular symmetry inside circular Petri dishes, but rather, in most cases, the SAR isolines for constant z resemble, at least partially, ellipses (Fig. 14.5).

Figs. 14.6 and 14.7 display the average SAR, μ_S , and the inhomogeneity factor, F_H , for different values of S_x and S_y . In all cases, both parameters are evaluated over the region S_I of radius=15mm defined in the previous section, and a height of the liquid, measured at the center of the dish, of $h = 5\text{mm}$ is always considered, with the meniscus profile given by (14.1).

From Fig. 14.7 we note:

1. There is a decay of F_H for increasing S_y values if $1 < S_y < 1.2$ or $1.6 < S_y < 1.8$.
2. Increasing S_x does not always improve homogeneity, as this depends on the specific value of S_y .
3. For all the circular cases analyzed ($S_x = S_y$), it is always possible to find a design with the same S_y but different S_x , which present a more uniform SAR distribution than the circular one. For instance, for $S_x = S_y = 1.4$ there is even a smaller dish (with $S_x = 1.4$, $S_y = 1.3$) with better F_H .

From Fig. 14.6, we find relative variations which are smaller in μ_S than in F_H , when S_x and S_y change. The highest values correspond to the largest Petri dishes considered ($S_x = 1.6$ and $S_y = 1.8$), which also provide the most uniform SAR distributions. The latter would constitute a good choice unless the experimental set-up requires smaller-sized dishes. For an experiment having size restrictions, we could choose from Figs. 14.6 and 14.7, a smaller dish, like $S_x = 1.2$ and $S_y = 1.25$, which gives a tradeoff solution, providing a low F_H (13%), and a rather high average SAR value.

In conclusion, we have shown that the uniformity and level of SAR can be improved by considering Petri dishes of elliptical shape, which can be optimized via numerical analysis.

14.4 Metallic additions

In this section, we show that metallic additions at the bottom of the dish, with the appropriate shape, also serve to improve both the homogeneity and the level of the SAR. The shape of the metallic parts have been designed by trial and error, examining the inhomogeneous SAR patterns. For instance, the SAR distribution of Fig. 14.5 shows higher values of the fields inside a region with its borders resembling the shape of a "D". A possible way to raise the level of the fields in the regions

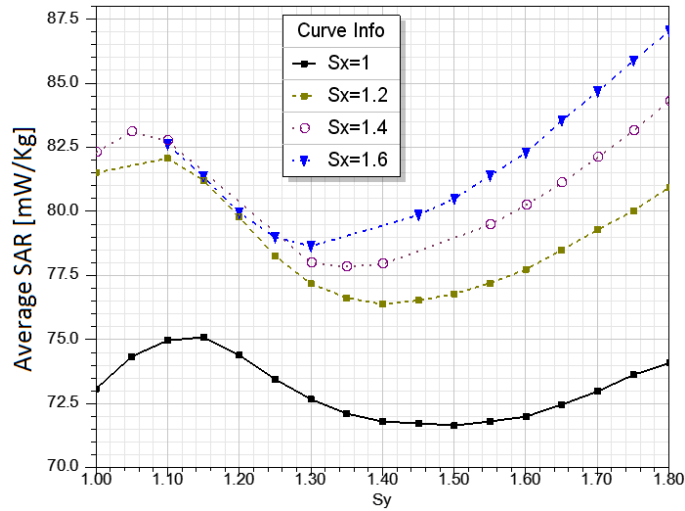


FIGURE 14.6: Average SAR for different values of S_x and S_y .

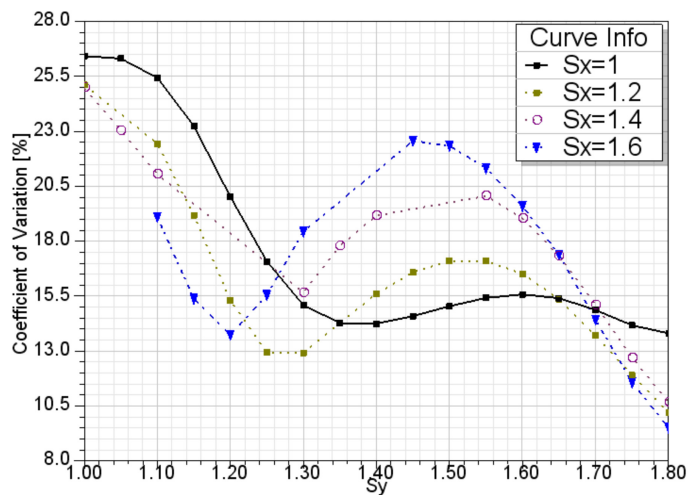


FIGURE 14.7: Inhomogeneity factor for different values of S_x and S_y

where their value is lower, is given by the placement underneath the dishes, of metallic patches with their borders in areas of low field intensity, to take advantage of the extra radiation at these zones.

To provide the optimum shape of the metallic patches, a systematic analysis could also be employed, for instance, by optimization techniques, which is beyond the scope of this work. Once again, our goal is only to introduce the idea of improving the SAR homogeneity using this technique, and not to present the best possible shape of the metal additions for this or any other case. To illustrate the procedure, we have considered again the circular Petri dish filled with a liquid a liquid of height $h = 5\text{mm}$, measured at the center of the dish, with the meniscus profile given by (14.1).

Fig. 14.8 shows the shape of the four different kinds of metallic attachments proposed, and their relative location⁵. We call them: *plate*, *plate-ring*, *ring* and *ring-ring* metallization. The height of the metal (copper) is 0.1mm and they are printed on a 1mm thick FR4 epoxy layer ($\epsilon_r = 4.4$, $\tan \delta = 0.02$), commonly used to build printed circuit boards, on top of which the Petri dish is placed.

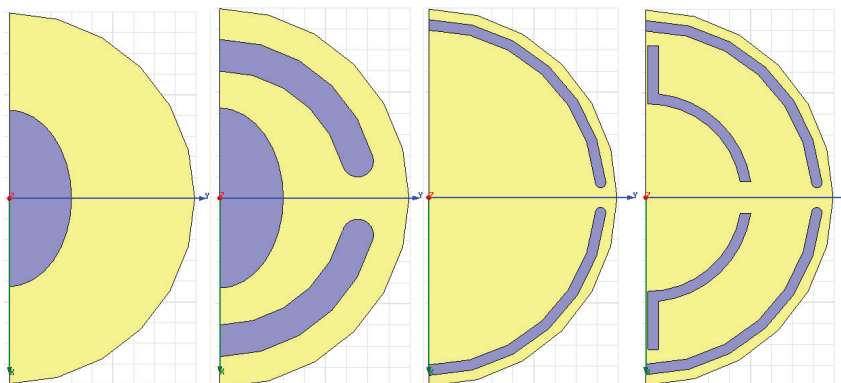


FIGURE 14.8: Geometry of the different metallic additions: From left to right: a) *plate*, b) *plate-ring*, c) *ring* and d) *ring-ring*

Fig. 14.9 shows, the inhomogeneity factor F_H calculated between 2 GHz and 3 GHz for all the metallic shapes considered, and for the case without metallization. Notice that the improved designs depend also on frequency, which needs to be taken into account in any systematic optimization study. Taking for instance the interval from 2.2 GHz to 2.5 GHz, we see that all the cases with metallic additions provide a better design than the case without metal. The one called *ring-ring* proves to be the best in the frequency range of approximately from 2.1 GHz to 2.7 GHz.

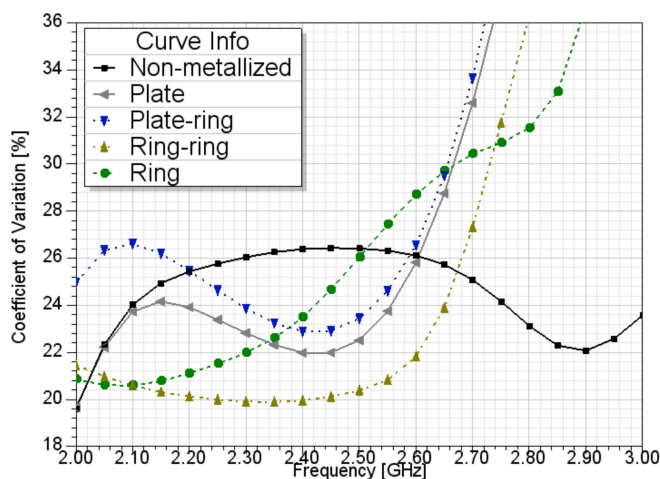


FIGURE 14.9: Inhomogeneity factors for different metallic shapes calculated from 2 to 3 GHz.

⁵Since the exact mechanical data are lengthy to be provided, IGES geometrical files for these lay-outs can be downloaded from <http://maxwell.ugr.es/metalic.tar>

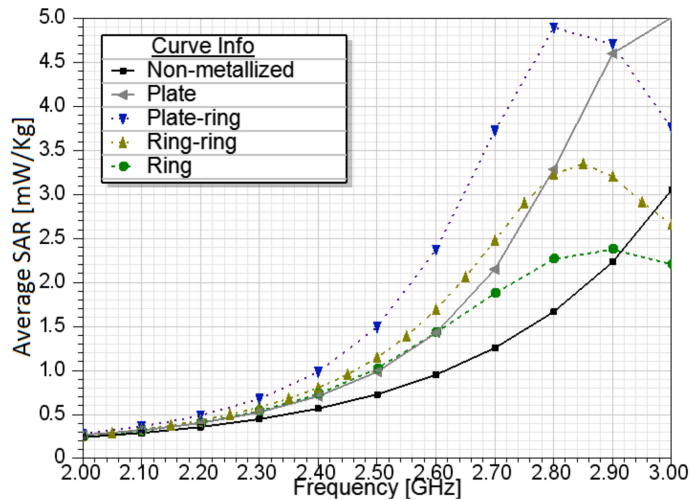


FIGURE 14.10: Average SAR compared for the different metallic shapes from 2 to 3 GHz.

Regarding the level of SAR μ_S (Fig. 14.10), all the metallic additions improve it with respect to the no-metal case (except for frequencies close to 3GHz in the *ring* and *ring-ring* configurations). The *plate-ring* achieves the highest μ_S values for almost all the frequencies considered, but at the cost of providing a bad performance in terms of uniformity. A tradeoff solution between uniformity and SAR level is seen to be the *ring-ring* shape (between 2.1 GHz and 2.7 GHz).

14.5 Conclusions

Many parameters strongly affect the SAR distributions of Petri-dish cell cultures under RF exposure: the presence of the meniscus, the amount of liquid in the dish, etc.. In this paper, we analyze the influence of the shape of the dish, and the presence of metallic elements on its underside, on the SAR level and on its uniformity.

Two novel techniques to improve the homogeneity and level of SAR values in Petri dishes are introduced. One is based on changing the shape of the Petri dish in an elliptical way, and the other one is based on the addition of thin metallic patches of different shapes. Particular improved designs are presented using both techniques.

Appendix A

Resumen

Esta tesis presenta una agrupación de trabajos académicos publicados o enviados para su publicación en revistas científicas. El tema principal de la tesis aborda el desarrollo del método discontinuo de Galerkin para la simulación de la propagación de ondas electromagnéticas en el dominio del tiempo. Está compuesta de 14 capítulos, cada uno de ellos correspondiente a un artículo, y agrupados en seis partes.

- La primera parte (Capítulo 1) es una revisión del estado del arte, a modo de introducción, del método discontinuo de Galerkin (DG) en el dominio del tiempo (TD). En este trabajo se enfatizan las técnicas que han sido testadas directamente por nuestro grupo de investigación en el desarrollo de un programa propio, SEMBA (Simulador Electromagnético de Banda Ancha). Se explican los fundamentos matemáticos del método y las técnicas específicas usadas para modelar diferentes fenómenos electromagnéticos.
- La segunda parte (Capítulos 2, 3, y 4) se enfoca en la semi-discretización espacial del método DG. En el Capítulo 2, se investiga la presencia de modos espurios en guías de onda y se plantean formas para eliminar su presencia. Los argumentos teóricos dados se validan mediante dos simulaciones de filtros de microondas de los cuales se poseen resultados experimentales. El Capítulo 3 presenta una hibridación de los métodos continuo de Galerkin (CG) y DG como un modo de reducir los consumos de memoria y mejorar la eficiencia computacional. Finalmente, en el Capítulo 4 se presenta un estudio de la precisión del método de DG incluyendo la integración temporal LF2 (Leap-Frog de segundo orden); como conclusión se presenta una comparativa con el método de diferencias finitas en el dominio del tiempo (FDTD) que permite establecer pautas de uso para uno y otro método.

-
- La tercera parte (Capítulos 5 y 6) se centra en dos técnicas que se pueden usar para realizar la integración temporal del método DG. El Capítulo 5 presenta una nueva técnica de paso temporal local (LTS). Esta técnica se puede usar tanto para el método Runge-Kutta (RK) como para LF2 y su funcionamiento se demuestra mediante una comparación con otras técnicas para distintos problemas de propagación. En el Capítulo 6, se analiza el método Discontinuo Galerkin en el espacio-tiempo (STDG), cuya diferencia principal es que el formalismo DG se usa también para la variable temporal. En este capítulo se muestra una novedosa forma de aplicar el método para que el algoritmo se pueda plantear de forma pseudo-explicita.
 - La cuarta parte (Capítulos 7 y 8) cubre el modelado de procesos electromagnéticos. El Capítulo 7 se centra a las fuentes electromagnéticas, trasladando a DGTD los principios de Huygens con los que se resuelve el problema en FDTD. Se muestra como modelar iluminación con ondas planas y con fuentes localizadas tales como dipolos eléctricos. El Capítulo 8 es un estudio sobre el modelado de materiales anisótropos. En particular se centra en como modelar adecuadamente los flujos numéricos para tener en cuenta la anisotropía de la impedancia. Los resultados son validados mediante comparaciones con los obtenidos por un software comercial.
 - La quinta parte (Capítulos 9, 10 y 11) presenta una validación del método en distintos casos de aplicación para problemas de ingeniería. En el Capítulo 9, se demuestra la validez del método para la evaluación del efecto de campos radiados de alta intensidad (HIRF) en la compatibilidad electromagnética (EMC). El Capítulo 10 muestra una comparativa de los resultados obtenidos por el método DGTD con LF2 para la simulación de una geometría compleja comúnmente utilizada como banco de pruebas por la NASA. Los resultados se comparan con los obtenidos mediante el Método de los Momentos (MoM) concluyéndose que el método DGTD es competitivo con las técnicas existentes. El Capítulo 11 demuestra las capacidades del método en un contexto de simulación de un radar de penetración de tierra (GPR). Se muestran resultados similares a los obtenidos experimentalmente con un dispositivo GPR.
 - La sexta parte (Capítulos 12, 13, y 14) presenta otros trabajos publicados que han sido llevados a cabo durante este periodo de tesis. La temática versa sobre otros métodos numéricos en diversos contextos. El Capítulo 12 muestra simulaciones de láminas de grafeno mediante la inclusión de modelos de materiales dispersivos en FDTD. El Capítulo 13 presenta un procedimiento para el cálculo de los modos de propagación discretos en una guía de onda usando el método

FDTD con Crank-Nicolson. Finalmente, el Capítulo 14 demuestra el uso de un simulador comercial, HFSS, que utiliza el método de elementos finitos en el dominio de la frecuencia (FEMFD) para la optimización de las dosis de radiación en el interior de placas Petri mediante la inclusión de metalizaciones y cambios geométricos en las placas.

A.1 Contribuciones Científicas y Futuras Líneas de Trabajo

Los objetivos principales que han guiado el desarrollo de esta tesis han sido dos. El primero ha sido explorar las posibilidades que ofrece la discretización espacial basada en elementos discontinuos de Galerkin en la resolución de las ecuaciones de Maxwell en el dominio del tiempo. El segundo ha sido proponer, implementar y aplicar distintas alternativas de esta metodología y aplicarlas en distintos contextos. A continuación se destacan las contribuciones científicas logradas a lo largo de este trabajo sirviendo como resumen de los resultados obtenidos. Finalmente, se enumera una lista de futuras líneas de trabajo en esta área.

A.1.1 Contribuciones Científicas

Podemos resumir abreviadamente los logros conseguidos en este trabajo de investigación en los siguientes puntos:

1. **Formulación del esquema espacial semi-discreto basado en elementos discontinuos de Galerkin.** La formulación se ha desarrollado de una forma general, unificando diferentes esquemas en la evaluación del flujo, que han sido aplicados con éxito a este método. La formulación incluye el tratamiento de las condiciones de contorno más comunes, materiales anisótropos, dispersivos, una implementación preliminar de láminas delgadas y condiciones de contorno absorbentes (Silver-Mueller de primer orden) además de las condiciones de frontera conformes y uniaxiales perfectamente adaptadas (PMLs).
2. **Desarrollo e implementación de algoritmos basados en DGTD.** Se han aplicado los métodos de integración temporal LF2 y Runge-Kutta explícito de cuarto orden y bajo almacenamiento (LSERK4). En este contexto, se han desarrollado con éxito estrategias de avance local en tiempo (LTS) que mitigan la limitación impuesta por la condición de estabilidad, crítica en los esquemas de discretización temporal explícitos.

3. **Desarrollo de nuevas técnicas de integración temporal.** Se han desarrollado dos técnicas nuevas para la integración temporal. La técnica de LTS por senda causal (CP-LTS) que permite realizar una integración temporal mediante los métodos LF2 y LSERK4 con importantes mejoras en la eficiencia computacional. Los resultados se validaron en una serie de casos de prueba y se compararon con otras técnicas existentes poniendo de manifiesto mejoras respecto a la dispersión numérica. Por otro lado se han implementado métodos DG en el espacio-tiempo (STDG) en dos dimensiones (una espacial y una temporal). Se ha planteado una mejora respecto a las técnicas existentes al proponer un esquema STDG pseudo-implícito que mejora drásticamente la eficiencia en problemas eléctricamente grandes.
4. **Propuesta y análisis de una técnica híbrida continua-discontinua de Galerkin (CDGTD).** Se ha propuesto un método novedoso consistente en el ensamblaje mediante funciones continuas de agrupaciones con un número moderado de elementos. Esto presenta ventajas claras en cuanto a los consumos de memoria, tamaño del paso temporal y, en consecuencia, eficiencia computacional para bases polinómicas de ordenes moderados. La técnica abre una puerta al uso de métodos implícitos, tradicionalmente prohibitivos, en el dominio del tiempo. También permite interfactar de forma natural mallas tetraédricas y hexaédricas mediante una región de acoplamiento en la que se usa el método CDGTD. La dispersión y disipación numérica de los esquemas resultantes se han analizado de forma teórica y mediante experimentos numéricos.
5. **Análisis del esquema semi-discreto DG y del algoritmo LFDG.** La dispersión y disipación de los métodos numéricos han sido estudiadas con especial énfasis en la identificación y mitigación de los modos espurios. Además, se han estimado los órdenes de convergencia en las relaciones de dispersión y disipación y estudiado la anisotropía de ambos errores. En el caso del algoritmo LFDG, se han estudiado otros temas como la estabilidad y el coste computacional. Se han explorado y evaluado los límites del algoritmo LFDG. Se ha llevado a cabo un análisis final estimando el coste computacional frente a precisión, comparando los resultados con el método FDTD.
6. **Validación y aplicación del algoritmo.** Los algoritmos DGTD implementados han sido validados con filtros de microondas, antenas, problemas de compatibilidad electromagnética y de sección recta radar (RCS). Los resultados se han comparado con medidas u otras técnicas numéricas. El método ha sido

aplicado a problemas reales de ingeniería, mostrando importantes propiedades: robustez, estabilidad, versatilidad, eficiencia, escalabilidad y precisión.

A.1.2 Futuras Líneas de Trabajo

Aunque muchos y muy diferentes métodos de cálculo electromagnético se han desarrollado en profundidad para estudiar la mayor parte de los problemas prácticos que nos encontramos en ingeniería, todavía existen vacíos para los que se hace imprescindible explorar nuevas técnicas. Estas son algunas de las posibles líneas que podría ser interesante desarrollar:

1. **Desarrollo e implementación de capacidades adicionales.** La técnica DGTD tiene muchas similitudes con FDTD permitiendo la adaptación de modelos ya existentes y extensamente probados. Entre ellos: modelos de capa delgada dispersivos y/o anisótropos, elementos circuitales discretos, modelos de hilo delgado, ranuras delgadas, etc..
2. **Mejora de la versatilidad en el uso de métodos de elementos finitos en el dominio del tiempo (FEMTD), en general.** Diferentes alternativas podrían ser desarrolladas para mejorar la versatilidad de los métodos FEMTD en simulaciones reales. Algunas son las siguientes: (i) utilización de mallas híbridas que contengan diferentes tipos de celdas, aprovechando las diferentes propiedades de cada una de ellas, por ejemplo tetraedros en regiones complejas, hexaedros en regiones sin detalles (ii) utilización de mallas estructuradas/no estructuradas, para reducir el uso de memoria en zonas estructuradas donde las matrices locales pueden compartirse; o (iii) el uso de elementos no conformes que permitan refinar localmente la malla, muy efectivo en la aplicación de técnicas de refinamiento h , y en la simulación de problemas con un alto contraste en las propiedades de los materiales.
3. **Desarrollo de técnicas de adaptatividad tipo hp .** Los problemas electromagnéticos tratados en este trabajo demuestran la importancia de la utilización de adaptabilidad tipo hp . El desarrollo de técnicas de adaptación eficientes tipo hp en simulaciones en el dominio del tiempo permitiría la aplicación del método de una forma más automática. Para ello, un punto crucial es una estrecha integración del mallador en el simulador electromagnético. El desarrollo de técnicas dinámicas de adaptatividad hp espaciales y de orden arbitrario en tiempo, capaces de adaptar dinámicamente la malla y el método de integración durante la simulación, pueden reducir notablemente los tiempos de cálculo de una simulación completa asegurando la precisión requerida.

4. **Simulación multifísica.** Existe una necesidad creciente de simulaciones acopladas térmicas-mecánicas-electromagnéticas capaces de manejar la complejidad de problemas reales (por ejemplo en la predicción de efectos de impacto de un rayo en estructuras de materiales compuestos). El uso de mallas no estructuradas basadas en tetraedros simplifica el acoplamiento multi-físico de diferentes modelos numéricos, que también utilizan este tipo de mallas.

Bibliography

- [1] LF Shampine. Stability of the leapfrog/midpoint method. *Applied Mathematics and Computation*, 208(1):293–298, 2009.
- [2] X.-Q. Sheng and z. peng. Analysis of scattering by large objects with off-diagonally anisotropic material using finite element-boundary integral-multilevel fast multipole algorithm. *Microwaves, Antennas Propagation, IET*, 4(4):492–500, April 2010. ISSN 1751-8725. doi: 10.1049/iet-map.2008.0088.
- [3] L. D. Angulo, J. Alvarez, M. F. Pantoja, S. G. Garcia, and A. R. Bretones. Discontinuous galerkin time domain methods in computational electrodynamics: State of the art. *Forum for Electromagnetic Research Methods and Application Technologies (FERMAT)*, Submitted.
- [4] Clint Dawson and Jennifer Proft. Coupling of continuous and discontinuous galerkin methods for transport problems. *Computer Methods in Applied Mechanics and Engineering*, 191(29–30):3213 – 3231, 2002. ISSN 0045-7825. doi: [http://dx.doi.org/10.1016/S0045-7825\(02\)00257-8](http://dx.doi.org/10.1016/S0045-7825(02)00257-8). URL <http://www.sciencedirect.com/science/article/pii/S0045782502002578>.
- [5] T. C. Warburton and G. E. Karniadakis. A discontinuous galerkin method for the viscous mhd equations. *J. Comput. Phys.*, 152:608–641, July 1999. ISSN 0021-9991. doi: 10.1006/jcph.1999.6248. URL <http://portal.acm.org/citation.cfm?id=329646.329668>.
- [6] Yan Xu and Chi-Wang Shu. Local discontinuous galerkin methods for nonlinear schrödinger equations. *Journal of Computational Physics*, 205(1):72 – 97, 2005. ISSN 0021-9991. doi: 10.1016/j.jcp.2004.11.001. URL <http://www.sciencedirect.com/science/article/pii/S0021999104004589>.
- [7] Michael Dumbser, Martin Käser, and Eleuterio F. Toro. An arbitrary high-order discontinuous galerkin method for elastic waves on unstructured meshes - v. local time stepping and p-adaptivity. *Geophysical Journal International*,

- 171(2):695–717, 2007. doi: 10.1111/j.1365-246X.2007.03427.x. URL <http://gji.oxfordjournals.org/content/171/2/695.abstract>.
- [8] Steffen Petersen, Charbel Farhat, and Radek Tezaur. A space–time discontinuous galerkin method for the solution of the wave equation in the time domain. *International Journal for Numerical Methods in Engineering*, 78(3):275–295, 2009. ISSN 1097-0207. doi: 10.1002/nme.2485. URL <http://dx.doi.org/10.1002/nme.2485>.
- [9] SEMBA, simulador electromagnetico de banda ancha. <http://www.ugrfdtd.es>, .
- [10] J. Alvarez, L.D. Angulo, M. Fernandez Pantoja, A. Rubio Bretones, and S.G. Garcia. Source and boundary implementation in vector and scalar dgtd. *Antennas and Propagation, IEEE Transactions on*, 58(6):1997–2003, 2010. ISSN 0018-926X. doi: 10.1109/TAP.2010.2046857.
- [11] J. Alvarez, L. D. Angulo, S. G. Garcia, M. F. Pantoja, and A. R. Bretones. A comparison between upwind/centered nodal/vector basis dgtd. In *IEEE International Symposium on Antennas and Propagation and CNC/USNC/URSI Radio Science Meeting*, 2010.
- [12] L. D. Angulo, J. Alvarez, S.G. Garcia, A. Rubio Bretones, and R. Gomez Martin. Discontinuous galerkin time-domain method for gpr simulation of conducting objects. *Near Surface Geophysics*, 9:257–263, 2011.
- [13] J. Alvarez, L. D. Angulo, A. Rubio Bretones, and S.G. Garcia. A spurious-free discontinuous galerkin time-domain method for the accurate modeling of microwave filters. *Microwave Theory and Techniques, IEEE Transactions on*, 60(8):2359–2369, 2012.
- [14] J. Alvarez, L. D. Angulo, A. Rubio Bretones, and S. Gonzalez Garcia. 3d discontinuous galerkin time–domain method for anisotropic materials. *Antennas and Wireless Propagation Letters, IEEE*, 11:1182–1185, 2012.
- [15] J. Alvarez. *A Discontinuous Galerkin Finite Element Method for the Time-Domain Solution of Maxwell Equations*. PhD thesis, Universidad de Granada, 2013. URL http://maxwell.ugr.es/wordpress/wp-content/uploads/bsk-pdf-manager/3_PhD_Jesus_Alvarez.pdf.
- [16] J. Alvarez, L. D. Angulo, M. Bandinelli, H. Bruns, M. Francavilla, S. Garcia, R. Guidi, G. Gutierrez, C. Jones, M. Kunze, J. Martinaud, I. Munteanu, M. Panitz, J. Parmantier, P. Pirinoli, Z. Reznicek, G. Salin, A. Schroder,

- P. Tobola, and F. Vipiana. HIRF interaction with metallic aircrafts. a comparison between fd and fd methods. In *Electromagnetic Compatibility (EMC EUROPE), 2012 International Symposium on*, pages 1–6, 2012. doi: 10.1109/EMCEurope.2012.6396703.
- [17] J. Alvarez, L. D. Angulo, A. R. Bretones, and S. G. Garcia. A comparison of the fdtd and lfdg methods for the estimation of hif transfer functions. In *Proceedings on Computational Electromagnetics And Electromagnetic Compatibility 2013 (CEMEMC13)*, 2013.
- [18] J. Alvarez, L. D. Angulo, A.R. Bretones, M.R. Cabello, and S.G. Garcia. A leap-frog discontinuous galerkin time-domain method for hif assessment. *Electromagnetic Compatibility, IEEE Transactions on*, 55(6):1250–1259, 2013. ISSN 0018-9375. doi: 10.1109/TEMC.2013.2265045.
- [19] J. Alvarez, Pascual E., Guadalupe G., Añon M., Fernandez S., Coll A., Ruiz-Cabello M., L. D. Angulo, and S. Gonzalez Garcia. Hif se. desarrollo y validación de un entorno sintético de simulación para soporte en el diseño y certificación de aeronaves. In *DESEI+D*, 2013.
- [20] G.G. Gutierrez, J. Alvarez, E. Pascual-Gil, M. Bandinelli, R. Guidi, V. Martorelli, M.F. Pantoja, M.R. Cabello, and S.G. Garcia. Hif virtual testing on the c-295 aircraft: On the application of a pass/fail criterion and the fsv method. *Electromagnetic Compatibility, IEEE Transactions on*, PP(99):1–10, 2013. ISSN 0018-9375. doi: 10.1109/TEMC.2013.2291680.
- [21] J. Alvarez, J. M. Alonso-Rodriguez, H. Carbajosa-Cobaleda, M. R. Cabello, L. D. Angulo, R. Gomez-Martin, and S. G. Garcia. Dgtd for a class of low-observable targets: A comparison with mom and (2,2) fdtd. *IEEE Antennas and Wireless Propagation Letters*, 13:241–244, 2014. doi: 10.1109/LAWP.2014.2300699.
- [22] J. Alvarez, L. D. Angulo, M.R. Cabello, A. R. Bretones, and S. G. Garcia. An analysis of the leap-frog discontinuous galerkin method for maxwell’s equations. *IEEE Transactions on Microwave Theory and Techniques*, 62(2): 197–207, February 2014.
- [23] L. D. Angulo, J. Alvarez, F.L. Teixeira, M.F. Pantoja, and S.G. Garcia. Causal-path local time-stepping in the discontinuous galerkin method for maxwell’s equations. *Journal of Computational Physics*, 256:678 – 695, 2014.

- [24] L. D. Angulo, J. Alvarez, M. F. Pantoja, and S. G. Garcia. An explicit nodal space-time discontinuous galerkin method for maxwell's equations. *IEEE Microwave and Wireless Components Letters*, Accepted.
- [25] J. Alvarez, L. D. Angulo, A. Rubio Bretones, Carlos M. de Jong, and S. G. Garcia. Efficient antenna modeling by dgt. *IEEE Antennas and Propagation Magazine*, Submitted.
- [26] L. D. Angulo, J. Alvarez, F. L. Teixeira, M. F. Pantoja, and S. G. Garcia. A nodal hybrid continuous-discontinuous galerkin time domain method for maxwell's equations. *IEEE Transactions On Microwave Theory And Techniques*, Submitted.
- [27] Jan S. Hesthaven and Tim Warburton. *Nodal Discontinuous Galerkin Methods: Algorithms, Analysis, and Applications*. Springer Publishing Company, Incorporated, 1st edition, 2007. ISBN 0387720650, 9780387720654.
- [28] J. S. Hesthaven and T. Warburton. Discontinuous galerkin methods for the time-domain maxwell's equations: An introduction. *ACES Newsletter*, 19(1): 10–29, 2004.
- [29] Jiefu Chen and Qing Huo Liu. Discontinuous galerkin time-domain methods for multiscale electromagnetic simulations: A review. *Proceedings of the IEEE*, 101(2):242–254, 2013. ISSN 0018-9219. doi: 10.1109/JPROC.2012.2219031.
- [30] K. Busch, M. Konig, and J. Niegemann. Discontinuous galerkin methods in nanophotonics. *Laser & Photonics Reviews*, 5(6):773–809, 2011. ISSN 1863-8899. doi: 10.1002/lpor.201000045. URL <http://dx.doi.org/10.1002/lpor.201000045>.
- [31] KYU-PYUNG HWANG. Computational efficiency of fang's fourth-order fdtd schemes. *Electromagnetics*, 23(2):89–102, 2003. doi: 10.1080/02726340390159450. URL <http://www.tandfonline.com/doi/abs/10.1080/02726340390159450>.
- [32] S. Dey and R. Mittra. A locally conformal finite-difference time-domain (fdtd) algorithm for modeling three-dimensional perfectly conducting objects. *Microwave and Guided Wave Letters, IEEE*, 7(9):273–275, Sep 1997. ISSN 1051-8207. doi: 10.1109/75.622536.
- [33] Costas D Sarris. Adaptive mesh refinement for time-domain numerical electromagnetics. *Synthesis Lectures on Computational Electromagnetics*, 1(1): 1–154, 2007.

- [34] Joonshik Kim and F.L. Teixeira. Parallel and explicit finite-element time-domain method for maxwell's equations. *Antennas and Propagation, IEEE Transactions on*, 59(6):2350–2356, June. ISSN 0018-926X. doi: 10.1109/TAP.2011.2143682.
- [35] Eric T. Chung and Bjorn Engquist. Optimal discontinuous galerkin methods for wave propagation. *SIAM J. Numer. Anal.*, 44(5):2131–2158, September 2006. ISSN 0036-1429. doi: 10.1137/050641193. URL <http://dx.doi.org/10.1137/050641193>.
- [36] Allen Taflove and Susan C. Hagness. *Computational Electrodynamics The Finite-Differences Time Domain Method*. 2005.
- [37] CA USA Kane Yee; University of California, Livermore. Numerical solution of initial boundary value problems involving maxwell's equations in isotropic media. *Antennas and Propagation, IEEE Transactions on*, 14 Issue:3:302 – 307, 1966.
- [38] S.V. Georgakopoulos, C.R. Birtcher, C.A. Balanis, and R.A. Renaut. Higher-order finite-difference schemes for electromagnetic radiation, scattering, and penetration .1. theory. *Antennas and Propagation Magazine, IEEE*, 44(1): 134–142, Feb 2002. ISSN 1045-9243. doi: 10.1109/74.997945.
- [39] J. L. Young. High-order, leapfrog methodology for the temporally dependent maxwell's equations. *Radio Science*, 36(1):9–17, 2001. ISSN 1944-799X. doi: 10.1029/2000RS002503. URL <http://dx.doi.org/10.1029/2000RS002503>.
- [40] C. Fumeaux, D. Baumann, P. Leuchtman, and R. Vahldieck. A generalized local time-step scheme for efficient fvtd simulations in strongly inhomogeneous meshes. *Microwave Theory and Techniques, IEEE Transactions on*, 52(3): 1067–1076, March 2004. ISSN 0018-9480. doi: 10.1109/TMTT.2004.823595.
- [41] K. Sankaran, C. Fumeaux, and R. Vahldieck. Cell-centered finite-volume-based perfectly matched layer for time-domain maxwell system. *Microwave Theory and Techniques, IEEE Transactions on*, 54(3):1269 – 1276, march 2006. ISSN 0018-9480. doi: 10.1109/TMTT.2006.869704.
- [42] D. Baumann, C. Fumeaux, R. Vahldieck, and Erping Li. Conformal perfectly matched absorber for finite-volume time-domain simulations. In *Electromagnetic Compatibility and 19th International Zurich Symposium on Electromagnetic Compatibility, 2008. APEMC 2008. Asia-Pacific Symposium on*, pages 188 –191, May 2008. doi: 10.1109/APEMC.2008.4559843.

- [43] C. Bommaraju, W. Ackermann, and T. Weiland. Convergence of error in fvtd methods on tetrahedral meshes in 3d. In *Applied Electromagnetics Conference (AEMC), 2009*, pages 1–4, Dec 2009. doi: 10.1109/AEMC.2009.5430655.
- [44] Jin-Fa Lee, R. Lee, and A. Cangellaris. Time-domain finite-element methods. *Antennas and Propagation, IEEE Transactions on*, 45(3):430–442, 1997. ISSN 0018-926X. doi: 10.1109/8.558658.
- [45] D.R. Lynch and K.D. Paulsen. Time-domain integration of the maxwell equations on finite elements. *Antennas and Propagation, IEEE Transactions on*, 38(12):1933–1942, Dec 1990. ISSN 0018-926X. doi: 10.1109/8.60982.
- [46] J-F Lee and Z. Sacks. Whitney elements time domain (wetd) methods. *Magnetics, IEEE Transactions on*, 31(3):1325–1329, May 1995. ISSN 0018-9464. doi: 10.1109/20.376272.
- [47] J-F Lee. Wetd - a finite element time-domain approach for solving maxwell's equations. *Microwave and Guided Wave Letters, IEEE*, 4(1):11–13, Jan 1994. ISSN 1051-8207. doi: 10.1109/75.267679.
- [48] S.D. Gedney and U. Navsariwala. An unconditionally stable finite element time-domain solution of the vector wave equation. *Microwave and Guided Wave Letters, IEEE*, 5(10):332–334, Oct 1995. ISSN 1051-8207. doi: 10.1109/75.465046.
- [49] Jian-Ming Jin, Mohammad Zunoubi, Kalyan C. Donepudi, and Weng C. Chew. Frequency-domain and time-domain finite-element solution of maxwell's equations using spectral lanczos decomposition method. *Computer Methods in Applied Mechanics and Engineering*, 169(3–4):279 – 296, 1999. ISSN 0045-7825. doi: [http://dx.doi.org/10.1016/S0045-7825\(98\)00158-3](http://dx.doi.org/10.1016/S0045-7825(98)00158-3). URL <http://www.sciencedirect.com/science/article/pii/S0045782598001583>.
- [50] W. P. Carpes Jr, L. Pichon, and A. Razek. A 3D finite element method for the modeling of bounded and unbounded electromagnetic problems in the time domain. *International Journal of Numerical Modelling: Electronic Networks, Devices and Fields*, 13(6):527–540, 2000.
- [51] D. Jiao and J. M. Jin. A general approach for the stability analysis of the time-domain finite-element method for electromagnetic simulations. *IEEE Transactions on Antennas and Propagation*, 50(11):1624–1632, November 2002.
- [52] D. Jiao and J. M. Jin. Three-dimensional orthogonal vector basis functions for time-domain finite element solution of vector wave equations. *IEEE Transactions on Antennas and Propagation*, 51(1):59–65, January 2003.

- [53] Zheng Lou and Jian-Ming Jin. Modeling and simulation of broad-band antennas using the time-domain finite element method. *Antennas and Propagation, IEEE Transactions on*, 53(12):4099–4110, Dec 2005. ISSN 0018-926X. doi: 10.1109/TAP.2005.859905.
- [54] R. Wang, H. Wu, A. C. Cangellaris, and J. M. Jin. Incorporation of a feed network into the time-domain finite-element modeling of antenna arrays. *IEEE Transactions on Antennas and Propagation*, 56(8):2599–2612, August 2008.
- [55] Ryan A. Chilton and Robert Lee. The discrete origin of fetd-newmark late time instability, and a correction scheme. *J. Comput. Phys.*, 224(2):1293–1306, June 2007. ISSN 0021-9991. doi: 10.1016/j.jcp.2006.11.021. URL <http://dx.doi.org/10.1016/j.jcp.2006.11.021>.
- [56] R. N. Rieben, G. H. Rodrigue, and D. A. White. A high order mixed vector finite element method for solving the time dependent Maxwell equations on unstructured grids. *Journal of Computational Physics*, 204:490–519, 2005.
- [57] B. He and F. L. Teixeira. Sparse and explicit FETD via approximate inverse Hodge (mass) matrix. *IEEE Microwave and Wireless Components Letters*, 16(6):348–350, June 2006.
- [58] B. He and F. L. Teixeira. Differential forms, Galerkin duality, and sparse inverse approximations in finite element solutions of Maxwell equations. *IEEE Transactions on Antennas and Propagation*, 55(5):1359–1368, May 2007.
- [59] B. Donderici and F.L. Teixeira. Conformal perfectly matched layer for the mixed finite element time-domain method. *Antennas and Propagation, IEEE Transactions on*, 56(4):1017–1026, 2008. ISSN 0018-926X. doi: 10.1109/TAP.2008.919215.
- [60] B. Donderici and F. L. Teixeira. Mixed finite-element time-domain method for transient Maxwell equations in doubly dispersive media. *IEEE Transaction on Microwave Theory and Techniques*, 56(1):113–120, January 2008.
- [61] R. S. Chen, L. Du, Z. Ye, and Y. Yang. An efficient algorithm for implementing the Crank-Nicolson scheme in the mixed finite-element time-domain method. *IEEE Transaction on Antennas and Propagation*, 57(10):3216–3222, October 2009.
- [62] J. S. Hesthaven and T. Warburton. High-order nodal discontinuous galerkin methods for the maxwell eigenvalue problem. *Philosophical Transactions of the Royal Society of London. Series A:Mathematical, Physical and Engineering*

- Sciences*, 362(1816):493–524, 2004. doi: 10.1098/rsta.2003.1332. URL <http://rsta.royalsocietypublishing.org/content/362/1816/493.abstract>.
- [63] E.K. Miller. A selective survey of computational electromagnetics. *Antennas and Propagation, IEEE Transactions on*, 36(9):1281–1305, Sep 1988. ISSN 0018-926X. doi: 10.1109/8.8607.
- [64] S. Dosopoulos and Jin-Fa Lee. Interior penalty discontinuous galerkin finite element method for the time-dependent first order maxwell’s equations. *Antennas and Propagation, IEEE Transactions on*, 58(12):4085 –4090, 2010. ISSN 0018-926X. doi: 10.1109/TAP.2010.2078445.
- [65] Stéphane Descombes, Stéphane Lanteri, and Ludovic Moya. Locally implicit time integration strategies in a discontinuous galerkin method for maxwell’s equations. *Journal of Scientific Computing*, 56(1):190–218, 2013. ISSN 0885-7474. doi: 10.1007/s10915-012-9669-5. URL <http://dx.doi.org/10.1007/s10915-012-9669-5>.
- [66] Marcello D’Amore. C27j airframe lighting certification using cem. In *EMC Europe 2010 Wroclaw*.
- [67] L. Pebernet, X. Ferrieres, S. Pernet, F. Rogier, and P. Degond. A discontinuous galerkin method to solve electromagnetic problems. *IET Conference Publications*, 2008(CP537):96–97, 2008. doi: 10.1049/cp:20080229. URL <http://link.aip.org/link/abstract/IEECPS/v2008/iCP537/p96/s1>.
- [68] Ping Li and Li Jun Jiang. Integration of arbitrary lumped multiport circuit networks into the discontinuous galerkin time-domain analysis. *Microwave Theory and Techniques, IEEE Transactions on*, 61(7):2525–2534, 2013. ISSN 0018-9480. doi: 10.1109/TMTT.2013.2261085.
- [69] Zheng Lou and Jian-Ming Jin. An accurate waveguide port boundary condition for the time-domain finite-element method. *Microwave Theory and Techniques, IEEE Transactions on*, 53(9):3014–3023, 2005. ISSN 0018-9480. doi: 10.1109/TMTT.2005.854223.
- [70] Tiao Lu, Wei Cai, and Pingwen Zhang. Discontinuous galerkin time-domain method for gpr simulation in dispersive media. *Geoscience and Remote Sensing, IEEE Transactions on*, 43(1):72 – 80, 2005. ISSN 0196-2892. doi: 10.1109/TGRS.2004.838350.
- [71] Bernardo Cockburn, G. E. Karniadakis, and C.-W. Shu. *Discontinuous Galerkin Methods*. Springer, 2000.

- [72] Chi-Wang Shu. Discontinuous galerkin methods: general approach and stability. 2009.
- [73] R.J. LeVeque. *Finite Volume Methods for Hyperbolic Problems*. Cambridge Texts in Applied Mathematics. Cambridge University Press, 2002. ISBN 9780521009249. URL <http://books.google.es/books?id=QazcnD7GUoUC>.
- [74] D. Sarmany, M. A. Botchev, and J. J. Vejt. Dispersion and dissipation error in high-order runge-kutta discontinuous galerkin discretisations of the maxwell equations. *J. Sci. Comput.*, 33:47–74, October 2007. ISSN 0885-7474. doi: 10.1007/s10915-007-9143-y. URL <http://portal.acm.org/citation.cfm?id=1288603.1288623>.
- [75] Mark Ainsworth. Dispersive and dissipative behaviour of high order discontinuous galerkin finite element methods. *J. Comput. Phys.*, 198:106–130, July 2004. ISSN 0021-9991. doi: 10.1016/j.jcp.2004.01.004. URL <http://portal.acm.org/citation.cfm?id=1027293.1027299>.
- [76] M. Ainsworth, P. Monk, and W. Muniz. Dispersive and dissipative properties of discontinuous galerkin finite element methods for the second-order wave equation. *Journal of Scientific Computing*, 27(1-3):5–40, 2006. ISSN 0885-7474. doi: 10.1007/s10915-005-9044-x. URL <http://dx.doi.org/10.1007/s10915-005-9044-x>.
- [77] E. Montseny, S. Pernet, X. Ferrières, and G. Cohen. Dissipative terms and local time-stepping improvements in a spatial high order discontinuous galerkin scheme for the time-domain maxwell’s equations. *J. Comput. Phys.*, 227(14): 6795–6820, July 2008. ISSN 0021-9991. doi: 10.1016/j.jcp.2008.03.032. URL <http://dx.doi.org/10.1016/j.jcp.2008.03.032>.
- [78] J.C. Nedelec. *Acoustic and Electromagnetic Equations: Integral Representations for Harmonic Problems*. Number v. 144 in Acoustic and electromagnetic equations: integral representations for harmonic problems. Springer, 2001. ISBN 9780387951553. URL <http://books.google.es/books?id=NABGVMOHbqEC>.
- [79] K. Sankaran. *Accurate domain truncation techniques for time-domain conformal methods*. PhD thesis, ETH Zurich, 2007.
- [80] Spencer Sherwin. Dispersion analysis of the continuous and discontinuous galerkin formulations. In *International Symposium on Discontinuous Galerkin Methods*, pages 425–431. Springer, 1999.

- [81] Nassif Nabil Rappaz Jacques Descloux, Jean. On spectral approximation. part 1. the problem of convergence. *ESAIM: Mathematical Modelling and Numerical Analysis - Modélisation Mathématique et Analyse Numérique*, 12 (2):97–112, 1978. URL <http://eudml.org/doc/193319>.
- [82] Peter P. Silvester and Ronald L. Ferrari. *Finite elements for electrical engineers*. Cambridge University Press, third edition, 1996.
- [83] Jianming Jin. *The Finite Element Method in Electromagnetics*. Wiley-Interscience, 1993.
- [84] Din Sun, J. Manges, Xingchao Yuan, and Z. Cendes. Spurious modes in finite-element methods. *Antennas and Propagation Magazine, IEEE*, 37(5):12–24, October 1995. ISSN 1045-9243. doi: 10.1109/74.475860.
- [85] J.P. Webb. Hierarchical vector basis functions of arbitrary order for triangular and tetrahedral finite elements. *Antennas and Propagation, IEEE Transactions on*, 47(8):1244–1253, Aug 1999. ISSN 0018-926X. doi: 10.1109/8.791939.
- [86] Gerrit Mur. Edge elements, their advantages and their disadvantages. *Magnetics, IEEE Transactions on*, 30(5):3552–3557, Sep 1994. ISSN 0018-9464. doi: 10.1109/20.312706.
- [87] Ruben Otin. Regularized maxwell equations and nodal finite elements for electromagnetic field computations. *Electromagnetics*, 30:190–204, 2010. URL <http://prod.informaworld.com/10.1080/02726340903485489>.
- [88] Martin Costabel and Monique Dauge. Weighted regularization of maxwell equations in polyhedral domains. *Numerische Mathematik*, 93:239–277, 2002. ISSN 0029-599X. 10.1007/s002110100388.
- [89] T. Warburton and Mark Embree. The role of the penalty in the local discontinuous galerkin method for maxwell’s eigenvalue problem. *Computer Methods in Applied Mechanics and Engineering*, 195(25–28):3205 – 3223, 2006. ISSN 0045-7825. doi: <http://dx.doi.org/10.1016/j.cma.2005.06.011>. URL <http://www.sciencedirect.com/science/article/pii/S0045782505002665>. Discontinuous Galerkin Methods.
- [90] Gary Cohen and Marc Duruflé. Non-Spurious Spectral Like Element Methods for Maxwell’s equations. *Journal of Computational Mathematics*, pages 282–304, 2007. URL <http://hal.archives-ouvertes.fr/hal-00385458>.
- [91] G. Cohen, X. Ferrieres, and S. Pernet. A spatial high-order hexahedral discontinuous galerkin method to solve maxwell’s equations in time domain.

- Journal of Computational Physics*, 217(2):340 – 363, 2006. ISSN 0021-9991. doi: <http://dx.doi.org/10.1016/j.jcp.2006.01.004>. URL <http://www.sciencedirect.com/science/article/pii/S0021999106000131>.
- [92] *The Discontinuous Galerkin Finite Element Time Domain Method (DGFETD): A High Order, Globally-Explicit Method for Parallel Computation*, 2007. doi: 10.1109/ISEMC.2007.196.
- [93] Serge Piperno. Symplectic local time-stepping in non-dissipative dgtd methods applied to wave propagation problems. *ESAIM: Mathematical Modelling and Numerical Analysis*, 40(5):815–841, 1 2007.
- [94] Alain Bossavit. A rationale for edge-elements in 3-d fields computations. *Magnetics, IEEE Transactions on*, 24(1):74–79, 1988. ISSN 0018-9464. doi: 10.1109/20.43860.
- [95] J.C. Nedelec. Mixed finite elements in r3. *Numerische Mathematik*, 35(3):315–341, 1980. ISSN 0029-599X. doi: 10.1007/BF01396415.
- [96] J.C. Nedelec. A new family of mixed finite elements in r3. *Numerische Mathematik*, 50(1):57–81, 1986. ISSN 0029-599X. doi: 10.1007/BF01389668.
- [97] Gerrit Mur. The fallacy of edge elements. *Magnetics, IEEE Transactions on*, 34(5):3244–3247, Sep 1998. ISSN 0018-9464. doi: 10.1109/20.717761.
- [98] J.S. Hesthaven. From electrostatics to almost optimal nodal sets for polynomial interpolation in a simplex. *SIAM J. Numer. Anal.*, 35:655–676, 1998.
- [99] S. Chun and J.S. Hesthaven. High-order accurate thin layer approximations for time-domain electromagnetics. part i: General metal backed coatings. *Journal of Computational and Applied Mathematics*, 231(2):598 – 611, 2009. ISSN 0377-0427. doi: <http://dx.doi.org/10.1016/j.cam.2009.04.019>. URL <http://www.sciencedirect.com/science/article/pii/S0377042709002520>.
- [100] H. Fahs. Recent achievements on a non-conforming dgtd method for time-domain electromagnetics. 2009.
- [101] H. Fahs. Improving accuracy of high-order discontinuous galerkin method for time-domain electromagnetics on curvilinear domains. *International Journal of Computer Mathematics*, 88(10):2124–2153, 2011. doi: 10.1080/00207160.2010.527960. URL <http://www.tandfonline.com/doi/abs/10.1080/00207160.2010.527960>.

- [102] T. Warburton. A low storage curvilinear discontinuous galerkin time-domain method for electromagnetics. In *Electromagnetic Theory (EMTS), 2010 URSI International Symposium on*, pages 996–999, Aug 2010. doi: 10.1109/URSI-EMTS.2010.5637392.
- [103] Gmsh, a three-dimensional finite element mesh generator with built-in pre- and post-processing facilities. <http://geuz.org/gmsh/>.
- [104] GiD the personal pre and post processor. <http://www.gidhome.com/>.
- [105] Per olof Persson and Jaime Peraire. Curved mesh generation and mesh refinement using lagrangian solid mechanics, 2012.
- [106] P. Silvester. Symmetric quadrature formulae for simplexes. *Mathematics of Computation*, 24:95–95, 1970. doi: 10.2307/2004880.
- [107] Hassan Fahs. High-order leap-frog based discontinuous galerkin method for the time-domain maxwell equations on non-conforming simplicial meshes. *Numerical Mathematics: A Journal of Chinese Universities*, 2(3):275 – 300, August 2009. URL <http://hal.archives-ouvertes.fr/hal-00600467/en/>.
- [108] Stylianos Dosopoulos, Bo Zhao, and Jin-Fa Lee. Non-conformal and parallel discontinuous galerkin time domain method for maxwell’s equations: {EM} analysis of {IC} packages. *Journal of Computational Physics*, 238(0):48 – 70, 2013. ISSN 0021-9991. doi: <http://dx.doi.org/10.1016/j.jcp.2012.11.048>. URL <http://www.sciencedirect.com/science/article/pii/S0021999112007309>.
- [109] Clement Durochat, Stéphane Lanteri, and Claire Scheid. High order non-conforming multi-element discontinuous galerkin method for time domain electromagnetics. *Applied Mathematics and Computation*, 224:681–704, November 2013. doi: 10.1016/j.amc.2013.08.069. URL <http://hal.inria.fr/hal-00797973>.
- [110] Raphael Leger, Jonathan Viquerat, Clement Durochat, Claire Scheid, and Stéphane Lanteri. A parallel non-confoming multi-element DGTD method for the simulation of electromagnetic wave interaction with metallic nanoparticles. *Journal of Computational and Applied Mathematics*, (0):–, 2013. ISSN 0377-0427. doi: <http://dx.doi.org/10.1016/j.cam.2013.12.042>. URL <http://www.sciencedirect.com/science/article/pii/S0377042713007152>.
- [111] Morgane Bergot and Marc Duruflé. Higher-order discontinuous galerkin method for pyramidal elements using orthogonal bases. *Numerical Methods*

- for *Partial Differential Equations*, 29(1):144–169, 2013. ISSN 1098-2426. doi: 10.1002/num.21703. URL <http://dx.doi.org/10.1002/num.21703>.
- [112] Morgane Bergot. *Elements finis d dordre eleve pour maillages hybrides*. PhD thesis, Universite Paris Daphine, 2012.
- [113] Richard Diehl, Kurt Busch, and Jens Niegemann. Comparison of low-storage runge-kutta schemes for discontinuous galerkin time-domain simulations of maxwell’s equations. *Journal of Computational and Theoretical Nanoscience*, 7(8):1572–1580, 2010. doi: doi:10.1166/jctn.2010.1521. URL <http://www.ingentaconnect.com/content/asp/jctn/2010/00000007/00000008/art00035>.
- [114] Jens Niegemann, Richard Diehl, and Kurt Busch. Efficient low-storage runge–kutta schemes with optimized stability regions. *Journal of Computational Physics*, 231(2):364 – 372, 2012. ISSN 0021-9991. doi: <http://dx.doi.org/10.1016/j.jcp.2011.09.003>. URL <http://www.sciencedirect.com/science/article/pii/S0021999111005213>.
- [115] Bernardo Cockburn and Chi-Wang Shu. Runge–kutta discontinuous galerkin methods for convection-dominated problems. *Journal of scientific computing*, 16(3):173–261, 2001.
- [116] M. Lilienthal, S. M. Schnepf, and T. Weiland. Non-dissipative space-time *hp*-discontinuous galerkin method for the time-dependent maxwell equations. *ArXiv e-prints*, July .
- [117] Roland Griesmaier and Peter Monk. Discretization of the wave equation using continuous elements in time and a hybridizable discontinuous galerkin method in space. *Journal of Scientific Computing*, pages 1–27, 2013. ISSN 0885-7474. doi: 10.1007/s10915-013-9741-9. URL <http://dx.doi.org/10.1007/s10915-013-9741-9>.
- [118] Marcus J Grote, Michaela Mehlin, and Teodora Mitkova. Runge-kutta based explicit local time-stepping methods for wave propagation. In *Scientific Computing in Electrical Engineering*, 2014. URL https://europa.unibas.ch/fileadmin/mathe/redaktion/Preprints/14_alle/Preprint-1405.pdf.
- [119] Peter Monk and Gerard R. Richter. A discontinuous galerkin method for linear symmetric hyperbolic systems in inhomogeneous media. *Journal of Scientific Computing*, 22-23:443–477, 2005. ISSN 0885-7474. URL <http://dx.doi.org/10.1007/s10915-004-4132-5>.

- [120] Victorita Dolean, Hassan Fahs, Loula Fezoui, and Stéphane Lanteri. Locally implicit discontinuous galerkin method for time domain electromagnetics. *J. Comput. Phys.*, 229(2):512–526, January 2010. ISSN 0021-9991. doi: 10.1016/j.jcp.2009.09.038. URL <http://dx.doi.org/10.1016/j.jcp.2009.09.038>.
- [121] Alex Kanevsky, Mark H. Carpenter, David Gottlieb, and Jan S. Hesthaven. Application of implicit-explicit high order runge-kutta methods to discontinuous-galerkin schemes. *Journal of Computational Physics*, 225(2):1753 – 1781, 2007. ISSN 0021-9991. doi: 10.1016/j.jcp.2007.02.021. URL <http://www.sciencedirect.com/science/article/pii/S0021999107000861>.
- [122] Stylianos Dosopoulos. *Interior Penalty Discontinuous Galerkin Finite Element Method for the Time-Domain Maxwell's Equations*. PhD thesis, Ohio State University, 2012.
- [123] J. H. Wilkinson. *The Algebraic Eigenvalue Problem*. Clarendon Press, 1964.
- [124] Loula Fezoui, Stéphane Lanteri, Stéphanie Lohrengel, and Serge Piperno. Convergence and stability of a discontinuous galerkin time-domain method for the 3d heterogeneous maxwell equations on unstructured meshes. *ESAIM: Mathematical Modelling and Numerical Analysis*, 39:1149–1176, 11 2005. ISSN 1290-3841. doi: 10.1051/m2an:2005049. URL http://www.esaim-m2an.org/action/article_S0764583X0500049X.
- [125] D. Sarmany, M.A. Botchev, and J.J.W. van der Vegt. Time-integration methods for finite element discretisations of the second-order maxwell equation. *Computers & Mathematics with Applications*, 65(3):528 – 543, 2013. ISSN 0898-1221. doi: 10.1016/j.camwa.2012.05.023. URL <http://www.sciencedirect.com/science/article/pii/S0898122112004713>.
- [126] J. H. Williamson. Low-storage runge-kutta schemes. *Journal of Computational Physics*, 35(1):48 – 56, 1980. ISSN 0021-9991. doi: DOI:10.1016/0021-9991(80)90033-9. URL <http://www.sciencedirect.com/science/article/B6WHY-4DD1NRP-H1/2/a1a09857d87c5a3538d4800fd648be47>.
- [127] Christopher A. Kennedy, Mark H. Carpenter, and R. Michael Lewis. Low-storage, explicit runge-kutta schemes for the compressible navier-stokes equations. *Appl. Numer. Math.*, 35:177–219, November 2000. ISSN 0168-9274. doi: 10.1016/S0168-9274(99)00141-5.
- [128] C. Chauviere, J.S. Hesthaven, A. Kanevsky, and T. Warburton. High-order localized time integration for grid-induced stiffness. In K.J. Bathe, editor,

- Computational Fluid and Solid Mechanics 2003*, pages 1883 – 1886. Elsevier Science Ltd, Oxford, 2003. ISBN 978-0-08-044046-0. doi: <http://dx.doi.org/10.1016/B978-008044046-0.50461-9>. URL <http://www.sciencedirect.com/science/article/pii/B9780080440460504619>.
- [129] Arne Taube, Michael Dumbser, Claus-Dieter Munz, and Rudolf Schneider. A high-order discontinuous galerkin method with time-accurate local time stepping for the maxwell equations. *International Journal of Numerical Modelling: Electronic Networks, Devices and Fields*, 22(1):77–103, 2009. ISSN 1099-1204. doi: 10.1002/jnm.700. URL <http://dx.doi.org/10.1002/jnm.700>.
- [130] Meilin Liu, K. Sirenko, and H. Bagci. An efficient discontinuous galerkin finite element method for highly accurate solution of maxwell equations. *Antennas and Propagation, IEEE Transactions on*, 60(8):3992–3998, 2012. ISSN 0018-926X. doi: 10.1109/TAP.2012.2201092.
- [131] Andreas Glaser and Vladimir Rokhlin. A new class of highly accurate solvers for ordinary differential equations. *Journal of Scientific Computing*, 38(3):368–399, 2009. ISSN 0885-7474. doi: 10.1007/s10915-008-9245-1. URL <http://dx.doi.org/10.1007/s10915-008-9245-1>.
- [132] Richard S. Falk and Gerard R. Richter. Explicit finite element methods for symmetric hyperbolic equations. *SIAM J. Numer. Anal.*, 36(3):935–952, March 1999. ISSN 0036-1429. doi: 10.1137/S0036142997329463. URL <http://dx.doi.org/10.1137/S0036142997329463>.
- [133] F Kretzschmar, S M Schnepf, I Tsukerman, and T Weiland. Discontinuous galerkin methods with trefftz approximation. *arXiv (submitted)*, 2013. URL <http://arxiv.org/abs/1302.6459>.
- [134] Susan C. Hagness Allen Taflove. *Computational Electrodynamics The Finite-Differences Time Domain Method*. British Library, 2000.
- [135] D.E. Merewether, R. Fisher, and F.W. Smith. On implementing a numeric huygen’s source scheme in a finite difference program to illuminate scattering bodies. *Nuclear Science, IEEE Transactions on*, 27(6):1829–1833, Dec 1980. ISSN 0018-9499. doi: 10.1109/TNS.1980.4331114.
- [136] R.J. Luebbers, K.S. Kunz, M. Schneider, and F. Hunsberger. A finite-difference time-domain near zone to far zone transformation [electromagnetic scattering]. *Antennas and Propagation, IEEE Transactions on*, 39(4):429 – 433, apr 1991. ISSN 0018-926X. doi: 10.1109/8.81453.

- [137] Higher-order time-domain methods for the analysis of nano-photonic systems. *Photonics and Nanostructures - Fundamentals and Applications*, 7(1):2 – 11, 2009. ISSN 1569-4410. doi: <http://dx.doi.org/10.1016/j.photonics.2008.08.006>.
- [138] R. Gomez Martin. *Electromagnetic field theory for physicist and engineers: Fundamentals and Applications*. Grupo de Electromagnetismo de Granada, 2006.
- [139] Milton Abramowitz and Irene A. Stegun. *Handbook of Mathematical Functions: with Formulas, Graphs, and Mathematical Tables*. Dover books on mathematics. Dover, New York, June 1972. ISBN 0486612724. URL <http://www.worldcat.org/isbn/0486612724>.
- [140] Jean-Pierre Berenger. A perfectly matched layer for the absorption of electromagnetic waves. *Journal of Computational Physics*, 114:185–200, 1994. doi: 10.1006/jcph.1994.1159.
- [141] S.D. Gedney and Bo Zhao. An auxiliary differential equation formulation for the complex-frequency shifted pml. *Antennas and Propagation, IEEE Transactions on*, 58(3):838 –847, 2010. ISSN 0018-926X. doi: 10.1109/TAP.2009.2037765.
- [142] Stephen D Gedney. An anisotropic perfectly matched layer-absorbing medium for the truncation of fdtd lattices. *Antennas and Propagation, IEEE Transactions on*, 44(12):1630–1639, 1996.
- [143] S Gonzalez Garcia, I Villó Pérez, R Gomez Martin, and B García Olmedo. Applicability of the pml absorbing boundary condition to dielectric anisotropic media. *Electronics Letters*, 32(14):1270–1271, 1996.
- [144] S Gonzalez Garcia, I Villo Perez, R Gomez Martin, and B Garcia Olmedo. Bipml: A pml to match waves in bianisotropic media. *Microwave and Optical Technology Letters*, 20(1):44–48, 1999.
- [145] M.A. Gribbons, A.P. Pinello, and A.C. Cangellaris. A stretched coordinate technique for numerical absorption of evanescent and propagating waves in planar waveguiding structures. *Microwave Theory and Techniques, IEEE Transactions on*, 43(12):2883 –2889, December 1995. ISSN 0018-9480. doi: 10.1109/22.475650.
- [146] F. L. Teixeira and W. C. Chew. Analytical derivation of a conformal perfectly matched absorber for electromagnetic waves. *Microwave and Optical Technology Letters*, 17(4):231–236, 1998. ISSN

- 1098-2760. doi: 10.1002/(SICI)1098-2760(199803)17:4<231::AID-MOP3>3.0.CO;2-J. URL [http://dx.doi.org/10.1002/\(SICI\)1098-2760\(199803\)17:4<231::AID-MOP3>3.0.CO;2-J](http://dx.doi.org/10.1002/(SICI)1098-2760(199803)17:4<231::AID-MOP3>3.0.CO;2-J).
- [147] J Alan Roden and Stephen D Gedney. Convolution pml (cpml): An efficient fdtd implementation of the cfs-pml for arbitrary media. *Microwave and Optical Technology Letters*, 27(5):334–339, 2000.
- [148] F.L. Teixeira, K.-P. Hwang, W.C. Chew, and J.-M. Jin. Conformal pml-fdtd schemes for electromagnetic field simulations: a dynamic stability study. *Antennas and Propagation, IEEE Transactions on*, 49(6):902–907, June 2001. ISSN 0018-926X. doi: 10.1109/8.931147.
- [149] Mustafa Kuzuoglu and Raj Mittra. Frequency dependence of the constitutive parameters of causal perfectly matched anisotropic absorbers. *Microwave and Guided Wave Letters, IEEE*, 6(12):447–449, 1996.
- [150] F.L. Teixeira and W.C. Chew. Extension of the pml absorbing boundary condition to 3d spherical coordinates: scalar case. *Magnetics, IEEE Transactions on*, 34(5):2680–2683, September 1998. ISSN 0018-9464. doi: 10.1109/20.717621.
- [151] C. H. Wilcox. An expansion theorem for electromagnetic fields. *Communications on Pure and Applied Mathematics*, 9(2):115–134, 1956. ISSN 1097-0312. doi: 10.1002/cpa.3160090202. URL <http://dx.doi.org/10.1002/cpa.3160090202>.
- [152] Julius Adams Stratton. *Electromagnetic theory*. McGraw-Hill New York, 1st ed. edition, 1941.
- [153] S.G. Garcia, R.G. Rubio, A.R. Bretones, and R.G. Martin. Extension of the adi-fdtd method to debye media. *Antennas and Propagation, IEEE Transactions on*, 51(11):3183–3185, nov. 2003. ISSN 0018-926X. doi: 10.1109/TAP.2003.818770.
- [154] Claire Scheid and Stephane Lanteri. Convergence of a discontinuous galerkin scheme for the mixed time domain maxwell’s equations in dispersive media. Research Report RR-7634, INRIA, May 2011. URL <http://hal.inria.fr/inria-00597374/en/>.
- [155] Jonathan Viquerat, Klemm Maciej, Stéphane Lantéri, and Claire Scheid. Theoretical and numerical analysis of local dispersion models coupled to a

- discontinuous galerkin time-domain method for maxwell's equations. Rapport de recherche RR-8298, INRIA, May 2013. URL <http://hal.inria.fr/hal-00819758>. MIBC VF.
- [156] Soon-Cheol Kong, J.J. Simpson, and V.; Backman. Ade-fdtd scattered-field formulation for dispersive materials. *IEEE Microwave and Wireless Components Letters*, 18:1, 2008. doi: 10.1109/LMWC.2007.911970. URL http://ieeexplore.ieee.org/xpls/abs_all.jsp?arnumber=4407751.
- [157] Xia Ji, Wei Cai, and Pingwen Zhang. High-order dgtd methods for dispersive maxwell's equations and modelling of silver nanowire coupling. *International Journal for Numerical Methods in Engineering*, 69(2):308–325, 2007. doi: 10.1002/nme.1762. URL <http://dx.doi.org/10.1002/nme.1762>.
- [158] S.D. Gedney, J. Young, and T. Kramer. Modeling of dispersive media within the discontinuous galerkin finite element time-domain method. In *Antennas and Propagation Society International Symposium (APSURSI), 2010 IEEE*, pages 1–4, july 2010. doi: 10.1109/APS.2010.5561914.
- [159] H.T. Banks, V.A. Bokil, and N.L. Gibson. Analysis of stability and dispersion in a finite element method for debye and lorentz dispersive media. *Numerical Methods for Partial Differential Equations*, 25(4):885–917, 2009. ISSN 1098-2426. doi: 10.1002/num.20379. URL <http://dx.doi.org/10.1002/num.20379>.
- [160] Bo Wang, Ziqing Xie, and Zhimin Zhang. Error analysis of a discontinuous galerkin method for maxwell equations in dispersive media. *Journal of Computational Physics*, 229(22):8552 – 8563, 2010. ISSN 0021-9991. doi: 10.1016/j.jcp.2010.07.038. URL <http://www.sciencedirect.com/science/article/pii/S0021999110004316>.
- [161] Minghui Han, R.W. Dutton, and Shanhui Fan. Model dispersive media in finite-difference time-domain method with complex-conjugate pole-residue pairs. *Microwave and Wireless Components Letters, IEEE*, 16(3):119–121, 2006. ISSN 1531-1309. doi: 10.1109/LMWC.2006.869862.
- [162] H. Lin, M. F. Pantoja, L. D. Angulo, J. Alvarez, R. G. Martin, and S. G. Garcia. Fdtd modeling of graphene devices using complex conjugate dispersion material model. *Microwave and Wireless Components Letters, IEEE*, 22(12):612–614, dec. 2012. ISSN 1531-1309. doi: 10.1109/LMWC.2012.2227466.
- [163] Dirk Deschrijver, Michal Mrozowski, Tom Dhaene, and Daniël De Zutter. Macromodeling of multiport systems using a fast implementation of

- the vector fitting method. *IEEE MICROWAVE AND WIRELESS COMPONENTS LETTERS*, 18(6):383–385, 2008. ISSN 1531-1309. URL <http://dx.doi.org/10.1109/LMWC.2008.922585>.
- [164] B. Gustavsen. Improving the pole relocating properties of vector fitting. *IEEE Trans. Power Delivery*, 21(3):1587–1592, July 2006.
- [165] B. Gustavsen and A. Semlyen. Rational approximation of frequency domain responses by vector fitting. *Power Delivery, IEEE Transactions on*, 14(3):1052–1061, jul 1999. ISSN 0885-8977. doi: 10.1109/61.772353. Some codes about vector fitting: <http://www.energy.sintef.no/Produkt/VECTFIT/index.asp>.
- [166] Fang Q. Hu, M. Y. Hussaini, and Patrick Rasetarinera. An analysis of the discontinuous galerkin method for wave propagation problems. *Journal of Computational Physics*, 151(2):921 – 946, 1999. ISSN 0021-9991. doi: DOI: 10.1006/jcph.1999.6227. URL <http://www.sciencedirect.com/science/article/B6WHY-45GMWB0-4W/2/664d638d79e7dbae02e4b04792ee61e3>.
- [167] Jichun Li. Unified analysis of leap-frog methods for solving time-domain maxwell’s equations in dispersive media. *J. Sci. Comput.*, 47:1–26, April 2011. ISSN 0885-7474. doi: <http://dx.doi.org/10.1007/s10915-010-9417-7>. URL <http://dx.doi.org/10.1007/s10915-010-9417-7>.
- [168] Michael Konig, Kurt Busch, and Jens Niegemann. The discontinuous galerkin time-domain method for maxwell’s equations with anisotropic materials. *Photonics and Nanostructures - Fundamentals and Applications*, 8(4):303 – 309, 2010. ISSN 1569-4410. doi: <http://dx.doi.org/10.1016/j.photonics.2010.04.001>. URL <http://www.sciencedirect.com/science/article/pii/S1569441010000246>. Tacona Photonics 2009.
- [169] Stylianos Dosopoulos and Jin-Fa Lee. Interconnect and lumped elements modeling in interior penalty discontinuous galerkin time-domain methods. *Journal of Computational Physics*, 229(22):8521 – 8536, 2010. ISSN 0021-9991. doi: 10.1016/j.jcp.2010.07.036. URL <http://www.sciencedirect.com/science/article/pii/S0021999110004298>.
- [170] B. Zhao. *The application of Discontinuous Galerkin Finite Element Time-Domain Method in the design, simulation and analysis of modern radio frequency systems*. PhD thesis, University of Kentucky Doctoral Dissertations, 2011. URL http://uknowledge.uky.edu/gradschool_diss/186.
- [171] Bo Zhao, J.C. Young, and S.D. Gedney. Spice lumped circuit subcell model for the discontinuous galerkin finite-element time-domain method. *Microwave*

- Theory and Techniques, IEEE Transactions on*, 60(9):2684–2692, sept. 2012. ISSN 0018-9480. doi: 10.1109/TMTT.2012.2203923.
- [172] L. Li, S. Lanteri, and R. Perrussel. A hybridizable discontinuous galerkin method for solving 3d time-harmonic maxwells equations. In Andrea Cangiani, Ruslan L. Davidchack, Emmanuil Georgoulis, Alexander N. Gorban, Jeremy Levesley, and Michael V. Tretyakov, editors, *Numerical Mathematics and Advanced Applications 2011*, pages 119–128. Springer Berlin Heidelberg, 2013. ISBN 978-3-642-33133-6. doi: 10.1007/978-3-642-33134-3_13. URL http://dx.doi.org/10.1007/978-3-642-33134-3_13.
- [173] M.S. Sarto. A new model for the fdtd analysis of the shielding performances of thin composite structures. *Electromagnetic Compatibility, IEEE Transactions on*, 41(4):298–306, November 1999. ISSN 0018-9375. doi: 10.1109/15.809798.
- [174] Christopher L Holloway, M Sabrina Sarto, and Martin Johansson. Analyzing carbon-fiber composite materials with equivalent-layer models. *Electromagnetic Compatibility, IEEE Transactions on*, 47(4):833–844, 2005.
- [175] L. D. Angulo, S. Greco, M. Ruiz-Cabello, S. G. Garcia, and M. S. Sarto. Fdtd techniques to simulate composite air vehicles for em. In *AES Symposium, Paris*, 2012.
- [176] S. Chun, H. Haddar, and J.S. Hesthaven. High-order accurate thin layer approximations for time-domain electromagnetics, part ii: Transmission layers. *Journal of Computational and Applied Mathematics*, 234(8):2587–2608, 2010. ISSN 0377-0427. doi: <http://dx.doi.org/10.1016/j.cam.2010.03.022>. URL <http://www.sciencedirect.com/science/article/pii/S0377042710001809>.
- [177] D.M. Pozar. *Microwave Engineering, 3Rd Ed.* Wiley India Pvt. Limited, 2009. ISBN 9788126510498. URL <http://books.google.es/books?id=UZgvwJ3Eex8C>.
- [178] R. Holland and L. Simpson. Finite-difference analysis of emp coupling to thin struts and wires. *Electromagnetic Compatibility, IEEE Transactions on*, EMC-23(2):88–97, may 1981. ISSN 0018-9375. doi: 10.1109/TEMC.1981.303899.
- [179] F. Edelvik and T. Weiland. Stable modelling of arbitrary thin slots in the finite-element time-domain method. *International Journal of Numerical Modelling: Electronic Networks, Devices and Fields*, 17(4):365–383, 2004. ISSN 1099-1204. doi: 10.1002/jnm.533. URL <http://dx.doi.org/10.1002/jnm.533>.

- [180] S.P. Gao, Q.S. Cao, J. Ding, M. Zhu, and Y.L. Lu. A hybrid dgtd-tdie method for solving complex electromagnetic problems. *Journal of Electromagnetic Waves and Applications*, 27(8):1017–1027, 2013. doi: 10.1080/09205071.2013.797371. URL <http://dx.doi.org/10.1080/09205071.2013.797371>.
- [181] OpenFOAM, the open source CFD toolbox. <http://www.openfoam.com/>.
- [182] Fu-Gang Hu and Chao-Fu Wang. Parallel higher-order dg-fetd simulation of antennas (invited paper). In *Antennas Propagation (ISAP), 2013 Proceedings of the International Symposium on*, volume 01, pages 71–72, Oct 2013.
- [183] A. Klockner, T. Warburton, J. Bridge, and J. S. Hesthaven. Nodal discontinuous galerkin methods on graphics processors. *J. Comput. Phys.*, 228:7863–7882, November 2009. ISSN 0021-9991. doi: 10.1016/j.jcp.2009.06.041. URL <http://portal.acm.org/citation.cfm?id=1613335.1613429>.
- [184] Andreas Klockner, Timothy Warburton, and JanS. Hesthaven. High-order discontinuous galerkin methods by gpu metaprogramming. In David A. Yuen, Long Wang, Xuebin Chi, Lennart Johnsson, Wei Ge, and Yaolin Shi, editors, *GPU Solutions to Multi-scale Problems in Science and Engineering*, Lecture Notes in Earth System Sciences, pages 353–374. Springer Berlin Heidelberg, 2013. ISBN 978-3-642-16404-0. doi: 10.1007/978-3-642-16405-7_23. URL http://dx.doi.org/10.1007/978-3-642-16405-7_23.
- [185] ParMETIS, parallel graph partitioning and fill-reducing matrix ordering. <http://glaros.dtc.umn.edu/gkhome/metis/parmetis/overview>.
- [186] L. Mattes and S. Kofuji. The use of overlapping subgrids to accelerate the fdtd on gpu devices. In *Radar Conference, 2010 IEEE*, pages 807–810, May 2010. doi: 10.1109/RADAR.2010.5494509.
- [187] Man-Fai Wong, O. Picon, and V. Fouad Hanna. A finite element method based on whitney forms to solve maxwell equations in the time domain. *Magnetics, IEEE Transactions on*, 31(3):1618–1621, May 1995. ISSN 0018-9464. doi: 10.1109/20.376343.
- [188] Alireza H. Mohammadian, Vijaya Shankar, and William F. Hall. Computation of electromagnetic scattering and radiation using a time-domain finite-volume discretization procedure. *Computer Physics Communications*, 68(1–3):175 – 196, 1991. ISSN 0010-4655. doi: [http://dx.doi.org/10.1016/0010-4655\(91\)90199-U](http://dx.doi.org/10.1016/0010-4655(91)90199-U). URL <http://www.sciencedirect.com/science/article/pii/001046559190199U>.

- [189] J.S Hesthaven and T Warburton. Nodal high-order methods on unstructured grids: I. time-domain solution of maxwell's equations. *Journal of Computational Physics*, 181(1):186 – 221, 2002. ISSN 0021-9991. doi: <http://dx.doi.org/10.1006/jcph.2002.7118>. URL <http://www.sciencedirect.com/science/article/pii/S0021999102971184>.
- [190] Fang Q. Hu and Harold L. Atkins. Eigensolution analysis of the discontinuous galerkin method with nonuniform grids: I. one space dimension. *Journal of Computational Physics*, 182(2):516 – 545, 2002. ISSN 0021-9991. doi: DOI: 10.1006/jcph.2002.7184. URL <http://www.sciencedirect.com/science/article/B6WHY-481663J-T/2/254a6251d0a26ffb20dbd50a48e187a5>.
- [191] S.D. Gedney, T. Kramer, C. Luo, J.A. Roden, R. Crawford, B. Guernsey, J. Beggs, and J.A. Miller. The discontinuous galerkin finite element time domain method (dgtfd). In *Electromagnetic Compatibility, 2008. EMC 2008. IEEE International Symposium on*, pages 1–4, Aug 2008. doi: 10.1109/ISEMC.2008.4652146.
- [192] Tian Xiao and Qing H. Liu. Three-dimensional unstructured-grid discontinuous galerkin method for maxwell's equations with well-posed perfectly matched layer. *Microwave and Optical Technology Letters*, 46(5):459–463, 2005. ISSN 1098-2760. doi: 10.1002/mop.21016. URL <http://dx.doi.org/10.1002/mop.21016>.
- [193] Min-Hung Chen, Bernardo Cockburn, and Fernando Reitich. High-order rkdg methods for computational electromagnetics. *J. Sci. Comput.*, 22-23(1-3):205–226, January 2005. ISSN 0885-7474. doi: 10.1007/s10915-004-4152-6. URL <http://dx.doi.org/10.1007/s10915-004-4152-6>.
- [194] Marc Bernacki, Loula Fezoui, Stéphane Lanteri, and Serge Piperno. Parallel discontinuous galerkin unstructured mesh solvers for the calculation of three-dimensional wave propagation problems. *Applied Mathematical Modelling*, 30(8):744 – 763, 2006. ISSN 0307-904X. doi: <http://dx.doi.org/10.1016/j.apm.2005.06.015>. URL <http://www.sciencedirect.com/science/article/pii/S0307904X0500212X>. Parallel and distributed computing for computational mechanics.
- [195] S.G. Garcia, M. Fernandez Pantoja, C.M. de Jong van Coevorden, A. Rubio Bretones, and R. Gomez Martin. A new hybrid dgtfd/fdtd method in 2-d. *Microwave and Wireless Components Letters, IEEE*, 18(12):764 – 766, 2008. ISSN 1531-1309. doi: 10.1109/LMWC.2008.2007688.

- [196] A.J. Jerri. The shannon sampling theorem 8212;its various extensions and applications: A tutorial review. *Proceedings of the IEEE*, 65(11):1565–1596, Nov 1977. ISSN 0018-9219. doi: 10.1109/PROC.1977.10771.
- [197] J.R. Montejo-Garai and J. Zapata. Full-wave design and realization of multicoupled dual-mode circular waveguide filters. *Microwave Theory and Techniques, IEEE Transactions on*, 43(6):1290–1297, 1995. ISSN 0018-9480. doi: 10.1109/22.390185.
- [198] F. Alessandri, M. Chiodetti, A. Giugliarelli, D. Maiarelli, G. Martirano, D. Schmitt, L. Vanni, and F. Vitulli. The electric-field integral-equation method for the analysis and design of a class of rectangular cavity filters loaded by dielectric and metallic cylindrical pucks. *Microwave Theory and Techniques, IEEE Transactions on*, 52(8):1790–1797, Aug 2004. ISSN 0018-9480. doi: 10.1109/TMTT.2004.831583.
- [199] Bernardo Cockburn, Fengyan Li, and Chi-Wang Shu. Locally divergence-free discontinuous galerkin methods for the maxwell equations. *J. Comput. Phys.*, 194:588–610, March 2004. ISSN 0021-9991. doi: 10.1016/j.jcp.2003.09.007. URL <http://dl.acm.org/citation.cfm?id=1008428.1008437>.
- [200] J Niegemann, W Pernice, and K Busch. Simulation of optical resonators using dgtd and fdtd. *Journal of Optics A: Pure and Applied Optics*, 11(11):114015, 2009. URL <http://stacks.iop.org/1464-4258/11/i=11/a=114015>.
- [201] Hassan Fahs, Abdelhamid Hadjem, Stephane Lanteri, Joe Wiart, and Man-Fai Wong. Calculation of the sar induced in head tissues using a high-order dgtd method and triangulated geometrical models. *IEEE Transactions on Antennas and Propagation*, 59(12):4669 – 4678, August 2011. doi: 10.1109/TAP.2011.2165471. URL <http://hal.inria.fr/hal-00664102>.
- [202] N. C. Nguyen, J. Peraire, and B. Cockburn. Hybridizable discontinuous galerkin methods for the time-harmonic maxwell’s equations. *J. Comput. Phys.*, 230(19):7151–7175, August 2011. ISSN 0021-9991. doi: 10.1016/j.jcp.2011.05.018. URL <http://dx.doi.org/10.1016/j.jcp.2011.05.018>.
- [203] Dan Kosloff and Hillel Tal-Ezer. A modified chebyshev pseudospectral method with an $o(n-1)$ time step restriction. *Journal of Computational Physics*, 104(2):457 – 469, 1993. ISSN 0021-9991. doi: <http://dx.doi.org/10.1006/jcph.1993.1044>. URL <http://www.sciencedirect.com/science/article/pii/S0021999183710442>.

- [204] Timothy Warburton and Thomas Hagstrom. Taming the cfl number for discontinuous galerkin methods on structured meshes. *SIAM J. Numerical Analysis*, 46(6):3151–3180, 2008.
- [205] V. Girault, S. Sun, M. Wheeler, and I. Yotov. Coupling discontinuous galerkin and mixed finite element discretizations using mortar finite elements. *SIAM Journal on Numerical Analysis*, 46(2):949–979, 2008. doi: 10.1137/060671620. URL <http://epubs.siam.org/doi/abs/10.1137/060671620>.
- [206] Philippe R.B. Devloo, Agnaldo M. Farias, Sônia M. Gomes, and João L. Gonçalves. Application of a combined continuous–discontinuous galerkin finite element method for the solution of the girkmann problem. *Computers & Mathematics with Applications*, 65(11):1786 – 1794, 2013. ISSN 0898-1221. doi: <http://dx.doi.org/10.1016/j.camwa.2013.03.015>. URL <http://www.sciencedirect.com/science/article/pii/S0898122113001673>.
- [207] Ilaria Perugia and Dominik Schotzau. On the coupling of local discontinuous galerkin and conforming finite element methods. *Journal of Scientific Computing*, 16(4):411–433, 2001. ISSN 0885-7474. doi: 10.1023/A:1013294207868.
- [208] B. Cockburn, J. Gopalakrishnan, and R. Lazarov. Unified hybridization of discontinuous galerkin, mixed, and continuous galerkin methods for second order elliptic problems. *SIAM Journal on Numerical Analysis*, 47(2):1319–1365, 2009. doi: 10.1137/070706616. URL <http://epubs.siam.org/doi/abs/10.1137/070706616>.
- [209] A. Cangiani, Geor, and M. Jensen. Continuous and discontinuous finite element methods for convection-diffusion problems: A comparison. Technical report, Dept. of Mathematics, University of Leicester., June 2006. URL <https://lra.le.ac.uk/handle/2381/4271>.
- [210] Andrea Cangiani, John Chapman, Emmanuil Georgoulis, and Max Jensen. On the stability of continuous–discontinuous galerkin methods for advection–diffusion–reaction problems. *Journal of Scientific Computing*, 57(2): 313–330, 2013. ISSN 0885-7474. doi: 10.1007/s10915-013-9707-y. URL <http://dx.doi.org/10.1007/s10915-013-9707-y>.
- [211] Clint Dawson, Joannes J. Westerink, Joannes J. Feyen, Jesse C. Feyen, and Dharhas Pthina. Continuous, discontinuous and coupled discontinuous-continuous galerkin finite element methods for the shallow water equations. *International Journal for Numerical Methods in Fluids*, 52(1):63–88, 2006. doi: 10.1002/flf.1156. URL <http://dx.doi.org/10.1002/flf.1156>.

- [212] W. Davies, Morgan K., and Hassan O. A high order hybrid finite element method applied to the solution of electromagnetic wave scattering problems in the time domain. *Computational Mechanics*, 44(3):321–331, 2009. doi: 10.1007/s00466-009-0377-4. URL <http://www.springerlink.com/content/287766688431j317/export-citation/>.
- [213] Tiao Lu, Pingwen Zhang, and Wei Cai. Discontinuous galerkin methods for dispersive and lossy maxwell's equations and pml boundary conditions. *Journal of Computational Physics*, 200(2):549 – 580, 2004. ISSN 0021-9991. doi: DOI: 10.1016/j.jcp.2004.02.022. URL <http://www.sciencedirect.com/science/article/B6WHY-4CHRFS6-1/2/1568a91c84815c07bf07e46e00b27469>.
- [214] A. Bossavit. Mixed finite elements and the complex of Whitney forms. In *The mathematics of finite elements and applications, VI (Uxbridge, 1987)*, pages 137–144. Academic Press, London, 1988.
- [215] Alain Bossavit. Whitney forms: a class of finite elements for three-dimensional computations in electromagnetism. *Physical Science, Measurement and Instrumentation, Management and Education - Reviews, IEE Proceedings A*, 135(8): 493–500, 1988. ISSN 0143-702X. doi: 10.1049/ip-a-1:19880077.
- [216] L. Demkowicz, P. Monk, Ch. Schwab, and L. Vardapetyan. Maxwell eigenvalues and discrete compactness in two dimensions. *Computers & Mathematics with Applications*, 40(4–5):589 – 605, 2000. ISSN 0898-1221. doi: [http://dx.doi.org/10.1016/S0898-1221\(00\)00182-6](http://dx.doi.org/10.1016/S0898-1221(00)00182-6). URL <http://www.sciencedirect.com/science/article/pii/S0898122100001826>.
- [217] Bo He and F.L. Teixeira. Differential forms, galerkin duality, and sparse inverse approximations in finite element solutions of maxwell equations. *Antennas and Propagation, IEEE Transactions on*, 55(5):1359–1368, 2007. ISSN 0018-926X. doi: 10.1109/TAP.2007.895619.
- [218] Douglas N Arnold, Richard S Falk, and Ragnar Winther. Finite element exterior calculus: from hodge theory to numerical stability. *Bull. Amer. Math. Soc.(NS)*, 47(2):281–354, 2010.
- [219] H. Moon, F.L. Teixeira, J. Kim, and Y.A. Omelchenko. Trade-offs for unconditional stability in the finite-element time-domain method. *Microwave and Wireless Components Letters, IEEE*, PP(99):1–1, 2014. ISSN 1531-1309. doi: 10.1109/LMWC.2014.2310481.

- [220] J. P. Webb and S. McFee. The use of hierarchal triangles in finite-element analysis of microwave and optical devices. *IEEE Transactions on Magnetics*, 27(5):4040–4043, September 1991.
- [221] J. Alvarez, L. D. Angulo, A. R. Bretones, C. M. de Jong, and S. G. Garcia. An efficient local time-stepping DGTD method: application to antenna modeling. *IEEE Transactions on Antennas and Propagation*, (submitted). Submitted.
- [222] J. L. Mead and R. A. Renaut. Optimal runge-kutta methods for first order pseudospectral operators. *J. Comput. Phys.*, 152(1):404–419, June 1999. ISSN 0021-9991. doi: 10.1006/jcph.1999.6260. URL <http://dx.doi.org/10.1006/jcph.1999.6260>.
- [223] A. Taflove. *Computational Electrodynamics: The Finite-Difference Time-Domain Method*. Artech House, Boston, 1995.
- [224] H. Fahs and S. Lanteri. A high-order non-conforming discontinuous Galerkin method for time-domain electromagnetics. *Journal of Computational and Applied Mathematics*, 234:1088–1096, 2010.
- [225] J. Diaz and M. Grote. Energy conserving explicit local time stepping for second-order wave equations. *SIAM Journal on Scientific Computing*, 31(3):1985–2014, 2009. doi: 10.1137/070709414. URL <http://epubs.siam.org/doi/abs/10.1137/070709414>.
- [226] Marcus J. Grote and Teodora Mitkova. Explicit local time-stepping methods for maxwell’s equations. *Journal of Computational and Applied Mathematics*, 234(12):3283 – 3302, 2010. ISSN 0377-0427. doi: 10.1016/j.cam.2010.04.028. URL <http://www.sciencedirect.com/science/article/pii/S0377042710002360>.
- [227] M. Kaser, M. Dumbser, J. de la Puente, and H. Igel. An arbitrary high order discontinuous galerkin method for elastic waves on unstructured meshes iii: Viscoelastic attenuation. *Geophysical Journal International*, 168(1):224–242, 2007. doi: 10.1111/j.1365-246X.2006.03193.x. URL http://www.geophysik.uni-muenchen.de/~igel/PDF/kaeseretal_{_}gji_{_}2006.pdf.
- [228] Li Liu, Xiaodong Li, and Fang Q. Hu. Nonuniform time-step runge kutta discontinuous galerkin method for computational aeroacoustics. *Journal of Computational Physics*, 229(19):6874 – 6897, 2010. ISSN 0021-9991. doi: 10.1016/j.jcp.2010.05.028. URL <http://www.sciencedirect.com/science/article/pii/S0021999110002895>.

- [229] Ryan Austin Chilton. *H-, P- and T-Refinement Strategies for the Finite-Difference-Time-Domain (FDTD) Method Developed via Finite-Element (FE) Principles*. PhD thesis, Graduate School of The Ohio State University, 2008.
- [230] J.J.W. van der Vegt and H. van der Ven. Space-time discontinuous galerkin finite element method with dynamic grid motion for inviscid compressible flows: I. general formulation. *Journal of Computational Physics*, 182(2): 546 – 585, 2002. ISSN 0021-9991. doi: <http://dx.doi.org/10.1006/jcph.2002.7185>. URL <http://www.sciencedirect.com/science/article/pii/S0021999102971858>.
- [231] J. C. Meza and Symes W. W. Domain decomposition algorithms for linear hyperbolic equations. Technical report, Rice University, 1987.
- [232] A. Catella, V. Dolean, and S. Lanteri. An unconditionally stable discontinuous galerkin method for solving the 2-d time-domain maxwell equations on unstructured triangular meshes. *Magnetics, IEEE Transactions on*, 44(6):1250 – 1253, 2008. ISSN 0018-9464. doi: 10.1109/TMAG.2007.916578.
- [233] T. Lau, E. Gjonaj, and T. Weiland. Investigation of higher order symplectic time integration methods for discontinuous Galerkin methods with a centered flux. *Workshop on Computational Electromagnetics in Time-Domain*, pages 1–4, October 2007.
- [234] A.R. Bretones, R. Mittra, and R.G. Martin. A hybrid technique combining the method of moments in the time domain and fdtd. *Microwave and Guided Wave Letters, IEEE*, 8(8):281–283, Aug 1998. ISSN 1051-8207. doi: 10.1109/75.704414.
- [235] Salvador Gonzalez Garcia. *Contribuciones al metodo de las diferencias finitas para la resolucion de las ecuaciones de Maxwell en el dominio del tiempo*. PhD thesis, Facultad de Ciencias - Universidad de Granada, 1994.
- [236] Vijaya Shankar, Alireza H. Mohammadian, and William F. Hall. A time-domain, finite-volume treatment for the maxwell equations. *Electromagnetics*, 10(1-2):127–145, 1990. doi: 10.1080/02726349008908232. URL <http://dx.doi.org/10.1080/02726349008908232>.
- [237] G. I. Marchuk. *Methods of Numerical Mathematics*. Springer-Verlag, New York, 1975.
- [238] G. G. Gutierrez, S. F. Romero, J. Alvarez, S. G. Garcia, and E. P. Gil. On the use of fdtd for hirc validation and certification. *Progress In Electromagnetics Research Letters*, 32:145–156, 2012. doi: <http://dx.doi.org/>

- 10.2528/PIERL12030206. URL <http://www.jpier.org/PIERL/pier.php?paper=12030206>.
- [239] P. B. Johns and R. L. Beurle. Numerical solutions of 2-dimensional scattering problems using a transmission-line matrix. *IEE Proceedings*, 118(9):1203–1208, 1971.
- [240] T. Weiland. A discretization method for the solution of Maxwell’s equations for six-component fields. *Archiv fuer Elektronik und Uebertragungstechnik*, 31(3):116–120, March 1977.
- [241] W. C. Chew and W. H. Weedon. A 3d perfectly matched medium from modified Maxwell’s equations with stretched coordinates. *Microwave Optical Tech. Letters*, 7(13):599–604, 1994.
- [242] K. Sankaran, C. Fumeaux, and R. Vahldieck. Uniaxial and radial anisotropy models for finite-volume Maxwellian absorber. *IEEE Transaction on Microwave Theory and Techniques*, 54(12):4297–4304, December 2006.
- [243] C. Fumeaux, K. Sankaran, and R. Vahldieck. Spherical perfectly matched absorber for finite-volume 3-D domain truncation. *IEEE Transaction on Microwave Theory and Techniques*, 55(12):2773–2781, December 2007.
- [244] S. D. Gedney, C. Luo, J. A. Roden, R. D. Crawford, B. Guernsey, J. A. Miller, T. Kramer, and E. W. Lucas. The discontinuous Galerkin finite-element time-domain method solution of Maxwell’s equation. *Journal in Applied Computational Electromagnetics Society*, 24(2):129–142, April 2009.
- [245] Hirf-se 7pm eu project. URL <http://www.hirf-se.eu>.
- [246] J. P. Bérenger. Numerical reflection from FDTD-PMLs: A comparison of the split PML with the unsplit and CFS PMLs. *IEEE Transaction on Antennas and Propagation*, 50(3):258–265, March 2002.
- [247] Ugrfdtd webpage. URL <http://www.ugrfdtd.com>.
- [248] S. Piperno. DGTD methods using modal basis functions and symplectic local time-stepping: Application to wave propagation problems. *Journal of Computational Physics*, 217:340–363, 2006.
- [249] Roger F. Harrington. *Field Computation by Moment Methods*. Wiley-IEEE Press, 1993. ISBN 0780310144.

- [250] A.C. Woo, H. T G Wang, M.J. Schuh, and M.L. Sanders. Em programmer's notebook-benchmark radar targets for the validation of computational electromagnetics programs. *Antennas and Propagation Magazine, IEEE*, 35(1): 84–89, Feb 1993. ISSN 1045-9243. doi: 10.1109/74.210840.
- [251] M. Taskinen and P. Yla-Oijala. Current and charge integral equation formulation. *IEEE Transactions on Antennas and Propagation*, 54(1):58–67, January 2006.
- [252] W.C. Chew, E. Michielssen, J. M. Song, and J. M. Jin, editors. *Fast and Efficient Algorithms in Computational Electromagnetics*. Artech House, Inc., Norwood, MA, USA, 2001. ISBN 1580531520.
- [253] A. Poggio and E. Miller. *Computer Techniques for Electromagnetics*. Pergamon Press, 1973.
- [254] R. Fernandez-Recio, D. Escot-Bocanegra, D. Poyatos-Martinez, and M. Mulero-Valenzuela. Technical report on the verification of radar cross section prediction of metallic targets by eads construcciones aeronaticas s.a. Technical report, INTA, 2011.
- [255] Workshop EM JINA, radar signatures, 2006.
- [256] Ozgur Ergul and L. Gurel. Rigorous solutions of electromagnetic problems involving hundreds of millions of unknowns. *Antennas and Propagation Magazine, IEEE*, 53(1):18–27, Feb 2011. ISSN 1045-9243. doi: 10.1109/MAP.2011.5773562.
- [257] M.A. Hernández-López, S. González García, A. Rubio Bretones, M. Fernández Pantoja, and R. Gómez Martín. A resistively loaded thin-wire antenna for mine detection. *Subsurface Sensing Technologies and Applications*, 2(3):265–271, 2001. ISSN 1566-0184. doi: 10.1023/A:1011970103562.
- [258] M. Fernandez-Pantoja, A. Monorchio, A. Rubio-Bretones, and R. Gomez-Martin. Direct ga-based optimisation of resistively loaded wire antennas in the time domain. *Electronics Letters*, 36(24):1988–1990, Nov 2000. ISSN 0013-5194. doi: 10.1049/el:20001400.
- [259] Nectaria Diamanti and Antonios Giannopoulos. Implementation of adi-fdtd subgrids in ground penetrating radar {FDTD} models. *Journal of Applied Geophysics*, 67(4):309 – 317, 2009. ISSN 0926-9851. doi: <http://dx.doi.org/10.1016/j.jappgeo.2008.07.004>. URL <http://www.sciencedirect.com/science/article/pii/S0926985108000815>. Advanced Applications, Systems and Modelling for {GPR}.

- [260] A. Giannopoulos. Modelling ground penetrating radar by gprmax. *Construction and Building Materials*, 19(10):755 – 762, 2005. ISSN 0950-0618. doi: <http://dx.doi.org/10.1016/j.conbuildmat.2005.06.007>. URL <http://www.sciencedirect.com/science/article/pii/S0950061805001509>. Non Destructive Testing: Selected papers from Structural Faults and Repair 2003.
- [261] Loula Fezoui, Stéphane Lanteri, Stéphanie Lohrengel, and Serge Piperno. Convergence and stability of a discontinuous galerkin time-domain method for the 3d heterogeneous maxwell equations on unstructured meshes. *ESAIM: Mathematical Modelling and Numerical Analysis*, 39:1149–1176, 11 2005. ISSN 1290-3841. doi: 10.1051/m2an:2005049. URL http://www.esaim-m2an.org/action/article_S0764583X0500049X.
- [262] Charles Amazeen Peyman Milanfar Joel Kositsky, Russel Cosgrove. Results from a forward-looking gpr mine detection system. *Proceedings of the SPIE*, v4632:206–217, 2002.
- [263] Rose M. Joseph, Susan C. Hagness, and Allen Taflove. Direct time integration of maxwell’s equations in linear dispersive media with absorption for scattering and propagation of femtosecond electromagnetic pulses. *Opt. Lett.*, 16(18): 1412–1414, Sep 1991. doi: 10.1364/OL.16.001412. URL <http://ol.osa.org/abstract.cfm?URI=ol-16-18-1412>.
- [264] F. Koppens, D. Chang, and J. Garcia de Abajo. Graphene plasmonics: A platform for strong light-matter interactions. *Nano letters*, 2011.
- [265] J. Christensen, A. Manjavacas, S. Thongrattanasiri, F.H.L. Koppens, and F.J. García de Abajo. Graphene plasmon waveguiding and hybridization in individual and paired nanoribbons. *ACS nano*, 2012.
- [266] Q. Bao and K.P. Loh. Graphene photonics, plasmonics, and broadband optoelectronic devices. *ACS nano*, 6(5):3677–3694, 2012.
- [267] A. Vakil and N. Engheta. Transformation optics using graphene. *Science*, 332 (6035):1291, 2011.
- [268] G.D. Bouzianas, N.V. Kantartzis, C.S. Antonopoulos, and T.D. Tsiboukis. Optimal modeling of infinite graphene sheets via a class of generalized fdtd schemes. *Magnetics, IEEE Transactions on*, 48(2):379–382, 2012. ISSN 0018-9464. doi: 10.1109/TMAG.2011.2172778.
- [269] A. Mock. Padé approximant spectral fit for fdtd simulation of graphene in the near infrared. *Optical Materials Express*, 2(6):771–781, 2012.

- [270] G.W. Hanson. Dyadic greens functions and guided surface waves for a surface conductivity model of graphene. *Journal of Applied Physics*, 103(6):064302–064302, 2008.
- [271] B. Wang, X. Zhang, X. Yuan, and J. Teng. Optical coupling of surface plasmons between graphene sheets. *Applied Physics Letters*, 100(13):131111, 2012.
- [272] S. G. Garcia, F. Costen, M. Fernandez Pantoja, L. D. Angulo, and J. Alvarez. Efficient excitation of waveguides in crank-nicolson fdtd. *Progress In Electromagnetics Research Letters*, 17:39–46, 2010. doi: 10.2528/PIERL10072008. URL <http://www.jpier.org/PIERL/pier.php?paper=10072008>.
- [273] Malgorzata Celuch-Marcysiak and W.K. Gwarek. Formal equivalence and efficiency comparison of the fd-td, tlm and sn methods in application to microwave cad programs. In *Microwave Conference, 1991. 21st European*, volume 1, pages 199–204, Sept 1991. doi: 10.1109/EUMA.1991.336433.
- [274] C.J. Railton and J.P. McGeehan. The use of mode templates to improve the accuracy of the finite difference time domain method. 2:1278–1283, Sept 1991. doi: 10.1109/EUMA.1991.336521.
- [275] Hang Jin, R. Vahldieck, and Shujun Xiao. A full-wave analysis of arbitrary guiding structures using a two dimensional tlm mesh. In *Microwave Conference, 1991. 21st European*, volume 1, pages 205–210, Sept 1991. doi: 10.1109/EUMA.1991.336434.
- [276] F. Arndt, V.J. Brankovic, and D.V. Krupezovic. An improved fd-td full wave analysis for arbitrary guiding structures using a two-dimensional mesh. In *Microwave Symposium Digest, 1992., IEEE MTT-S International*, pages 389–392 vol.1, June 1992. doi: 10.1109/MWSYM.1992.187994.
- [277] A. Asi and L. Shafai. Dispersion analysis of anisotropic inhomogeneous waveguides using compact 2d-fdtd. *Electronics Letters*, 28(15):1451–1452, July 1992. ISSN 0013-5194. doi: 10.1049/el:19920923.
- [278] W.K. Gwarek, T. Morawski, and Cezary Mroczkowski. Application of the fd-td method to the analysis of circuits described by the two-dimensional vector wave equation. *Microwave Theory and Techniques, IEEE Transactions on*, 41(2):311–317, Feb 1993. ISSN 0018-9480. doi: 10.1109/22.216473.
- [279] S. Xiao, R. Vahldieck, and H. Jin. Full-wave analysis of guided wave structures using a novel 2-d fdtd. *Microwave and Guided Wave Letters, IEEE*, 2(5):165–167, May 1992. ISSN 1051-8207. doi: 10.1109/75.134342.

- [280] W.K. Gwarek and M. Celuch-Marcysiak. Wide-band s-parameter extraction from fd-td simulations for propagating and evanescent modes in inhomogeneous guides. *Microwave Theory and Techniques, IEEE Transactions on*, 51(8):1920–1928, Aug 2003. ISSN 0018-9480. doi: 10.1109/TMTT.2003.815265.
- [281] Michal Mrozowski. Function expansion algorithms for the time-domain analysis of shielded structures supporting electromagnetic waves. *International Journal of Numerical Modelling: Electronic Networks, Devices and Fields*, 7(2):77–84, 1994. ISSN 1099-1204. doi: 10.1002/jnm.1660070203. URL <http://dx.doi.org/10.1002/jnm.1660070203>.
- [282] S.G. Garcia, R.G. Rubio, A.R. Bretones, and R.G. Lopez. Revisiting the stability of crank nicolson and adi-fdtd. *Antennas and Propagation, IEEE Transactions on*, 55(11):3199–3203, Nov 2007. ISSN 0018-926X. doi: 10.1109/TAP.2007.908794.
- [283] H.K. Rouf, F. Costen, and S.G. Garcia. 3d crank-nicolson finite difference time domain method for dispersive media. *Electronics Letters*, 45(19):961–962, September 2009. ISSN 0013-5194. doi: 10.1049/el.2009.1940.
- [284] H.K. Rouf, F. Costen, S.G. Garcia, and S. Fujino. On the solution of 3-d frequency dependent crank-nicolson fdtd scheme. *Journal of Electromagnetic Waves and Applications*, 23(16):2163–2175, 2009. doi: doi:10.1163/156939309790109261. URL <http://www.ingentaconnect.com/content/vsp/jew/2009/00000023/00000016/art00008>.
- [285] S.G. Garcia, R.G. Rubio, A.R. Bretones, and R.G. Martin. On the dispersion relation of adi-fdtd. *Microwave and Wireless Components Letters, IEEE*, 16(6):354–356, June 2006. ISSN 1531-1309. doi: 10.1109/LMWC.2006.875619.
- [286] L.D. Angulo, S.G. Garcia, M.F. Pantoja, C.C. Sanchez, and R.G. Martin. Improving the sar distribution in petri-dish cell cultures. *Journal of Electromagnetic Waves and Applications*, 24:815–826(12), 2010.
- [287] B.-I. Wu, F. C. A. I. Cox, and J. A. Kong. Experimental methodology for non-thermal effects of electromagnetic radiation on biologics. *Journal of Electromagnetic Waves and Applications*, 21(4):533–548, 2007. doi: 10.1163/156939307780616829. URL <http://dx.doi.org/10.1163/156939307780616829>.
- [288] S Lang. Recent advances in bioelectromagnetics research on mobile telephony and health—an introduction. *Epidemiology*, 39(7):215, 2006.

- [289] J. Schuderer, T. Samaras, W. Oesch, D. Spat, and N. Kuster. High peak sar exposure unit with tight exposure and environmental control for in vitro experiments at 1800 mhz. *Microwave Theory and Techniques, IEEE Transactions on*, 52(8):2057–2066, Aug 2004. ISSN 0018-9480. doi: 10.1109/TMTT.2004.832009.
- [290] J. Schuderer, D. Spat, T. Samaras, W. Oesch, and N. Kuster. In vitro exposure systems for rf exposures at 900 mhz. *Microwave Theory and Techniques, IEEE Transactions on*, 52(8):2067 – 2075, 2004. ISSN 0018-9480. doi: 10.1109/TMTT.2004.832010.
- [291] Niels Kuster and Frank Schönborn. Recommended minimal requirements and development guidelines for exposure setups of bio-experiments addressing the health risk concern of wireless communications. *Bioelectromagnetics*, 21(7):508–514, 2000. doi: 10.1002/1521-186X(200010)21:7. URL [http://dx.doi.org/10.1002/1521-186X\(200010\)21:7](http://dx.doi.org/10.1002/1521-186X(200010)21:7).
- [292] Frank Schönborn, Katja Poković, Michael Burkhardt, and Niels Kuster. Basis for optimization of in vitro exposure apparatus for health hazard evaluations of mobile communications. *Bioelectromagnetics*, 22(8):547–559, 2001. doi: 10.1002/bem.83. URL <http://dx.doi.org/10.1002/bem.83>.
- [293] Jürgen Schuderer and Niels Kuster. Effect of the meniscus at the solid/liquid interface on the sar distribution in petri dishes and flasks. *Bioelectromagnetics*, 24(2):103–108, 2003. doi: 10.1002/bem.10066. URL <http://dx.doi.org/10.1002/bem.10066>.
- [294] M.L. Calabrese, G. d’Ambrosio, R. Massa, and G. Petraglia. A high-efficiency waveguide applicator for in vitro exposure of mammalian cells at 1.95 ghz. *Microwave Theory and Techniques, IEEE Transactions on*, 54(5):2256–2264, May 2006. ISSN 0018-9480. doi: 10.1109/TMTT.2006.872784.
- [295] Michael Burkhardt, Katja Poković, Marcel Gnos, Thomas Schmid, and Niels Kuster. Numerical and experimental dosimetry of petri dish exposure setups. *Bioelectromagnetics*, 17(6):483–493, 1996.
- [296] Juan E. Page. El banco de irradiación in-vitro en la banda de 2 ghz del hospital ramón y cajal. In *Symposium Nacional URSI*, 2008.
- [297] M. A. Cid J. E. P. de la Vega M. A. Martinez, M. A. Trillo and A. Ubeda. Respuesta citostatica de celulas humanas nb69 a señales pulsadas en la banda de 2 ghz. In *XXIII URSI National Symposium*, 2008.

- [298] Le-Wei Li, Mook-Seng Leong, PS Kooi, and TS Yeo. Specific absorption rates in human head due to handset antennas: A comparative study using fdtd method. *Journal of Electromagnetic Waves and Applications*, 14(7):987–1000, 2000.
- [299] Yu Liu, Zheng Liang, and Ziqiang Yang. Computation of electromagnetic dosimetry for human body using parallel fdtd algorithm combined with interpolation technique. *Progress In Electromagnetics Research*, 82:95–107, 2008.
- [300] Dalia Nashaat, Hala Alsadek, and Hani Ghali. Investigation of the mutual effect between human head and new shapes of pifas used in mobile communication systems. *Microwave and Optical Technology Letters*, 46(3):243–248, 2005. doi: 10.1002/mop.20957. URL <http://dx.doi.org/10.1002/mop.20957>.
- [301] Mohammad Ali Ebrahimi-Ganjeh and Amir Reza Attari. Interaction of dual band helical and pifa handset antennas with human head and hand. *Progress In Electromagnetics Research*, 77:225–242, 2007.
- [302] Nikolaos K Kouveliotis and Christos N Capsalis. Prediction of the sar level induced in a dielectric sphere by a thin wire dipole antenna. *Progress In Electromagnetics Research*, 80:321–336, 2008.
- [303] Ansoft HFSS, high frequency structure simulator. http://www.ansys.com/es_es/Productos/Flagship+Technology/ANSYS+HFSS.
- [304] SEMCAD,full-wave 3d electromagnetic and thermal simulation software. <http://www.speag.com/products/semcad/>, .
- [305] Jürgen Schuderer, Thomas Schmid, Gerald Urban, Theodoros Samaras, and Niels Kuster. Novel high-resolution temperature probe for radiofrequency dosimetry. *Physics in Medicine and Biology*, 49(6):N83, 2004. URL <http://stacks.iop.org/0031-9155/49/i=6/a=N04>.

Luis Manuel Diaz Angulo

CONTACT INFORMATION

Department of Electromagnetism *Work:* (+34) 667-87-69-42
Facultad de Ciencias *Home:* (+34) 958-37-90-89
University of Granada *E-mail:* lm@diazangulo.com
Granada, 18003, Spain *Web:* www.diazangulo.com

RESEARCH INTERESTS

Computational Electromagnetics, Electromagnetic Phenomena, Numerical methods, Galerkin methods, Plasma technology, Terahertz technology, Electromagnetic Compatibility, High Performance Computing.

SKILLS

Languages

- Spanish, mother tongue.
- English, fluent (B2 certification).

Computer Related

- Programming: C/C++, Fortran, tcl/tk, Python, Unix shell.
- Simulation/CAD: Ansoft HFSS, OpenFoam (Advanced certification), Semcad, CST Microwave Studio, GiD.
- Numerical Tools: MatLab.
- Applications: Eclipse CDT, MS Visual Studio, L^AT_EX.
- Operating Systems: Unix/Linux, Windows.

EDUCATION

University of Granada (UGR), Granada, Spain

- Physics Ph.D. Candidate, July 2010 (expected graduation date: October 2014)
 - Dissertation Topic:
Discontinuous Galerkin Methods applied to Computational Electromagnetics
 - Advisors: Salvador G. Garcia, Mario F. Pantoja, Jesus G. Alvarez.
- Major degree in Electronics Engineering, (expected graduation date: October 2014)
 - *Licenciado en Ingeniería Electrónica.*
- Physics and Mathematics post-graduate, October 2009 - December 2010
 - *Master en Física y Matemáticas (FISYMAT).*
 - Obtained the highest mark in the final research project.
- Major degree in Physics, October 2003 - July 2008
 - *Licenciado en Física.*
 - 2007/08 academic year spent in The University of Manchester, UK.
 - With special focus on electromagnetics and plasma technology.

Polytechnic University of Catalonia (UPC), Barcelona, Spain

- Summer School on Discontinuous Galerkin Methods, June 2012
- Short Course on Terahertz technology and applications, May 2009

ACADEMIC EXPERIENCE

University of Granada, Granada, Spain

Instructor

March 2012 - Present

Co-taught undergraduate level courses. Shared responsibility for lectures, lab sessions, exams, coursework assignments, and grades.

- First year Electromagnetism course for the Master degree in Electronics Engineering.

- Third year Electromagnetism course for the Master degree in Physics.

The Ohio State University - ElectroScience Laboratory, Columbus, Ohio USA

Research Internship

January 2013 - April 2013

- Three months in the The Ohio State University under the supervision of Professor Fernando Teixeira.
- During this period I developed a new technique to improve the performance in full-wave simulations that has been published in the *Journal of Computational Physics*.

Inst. National de Recherche en Informatique et en Automatique (INRIA), Nice, France

Research Internship

September 2012 - December 2012

- Three months spent researching Space-Time Discontinuous Galerkin (STDG) Methods under the supervision of Stephane Lanteri.
- I lectured two sessions on Advanced Material Modelling for Electromagnetic Phenomena and STDG.

Int. Center for Numerical Methods in Engineering (CIMNE), Barcelona, Spain

Research Internship

May 2010

- Two weeks developing a user interface for the UGRFDTD (www.ugrfdtd.es)

Dassault Systems, Saint Cloud, Paris, France

Workshop instructor

March 2012

- As part of the HIRF-SE project, I trained other project partners on how to use the FDTD software developed by the University of Granada (UGRFDTD).

JOURNAL
REVIEWING

I regularly review articles for the following scientific journals:

- Journal Of Computational Physics (2012 impact factor: 2.84)
- IEEE Transactions On Microwave Theory and Techniques (2012 impact factor: 2.23).
- IEEE Antennas and Wireless Propagation Letters (2012 impact factor: 1.67).
- Progress In Electromagnetic Research - Journal of Electromagnetic Waves and Applications (PIER-JEMWA) (2012 impact factor: 1.60).
- Near Surface Geophysics (NSG) (2012 impact factor: 1.12).

PUBLICATIONS

Angulo, L. D.; Alvarez, J.; Pantoja, M.; Garcia, S.

A Nodal Space-Time Discontinuous Galerkin Method for the Maxwell Equations.

Accepted in *IEEE Microwave Component Letters*.

Angulo, L. D.; Alvarez, J.; Teixeira, F. L.; Pantoja, M.; Garcia, S.

Causal-Path Local Time-Stepping in the Discontinuous Galerkin method for Maxwell's equations.

Journal of Computational Physics, **2014**, 256, 678 - 695.

Alvarez, J.; **Angulo, L. D.**; Bretones, A. R.; Garcia, S. G.

An analysis of the Leap-Frog Discontinuous Galerkin method for Maxwell's equations.

IEEE Transactions on Microwave Theory and Techniques, **2014**, Accepted.

Alvarez, J.; Alonso-Rodriguez, J. M.; Carbajosa-Cobaleda, H.; Cabello, M. R.; **Angulo, L. D.**; Gomez-Martin, R.; Garcia, S. G.

DGTD for a Class of Low-Observable Targets: A Comparison with MoM and (2,2) FDTD.

IEEE Antennas and Wireless Propagation Letters, **2014**, 13, 241-244.

- Alvarez, J.; **Angulo, L. D.**; Bretones, A.; Cabello, M. ; Garcia, S.
A Leap-Frog Discontinuous Galerkin Time-Domain Method for HIRF Assessment.
Electromagnetic Compatibility, IEEE Transactions on, **2013**, 55, 1250-1259.
- Lin, H.; Pantoja, M. F.; **Angulo, L. D.**; Alvarez, J.; Martin, R. G. ; Garcia, S. G.
FDTD Modeling of Graphene Devices Using Complex Conjugate Dispersion Material Model.
Microwave and Wireless Components Letters, IEEE, **2012**, 22, 612 -614
- Alvarez, J.; **Angulo, L. D.**; Rubio Bretones, A. ; Gonzalez Garcia, S.
3D discontinuous Galerkin time-domain method for anisotropic materials.
Antennas and Wireless Propagation Letters, IEEE, **2012**, 11, 1182-1185.
- Alvarez, J.; **Angulo, L. D.**; Rubio Bretones, A. ; Garcia, S.
A Spurious-Free Discontinuous Galerkin Time-Domain Method for the Accurate Modeling of Microwave Filters.
Microwave Theory and Techniques, IEEE Transactions on, **2012**, 60, 2359-2369.
- Angulo, L. D.**; Alvarez, J.; Garcia, S.; Bretones, A. R. ; Martin, R. G.
Discontinuous Galerkin time-domain method for GPR simulation of conducting objects.
Near Surface Geophysics, **2011**, 9, 257-263
- Alvarez, J.; **Angulo, L. D.**; Fernandez Pantoja, M.; Rubio Bretones, A.; Garcia, S.
Source and Boundary Implementation in Vector and Scalar DGTD.
Antennas and Propagation, IEEE Transactions on, **2010**, 58, 1997 -2003.
- Garcia, S. G.; Costen, F.; Fernandez Pantoja, M.; **Angulo, L. D.**; Alvarez, J.
Efficient Excitation of Waveguides in Crank-Nicolson FDTD.
Progress In Electromagnetics Research Letters, **2010**, 17, 39-46.
- Sanchez, C. C.; Garcia, S. G.; **Angulo, L. D.**; Coevorden, C. M. D. J. V.; Bretones, A. R.
A divergence-free BEM method to model quasi-static currents: application to MRI coil design.
Progress In Electromagnetics Research B, **2010**, 20, 187-203.
- Angulo, L. D.**; Garcia, S.; Pantoja, M.; Sanchez, C.; Martin, R.
Improving the SAR Distribution in Petri-Dish Cell Cultures.
Journal of Electromagnetic Waves and Applications, **2010**, 24, 815-826(12).
- PAPERS IN
PREPARATION **Angulo, L. D.**; Alvarez, J.; Pantoja, M.; Garcia, S.; Bretones, A. R.
Discontinuous Galerkin Time Domain Methods in Comp. Electrodynamics: State of the Art.
Submitted to *Forum for Electromagnetic Res. Methods and App. Technologies (FERMAT)*.
- Angulo, L. D.**; Alvarez, J.; Teixeira, F. L.; Pantoja, M.; Garcia, S.
A Nodal Hybrid Continuous-Discontinuous Galerkin Time Domain Method for Maxwell's Curl Equations.
Submitted to the *Transactions On Microwave Theory and Techniques*.
- CONFERENCE
PRESENTATIONS Alvarez, J.; **Angulo, L. D.**; Bretones, A. R.; Garcia, S. G.
A comparison of the FDTD and LFDG methods for the estimation of HIRF transfer functions.
Proc. on Computational ElectroMagnetics And Electromagnetic Compatibility (CEMEMC13), **2013**.

Alvarez, J.; **Angulo, L. D.**; Bandinelli, M.; Bruns, H.; Francavilla, M.; Garcia, S.; Guidi, R.; Gutierrez, G.; Jones, C.; Kunze, M.; Martinaud, J.; Munteanu, I.; Panitz, M.; Parmantier, J.; Pirinoli, P.; Reznicek, Z.; Salin, G.; Schroder, A.; Tobola, P.; Vipiana, F.
HIRF interaction with metallic aircrafts. A comparison between TD and FD methods.
Electromagnetic Compatibility (EMC EUROPE), International Symposium on, 2012.

Angulo, L. D.; Greco, S.; Ruiz-Cabello, M.; G. Garcia, S.; Sarto, M. S.
FDTD techniques to simulate composite air vehicles for EMC.
AES Symposium, Paris, 2012.

Alvarez, J.; Gutierrez, G.; **Angulo, L. D.**; Lin, H.; R. Bretones, A.; G. Garcia, S.
Novel Time Domain FE/FD Solvers for EMC Assessment.
VIII EIEC Encontro Iberico de Electromagnetismo computacional, 2011

Alvarez, J.; Garcia, S.; **Angulo, L. D.**; Bretones, A.
Computational Electromagnetic Tools for EMC in Aerospace. *Computational Electromagnetics, Piers Proceedings, Marrakesh, 2011*

Alvarez, J.; **Angulo, L. D.**; Garcia, S. G.; Pantoja, M. F.; Bretones, A. R.
A Comparison Between Upwind/Centered Nodal/Vector Basis DGTD.
IEEE International Symposium on Antennas and Propagation and CNC/USNC/URSI Radio Science Meeting, 2010

Angulo, L. D.; Alvarez, J.; Bretones, A. R.; Garcia, S. G.
Time Domain Tools in EMC Assesment in Aeronautics.
EMC Europe, 2010.

Angulo, L. D.; Alvarez, J.; Garcia, S. G.; Pantoja, M. F.; Bretones, A. R.
CDGTD: A new reduced error method combining FETD and DGTD.
IEEE International Symposium on Antennas and Propagation and CNC/USNC/URSI Radio Science Meeting, 2010

Bahl, R.; **Angulo, L. D.**; G. Garcia, S.; Bretones, A.; F. Pantoja, M.; Moreno de Jong van Coevorden, C.; Gomez Martin, R.
Numerical Dosimetry of Cell Cultures.
Proceedings of the VI Iberian Meeting on Computational Electromagnetism, 2008

RESEARCH PROJECTS

University of Granada - Electromagnetics Group of Granada (GEG), Granada, Spain

A-UGRFDTD

August, 2012 - Present

This project consists on the development of a fully functional geometrically conforming FDTD simulator. It is being funded by the *Airbus Group* and the University of Granada.

Teralab

November, 2009 - November, 2009

The TeraLab project aims to develop a numerical laboratory for the design and simulation of Terahertz technology. To do so, physical models of materials in that range of frequency are being developed and integrated in the numerical solvers.

HIRF: SE

December, 2008 - June, 2013

The High Intensity Radiated Fields: Synthetic Environment aims to develop a computer framework to simulate electromagnetic phenomena during the development phase. This project is funded by the European Commission and 44 other partners from the EU. The contribution by our group consisted in a fully functional FDTD volumic solver to be integrated within the framework. More information in: <http://www.hirf-se.eu>

Terasense

October 2008 - March 2012

The aim of Terasense (Terahertz Technology for Electromagnetic Sensing applications) was to develop devices that, working in the range of frequency of Terahertz, are able to detect objects or substances in real time. This project is funded by the Spanish CONSOLIDER research program.

Biological Effects of Radiofrequency

July 2008 - December 2008

The aim of this project was to assess the SAR of different biological tissues. During the course of this project several CEM commercial tools were used, particularly HFSS and Semcad. The project was funded by the European Defence Agency (EDA).

GPR techniques for the assessment of architectural patrimony

July 2008 - March 2010

In this project Ground Penetrating Radar (GPR) techniques were developed and employed to evaluate the state of conservation of some of the Andalusian architectural patrimony. The project was funded by the Tourism and Commerce National Department and was carried on by the Marble Technological Center of Murcia and the University of Granada.

Optimization techniques for UWB antennas

October 2007 - December 2010

This project used CST software together with MatLab and in-house software to design UWB antennas. It was carried out by a partnership of four Spanish universities (UGR, UPC, UPV and UPCT) and funded by a national Research and Development program.